Solar pyrolysis of biomass at laboratory scale

Kuo Zeng

THÈSE

Pour obtenir le grade de

Docteur

Délivré par

UNIVERSITE DE PERPIGNAN VIA DOMITIA

Préparée au sein de l'école doctorale ED305

Et de l'unité de recherche CNRS-PROMES

Spécialité: SCIENCES POUR L'INGENIEUR

Présentée par Kuo ZENG

Solar pyrolysis of biomass at laboratory scale

Soutenue le 1 avril 2016 devant le jury composé de

M. Anthony DUFOUR, Chargé de Recherche, LRGP-ENSIC	Rapporteur
M. Frédéric MARIAS, Professeur, Université de Pau et des Pays de l'Adour	Rapporteur
M. Ange NZIHOU, Professeur, École des mines d'Albi-Carmaux	Examinateur
M. Laurent VAN DE STEENE, Directeur de Recherche, CIRAD UPR114	Examinateur
M. Gilles FLAMANT, Directeur de Recherche, CNRS-PROMES	Directeur de thèse
M. Daniel GAUTHIER, Ingénieur de recherche , CNRS-PROMES	Co-Directeur
M. Doan PHAM MINH, Maître de Conférences, École des mines d'Albi-Carmaux	Invité
Mme. Elsa WEISS, Maître de Conférences, École des mines d'Albi-Carmaux	Invitée

Contents

ABSTRACT

Concentrated solar energy provides heat to drive biomass pyrolysis reactions, which upgrades the feedstock energy by storing solar energy in chemical forms (bio-gas, bio-oil and bio-char). Thanks to high temperature and fast heating rate, more pyrolytic gas with high lower heating value (LHV) can be produced by direct solar pyrolysis.

Experiments have highlighted the effect of solar pyrolysis parameters on products yields, composition and properties. The temperature drastically affects the final product distribution and gas composition. It is the key parameter governing solar pyrolysis reactions. The heating rate and argon flow rate also have a significant influence. By contrast, the pressure has minimal influence on the product distribution. The total gas LHV dramatically increases (5-fold) with increasing temperature (from 600 ℃ to 1200 ℃) and sample heating rate (from 5 ℃/s to 50 ℃/s), which is mainly due to variations in the CO and H_2 yields. The interaction between temperature and heating rate enhances at both high ranges. The maximum gas products LHV (14 589 kJ/kg of beech wood) was obtained at 2000 ℃ and 450 ℃/s heating rate. The collected char and tar were analyzed and characterized, which emphasizes the temperature and heating rate effects. And the energy upgrade factor is determined as about 1.5 independent of temperature.

At the same time, a 2D unsteady CFD particle model (simplified assumption using first-order Arrhenius type reactions) with heat and mass transfers was developed for solar pyrolysis. Numerical model predictions are in good agreement with experimental observations. Stoichiometric coefficients about the mass fraction of primary tar converted by the reaction to gas and secondary tar were determined at different temperatures and heating rates for the first time. The evolution of the final products and mass losses of biomass are enhanced with temperature and heating rate.

Key words: Solar energy, Pyrolysis, Beech wood, Product yield, Gas LHV, Modeling

Nomenclature

Latin letters

A	pre-exponential factor	1/s
a	stoichiometric coefficient	-
B	permeability	m^2
b	stoichiometric coefficient	-
C_p	heat capacity	J/kg/K
D	diffusion coefficient	m^2/s
d_{pore}	pore diameter	m
E	activation energy	J/mol
e	emissivity	-
g	gravity	m/s^2
HHV	higher heating value	J/kg
k	reaction rate constant	1/s
L	length	m
LHV	Lower heating value	J/kg
M	molar mass	kg/mol
m	mass	kg
P	pressure	Pa
Q	heat generation	W/m^3
R	radius	m
R_g	ideal gas constant	J/mol/K
R(t)	char reactivity at time	1/s
x	cylindrical coordinate (heating direction)	m
r	cylindrical coordinate (radius direction)	m
S	source term	$kg/m^3/s$
T	temperature	K
t	time	s
U	upgrade factor	-
V	volume	m^3
v	velocity	m/s
X	char conversion degree	-
Z	dry mass fraction	%

Greek letters

Δh	Reaction heat	J/kg
ΔT	Temperature difference	K
Δt	time difference	s
ε	porosity	-
λ	thermal conductivity	W/m/K
μ	viscosity	Pa.s
ρ	apparent density	Kg/m^3
η	pyrolysis degree	-

Subscripts

Ar	Argon
c	char
cond	conductive
g	gas
is	intermediate solid
r	radial direction
rad	radiative
t1	primary tar
t2	secondary tar
v	total volatiles
w	wood
x	x direction

Chapter 1: Introduction

Historically, economic development has been strongly correlated with increasing energy use. Currently, fossil fuels supply 82% of the world's overall energy needs [1]. Global energy demand is set to grow by 37% by 2040 due to the growing world population and economy. The fossil fuels consumption rate is higher than their formation rate, which inevitably leads to energy crisis in the future. At the same time, the fossil fuels combustion is a major source of greenhouse gas emissions and thus dramatically contributes to global warming.

To match energy demand in the long term while limiting CO_2 emissions, more and more renewable energy should be utilized. Renewable energy only contributed 19 percent to our global energy consumption according to REN21's 2014 report [2]. Renewable sources, such as solar and biomass, are substantial in potential, however they only constitute a very small share of the renewable energy supply [3]. As shown in Figure 1-1, solar energy has a tiny contribution in the world total primary energy supply, less than 1.0% [4]. Biomass represents only approximately 9% of the world's energy needs. Table 1-1 shows the global renewable energy scenario by 2040. Renewable energy will represent approximately 50% of the global energy needs in 2040 according to the European Renewable Energy Council (EREC 2006). Between 2010 and 2040 the significant developments in renewable energy production will be observed in solar energy (from 4.4 to 1332 Mtoe) and biomass energy (from 1080 to 3271 Mtoe)[1].

[1] 1 Mtoe (million ton oil equivalent) is 4.1868×10^{16}J.

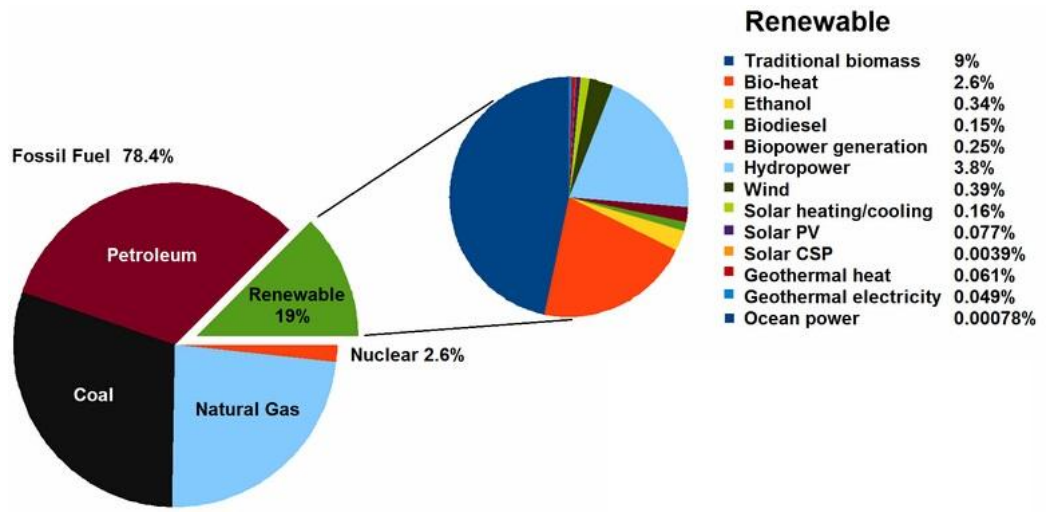

Figure 1-1: Total world energy consumption by source (2013) [2]

Table 1-1: Global renewable energy scenario by 2040 [2]

	2001	2010	2020	2030	2040
Total consumption (Million ton oil equivalent)	10038	10549	11425	12352	13310
Biomass	1080	1313	1791	2483	3271
Large hydro	22.7	266	309	341	358
Geothermal	43.2	86	186	333	493
Small hydro	9.5	19	49	106	189
Wind	4.7	44	266	542	688
Solar thermal	4.1	15	66	244	480
Photovoltaic	0.2	2	24	221	784
Solar thermal electricity	0.1	0.4	3	16	68
Marine (tidal/wave/ocean)	0.05	0.1	0.4	3	20
Total renewable energy source	1365.5	1745.5	2694.4	4289	6351
Contribution of renewable energy source (%)	13.6	16.6	23.6	34.7	47.7

The solar energy reserve is virtually unlimited, free of charge, and its use is ecologically benign. The energy amount from the sun that falls on Earth's surface is enormous. All the energy stored in Earth's reserves of coal, oil, and natural gas is matched by the energy from just 20 sunshine days. However, solar radiation is dilute,

intermittent, and unequally distributed over the Earth's surface. Two main types of solar energy systems are in use today: photovoltaic (for electricity), and thermal systems (storable heat) including low temperature heat and high temperature heat provided by concentrating systems.

Biomass is the fourth wider energy source available, after coal, oil and natural gas [5]. It has the advantages to be widely available and CO_2-neutral, allow continuous power supply and offer several synthesis products [6]. Biomass can be burnt for direct heat or electricity production, or it can be used as raw material to synthesize bio-fuels through biological or thermochemical treatment. Pyrolysis is probably the most attractive process to convert biomass into pyrolytic liquid (tar and water), gases (H_2, CO, CO_2, CH_4, C_2H_6) and char [7]. On the other hand, conventional pyrolysis requires extra energy inputs classically derived from a non-renewable source, which reduces the energy conversion efficiency and causes some environmental problem. Therefore these drawbacks have restricted solar and biomass energy utilization to some extent.

One strategy to overcome these drawbacks is to combine these two energy sources. Indeed concentrated solar energy may provide the heat input for biomass pyrolysis process to convert biomass into solar fuels as shown in Figure 1-2. Three main advantages come from this combination [8]: (1) Gas pollutants' discharge is avoided. (2) The feedstock calorific value is upgraded. (3) The intermittent solar energy is chemically stored in the form of solar fuels. These advantages of solar fuels make them an attractive solution in the quest for clean and renewable fuels.

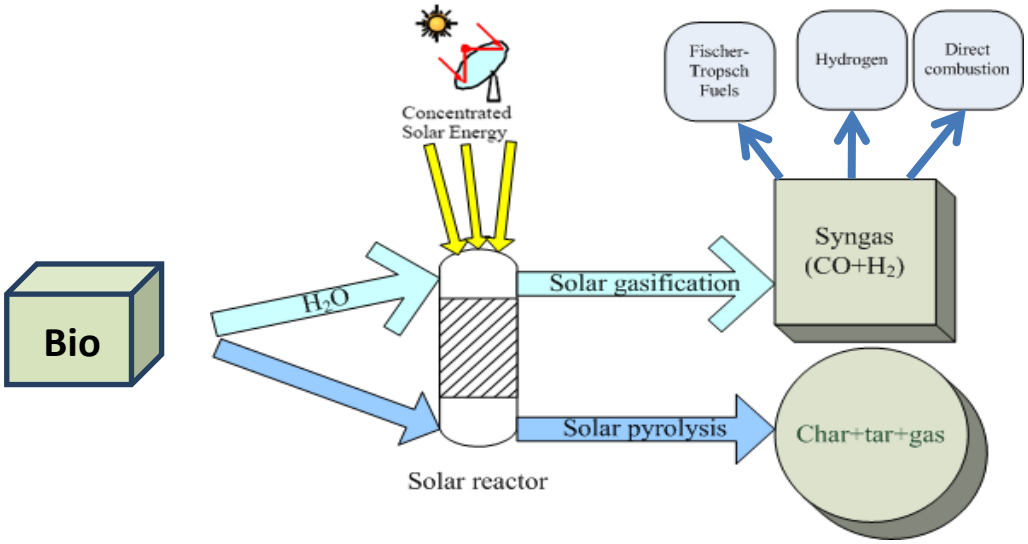

Figure 1-2: Solar-driven steam gasification and pyrolysis process flow sheet.

Solar pyrolysis of biomass uses highly concentrated solar radiation as source of high-temperature process heat to drive biomass pyrolysis reactions in an inert atmosphere. Thus, solar energy in an amount equal to the enthalpy change of the pyrolysis reactions is chemically stored, which upgrades the feedstock energy. Concentrated solar radiation systems generate very high heat flux densities by using mirrors or lenses to concentrate a large area of sunlight onto a small area (solar reactor). Two possible ways are used for transferring solar heat to biomass: indirect or direct. By applying direct solar irradiation, biomass can reach pyrolytic temperatures faster with higher efficiency than with indirect heating. Therefore, more pyrolytic gas can be produced by direct solar pyrolysis (thanks to high temperature and fast heating rate).

The products yields, composition and properties depend on pyrolysis parameters. Temperature, heating rate, pressure are the primary pyrolysis parameters [9], and sweep gas flow rate is typically considered as secondary parameter [10]. Many researchers have investigated pyrolysis parameters in conventional reactors for maximizing the liquid's [11] or char's [12] yield. Pyrolysis gas products have a higher heating value compared with conventional gasification gas [13, 14], and therefore they can be utilized as fuel gas for power generation, heat and transportable fuel production. However, there is scare information about producing high calorific value

gas products through pyrolysis [15].

This thesis's aim is to better understand the biomass pyrolysis in a solar reactor, to quantify the product distribution and composition as a function of the process parameters, and to determine the energetic upgrade factor due to solar input in the process. The upgrade energetic factor quantifies the ratio of solar energy stored in the pyrolysis products with respect to the energetic value of the initial biomass.

In order to reach the objectives, the influence of several operating parameters on biomass pyrolysis was experimentally investigated in a vertical-axis solar reactor. Beech wood pellet was selected as feedstock. There were two steps for experiments, as follows: (1) one-factor-at-a-time (OFAT) approach and (2) response surface methodology (RSM). Firstly, the influences of single-factor: temperature (600-2000 ℃), heating rate (5-450 ℃/s), pressure (0.48-1.18bar) and argon flow rate (6-12NL/min) on product distribution were determined. Then the combined effects of temperature (800-2000 ℃), heating rate (50-450 ℃/s) and argon flow rate (4-8NL/min) were investigated. The gaseous product was characterized to determine the optimum parameters required to maximise the gas products LHV (lower heating value). Besides, some attention was paid to the characterization of co-products, the bio-char and bio-oil obtained from these experiments. Finally, for the first time (not a single published paper) the energetic upgrade factor for solar pyrolysis process was determined.

Moreover, a two-dimensional unsteady single particle model was developed and used to simulate the solar pyrolysis process, under different temperatures with different heating rates. The experimental and modelling results put together allow establishing an integral description of the phenomena involved during wood pellets solar pyrolysis.

1.1 Thesis Outline

This thesis aims at developing solar pyrolysis technology for upgrading biomass into mainly combustible bio-gas, and a few bio-char and bio-tar. This work was supported by SOLSTICE Labex, French "Investments for the future" programme

managed by the National Agency for Research under contract ANR-10-LABX-22-01.

Chapter 2 gives the description of wood, principles of biomass pyrolysis, the product evolution in pyrolysis process and different conventional pyrolysis technologies. In Chapter 3, the state-of-the-art of solar pyrolysis technologies, experimental setup and preparation, beech wood characterization and solar pyrolysis products characterization are introduced. Chapter 4 uses One-factor-at-a-time approach to study the effect of temperature (600-2000 ℃), heating rate (5-450 ℃/s), pressure (0.48-1.18 bar) and argon flow rate (6-12 NL/min) on the product distribution. In Chapter 5, Box-Behnken experimental design and response surface methodology (RSM) is used to investigate the interaction effects of temperature, heating rate and argon flow rate on products distribution. Chapter 6 presents the characterization of char and tar prepared at different temperatures and heating rates. Further, the energy upgrade factor of solar pyrolysis process is determined. In Chapter 7, a two-dimensional unsteady single particle heat and mass transfer model coupling chemical reactions is developed. Its predictions of product distribution are compared to the experimental measurements and its sensitivity to temperature and heating rate changes is analysed. Finally, the overall conclusions and an outlook are presented in Chapter 8.

References

[1] IEA, World Energy Outlook 2014: IEA, 2014.

[2] REN21. 2014. Renewables 2014 Global Status Report.

[3] Lund H. Renewable energy strategies for sustainable development. Energy 2007;32:912-919.

[4] Ramachandra, T.V. Solar energy potential assessment using GIS. Energy Education Science and Technology 2007;18:101–114.

[5] Blasi CD. Combustion and gasification rates of lignocellulosic chars. Progress in Energy and Combustion Science 2009;35:121-140.

[6] Puig-Arnavat M, Tora E.A, Bruno J.C, Coronas A. State of the art on reactor designs for solar gasification of carbonaceous feedstock. Solar Energy 2013;97:67-84.

[7] Babu B.V, Chaurasia A.S. Modeling, simulation and estimation of optimum parameters in pyrolysis of biomass. Energy Conversion and Management 2003;44:2135-2158.

[8] Nzihou A, Flamant G, Stanmore B. Synthetic fuels from biomass using concentrated solar energy - A review. Energy 2012;42:121-131.

[9] Blasi CD. Modeling chemical and physical processes of wood and biomass pyrolysis. Progress Energy Combustion Science 2008;34:47-90.

[10] Akhtar J, Amin NS. A review on operating parameters for optimum liquid. Renewable Sustainable Energy Review 2012;16:5101-5109.

[11] Kin J-Y, Oh S, Hwang H, Moon Y-H, Choi JW. Assessment of miscanthus biomass (Miscanthus sacchariflorus) for conversion and utilization of bio-oil by fluidized bed type fast pyrolysis. Energy 2014;76:284-291.

[12] Antal MJ, Grønli M. The art, science and technology of charcoal production. Industrial & Engineering Chemistry Research 2003;42:1619-1640.

[13] Abnisa F, Daud WMAW. A review on co-pyrolysis of biomass: An optional technique to obtain a high-grade pyrolysis oil. Energy Conversion and Management 2014;87:71-85.

[14] Chen G, Andries J, Luo Z, Spliethoff H. Biomas pyrolysis/gasification for

product gas production: the overall investigation of parametric effects. Energy Conversion and Management 2003;44:1875-1884.

[15] Görling M, Larsson M, Alvfors P. Bio-methane via fast pyrolysis of biomass. Applied Energy 2013;112:440-447.

.

Chapter 2: Background

2.1 Wood description

Wood remains the largest biomass energy source providing over 9% of the world global total primary energy supply. It has been widely chosen for pyrolysis raw materials because of its worldwide abundance. The wood chemical structure and basic organic components are extremely important in pyrolysis processes for producing derived fuels and chemicals.

2.1.1 Wood structure

Wood complex structure is presented in Figure 2-1. It is mainly composed of cellulose, hemicelluloses and lignin. The cellulose polymers are arranged in micro fibrils, that are combined into wood cell wall. Cellulose fibrils are embedded in the matrix formed by hemicellulose with lignin [1].

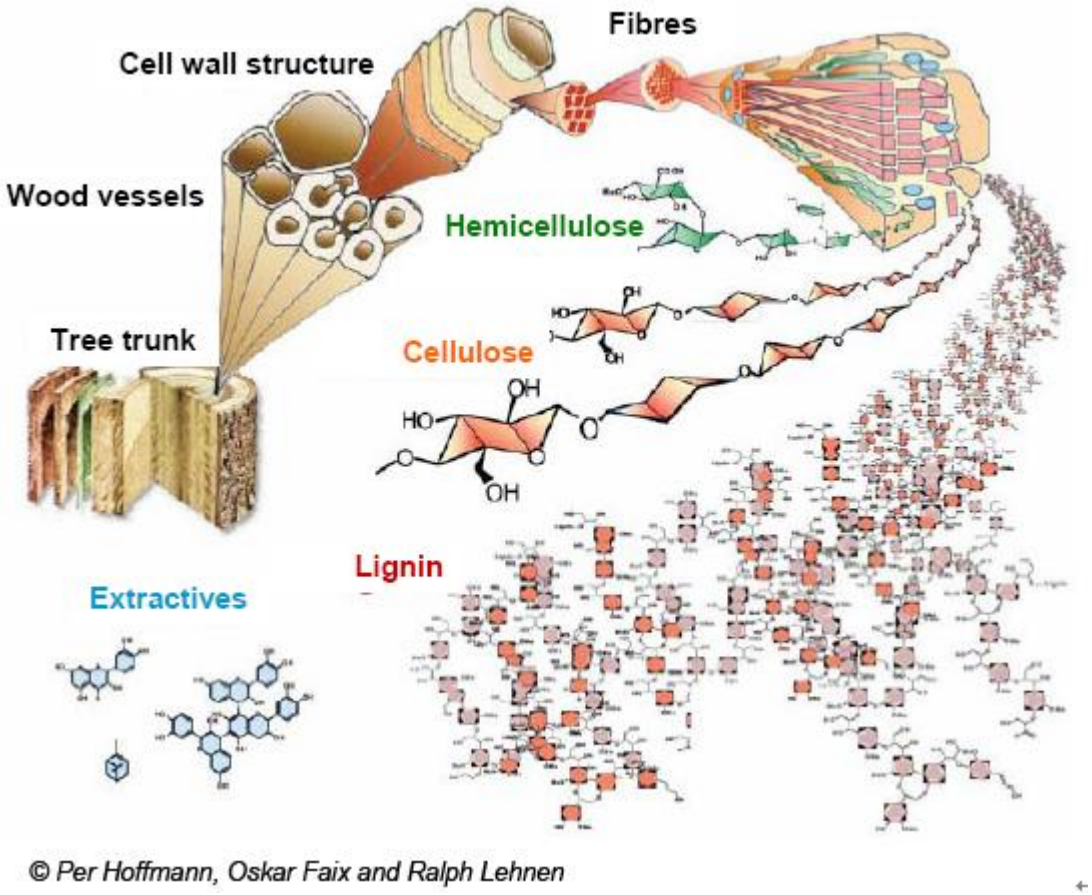

Figure 2-1: Wood structure [2]

2.1.2 Wood multiscale nature

Length scales within wood span eleven magnitude orders (10^{-10} to 10^{1} m) as shown in Figure 2-2. At the smallest length scale (10^{-10} m), wood is comprised of C–C, C–H, C–O and O–H bonds as well as oxygenated and aromatic rings. These functional groups make up three biopolymers (10^{-9} to 10^{-8} m): cellulose, hemicelluloses and lignin. Cellulose microfibrils (cellulose bound together) groups are connected by hemicellulose and lignin to produce plant cells (10^{-8} to10^{-7} m) [3]. Adjacent cells groups form a multicellular porous structure comprised of smaller (lumen) and larger (parenchyma) cavities (10^{-5} to 10^{-4}m) [4]. Multicellular structures then combine to form fibers (plant macrostructure 10^{-3} to 10^{-2} m), which is the right size for feeding pyrolysis reactors.

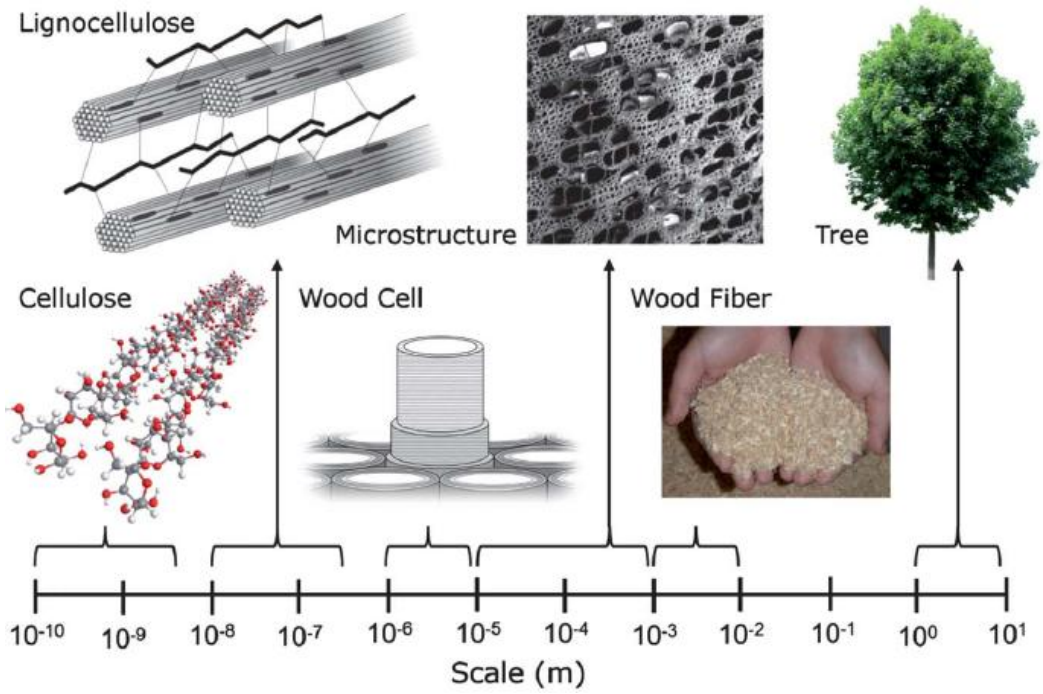

Figure 2-2: Multiscale nature of wood [5].

2.1.3 Wood composition and heating value

Wood has an elemental composition of about 45-50 wt% carbon, 6-6.5 wt% hydrogen, 38-42 wt% oxygen, 0.1-0.5 wt% nitrogen, max 0.05 wt% sulphur and trace amounts of several metal ions. Softwoods tend toward higher carbon and lower oxygen content than hardwoods. The proximate analysis of wood shows the following

components : volatile matter (about 80 wt.%), fixed carbon (19 wt.%) and ash (0.65 wt.%). Raw wood can contain up to 50 wt% of water. After natural drying, moisture can be decreased to about 10 wt% to 20 wt%, depending on the storage conditions.

Depending on the plant species, softwoods contain 40-45 wt% cellulose, 25-35 wt% lignin, and 25-30 wt% hemicelluloses. Hardwoods contain 40-50 wt% cellulose, 20-25 wt% lignin, and 25-35 wt% hemicelluloses. A smaller amount of (organic and inorganic) extractives (2-3 wt%) and other inorganic compounds (0.3-0.4 wt%) are also included in the wood.

Given that the concentrations of lignin tend to be higher in softwoods than in hardwoods, softwoods tend to have slightly higher heating values. Telmo and Lousada [6] have determined the calorific values of wood pellets from different wood species using a Parr 6300 bomb calorimeter, following the CEN/TS 14918:2005. They found that softwoods had HHV (Higher Heating Value) between 19660.02 and 20360.45 kJ/kg, and hardwoods had HHV ranging between 17631.66 and 20809.47 kJ/kg. Concerning the LHV (Lower Heating Values), softwoods ranged from 15629.71 to 16935.72 kJ/kg and hardwoods ranged from 14411.54 to 17907.85 kJ/kg, when the moisture content was about 7.3-17.8 wt%.

2.2 Principles of biomass pyrolysis

Biomass pyrolysis is the heating of feedstock in an inert atmosphere to decompose it into gaseous products (mainly CO_2, CO, H_2, CH_4, C_2H_2, C_2H_4, C_2H_6, etc), liquid products (tar, high molecular hydrocarbon and water) and solid products (char). Figure 2-3 illustrates wet biomass pyrolysis processes. The sample is firstly dried between 100℃ and 200℃ with a slight weight loss, when some internal rearrangements such as bond breakage, appearance of free radicals and formation of carbonyl groups take place, with a corresponding water, carbon monoxide and carbon dioxide small release. The primary pyrolysis occurs and produces primary products (denoted by “1” in Figure 2-3) when temperatures increases to above 250℃. The primary pyrolysis is the main pyrolysis process finished at temperatures around 500℃, during which solid decomposition occurs, accompanied by a significant weight loss.

The primary products can further participate in a variety of secondary reactions forming final products (denoted by "2" in Figure 2-3) if the sample is heated at higher temperatures. There are three stages for primary vapors secondary reactions as shown in Figure 2-4 [7]. Between 500 and 600 ℃, the higher molecular weight products from lignin are slightly cracked into lighter aromatics and oxygenate in less than one second. Around 700 ℃, the formation of CO, light olefins, aromatics (from carbohydrates) is the secondary stage. At higher temperatures, the third stage leads to tertiary products (polynuclear aromatics) formation.

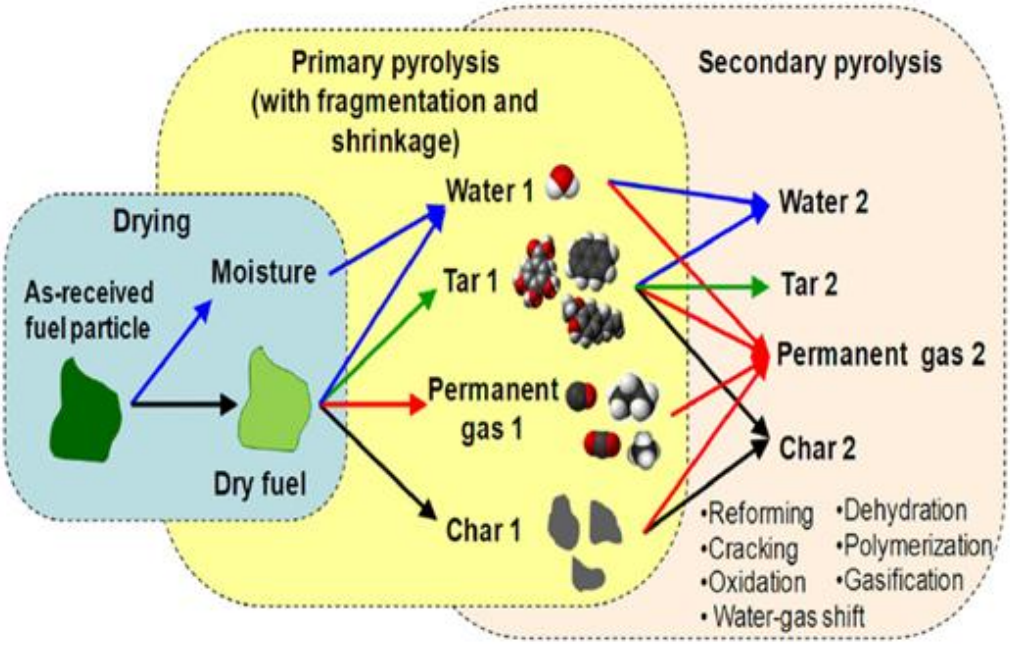

Figure 2-3: Pyrolysis of wet sample: drying, primary pyrolysis and secondary pyrolysis. The arrows indicate the main routes for products' formation [8].

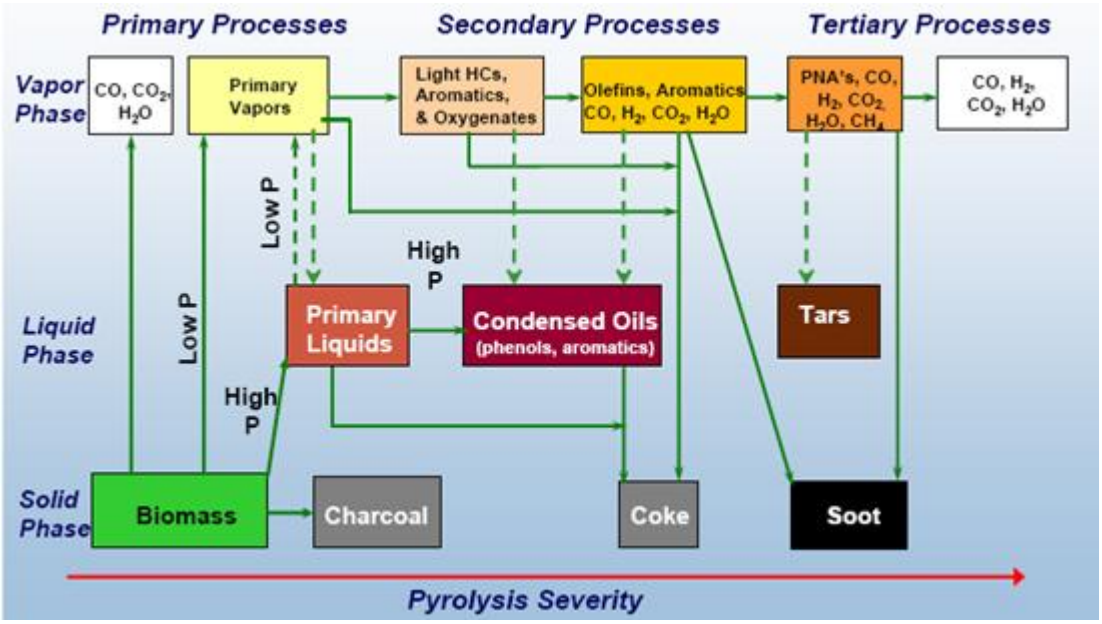

Figure 2-4: Biomass pyrolysis pathways [7].

The pyrolysis products' distribution depends on the pyrolysis method, the characteristics of the biomass and the reaction parameters. Table 2-1 summarizes the main pyrolysis technologies and their major products [9]. Slow pyrolysis has been mainly used for charcoal production at low temperature and heating rate [10]. In slow pyrolysis, the vapor residence time is high (5 min to 30 min) and vapor phase components continue to react with each other resulting in solid char and other liquids formation [11]. Fast pyrolysis process is receiving incredible popularity in producing liquid products [12]. The fast pyrolysis process basic characteristics are high heat transfer and heating rate, very short vapor residence time, rapid cooling of vapors and precision control of reaction temperature around 500 ℃ [13]. Fast pyrolysis process produces 60-75 wt% of liquid bio-oil, 15-25 wt% of solid char and 10-20 wt% of non condensable gas, depending on the used feedstock [14]. Flash pyrolysis is sometimes considered as very fast pyrolysis [13], usually in the context of laboratory studies involving small particle rapid movement through a heated tube under gravity or in a gas flow. Higher temperatures and shorter residence times than fast pyrolysis are used. At higher temperatures, primary vapors secondary reactions are more likely to happen, which leads to more gas production (up to 75%) in flash pyrolysis.

Table 2-1: Pyrolysis technology, process conditions and product distribution [9].

Pyrolysis Technology	Process conditions			Product yields		
	Residence Time	Heating rate	Temperature (℃)	Liquid (wt.%)	Solid (wt.%)	Gas (wt.%)
Slow	5-30min	<50 ℃/min	400-600	<30	<35	<40
Fast	5s<	10-200 ℃/s	400-600	<75	<25	<20
Flash	0.1s<	~1000 ℃/s	650-900	<20%	<20%	<70%

2.2.1 Physical phenomena

The biomass particle external surface is initially heated by transient heat radiation, convection and conduction when exposed to high-temperature source with surrounding gas. Then the moisture evaporates. Successively, the yet dried particle portion undergoes thermal degradation. A char layer is formed when all the volatile species are removed from the solid. Therefore, the following spatial zones appear during the process transients: an inert char layer, a pyrolysis region, a drying region and the virgin moist solid shown in Figure 2-5 [15].

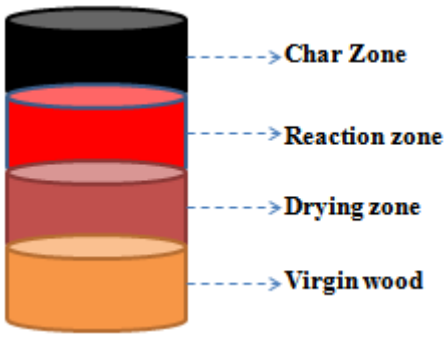

Figure 2-5: 1D scheme of the propagating thermal front moving through the pellet undergoing pyrolysis reaction

The wood pyrolysis chemistry and occuring transport phenomena are presented in Figure 2-6. The wood fibers (lignocellulosic materials) decomposition occurs through the solid cellular wall material thermal degradation, forming an intermediate liquid that subsequently decomposes at high temperature and generates volatile organic compounds (VOCs) flowing through the wood pore (cellular lumen) [5]. Water vapor diffusive transport and bound water diffusion and convection with free water capillary flow through the voids are controlled by initial moisture content. Pyrolysis VOCs (volatile products and water vapor) mainly leave the particle flowing

across the heat-exposed surface owing to larger permeability. Tar secondary reactions may occur at the high-temperature regions of the particle. Indeed, primary tar vapors secondary reactions also take place outside the biomass particle, given sufficiently high temperature and residence times. Besides, a fraction of VOCs may also move toward low-temperature regions, where re-condensation may occur. In addition to heat, momentum and mass transfers, reacting particle physical structure changes are observed with the cracks network development in the already pyrolyzed region, surface regression, internal shrinkage and/or swelling and primary fragmentation in some cases [15].

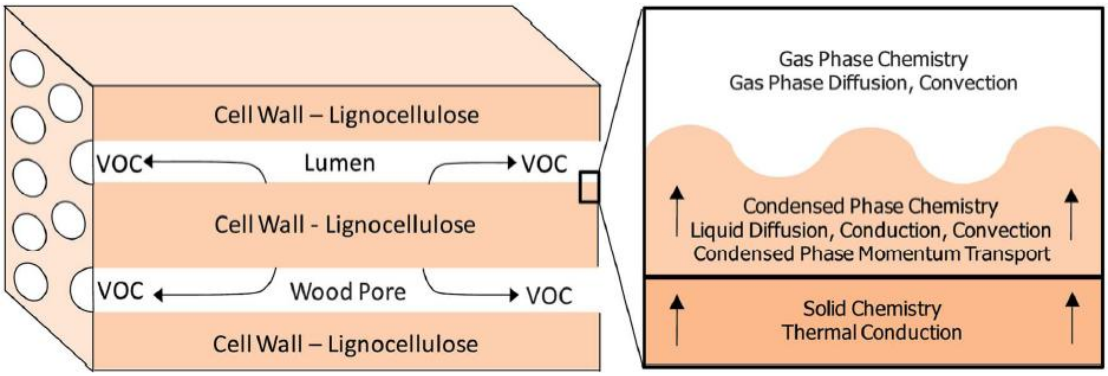

Figure 2-6: Wood pyrolysis chemistry and transport phenomena [5].

2.2.2 Chemical phenomena

Biomass is mainly composed of cellulose, hemicellulose, and lignin in addition to extractives (tannins, fatty acids, and resins) and inorganic salts [3]. Woody biomass typically contains about 40-47 wt% cellulose, 25-35 wt% hemicellulose, and about 16-31 wt% lignin [14]. Biomass main components degrade differently depending on the temperature to yield different product spectra [16]. Figure 2-7 gives a schematic overview of the main biomass fractions thermal stability regimes [17]. The thermal stability bars height corresponds to the approximate temperature level at which the thermal degradation rate under isothermal conditions and in inert atmosphere reaches a maximum value [18]. It can be noticed that hemicellulose decomposes at the lower temperatures (from 200 to 300 ℃), followed by cellulose (from 300 to 400 ℃) and then lignin (from 250 to 500 ℃). Hemicellulose and cellulose decompose into condensable vapors (liquid products) and gas. Lignin decomposes into liquid, gas and

solid char products. Extractives contribute to liquid and gas products either through simple volatilization or decomposition. In general, minerals remain in the char termed as ash.

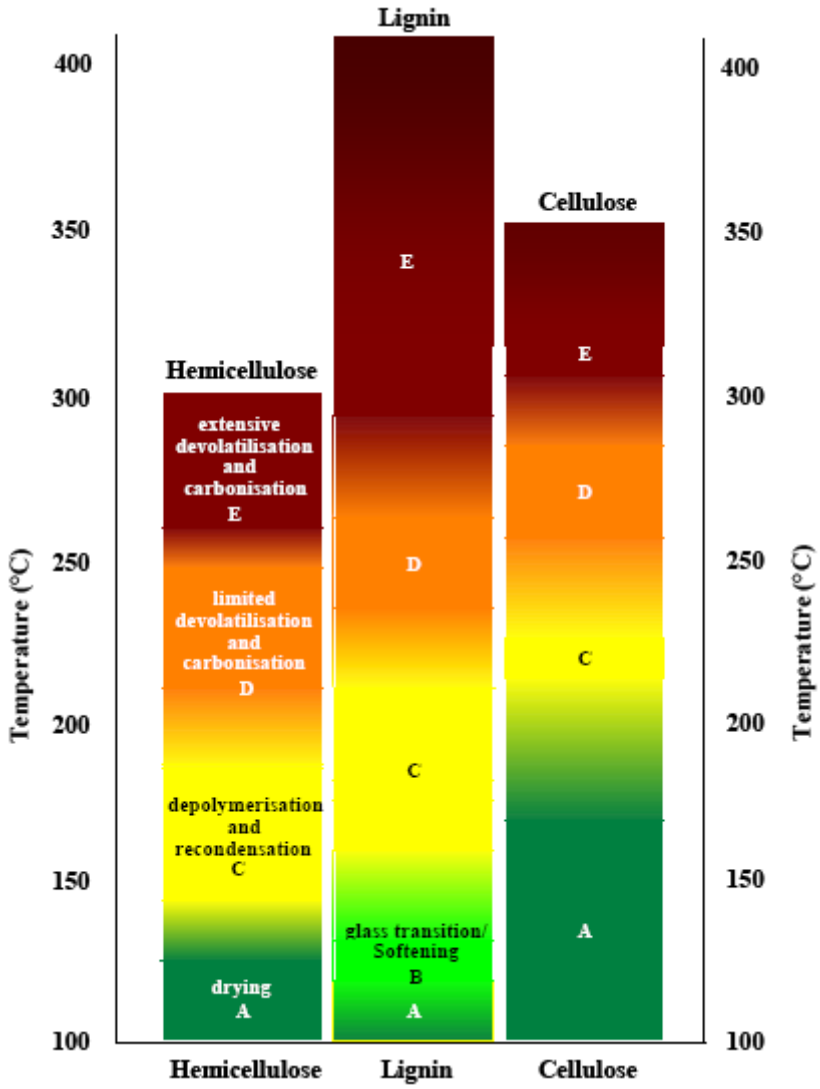

Figure 2-7: Thermal stability regimes for hemicellulose, lignin and cellulose [17].

Hemicellulose is a complex polysaccharide usually with the general formula $(C_5H_8O_4)_m$ and polymerization degree of 50–200 [19]. Water, methanol, formic, acetic, propionic acids, hydroxyl-1-propanone, hydroxyl-1-butanone, 2-methylfuran, 2-furfuraldehyde, dianhydroxylopyranose, and anhydroxylopyranose are identified as the main products through complex pathways shown in Figure 2-8 [9].

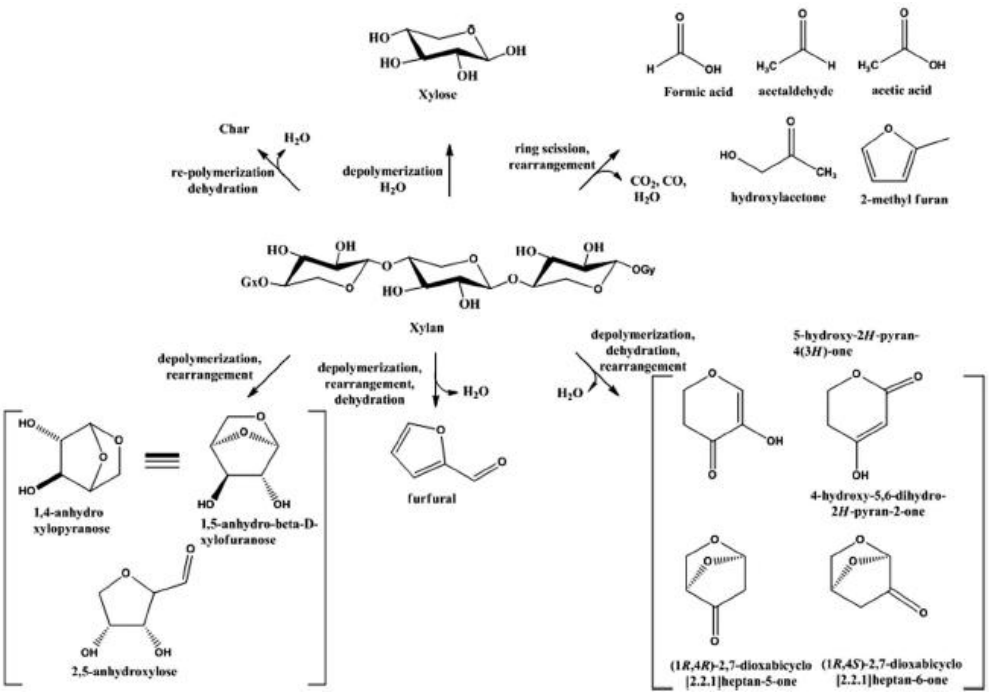

Figure 2-8: Hemicellulose pyrolysis pathway [20].

Cellulose is a glucose polymer, composed of (1, 4)-D-glucopyranose with the general formula $(C_6H_{10}O_5)_n$ and polymerization degree often exceeding 2000 [21]. The major products are levoglucosan, hydroxyacetaldehyde, furfural, formic acid, acetic acid, and aldehyde compounds shown in Figure 2-9 [9].

.

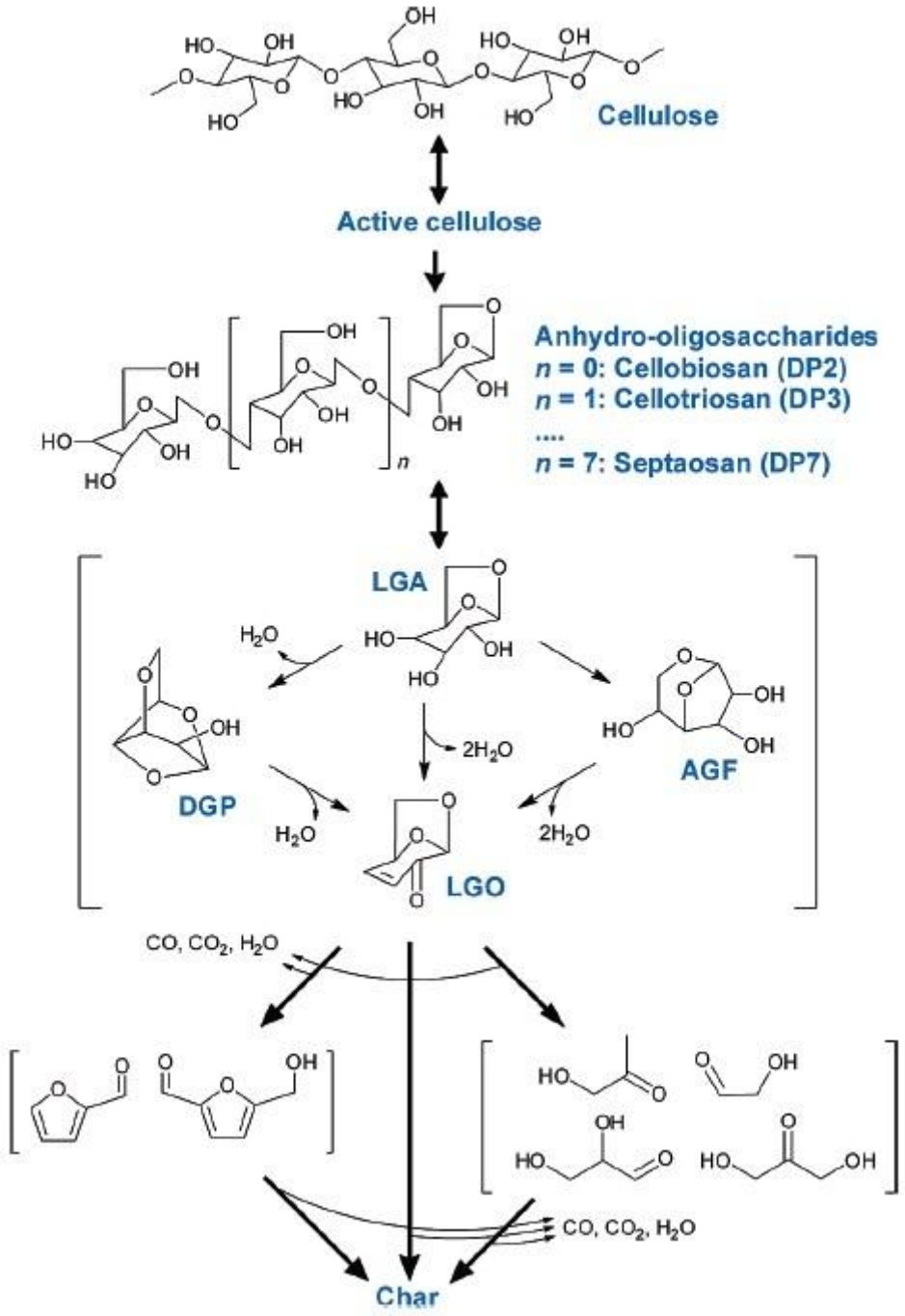

Figure 2-9: Cellulose pyrolysis pathway [22].

Lignin has a three-dimensional network formed by different non-phenolic phenylpropanoid units linked with a variety of ether and C–C bonds [19]. Figure 2-10 shows a proposed mechanism of lignin pyrolysis leading to the formation of 2-methoxy-4-methyl phenol, guaiacol, 1,2-ethanediol diacetate, 1,4-butanediol vanillin, eugenol, and polyaromatic char from the model compound [23].

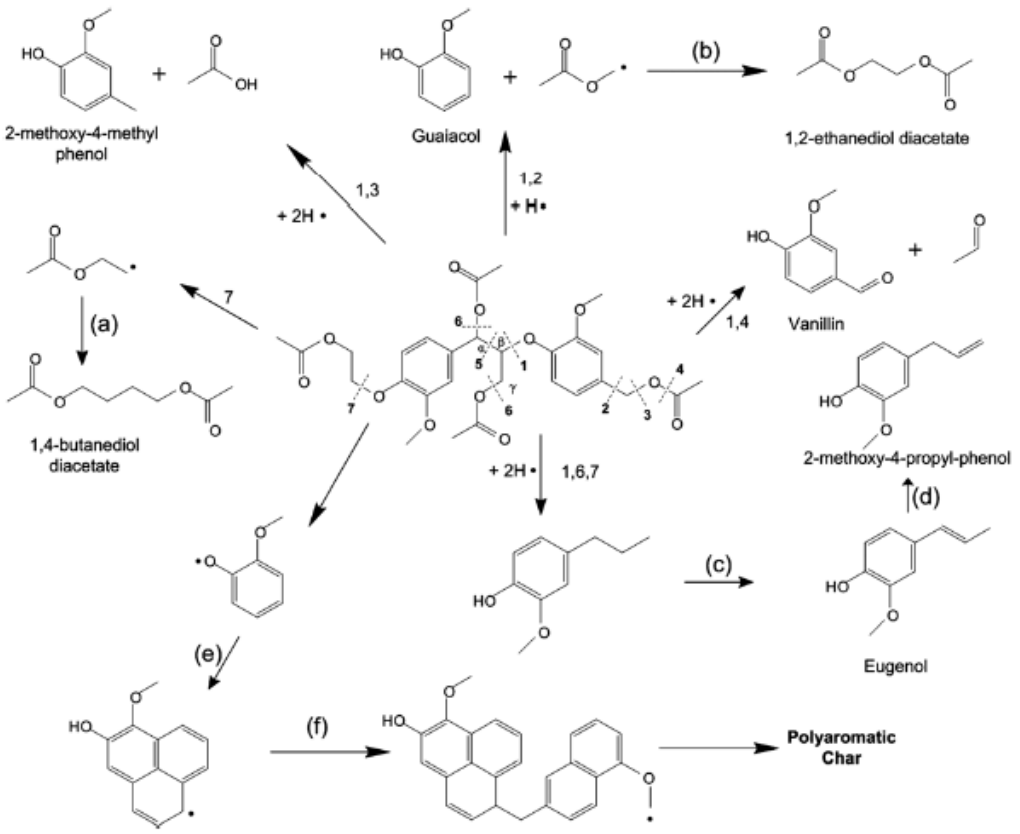

Figure 2-10: Lignin pyrolysis pathway [24].

2.3 Product distribution from biomass pyrolysis

Extensive information is available on product yields and composition for biomass pyrolysis. The pyrolysis products distribution depend mostly on the particle heating rate and temperature, partly on the pressure and sweep gas flow rate. A low temperature, fast heating rates and short vapor residence time are applied to maximize the yields of bio-oil [25]. A high temperature, low heating rate and long residence time process are preferred for maximizing gas yield [26]. A low temperature, low heating rate and long residence time is the optimum process for getting maximum char yield [27].

Pyrolysis products (tar, gas and char) result from both solid fuel primary decomposition and volatile condensable organic products secondary reactions into low-molecular gases and char when they are transported through the particle and the reaction environment [28]. Gaseous products can be used for heat production and power generation, which is usually used to provide energy to sustain the pyrolysis

process or to dry the feedstock. Liquid products can be transported and stored for use in energy and heat generation in boilers as a fuel-oil substitute (or in co-firing) and they have the potential to be employed as a liquid transportation fuel for internal combustion engines. Char can be used as a fuel in form of briquettes or as a char-oil, char-water slurry; alternatively char can be upgraded to activated carbon and used in purification processes.

2.3.1 Liquid evolution

Tar is a complex mixture of condensable hydrocarbons, which includes single to 5-ring species, other oxygen-containing and complex polycyclic aromatic hydrocarbons [29]. The tar transformation and main components are shown in Figure 2-11. In the temperature range 400-700 ℃, the biomass breaks down into primary tar characterized by oxygenated compounds. The primary tar release is mostly contributed by hemicellulose (<400 ℃) and cellulose (<400 ℃) whilst that from lignin is negligible. After its evolution from the solid phase, the primary tar vapor is subjected to secondary tar reaction forming secondary and tertiary tars. Tar secondary reactions are classified as homogeneous and heterogeneous and include processes such as cracking, partial oxidation, (re)polymerization and condensation [30]. In the temperature range 700-850 ℃, primary tar components decompose into lighter non-condensable gases and secondary tar including phenolics and olefins. Tertiary tar such as aromatics appear in the temperature range 850-1000 ℃ [7]. CO is the quantitatively most important product from tar homogenous conversion while H_2 is even a better indicator for secondary tar reaction [30].

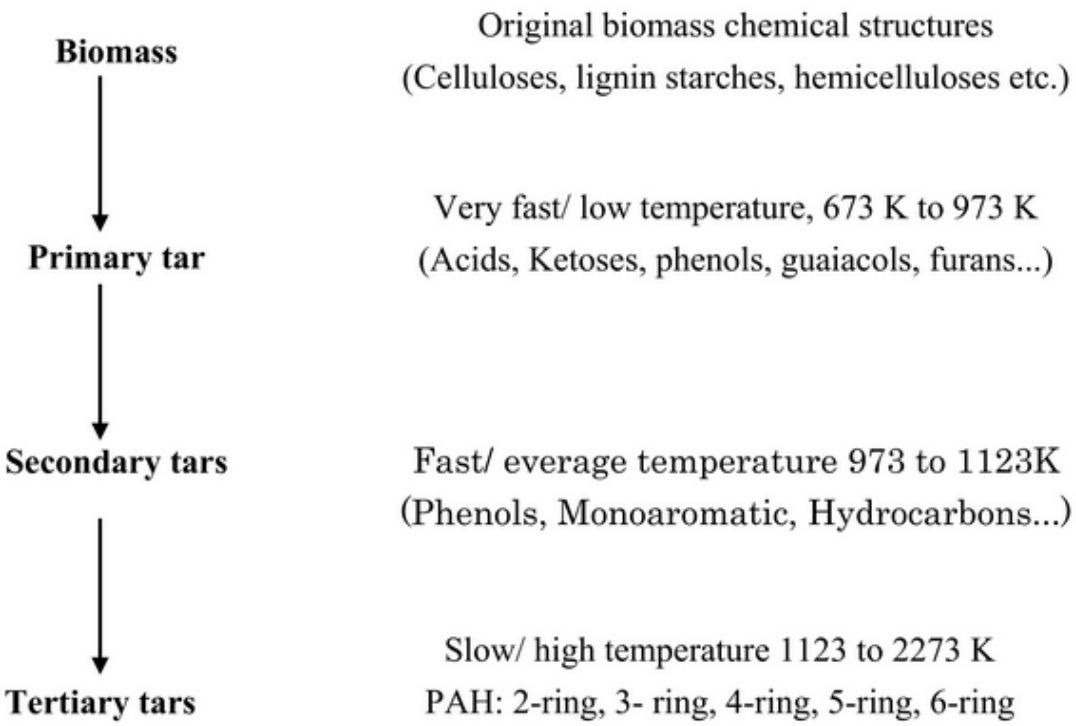

Figure 2-11: Biomass tars formation [31].

Typical woody biomass fast pyrolysis bio-oil has higher oxygen and water content and lower HHV, H/C ratio compared to crude oil, as shown in Table 2-2. The immediate bio-oil consumption in boilers/turbines is hindered by the poor fuel characteristics (highly oxygen content), chemical complexity (hundreds of compounds) and instability (due to oxygen content and acidity) [32]. It is desirable and necessary to improve the quality and stability. Oxygen must be removed before the bio-oil can be used as a replacement for diesel and gasoline [33]. The chemical composition classified by functional groups with relative abundance is shown in Figure 2-12. The main bio-oil includes three major compound families [9]: (i) small carbonyl compounds such as acetic acid, acetaldehyde, acetone, hydroxyaldehydes, hydroxyketones, and carboxylic acids; (ii) sugar-derived compounds, which are mainly furfural, levoglucosan, anhydrosugars, furan/pyran ring-containing compounds; and (iii) lignin-derived compounds such as phenols and guaiacols; molecular weight ranging from 900 to 2500 oligomers [34]. Compound distribution influences bio-oil physical properties. Its distribution mostly depends on the biomass type and the process severity [35].

Table 2-2: Typical elementary composition of bio-oil and crude oil [36].

Composition	Bio-oil	Crude oil
Water (wt%)	15–30	0.1
pH	2.8–3.8	—
Density (kg/L)	1.05-1.25	0.86-0.94
Viscosity 50 ℃ (cP)	40-100	180
HHV (MJ/kg)	16-19	44
C (wt%)	55–65	83.86
O (wt%)	28–40	<1
H (wt%)	5–7	11-14
S (wt%)	<0.05	<4
N (wt%)	<0.4	<1
Ash (wt%)	<0.2	0.1
H/C	0.9–1.5	1.5–2.0
O/C	0.3–0.5	~0

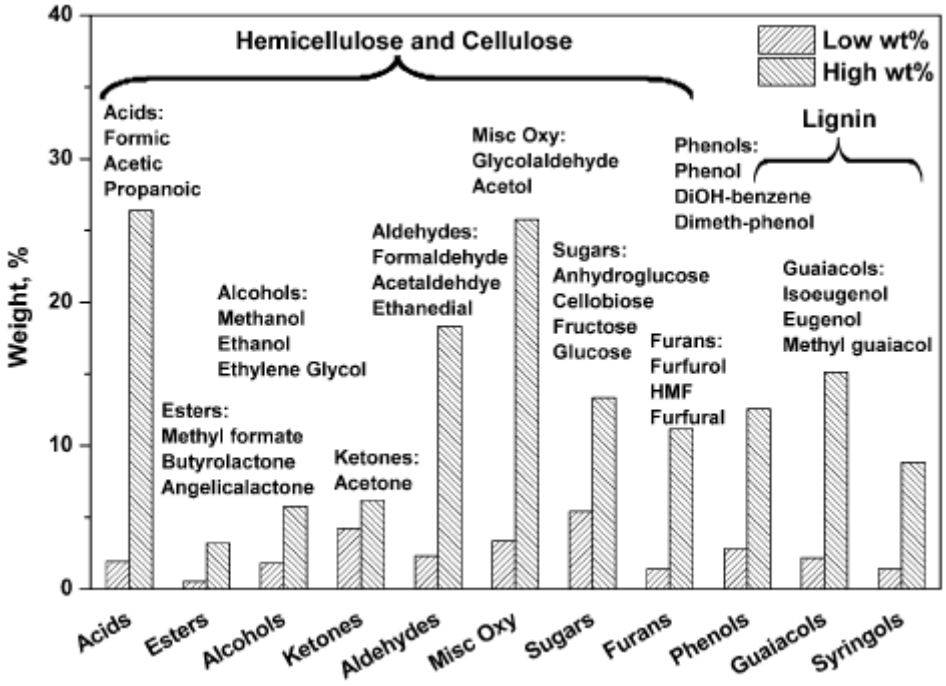

Figure 2-12: Chemical composition of bio-oil from wood biomass and the most abundant molecules of all components [33].

2.3.2 Gas evolution

The pyrolysis gas consists mainly of CO_2, CO, CH_4 and lower amounts of H_2 and C_2 hydrocarbons [37, 38]. At low temperatures, CO and CO_2 (and water vapor) evolution is mainly due to extractives and hemicellulose degradation and cellulose degradation in first path leading to gas and char formation [39]. As temperature increases, the formation of tar vapors from cellulose becomes predominant, while

lignin degradation also attains fast rates and leads to additional gas (CO_2, CO, CH_4 and H_2) and char formation. The secondary reaction of tar (mainly from cellulose degradation at high temperature) also influences the gas yields and composition [40-43]. Carbon dioxide is a product of both primary and secondary reactions (it can account up to 14% of tar conversion [30].). Carbon monoxide and methane are produced in small quantities from primary reactions. A large part of their production, with acetylene, ethylene, ethane and hydrogen, arises from secondary decomposition [28]. In particular, carbon monoxide and methane yields almost linearly increase with temperature for values above 675 ℃ [30]. It is suggested that carbon monoxide concentration can be considered as an indicator for secondary reaction activity extent as it may account for about 50-70% of tar conversion (methane and ethylene account for 11 and 12%, respectively) [40]. However, Morf et al. [30] observe that hydrogen yield presents an exponential increase with temperature, which is even a better indicator for tar secondary reactions. High temperatures also make possible contribution from reforming reactions of hydrocarbons (tar species) and water gas shift reactions on gas composition [43].

Yang et al. [44] have investigated the main gas products release from biomass pyrolysis in TGA with Fourier transform infrared (FTIR) spectroscopy. The C-C and C-O bonds of cracking and abscission from hemicellulose at low temperature (280 ℃<500 ℃) contribute a lot to CO_2 release. It is also mostly contributed by lignin at high temperature (700 ℃>500 ℃), while cellulose only contributes a small quantity at low temperature (380 ℃). CO is mainly released with the cracking of carbonyl (C-O-C) and carboxyl (C=O). CO release is mostly caused by hemicellulose in the whole temperature range and by lignin at high temperature (760 ℃>600 ℃) owing to tar thermal cracking in the solid sample, whilst cellulose only contributes minor portion. The cracking of methoxyl-O-CH3 from lignin, hemicellulose and cellulose at low temperature (500 ℃<600 ℃) causes the CH_4 release. H_2 is released at temperatures higher than 400 ℃, and the release increases greatly with temperature. Hemicellulose and lignin significantly contribute H_2 release and get maximum rate at

600 ℃.

The detailed gas reactions involved in pyrolysis are generally listed as:

$$C + CO_2 \leftrightarrow 2CO \quad \Delta H^0_{298} = +168\ MJ/kmol, \quad (1)$$

$$C + H_2O \leftrightarrow CO + H_2 \quad \Delta H^0_{298} = +175\ MJ/kmol, \quad (2)$$

$$CH_4 + H_2O \leftrightarrow CO + 3H_2 \quad \Delta H^0_{298} = +206\ MJ/kmol, \quad (3)$$

$$CH_4 + 2H_2O \leftrightarrow CO_2 + 4H_2 \quad \Delta H^0_{298} = +165\ MJ/kmol, \quad (4)$$

$$CO + H_2O \leftrightarrow CO_2 + H_2 \quad \Delta H^0_{298} = -41\ MJ/kmol, \quad (5)$$

$$C + 2H_2 \leftrightarrow CH_4 \quad \Delta H^0_{298} = -75\ MJ/kmol, \quad (6)$$

$$[C_xH_yO_z] + H_2O \rightarrow CO + H_2 + Tar \quad (7)$$

$$[C_xH_yO_z] + CO_2 \rightarrow CO + H_2O + Tar \quad (8)$$

where $[C_xH_yO_z]$ indicates intermediate tar phase, which can further decompose, steam gasify and partially oxidize into gases and final tars.

The palm oil waste fiber pyrolysis thermodynamic calculations using HSC-Chemistry 4.0 software are plotted in Figure 2-13 [45].

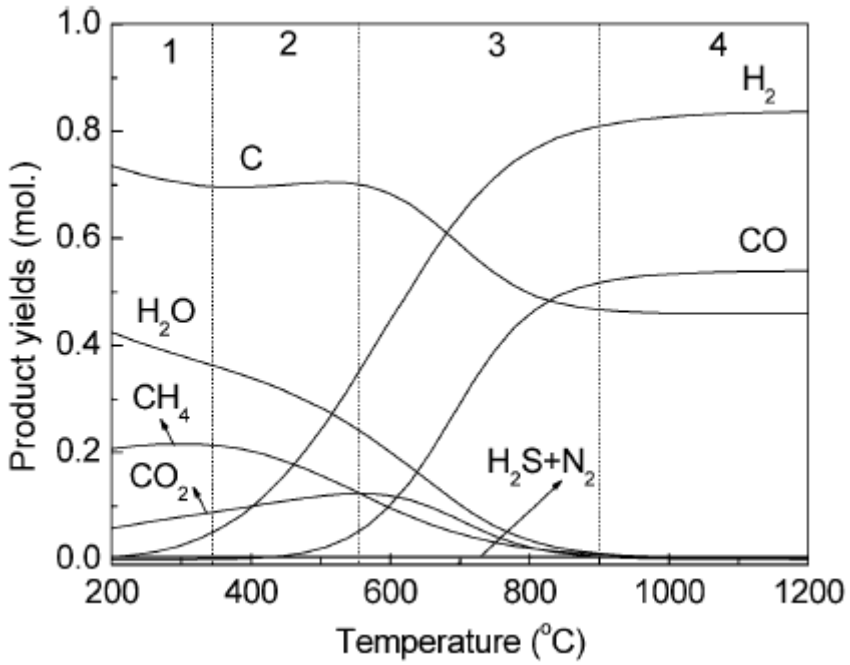

Figure 2-13: Calculated species from the pyrolysis of fiber [45].

As shown in Figure 2-13, four temperature zones exist for biomass pyrolysis. In the first zone (<340 ℃), water vapor, CO_2 and CH_4 are released as biomass becomes dehydrated. They are likely to react with carbon (char) in reactions (1) and (2), which form H_2 and CO at higher temperatures (600-1000 ℃). The decrease of C and water, and increase of CH_4 and CO_2 are contributed by the slightly exothermic reactions (5) and (6) at low temperatures (500-600 ℃). In the second zone (340-560 ℃), the main reactions are (3) and (4), which favor the CH_4 and water decrease but CO_2 increase. In the third zone (560-900 ℃), the pyrolysis is controlled by the secondary reaction in (1) and (2), which increases the CO and H_2 contents. The further decrease of CH_4 is caused by the continuous homogeneous reaction (3). In the last zone (>900 ℃), almost no reaction occurs as the pyrolysis ends. 45 mol% H_2 and 30 mol% CO remains high and stable. Temperature increase favors endothermic reactions. Therefore with temperature increase, reactions (1)-(4), (7) and (8) shift to the right, whereas reactions (5) and (6) shift to the left. The highest yields of CO and H_2 are obtained at the highest temperatures, whereas the lowest temperatures favor the CH_4 and H_2O formation.

2.3.3 Solid evolution

The solid products are a complex mix of char, coke and soot. Primary charcoal is porous and amorphous retaining original lignocellulosic morphology. It is composed of carbon with small amounts of hydrogen, oxygen and minerals. However, there is no unified distinction between coke and soot. Sometimes, both of them are named as secondary char [27]. Soot is black solid mainly composed of carbon, hydrogen and traces of oxygen, sulfur and nitrogen.

From temperature 250 ℃ to 290 ℃, Primary charcoal is formed [46]. Primary char continues devolatilization due to the further cleavage of the C--H and C--O bonds resulting in the carbon enrichment of the residual solid (typically more than 90 wt%) [47]. During this process, tar intra-particle polymerization progresses at approximately 380 ℃ and intra-particle tar decomposition to form secondary gas (mainly CO) occurrs at 400-500 ℃ [48]. And tar decomposed onto the solid surface when the temperature is higher than 500 ℃ [27]. The tar decomposition and intra-particle tar polymerization help coke formation. When pyrolysis temperature is higher than 900 ℃, Soot is also formed in the char product. Soot forms through homogeneous nucleation of high temperature hydrocarbons decomposition products [7]. High hydrocarbons, mainly oxygenated tar compounds, crack into phenolics that subsequently decompose into small aromatic rings, light hydrocarbons (mainly CH_4 and olefins) and non hydrocarbon gas (CO and H_2). Light hydrocarbons decompose and form C_2H_2, which is the original compound for aromatic compounds. At high temperature (above 900 ℃), benzenic rings grow with C_2H_2 or C_6H_6 to form PAH. The nucleation of primary soot particle takes place in the first stage when PAH reaches a critical size. Then C_2H_2 and PAHs molecules are polymerized in the soot particles surface. Finally, particles agglomerate by sticking to form cluster-like or chain-like structure [49].

Soot is sometimes called “coke”. Zhang et al. [50] found that coke formation begins at 900 ℃ and reaches a maximum at 1100 ℃ owing to reaction (9), above 1100 ℃ reactions (1) (partial oxidation) and (2) (steam gasification) lead to its decrease. It was suggested that the secondary decomposition of light hydrocarbon

gases and some tar species are the principal origins of coke formation at temperature above 900 ℃ [51]. CH_4 is the most abundant hydrocarbon specie, which exhibits the maximum yield at 900 ℃ and then decreases with temperature, leaded by reaction (6). The secondary hydrocarbons decomposition (reaction (9)) and carbon gasification reactions (reactions (1) and (2)) competitively progress in the high temperature pyrolysis process (above 900 ℃), which determines the final carbon (char and coke) yield. Char yields almost linearly decrease with temperature.

$$CnHm \leftrightarrow m/2\ H_2 + nC \quad (9)$$

Septien et al. distinguished two solid products (char and soot) fast pyrolysis at high temperature (above 1000 ℃) [52]. They found a constant char yield and considerable soot amounts over 1200 ℃, which stabilizes at higher temperature. Soot is formed through a complex series of polymerization and condensation reactions between hydrocarbon gases, simplified by reaction (9).

2.4 Conventional biomass pyrolysis technology

A variety of reactors are currently studied or industrially used for biomass pyrolysis. The typical conventional pyrolysis reactors are listed in Table 2-3 adapted from ref. [25]. They include fluid bed (bubbling and circulating), rotating cone, ablative, entrained flow, vacuum bed, fixed-bed and drop-tube reactors, of which a brief description is given below. Figure 2-14 gives a schematic overview of these pyrolysis reactors and their main flow streams.

Table 2-3: Comparison of conventional pyrolysis reactors

Technology	Organization	Capacity (kg/h)	Desired product	Gas/Tar/char (Wt%)	T (℃)	Heating method
Bubbling fluid bed	Alten (KTI+ Itaenergy)	500	Tar	59/20.5/20.5	500	Partial gasification with air
Circulating fluid bed	Ensyn Engineering	30	Tar	25/65/10	450-800	In-bed char gasification to heat sand
Rotating cone	Univ. Twente	10	Tar	20/70/10	500-700	Wall and sand heating
Ablative	Solar Energy research Ins.	30	Tar	35/55/10	475-725	Wall heating
Entrained flow	Georgia Tech Research Ins.	50	Tar	30/60/10	400-550	Combustion products
Vacuum	Laval University	30	Tar	15/65/20	250-450	Wall heating
Fixed-bed	Bio-Alternative	2000	Char	55/15/30	500-800	Partial gasification with air
Drop-tube	Univ. Zaragoza	100	Gas	90/8/2	1000-2000	Fire tube

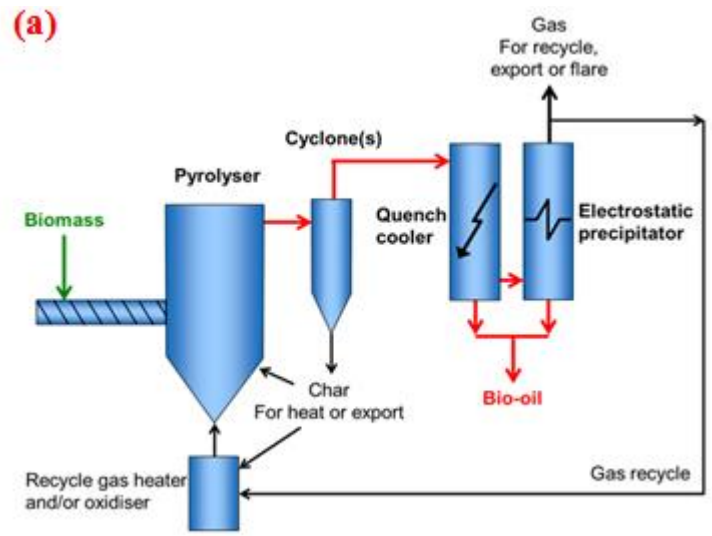

Bubbling fluid bed reactor [53]

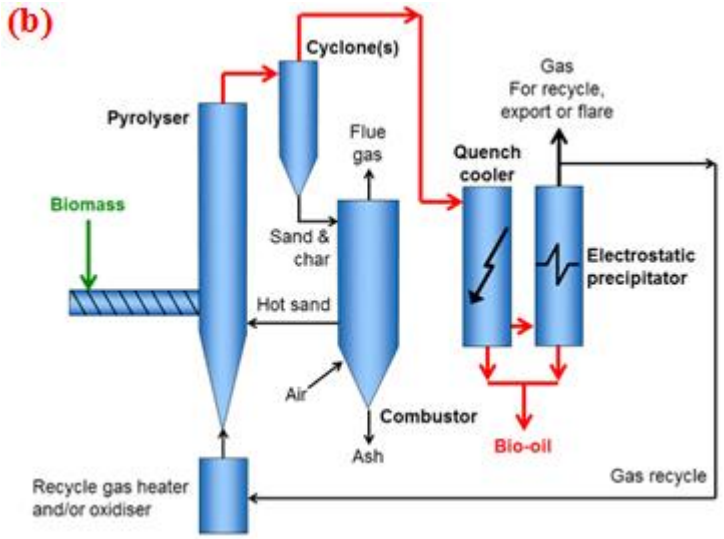

Circulating fluid bed [53]

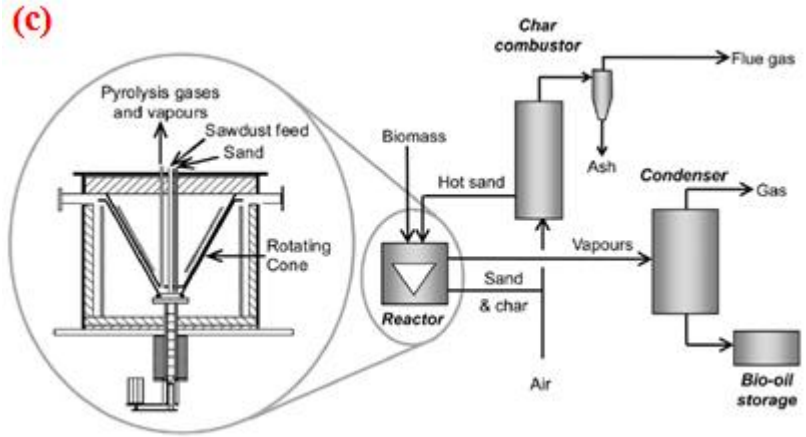

Rotating cone pyrolysis reactor [53]

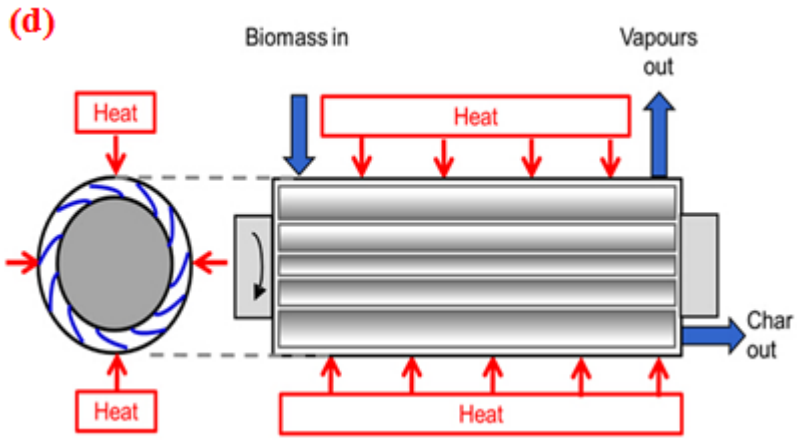

Ablative pyrolysis reactor [53]

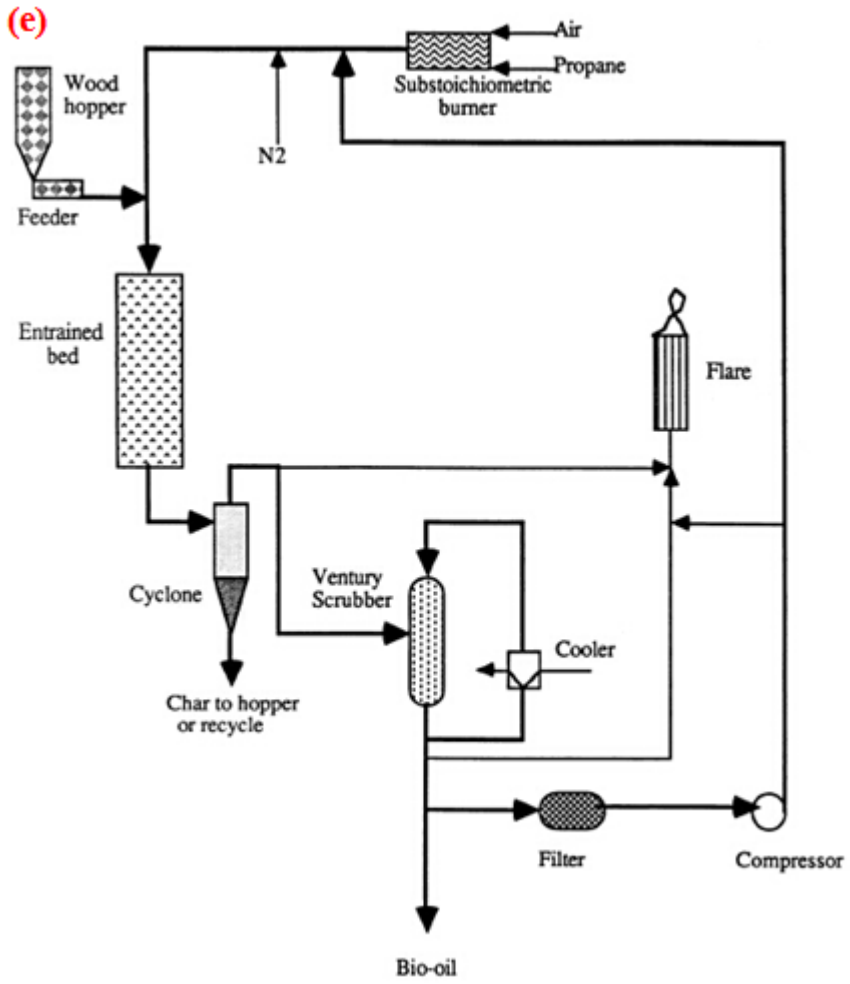

Entrained flow reactor [54]

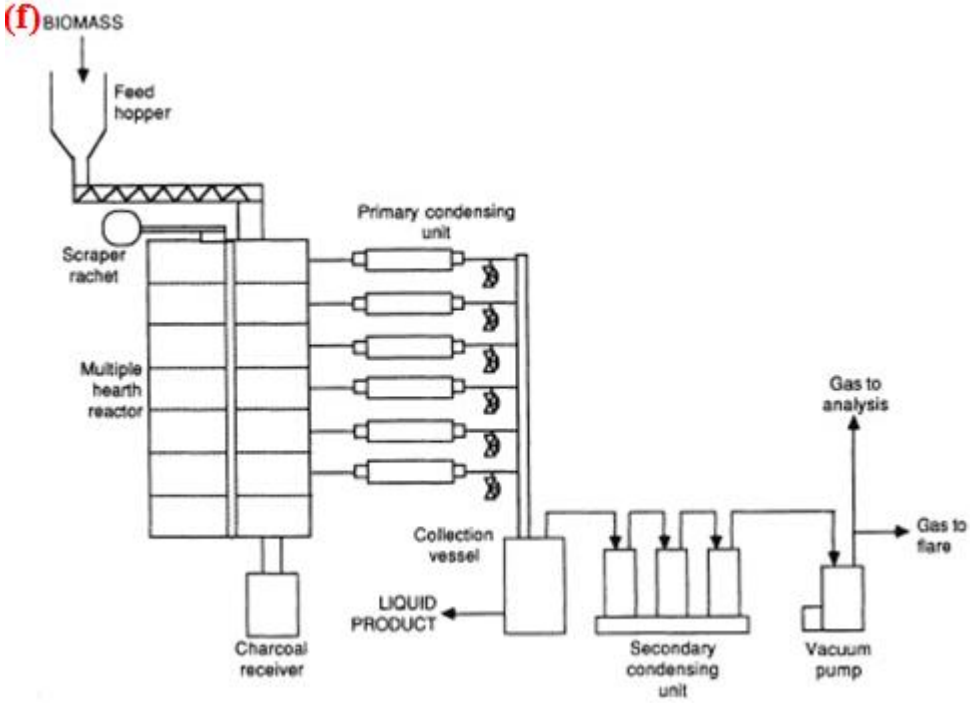

Vacuum bed reactor [54]

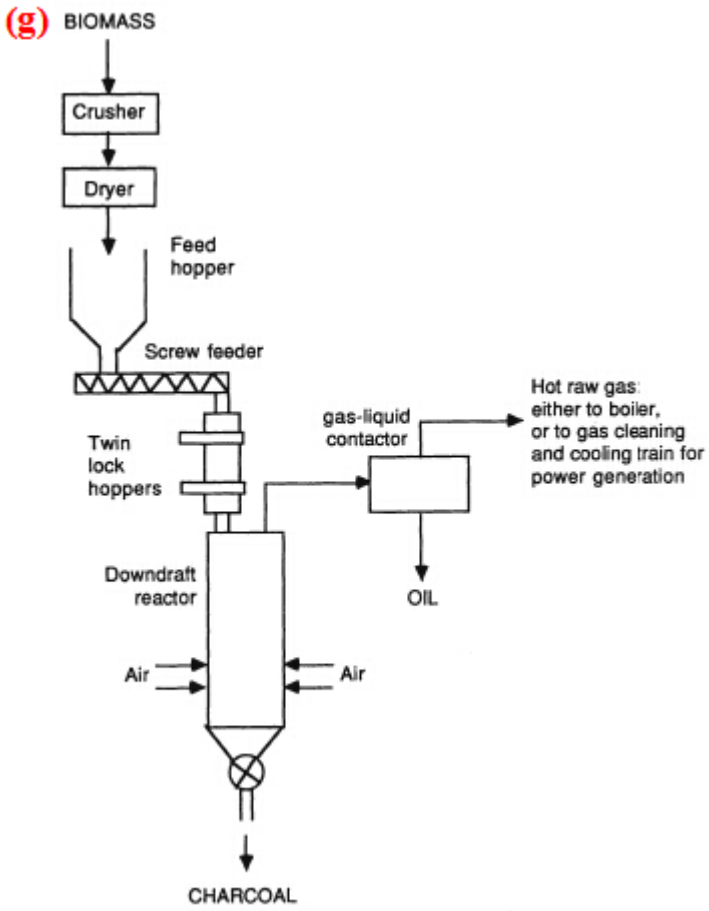

Fixed-bed reactor [54]

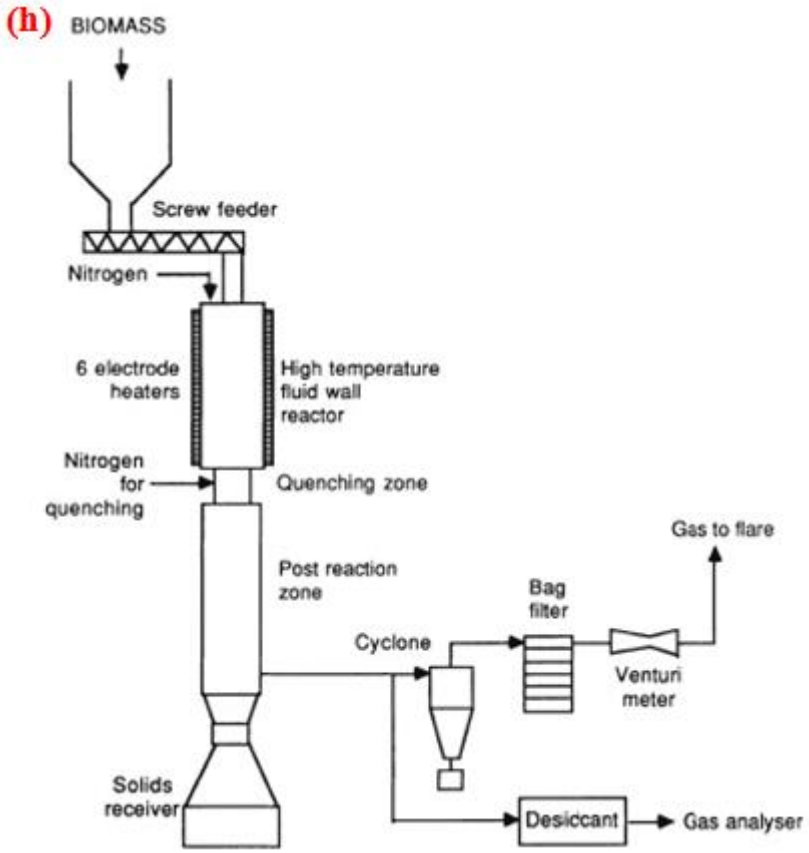

Drop-tube reactor [55]

Figure 2-14: Typical conventional pyrolysis reactors (a**)** Bubbling fluid bed, (b) Circulating fluid bed, (c) Rotating cone, (d) Ablative, (e) Entrained flow, (f) Vacuum bed, (g) Fixed-bed and (h) Drop-tube

As shown in Figure 2-14a, the bubbling fluid bed reactor can well control the temperature with high liquid yields of typically 70-75 wt.% from wood (dry-basis) [53]. Small biomass particle size of less than 2-3mm is needed to achieve high heating rate. The byproduct char yield is typically about 15 wt.% containing about 25% biomass feed energy. There are two ways to provide the heat requirements for pyrolysis reactions: 1) Char and gas products can be burnt; 2) An alternative fuel is required. Circulating fluid bed (CFB) reactor, as depicted in Figure 2-14b, has all the features of bubbling beds described above and higher void fraction. Heat supply is usually from circulation of heated sand from a secondary char combustor.

In the rotating cone reactor (Figure 2-14c), the biomass and hot sand are driven up a rotating heated cone by centrifugation [53]. The biomass is heated by the hot sand, heated by the char combustion. Finally, 60-70 wt.% liquid yields (dry basis) are typically obtained. The ablative plate reactor drives the biomass by pressure and motion shown in Figure 2-14d [53]. There is no limit of particle size and no requirement for inert gas. Liquid yields of 70-75 wt.% on dry basis are typically got under reactor temperature less than 600 ℃.

In the entrained-flow reactor (Figure 2-14e), the solid feedstock with sweeping gas are injected into the reactor top or side with a high gas flow rate. Lower liquid yields at 50-55 wt.% are usually obtained [54]. The vacuum reactor mainly includes a multiple hearth furnace and a vacuum pump shown in Figure 2-14f. It is usually operated at 450 ℃ and 100 kPa producing 35-50% liquid yield (dry basis) [54].

In the updraft fixed-bed reactor (Figure 2-14g), the necessary reaction heat is obtained through internal combustion with air injection [54]. The objective is the char and oil production. Biomass free falls in a very high temperature tube reactor with heating rate up to 10000 ℃/s (theoretical value) maximizing the gas yields. It is formerly named drop-tube reactor, which can be used for flash pyrolysis of biomass [55]. It typically results in gas yield more than 75 wt.%.

References

[1] Fengel D, Wegener G. (Eds.). Wood: chemistry, ultrastructure, reactions. Walter de Gruyter. 1983;167-174.

[2] De Wild P. Biomass pyrolysis for chemicals. PhD thesis. 2011.

[3] Rubin E.M. Genomics of cellulosic biofuels. Nature 2008;454:841–845.

[4] Rowell R.M. Handbook of Wood Chemistry and Wood Composites, CRC Press, 2005.

[5] Mettler M.S. Vlachos D.J. Dauenhauer P.J. Top ten fundamental challenges of biomass pyrolysis for biofuels. Energy & Environmental Science 2012;5:7797-7809.

[6] Telmo C, Lousada J. Heating values of wood pellets from different species. Biomass and Bioenergy 2011;35:2634-2639.

[7] Evans RJ. Milne TA. Molecular characterization of the pyrolysis of biomass. 1. Fundamentals. Energy & Fuels 1987;1(2):123-137.

[8] Neves D, Thunman H, Matos A, Tarelho L, Gómez-Barea A. Characterization and prediction of biomass pyrolysis products. Progress in Energy and Combustion Science 2011;37:611-630.

[9] Liu CJ, Wang HM, K AM, Sun JM, Wang Y. Catalytic fast pyrolysis of lignocellulosic biomass. Chemical Society Reviews 2014;43:7594-7623.

[10] Antal MJ, Mok WSL, Varhegyi G, Szekely T. Review of methods for improving the yield of charcoal from biomass, Energy & Fuels 1990;4:221-225.

[11] Bridgwater A.V, Czernik S, Piskorz J. An overview of fast pyrolysis. Progress in Thermochemical Biomass Conversion 2001;2:977–997.

[12] Pütün AE. Biomass to bio-oil via fast pyrolysis of cotton straw and stalk. Energy Source 2002;24:275-285.

[13] Demibas A, Arin G. An overview of biomass pyrolysis. Energy Source 2002; 24(5):471–482.

[14] Mohan D, Pittman CU, Steele PH. Pyrolysis of wood/biomass for bio-oil: a critical review. Energy & Fuels 2006;20:848-889.

[15] Blasi CD. Modeling chemical and physical processes of wood and biomass

pyrolysis. Progress in Energy and Combustion Science 2008;34:47-90.

[16] Orfao J, Ganesh A, Khilar KC. Pyrolysis kinetics of lignocellulosic materials-three independent reaction model. Fuel 1999;78:349-358.

[17] Koukios EG. Progress in thermochemical, solid-state refining of biofuels—from research to commercialization. In Advances in Thermochemical Biomass Conversion. Springer Netherlands 1993:1678-1692.

[18] Yang H, Yan R, Chen H, Zheng C, Lee DH, Liang DT. In-depth investigation of biomass pyrolysis based on three major components: hemicellulose, cellulose and lignin. Energy and Fuels 2006;20:383-393.

[19] Balat M. Mechanisms of thermochemical biomass conversion processes. Part 1: reactions of pyrolysis. Energy Sources, Part A 2008;30:620-635.

[20] Patwardhan PR, Brown RC, Shanks BH. Product distribution from the fast pyrolysis of hemicellulose. ChemSusChem 2011;4:636-643.

[21] Talmadge MS, Baldwin RM, Biddy MJ, McCormick RL, Beckham GT, Ferguson GA. A perspective on oxygenated species in the refinery integration of pyrolysis oil. Green Chemistry 2014;16:407-453.

[22] Lin YC, Cho J, Tompsett GA, Westmoreland PR, Huber GW. Kinetics and Mechanism of Cellulose Pyrolysis. The Journal of Physical Chemistry C 2009;113:20097-20107.

[23] Bond JQ, Upadhye AA, Olcay H, Tompsett GA, Jae J, Xing R. Production of renewable jet fuel range alkanes and commodity chemicals from integrated catalytic processing of biomass. Energy & Environmental Science 2014;7:1500-1523.

[24] Chu S, Subrahmanyam AV, Huber GW. The pyrolysis chemistry of a β-O-4 type oligomeric lignin model compound. Green Chemistry 2013;15:125-136.

[25] Bridgwater AV. Principles and practice of biomass fast pyrolysis processes for liquids. J. Anal. Appl. Pyrolysis 1999;51:3-22.

[26] Demirbas A. Effect of initial moisture content on the yields of oily products from pyrolysis of biomass. J. Anal. Appl. Pyrolysis 2004;71:803-815.

[27] Antal MJ, Gronli M. The art, science and technology of charcoal production. Ind.

Eng. Chem. Res 2003;42:1619-1640.

[28] Blasi CD. Combustion and gasification rates of lignocellulosic chars. Progress in Energy and Combustion Science 2009;35:121-140.

[29] Devi L, Ptasinski K.J, Janssen F.J. A review of the primary measures for tar elimination in biomass gasification processes. Biomass and Bioenergy 2003;24:125-140.

[30] Morf P, Hasler P, Nussbaumer T. Mechanisms and kinetics of homogeneous secondary reactions from continuous pyrolysis of wood chips. Fuel 2002;81:843-853.

[31] Le Duc Dung KM, Takarada T. Catalytic Decomposition of Biomass Tars at Low-Temperature. 2013, DOI: 10.5772/55356.

[32] Oasmaa A, Dietrich M. Norms and standards for fast pyrolysis liquids: 1. Round robin test. Journal of Analytical and Applied Pyrolysis 2005;73:323-334.

[33] Huber GW, Iborra S, Corma A. Synthesis of transportation fuels from biomass: chemistry, catalysts, and engineering. Chemical Reviews 2006;106:4044-4098.

[34] Czernik S, Bridgwater AV. Overview of applications of biomass fast pyrolysis oil. Energy & Fuels 2004;18:590-598.

[35] Greenhalf CE, Nowakowski DJ, Harms AB, Titiloye JO, Bridgwater AV. A comparative study of straw, perennial grasses and hardwoods in terms of fast pyrolysis products. Fuel 2013;108:216-230.

[36] Dickerson T, Soria J. Catalytic fast pyrolysis: a review. Energies 2013;6:514-538.

[37] Blasi CD, Branca C, Santoro A, Gonzalez HE. Pyrolytic behavior and products of some wood varieties. Combust and Flame 2001;124:165-177.

[38] Branca C, Giudicianni P, Blasi CD. GC/MS characterization of liquids generated from low-temperature pyrolysis of wood. Ind Eng Chem Res 2003;42:3190-3202.

[39] Blasi CD. Modeling and simulation of combustion processes of charring and non-charring solid fuels. Prog Energy Combust Sci 1993;19:71-104.

[40] Boroson ML, Howard JB, Longwell JP, Peters AW. Products yields and kinetics from the vapor phase cracking of wood pyrolysis tars. AIChE J. 1989;35:120-128.

[41] Boroson ML, Howard JB, Longwell JP, Peters WA. Heterogeneous cracking of

wood pyrolysis tars over freshwood char surfaces. Energy Fuels 1988;3:735-740.

[42] Rath J, Staudinger G. Cracking reactions of tar from pyrolysis of spruce wood. Fuel 2001;80:1379-1389.

[43] Baumlin S, Broust F, Ferrer M, Meunier N, Marty E, Lede J. The continuous self stirred tank reactor: measurement of the cracking kinetics of biomass pyrolysis vapors. Chem Eng Sci 2005;60:41-55.

[44] Yang HP, Yan R, Chen HP, Lee DH, Zheng CG. Characteristics of hemicellulose, cellulose and lignin pyrolysis. Fuel 2007;86:1781-1788.

[45] Yang R, Yang HP, Chin T, Liang DT, Chen HP, Zheng CG. Influence of temperature on the distribution of gaseous products from pyrolyzing palm oil wastes. Combustion and Flame 2005;142:24-32.

[46] Boon J.J, Pastorova I, Botto R.E, Arisz P.W. Structural studies on cellulose pyrolysis and cellulose chars by PYMS, PYGCMS, FTIR, NMR, and by wet chemical techniques. Biomass Bioenergy 1994;7:25-32.

[47] Maschio G, Koufopanos C, Lucchesi A. Pyrolysis, a Promising Route for Biomass Utilization. Bioresource Technology 1992;42:219-231.

[48] Pattanotai T, Watanabe H, Okazaki K. Experimental investigation of intraparticle secondary reactions of tar during wood pyrolysis. Fuel 2013;104:468-475.

[49] Septien S. 2011. High temperature gasification of millimetric wood particles between 800 ℃ and 1400 ℃. PhD thesis, Ecoles des Mines De Paris.

[50] Zhang Y, Kajitani S, Ashizawa M, Oki Y. Tar destruction and coke formation during rapid pyrolysis and gasification of biomass in a drop-tube furnace. Fuel 2010;89:302-309.

[51] Zhang Y, Kajitani S, Ashizawa M, Miura K. Peculiarities of rapid pyrolysis of biomass covering medium- and high-temperature range. Energy and Fuels 2006;20:2705-2712.

[52] Septien S, Valin S, Dupont C, Peyrot M, Salvador S. Effect of particle size and temperature on woody biomass fast pyrolysis at high temperature (1000-1400 ℃). Fuel 2012;97:202-210.

[53] Bridgwater AV. Review of fast pyrolysis of biomass and product upgrading. Biomass and Bioenergy 2012;38:68-94.

[54] Bridgwater AV. Renewable fuels and chemicals by thermal processing of biomass. Chemical Engineering Journal 2003;91:87-102.

[55] Corella J, Monzon A, Santamaria J, González-Cañibano J. Ultra-fast biomass pyrolysis in a high-temperature (2200 ℃) fluid-wall reactor. Journal of Solar Energy Engineering 1988;110:10-13.

Chapter 3: Solar pyrolysis experimental study and methods

3.1 State of the art of solar pyrolysis

The biomass pyrolysis is globally endothermic, and the required heat can be supplied by concentrated solar energy, which enhances the feedstock calorific value and reduces pollution discharge [1]. Moreover, solar pyrolysis gas products are not contaminated with combustion by-products. A very high heat flux density can be quickly reached with concentrated solar radiation and in very clean conditions. So fast heating rates and high temperatures can be available with well-controlled heating time in the solar pyrolysis process. Only the radiation-absorbing feedstock is heated, not the reactor wall and sweep gas. Then, the thermal conditions (temperature and heating rate) imposed to the solid can be varied independently of the sweep gas and reactor [2]. However, the direct solar pyrolysis process proposed so far has some disadvantages that should be improved in the future. On the one hand, the intermittent solar radiation makes the solar reactor subject to thermal shock. On the other hand, in direct heating systems, by-products can deposit on the reactor wall thus reducing the available radiation over long exposure times [3].

A few researchers have investigated the pyrolysis of carbonaceous materials using concentrated radiation (Table 3-1). In the 1980s, Beatie et al. [4] obtained a maximum gas yield of 31 mmol/g coal from direct solar pyrolysis at flux level of 1 MW/m^2. Antal et al. [5] used an arc image furnace (simulating a solar furnace with flux density up to 2 MW/m^2) with a spouted bed for biomass flash pyrolysis and obtained 63% liquid, 11% char and 26% gas yields. Tabatabaie-Raissi et al. [6] got 6.6-8.4% char yield from pyrolysis of cellulose under radiation up to $10MW/m^2$ in a TGA. Chan et al. [7, 8] investigated the pyrolysis of pinewood with concentrated lamp radiation and found that the char, tar and gas yield were 20-26%, 33-52% and 11-27%, respectively, depending on the flux density.

Later, 21-29% char, 25-40% tar and 30-50% gas yield have been reported for

pyrolysis of different woods under concentrated lamp radiation (0.08 and 0.13 MW/m^2) [9]. Lédé et al. [10-12] found that the liquid yield (approximately 62%) did not change with the heat flux density (from 0.3 to 0.8 MW/m^2), whereas the gas and char yields increased and decreased, respectively. Recently, there were some works regarding the application of an image furnace for biomass pyrolysis [13, 14]. However, works related to pyrolysis using a real solar furnace for bio-char [15] and bio-oil [16, 17] are scarce. Further analysis of the influence of the pyrolysis parameters on the product distribution in a real solar reactor has yet to be reported. It should differ from that in conventional reactors due to two temperature zones existing in a solar reactor, as described in [5] and modeled in [18]. It is believed that the intermittent solar energy is chemically stored in the form of solar fuel (bio-oil, bio-gas and bio-char). Almost all researchers have characterized only the bio-oil products, showing only one part of the gains obtained through solar pyrolysis. However, the total gain, particularly the energy upgrade factor of solar pyrolysis, has yet to be reported, which is a very important evaluation index for solar biomass conversion. Therefore, it is necessary to characterize all solar pyrolysis products.

Table 3-1: The reactor for solar pyrolysis of carbonaceous feedstock.

Reference	Reactor design			Radiation concentrator	Heating source	Incident flux	Feedstock		Product distribution (wt.)		
	Variety	Shape	Dimensions				Variety	Size	Solid	Liquid	Gas
Beattie et al. [4]	Fixed bed	Dome-like cylindrical with quartz window	399cm^3	1 heliostat and 1 parabolic concentrator	Sun	1-9 MW/m^2	Coal 50mg	Powdered sample with diameter 0.15-0.30mm	49%	0	51%
Hopkins et al. [5]	Spouted bed	Cylinder	22mm i.d.	2 parabolic mirrors, 24 flat glass mirrors	5 kW Xenon lamp	2 MW/m^2	Cellulose	Particles with μm diameter	11%	63%	26%
							Kraft paper 2-8g		15%	30%	55%
Tabatabaie-Rassi et al. [6]	Fixed bed (TGA)	Cylinder	35mm o.d. and 640mm long tube	2 parabolic mirrors, 24 flat glass mirrors	2 kW Xenon lamp	Up to 10 MW/m^2	Cellulose 5-10mg	Particles with μm diameter	6.6-8.4 %	-	-

Chan et al. [7,8]	Fixed bed	Dome-like cylindrical with quartz window	-	-	1 kW Xenon arc lamp	0.083, 0.167 and 0.25 MW/m^2 (150 -900 ℃)	Pine	Pellet (diameter, 10mm; thickness, 5, 10 and 15mm)	20-26%	33-52%	11-27%
Gronli and Melaaen [9]	Fixed bed	bell-shaped Pyrex reactor	-	Reflector	Xenon lamp	0.08 and 0.13 MW/m^2 (150 -970 ℃)	Birch, pine, and spruce ~5g	Pellet (diameter, 20mm; thickness, 30mm)	21-29%	25-40%	30-50%
Boutin et al. [10]	Fixed bed	Cylinder with conical parts at its bottom and top	30mm o.d. and 50mm long tube	2 parabolic mirrors	5 kW Xenon lamp	0.2-4, 5 and 7.4 MW/m^2	Cellulose	Pellet having a circular cross-section of 0.2 cm^2	-	-	-

Authier et al. [11]	Fixed bed	Cylinder	30mm o.d. and 50mm long tube	2 parabolic mirrors	5 kW Xenon lamp	0.3-0.8 MW/m^2	Oak 0.125g	Pellet (radius, 5mm; thickness, 3mm)	20%	61%	12%
Authier et al. [12]	Fixed bed	Cylinder	30mm o.d. and 50mm long tube	2 parabolic mirrors	5 kW Xenon lamp	0.08, 0.17, 0.55 and 0.85 MW/m^2	Oak 0.13g	Pellet (radius, 5mm; thickness, 3mm)	11.1-24 %	61.7-62.3 %	2.2-20.2 %
Pozzobon et al. [13]	No Reactor	-	-	2 elliptical mirrors	0.75 kW tungsten lamp	0.06, 0.09, 0.12, 0.15 and 0.18 MW/m2	Beech	Cylinder (diameter, 5mm; height, 5mm); Sphere (10 and 20mm diameter)	9-13%; 14-20%	-	-
Morales et al. [16]	Fixed bed	Tubular reactor	50.8mm of diameter and	Parabolic trough concentrator	Sun (15.65 suns)	0.01255 MW/m^2 (average	Orange peel	Particle sizes of 20mm×20mm×3 mm and	21%	1.4%	77.6%

			406.4mm length			reactor temperature 290 ℃, peak temperature 465 ℃)		30mm ×3mm ×3mm			
Zeaiter et al. [17]	Fixed bed	Tubular reactor	200mm long with small diameter	Fresnel lens	Sun	- (average reactor temperature 550 ℃)	Scrap rubber 1g	3-5mm ground pieces	42%	28%	30%

For the reported direct solar pyrolysis of carbonaceous feedstock, the flux density on the sample or reactor was in the range of 0.01-10 MW/m^2. The corresponding pyrolysis temperature range is 150 up to 2000 ℃. The pyrolysis temperature differs depending on the target product. For getting maximum bio-char or bio-liquid, the lower temperature range from 450-550 ℃ is preferred. Providing this temperature by solar energy requires low solar concentration ratio, then parabolic-trough [15] and Fresnel lens [16] can be chosen. For low solar concentration, large scale system can be operated. Temperature higher than 900 ℃ must be reached for maximizing the gas yield from solar pyrolysis of carbonaceous feedstock. In this case, a mean solar concentration ratio on the order of 1000 suns should be attained. Solar pyrolysis reactors are usually designed to operate in conjunction with a vertical [4, 13-15] or horizontal setup [5-12]. In both the horizontal and vertical setups, parabola or elliptical mirror is used as concentrator for higher concentration. The radiation is focused onto a very small area, then only relatively smaller scale of system can be operated. As shown in Figure 3-1a and 3-1b, the tubular transparent reactor is positioned in the focus of parabolic-trough [15] and Fresnel lens [16]. The incident solar radiation is reflected by parabolic-trough mirror and concentrated onto the feedstock surface through reactor wall. The Fresnel lens directly concentrates the incident solar radiation onto the feedstock. For horizontal and vertical 2-reflexion solar setups shown in Figure 3-1c and Figure 3-1d, the solar or lamp radiation is reflected by the heliostat then concentrated by the parabola. The feedstock is heated by the concentrated radiation through the transparent reactor wall.

Since no heat is generated within the pyrolysis reactor during solar-driven pyrolysis, the efficient concentrated solar radiation transfer to the reaction site is critical for high productivity and favorable vapor secondary reactions. Directly-irradiated solar pyrolysis reactors, where the solar radiation is absorbed directly by the feedstock at the reaction site, enable high heat transfer rates and temperature. Yet, they also require a transparent window that has to be kept clean during operation. Then the sweep gas is used to keep the reactor wall window clean,

which increases the operation cost. In addition, the window introduces limitations in the operating pressure and scale-up as the window design becomes complex [19].

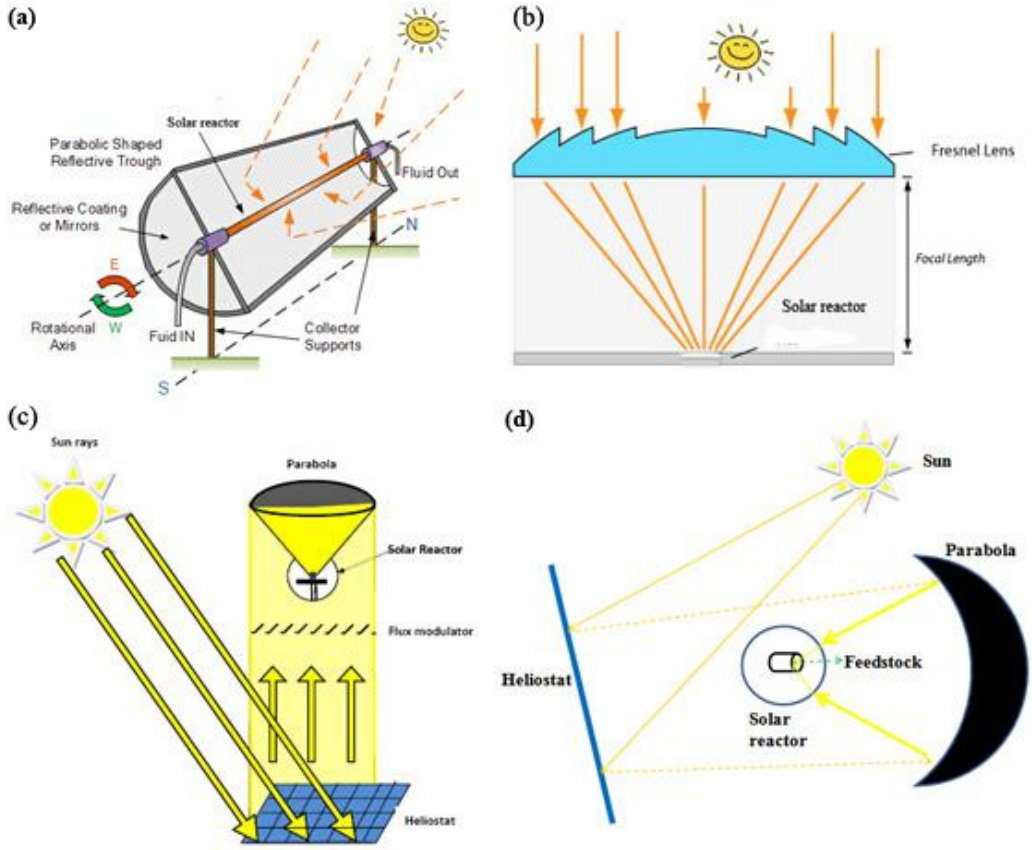

Figure 3-1: Solar pyrolysis systems: (a) parabolic-trough; (b) Fresnel lens; (c) vertical setup and (d) horizontal setup

3.2 Experimental setup and preparation

3.2.1 Experimental setup

Figure 3-2 shows a schematic of the laboratory-scale solar pyrolysis setup implemented in this study. A solar pyrolysis system was designed and constructed by setting a biomass pyrolysis reactor at the focal point of a vertical solar furnace. In such a solar furnace, a sensor detects the sun location and sends an order to a tracking system. The heliostat is continuously adjusted to face the sun correctly such that its reflected beam is perfectly vertical to illuminate a down-facing parabolic mirror (2 m diameter and 0.85 m focal length). The maximum power and maximum flux density are approximately 1.5 kW and 12 000 kW/m^2, respectively. A shutter with moving parallel carbon composite blades modulates the reflected solar beam and thus the

incident radiation, and therefore the concentrated flux impinging the sample and its temperature. A transparent Pyrex balloon reactor with 185 mm diameter (6 L volume), set at the focus, is swept with an argon flow controlled by a mass flowmeter (Bronkhorst, EL-FLOW®). A portable infrared gas analyzer (3100 SYNGAS) is used to monitor the oxygen concentration during the sweeping process. The sweep gas is used to keep the reactor wall and fluorine window clean. A needle valve adjusts the reactor outlet gas flow, which eventually controls the reactor pressure. The sample surface temperature is measured by a "solar-blind" optical pyrometer (KLEIBER monochromatic operating at 5.2 μm, in a H_2O absorption band) through a fluorine window (transparent at this wavelength). The target heating rate and final temperature are set on a PID controller, which controls the shutter opening based on the measured sample temperature.

Following pyrolysis, the pyrolysis products (the condensable vapors and incondensable gases) firstly pass through a liquid collection system, which consists in a heated copper tube and one dry ice condensation train. The dry ice condensation train consists of three impinger bottles containing approximately 100 ml isopropanol solvent (2-propanol) for each one. The copper tube is maintained at about 250 ℃. All the impinger bottles are immersed in dry ice (temperature between around -25 ℃ and -15 ℃). A needle valve and a vacuum pump are placed downstream the condensation train. Then the incondensable gases are aspirated by the vacuum pump and collected in a sampling bag. Finally, the composition of the gaseous products is analyzed by gas chromatography (SRA Instruments MicroGC 3000).

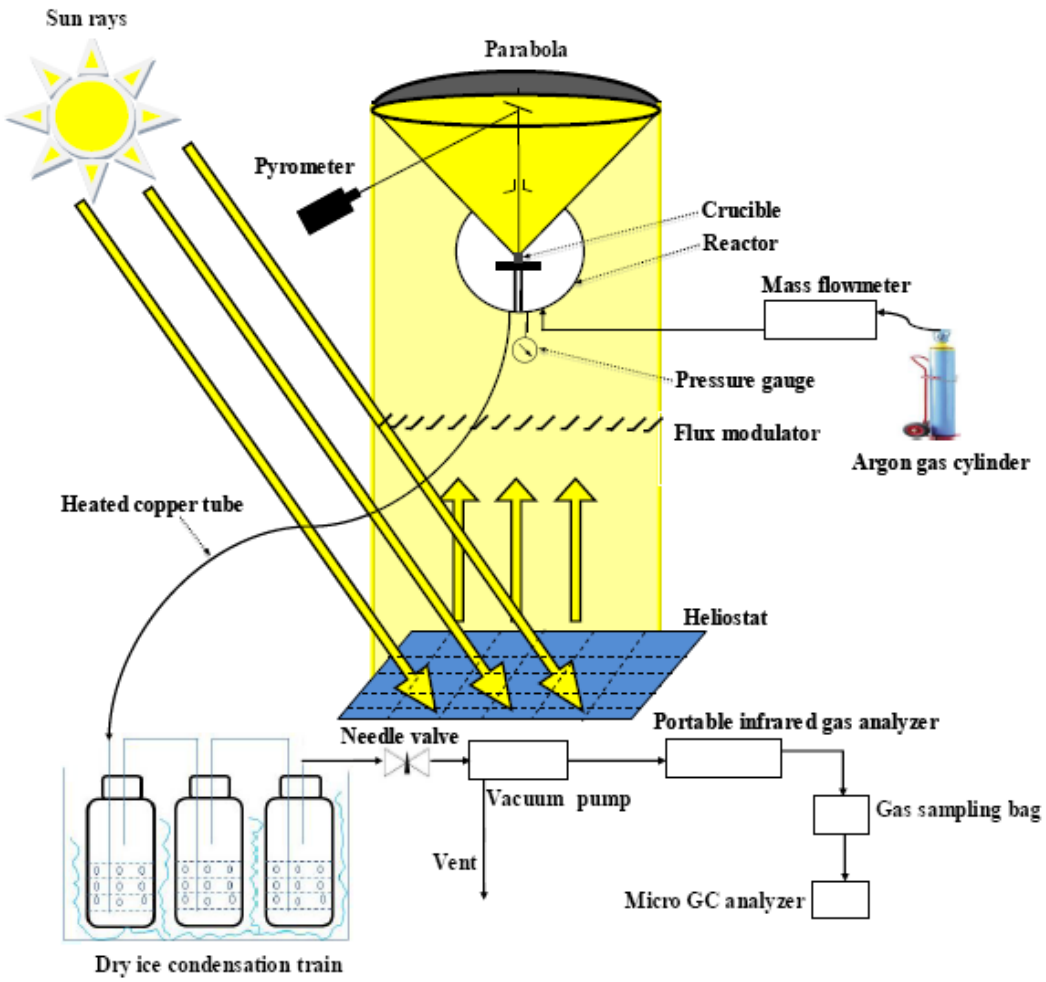

Figure 3-2: Schematic of the solar pyrolysis setup

A few pictures showing the solar radiation tracking system, solar radiation concentration system, shutter (flux modulator), reactor with pyrometer, PID controller with argon mass flowmeter, vacuum pump, infrared gas analyzer, dry ice condenser and Micro-GC are given in Figure 3-3.

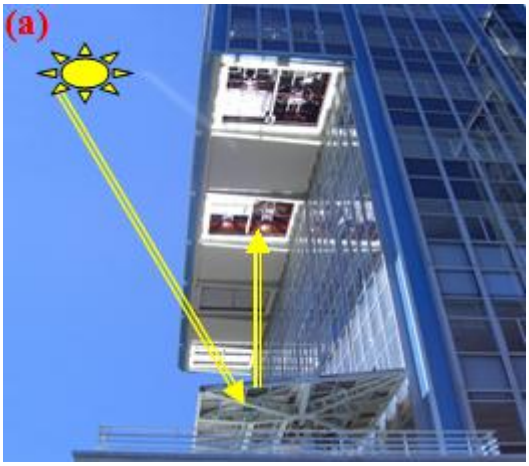
(a)

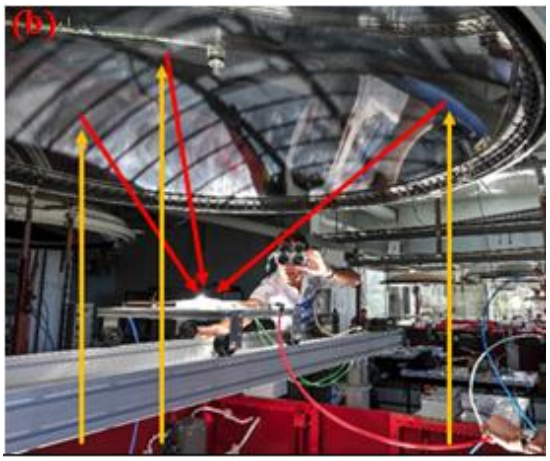
(b)

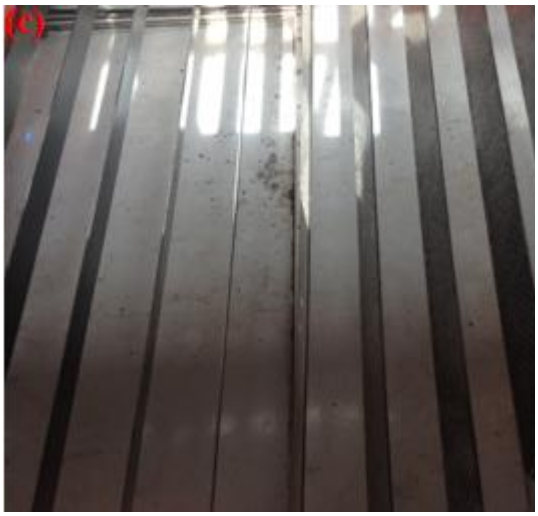
(c)

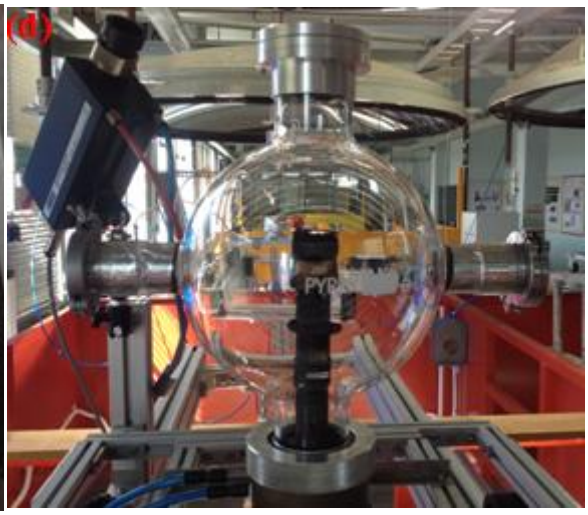
(d)


(e)


(f)

Figure 3-3: Solar pyrolysis setup: (a) tracking system, (b) concentration system, (c) shutter, (d) reactor with pyrometer, (e) PID controller with mass flowmeter, (f) vacuum pump, (g) infrared gas analyzer, (h) dry ice condenser and (i) MicroGC 3000

Directly-irradiated solar reactors are characterized by two temperature zones, depicted in Figure 3-4. As shown in Figure 3-4, the wood pellet is placed in a graphite crucible and wrapped with black graphite foam. It is directly heated by solar radiation. The argon gas does not absorb the solar radiation because it is transparent in these wavelengths. It can only be heated by contact with the sample surface or by convection mixing with pyrolysis volatile products. Because the sample (crucible) sides and bottom part are insulated with graphite foam, the zone near the sample top surface is a high-temperature zone. The remaining zone in the solar reactor remains relatively “cold” compared to the crucible. Consequently, the tar secondary reactions in the particle surroundings can only occur in the high-temperature zone.

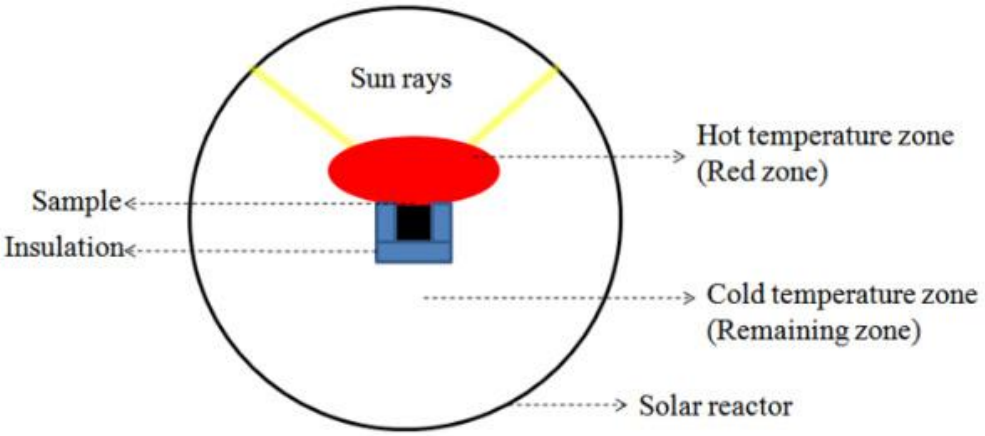

Figure 3-4: Two temperature zones distribution in the solar reactor

The solid remaining in the crucible after the experiment was considered to be "char". Gases (Ar, H_2, CO, CO_2, CH_4, and C_2H_6) were collected in a plastic bag. The product trapped by the dry ice condensation train was taken as "liquid". The char mass was weighed at the end of the experiments. The gases were injected into a microGC for analysis. The gaseous volumes were quantified from the volumetric percentage of each gas, using argon as tracer. Then, the gases molar quantities and masses were calculated based on the ideal gas law. The mass values were converted to yields by dividing them by the original pellet mass, and the liquid yield was calculated from the difference. The LHVs (lower heating values) of the gas products were calculated based on the yield and lower heating values of CO, H_2, CH_4 and C_2H_6 reported in [20].

3.2.2 Experimental preparation

3.2.2.1 Argon injection system design

The gaseous products evolve from the pellet and mix with the argon flow in the reactor. Obviously, the exhaust gas composition highly depends on the mixing situation of produced gases and argon inside the reactor. The gas mixing in the reactor should be complete to make sure the measured value from gas analyzer is representative of the mean value of gas composition.

Three ways for sweep gas injection system were modeled: one straight tube (Figure 3-5a), twelve upward holes in a circular tube (Figure 3-5b), six upward holes (gas outlet side) and six downward holes (outlet opposite side) in a circular tube

(Figure 3-5c). In order to study the gas distribution in 2-D, the injection flows were simplified into: one flow, two co-current flows and two counter-current flows.

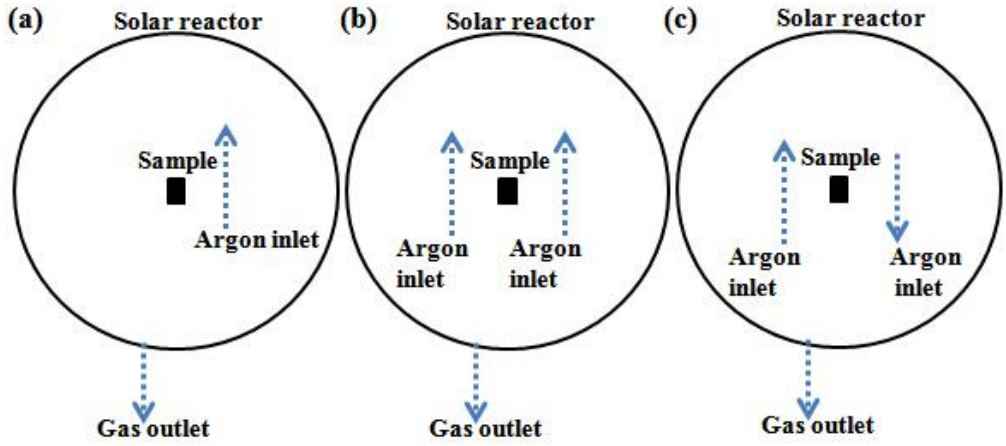

Figure 3-5: Sweep gas injection system: (a) one single injector; (b) two co-current injectors and (c) two counter-current injectors

ICEMCFD 14.5 was used to create the 2D geometry and generate the grids. The first step consists in defining the global element size. The scale factor is 1 and the biggest element is 0.02. The second step defines the shell meshing parameters. The mesh type is quad dominant and the mesh method is patch dependent. There are at least 293903 cells, 447219 faces and 153317 nodes are created automatically. Fluent 14.5.7 was used for the simulations at steady state. The solver type was Pressure-Based. The velocity formulation was absolute. The model included energy conservation laminar flow and species transport, and the wall was modeled using no-slip boundary conditions for both phases. The gas emission at pellet top and argon flow at tube top were defined as mass flow inlets. Pressure outlet boundary condition was employed for the reactor outlet.

The CFD simulation settings and the difference between calculation and simulation results are indicated in Table 3-2. Calculation of CO and CH_4 during solar pyrolysis requires assumptions and simplifications. They are as follows: 1. The pyrolysis reaction time is 3.3s; 2. The main flow in the reactor is laminar; 3. Local thermal equilibrium exisists between the solid and gas phase; 4. The gas concentration is stable over time and uniform in the reactor depending on the total argon flow. For one single injector, the difference is 25.3%. It decreases to 7.3% for the two injectors

co-current. Finally, it is 6.9% less when the gas feeding system is six upward holes (gas outlet side) and six downward holes (opposite side) in a circular tube. It means that the measured values from gas analyzer are closest to the representative values in this way.

Table 3-2: The setting and results of CFD modeling.

The setting of Fluent				
Sample temperature		1000 ℃		
Sample mass		0.5g		
Ar flow rate		11.1NL/min		
The results of simulation				
Case	Reference	One single injector	Two injectors co-current	Two injectors counter-current
CO %vol	8.38%	10.52%	9.09%	9.09%
CH_4 %vol	1.47%	1.84%	1.56%	1.55%
Difference with mean values	0	25.3%	7.30%	6.95%

The contours of CO molar fraction distribution in the reactor for three different sweep gas injection systems are given in Figure 3-6 (a, b, and c). The mixing situation is clearly best for the third option (Fig. 3-6c).

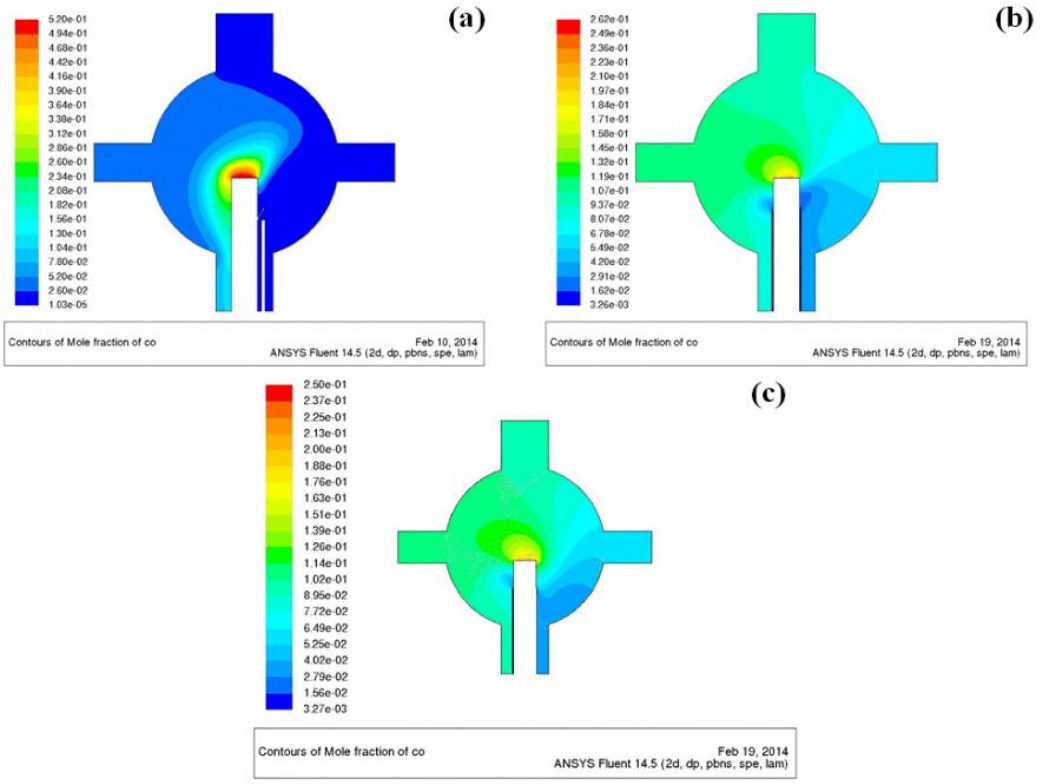

Figure 3-6: Contours of CO molar fraction distribution: (a) one straight tube; (b) two co-current injections and (c) two counter-current injections

According to the CFD simulation results, the configuration with six upward holes (gas outlet side) and six downward holes (opposite side) in a circular tube is chosen as sweep gas injection system. The special design of the counter-current argon injector system causes a rotational flow field in the solar reactor as shown in Figure 3-7, which can be observed during the experiments and was modeled [21]. The average residence time is 60s when the argon flow rate is 6NL/min. Actually, the tar residence time is longer than 60s owing to the rotational flow. And, there is almost no influence of the argon flow rate on the tar residence time.

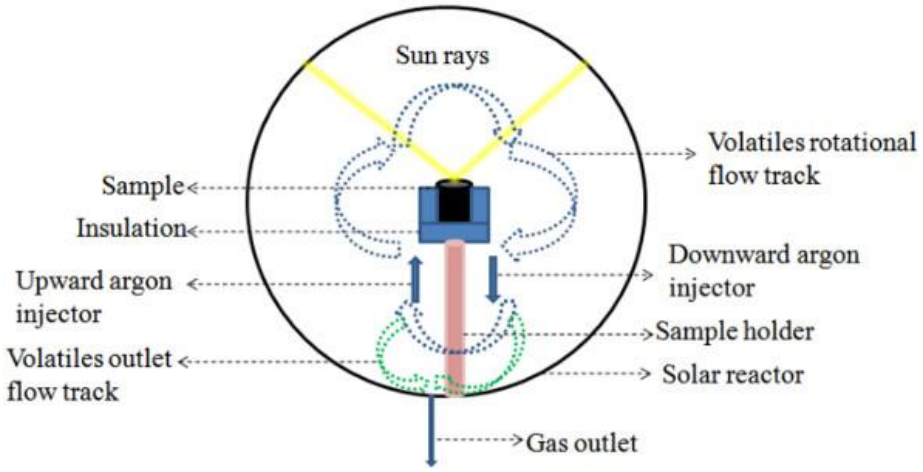

Figure 3-7: Rotational flow field

3.2.2.2 Temperature calibration

The schematic view of temperature measurement is shown in Figure 3-8. The radiation intensity emitted by the sample is measured by a pyrometer which gives the temperature based on Planck's law. The pyrometer was first calibrated using blackbody radiation. In addition, the sample temperature indicated by pyrometer was tentatively validated by comparison with a K-type thermocouple measurement. The sample height was 5 mm, and the thermocouple was located at a height of 2.5 mm. The thermocouple was introduced in a previously drilled hole such that direct exposure to radiation was prevented. This procedure also ensured good thermal contact between the thermocouple and wood. The temperature indicated by the thermocouple was approximately 50 ℃ (at the middle of the sample) lower than that indicated by the pyrometer (on the top of the sample), as expected due to the temperature gradient between the sample upper part (exposed to the sun) and bottom part (set on a 10mm-thick alumina layer laying on the water-cooled sample holder (Figure 3-9). Moreover, this small difference decreased with time, which means that the sample surface temperature can be assumed to represent well the temperature of the entire sample. As shown in Figure 3-9, the values of temperature and heating rate set in the PID controller were almost the same as the real values measured by the pyrometer. This result indicates that the temperature control system was accurate enough for the experiments.

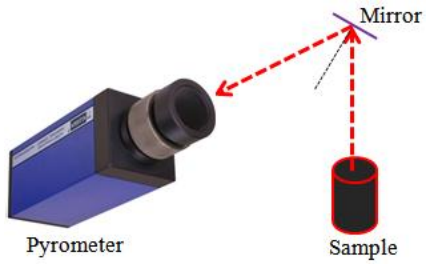

Figure 3-8: Temperature measurement schematic diagram

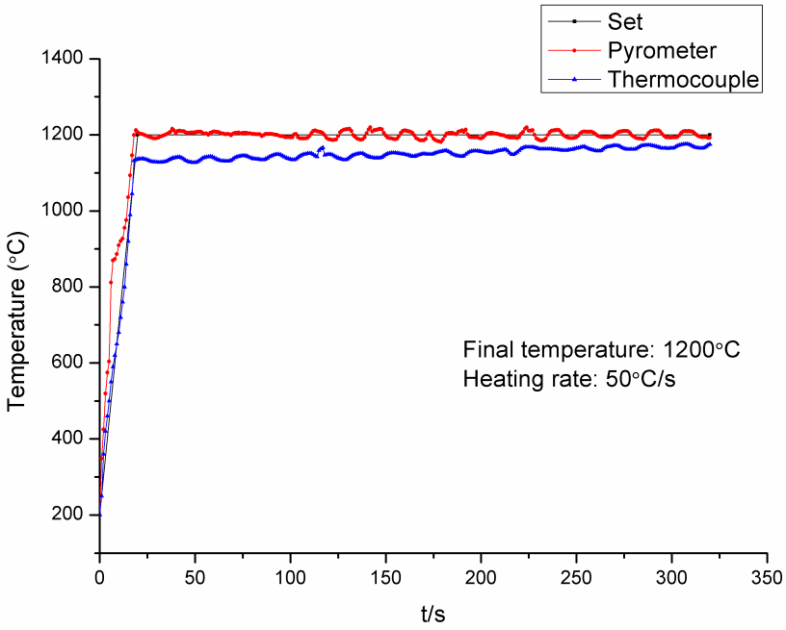

Figure 3-9: The set and real measurement temperature curves for heating rate 50^{o}C/s to final temperature 1200^{o}C.

3.3 Preliminary experiments

3.3.1 Temperature measurement

In order to check the temperature and heating rate control accuracy in the previous defined ranges (heating rate from 5 to 450 ℃/s and temperature from 600 ℃ to 2000 ℃), some temperature measurement experiments using the pyrometer have been conducted. As the pyrometer is not sensitive at temperature lower than 200 ℃, the sample was manually pre-heated by opening the shutter a little. As shown in Figure 3-10 and Figure 3-11, the heating rate control was very accurate in the whole parameter ranges, and the final temperature fluctuated a little. In general, the control system is good enough for pyrolysis experiments.

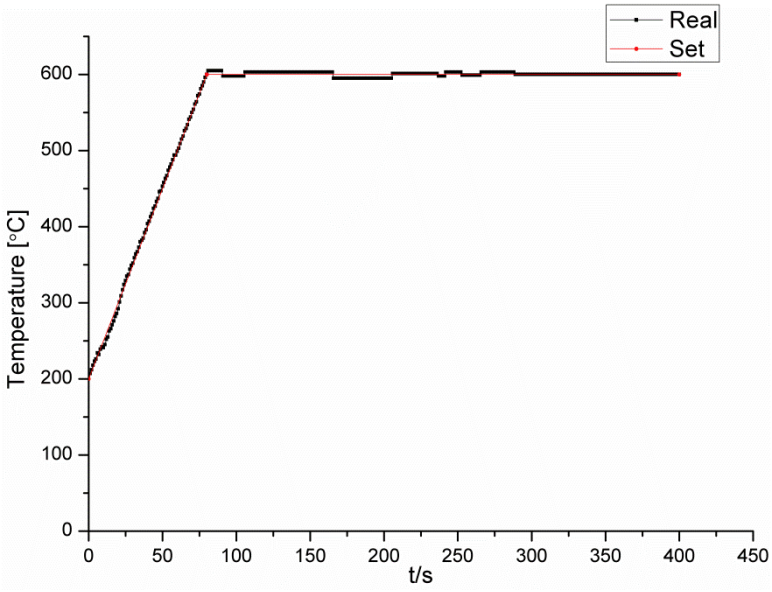

Figure 3-10: The set and real measurement temperature curves for heating rate 5°C/s to final temperature 600°C.

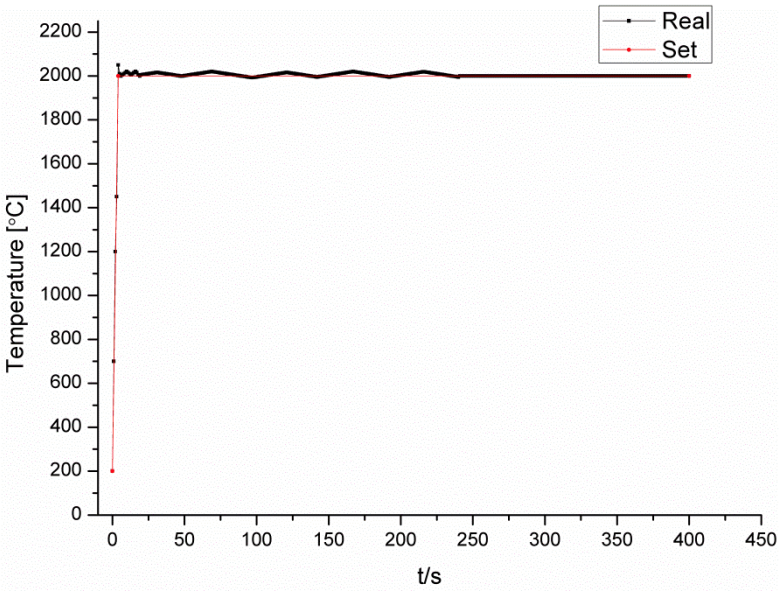

Figure 3-11: The set and real measurement temperature curves for heating rate 450°C/s to final temperature 2000°C.

3.3.2 Gas evolution from infrared gas analyzer

Gas composition was analyzed by both IR and GC measurements. IR measurements were not sufficient to quantify the gas composition due to low sensitivity of the apparatus but it allows continuous analysis of the pyrolysis gas emission. Thus this on-line data gives the typical duration of the reaction. As shown

in Figure 3-12, CH4 was produced before CO and increased to the maximum of 0.23% at 320s. CO showed up 128s later and then increased to the maximum of 1.02% and kept constant for 20s. Taking into account of the RTD inside the reactor, the reaction time should be less than 300s. The start time of sampling is 100s later than PID start time. It means that all of the gas products have been collected with 5min sampling time for MicroGC.

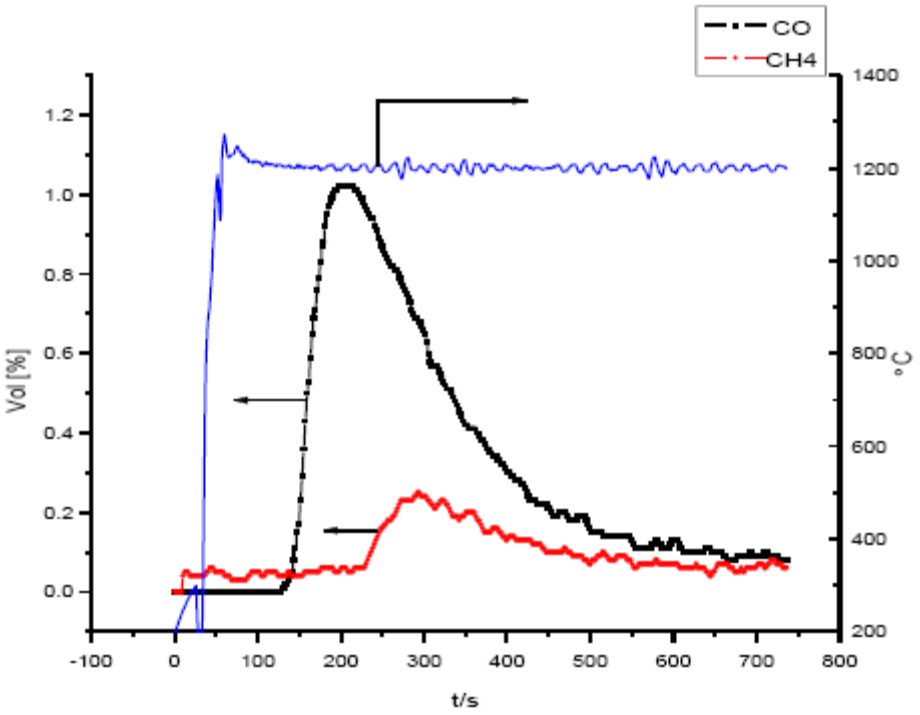

Figure 3-12: Gas release at heating rate 50°C/s and temperature 1200°C, Argon flow rate 6 NL/min.

3.3.3 Experiment with alumina crucible

As the graphite crucible was used for high temperature experiments, the reaction between CO_2 and graphite crucible might exist. And it would change the CO_2 and CO yield. Then alumina crucible was used for comparison for the following conditions: temperature 1200°C and heating rate 50°C/s. The experiment results showed that there was no influence of crucible type on the gas composition. It means that the experiment results with graphite crucible are accurate.

3.4 Feedstock

Beech wood (Fagus) is native to Asia, North America and temperate Europe, and

it can serve as an ideal substrate for pyrolysis conversion. The feedstock used for the experiments was beech wood pellets composed of compressed sawdust (Figure 3-13). They are cylinders with 10 mm diameter and 5 mm height, corresponding to approximately 0.3 g. Sawdust with size 0.35–0.80 mm was provided by the French company SPPS (www.sppsfrance.com).

Figure 3-13: Beech sawdust and pellet

The feedstock was characterized by proximate analysis (ash, moisture, volatile matter and fixed carbon), ultimate analysis (C, H, O, N, S) and chemical constituents. The characteristic values are reported in Table 3-3.

Table 3-3: The main properties of beech wood.

Ultimate analysis	C	wt.%	50.8
	H	wt.%	5.9
	O*	wt.%	42.9
	N	wt.%	0.3
	S	wt.%	0.02
Proximate analysis	Volatile matter	wt.%, dry	85.3
	Fixed Carbon*	wt.%, dry	14.3
	Ash	wt.%, dry	0.4
	Moisture	wt.%	6
Chemical components	Hemicellulose*	wt.%	20.5
	Cellulose	wt.%	64.0
	Lignin	wt.%	15.5

* by difference

The measurements of moisture and volatile matter were performed following the French Standards: NF-M-03-002 (AFNOR 1995), NF-M-03-003 (AFNOR 1994), NF-M-03-004 (AFNOR 2003). The ash content was measured at 550 ℃ following the standard CEN/TS 14775. The fixed carbon content was determined by difference (% fixed carbon = 100 - % ash - % volatile matter - % moisture). C and H contents were determined from an ultimate analysis following the standard CEN/TS 15104,

performed by the laboratory SOCOR (www.socor-sp.com). The O content was deduced by difference (% O = 1 - % H - % C - % ash). The hemicellulose, cellulose and lignin contents were also measured by laboratory SOCOR.

3.5 Solar pyrolysis products characterization

3.5.1 Gas product characterization

The composition of the gaseous products was analyzed by gas chromatography (SRA Instruments MicroGC 3000). After injection of 1-10 μL gas, the columns A and B separate the sample into component gas in less than 180 seconds. Then the micro thermal conductivity detector (TCD) detects the gas compositions with a response time of 5 ms. The detected gases are CO, H_2, CO_2, CH_4 and C_2H_6 in our case.

3.5.2 Solid product characterization

Solid was recovered in the crucible after each experiment shown in Figure 3-14. It was observed that solid is a mixture of charcoal, coke and soot (white color). In this thesis, all the solids are collectively called as "char". CHNS, SEM/EDS (Scanning electron microscopy analysis/Energy-dispersive X-ray spectroscopy), XRD (X-ray diffractometry, Brunauer-Emmett-Teller) were employed to investigate the effect of temperature and heating rate on char composition and structure. All the apparatuses used for solid characterization are shown in Figure 3-15.

Figure 3-14: Char sample in crucible

The elemental composition of char (CHNS) was determined by NA 2100 protein. Surface morphology was investigated by scanning electron microscopy (Philips XL30

FEG). XRD analysis was performed at room temperature using a PANalytical XPert Pro diffractometer (CuK radiation, k = 0.15418 nm, 40 kV – 20 mA). The surface area and pore volume were observed by Brunauer-Emmeet-Teller (BET Tristar II 3020 Micromeritics). The reactivity measurements were performed under isothermal conditions using thermogravimetric analyzer (TG-DSC 111 Setaram). In TGA experiments, 20 mL/min of nitrogen was used during the heating up period with heating rate 20 ℃/min from room temperature to 800 ℃. After that, the sweeping gas was switched on to air for starting the oxidation reaction. The total gas flow rate was 2 L/h with 20% oxygen ratio. The experiment was finished when the weight loss decreased close to zero.

Figure 3-15: Solid characterization apparatuses (RAPSODEE-EMAC Albi): (a) CHNS, (b) SEM/EDS, (c) XRD, (d) BET and (e) TGA

3.5.3 Liquid product characterization

Liquid was recovered in the in impinger bottles after each experiment, as shown in Figure 3-16. It was observed that liquid was a mixture of aqueous and oil phases, which was dark brown in color. In this thesis, all collected liquids are abbreviated as "tar". CHNS, FTIR (Fourier transform infrared spectroscopy), Karl-Fisher and GC-MS were employed to investigate the effect of temperature and heating rate on tar composition and compounds. All apparatuses used for liquid characterization are shown in Figure 3-17.

Figure 3-16: Tar sample in impinger bottles

The GC-MS analysis was performed on a Shimadzu GC-17A gas chromatograph directly coupled to a Shimadzu QP5050A mass spectrometer. The injection mode was manual in this case. The carrier gas used was He 5.0 with a linear velocity of 35 cm s^{-1}. Mass spectra were obtained in electron impact mode (EI) between 40 and 600 a.m.u. using 70 eV with a quadripole analyzer. For GC-MS analyses, the internal standard betulin was not added to the samples. The FTIR spectra of the liquid were scanned in the range 4000-500 cm^{-1} by using Shimadzu's FTIR 8400S.

Figure 3-17: Liquid characterization apparatuses (RAPDODEE-EMAC Albi): (a) GC/MS, (b) FTIR and (c) Karl-Fisher

References

[1] Nzihou A, Flamant G, Stanmore B. Synthetic fuels from biomass using concentrated solar energy - A review. Energy 2012;42:121-131.

[2] Antal MJ, Hofmann L, Moreira JR. Design and operation of a solar fired biomass flash pyrolysis reactor. Sol Energy 1983;30:299-312.

[3] Lédé J. Solar thermochemical conversion of biomass. Solar Energy 1999;65:3-13.

[4] Beattie WH, Berjoan R, Coutures J-P. High-temperature solar pyrolysis of coal. Sol Energy 1983;31:137-143.

[5] Hopkins MW, Dejenga C, Antal MJ. The flash pyrolysis of cellulosic materials using concentrated visible light. Sol Energy 1984;32:547-551.

[6] Tabatabaie-Raissi A, Mok WSL, Antal MJ. Cellulose pyrolysis kinetics in a simulated solar environment. Ind. Eng. Chem. Research 1989;28:856-865.

[7] Chan W-C.R, Kelbon M, Krieger BB. Modelling and experimental verification of physical and chemical processes during pyrolysis of a large biomass particle. Fuel 1985;64:1505-1513.

[8] Chan W-C.R, Kelbon M, Krieger BB. Single-particle biomass pyrolysis: correlations of reaction products with process conditions. Ind. Eng. Chem. Research 1988;27:2261-2275.

[9] Gronli MG, Melaaen MC. Mathematical model for wood pyrolysis – comparison of experimental measurements with model predictions. Energy & Fuels 2000;14:791-800.

[10] Boutin O, Ferrer M, Lédé J. Flash pyrolysis of cellulose pellets submitted to a concentrated radiation: experiments and modeling. Chem. Eng. Sci 2002;57:15-25.

[11] Authier O, Ferrer M, Mauviel G, Khalfi A-E, Lédé J. Wood Fast pyrolysis: Comparison of Lagrangian and Eulerian modeling approaches with experimental measurements. Ind Eng Chem Research 2009;48:4796-4809.

[12] Authier O, Lédé J. The image furnace for studying thermal reactions involving solids. Application to wood pyrolysis and gasification, and vapours catalytic cracking. Fuel 2013;107:555-569.

[13] Pozzobon V, Salvador S, Bézian JJ, El-Hafi M, Maoult YL, Flamant G. Radiative pyrolysis of wet wood under intermediate heat flux: Experiments and modeling. Fuel Process Technol 2014;128:319-330.

[14] Christodoulou M, Mauviel G, Lédé J, Beaurain P, Weber M, Legall H, Billaud F. Novel vertical image furnace for fast pyrolysis studies. Journal of Analytical and Applied Pyrolysis 2013;103:255-260.

[15] Zeng K, Minh DP, Gauthier D, Weiss-Hortala E, Nzihou A, Flamant G. The effect of temperature and heating rate on char properties obtained from solar pyrolysis of beech wood. Bioresour Technol 2015;182:114-119.

[16] Morales S, Miranda R, Bustos D, Cazares T, Tran H. Solar biomass pyrolysis for the production of bio-fuels and chemical commodities. J Anal Appl Pyrol 2014;109: 65-78.

[17] Zeaiter J, N.Ahmad M, Rooney D, Samneh B, Shammas E. Design of an automated solar concentrator for the pyrolysis of scrap rubber. Energy Conversion and Management 2015;101:118-125.

[18] Zeng K, Flamant G, Gauthier D, Guillot E. Solar pyrolysis of wood in a labscale solar reactor: influence of temperature and sweep gas flow rate on products distribution. Energy Procedia 2015;69:1849-1858.

[19] Z'Graggen A, Haueter P, Trommer D, Romero M, De Jesus J, Steinfeld A. Hydrogen production by steam-gasification of petroleum coke using concentrated solar power-II Reactor design, testing, and modeling. International Journal of Hydrogen Energy 2006;31:797-811.

[20] Fossum M, Beyer RV. Co-combustion of natural gas and low calorific value gas from biomass. SINTEF Energy Research, Report prepared for IEA Biomass Gasification Activity, Trondheim; 1998.

[21] Zeng, K, Gauthier, D, Flamant, G. High temperature flash pyrolysis of wood in a lab-scale solar reactor. In: Proceedings of ASME 2014 8th International Conference on Energy Sustainability. Boston, USA (June 30–July 2).

Chapter 4: One-factor-at-a-time experimental results on gas characterization

In this chapter, the pyrolysis of beech wood was investigated in a lab-scale vertical axis solar furnace. First, the influences of temperature (600-2000 ℃), heating rate (5-450 ℃/s), pressure (0.48-1.18 bar) and argon flow rate (6-12 NL/min) on the product distribution were experimentally determined. Then, the gaseous product was characterized with the objective of determining the optimum parameters that are required to maximize the LHVs (lower heating value) of the gaseous products. Material of this chapter has been published in Energy[2].

4.1 State-of-the-art

Up to now, analysis of pyrolysis parameters influence on product distribution in real solar reactor has yet to be reported, although it is very important for the development of solar pyrolysis process. Several differences exist between solar and conventional pyrolysis: solar pyrolysis uses a heat source different from that of conventional pyrolysis, and moreover the heating mode is totally different. In conventional pyrolysis, the heat is transferred from surrounding gas and walls to feedstock. In solar pyrolysis, only the feedstock that absorbs radiation is heated, conversely to the reactor wall and sweep gas. The zone near the feedstock heated surface is at high temperature, whereas the rest of the solar reactor remains relatively "cold" in comparison to the crucible, since its sides and bottom are insulated by graphite foam. However, there is no difference between principles of conventional and solar pyrolysis processes. The chemical reactions (liquid, gas and solid evolution laws) are the same. It is then necessary to review the parameters' effect on the product distribution in conventional reactor, they will afterwards guide the studying in solar reactor.

The liquid yield increases with the temperature and reaches a maximum in the

[2] Zeng K, Gauthier D, Li R, Flamant G. Solar pyrolysis of beech wood: Effects of pyrolysis parameters on the product distribution and gas product composition. Energy 2015;93:1648-1657.

range 400-550 ℃ before decreasing with further temperature increase [1-4]. This behavior results from primary tars that easily crack into light gases at temperatures greater than approximately 500 ℃ [5]. The char yield initially decreases with increasing temperature and remains approximately constant above 600 ℃ [6]. The decrease in char yield with temperature is mainly due to primary pyrolysis reactions [1]. There is a small increase in gas yield with temperature (below 500 ℃) as a result of primary pyrolysis reactions. Subsequently, the gas yield substantially increases with temperature due to the secondary pyrolysis reactions [7]. For instance, the wood pyrolysis gas yield in an entrained flow reactor increases from 29% to 76% as the temperature increases from 650 to 950 ℃ [8]. However, the gas yield of wood fast pyrolysis in a drop tube reactor decreases from 85% to 80% as the temperature increases from 1000 to 1400 ℃ due to hydrocarbon polymerization [9]. Below approximately 450-500 ℃, a small amount of CO_2 (2/3 of total gas) and CO with small quantities of CH_4 arises from the primary decomposition [10]. CO (from 2-15% to 30-55%) and H_2 (from <0.2% to >1%) increase as the temperature increases from 550 ℃ to higher than 850 ℃, as the result of tar secondary reactions [11]. Simultaneously, CH_4 and C_xH_y increase from approximately 1% to greater than 10% [6] and then decrease by 75% as the temperature increases to more than 1000 ℃ due to steam reforming, carbon dioxide reforming and polymerization reactions [9]. There is a limited temperature effect on the CO_2 yield [6], which may decrease due to the reforming reaction with C_xH_y when the temperature is higher than 1200 ℃ [9].

Heating rate is another important parameter that influences the distribution of biomass pyrolysis products. A fast heating rate reduces the heat and mass transfer limitations, which favor bond-scission reactions and enhance the yield of primary volatiles (tar and gases). The liquid yield significantly increases with increasing heating rate at a final temperature below 500 ℃ and rapid quenching before further tar cracking reactions. Subsequently, char formation is minimized under this condition due to the competing reactions between tar evaporation and char formation [12]. However, there is no distinctive effect of heating rate on gas yield at the same time.

For example, the oil yield at heating rate 40 ℃/min was found by Demiral et al. [13] approximately 19.33% higher than that at 7 ℃/min when the final temperature was 500 ℃. At a final temperature of 720 ℃, William and Besler [14] noticed the liquid and gas yields markedly increased as the heating rate increased from 5 ℃/min to 80 ℃/min. The yields of CO, CO_2, H_2, CH_4 and C_2H_6 increased at the same time. Once heat and mass transfer limitations are overcome, the liquid and gas yields may not improve with further heating rate increase [5]. For example, at 1000 ℃, an increase in the heating rate from 2 to 100 ℃/s was observed to enhance the liquid yield by 6%; then, no apparent impact of the heating rate increase from 100 to 2000 ℃/s on the liquid and gas yields was observed [7].

Pressure influences tar secondary reactions and it determines the distribution of pyrolysis products by affecting the volatiles' release, the physical mass transfer inside the biomass sample [15] and the free convection surrounding the sample [16]. In general, three intervals (variation in vacuum pressure range, from vacuum to atmospheric pressure, and from atmospheric to medium pressure) are distinguished. In the vacuum pressure range, the outside of the particle is the important location for tar secondary reactions. The slight reduction in liquid yield with increasing pressure in the vacuum region is caused by extra-particle tar secondary reactions. For example, Murwanshyaka et al. [17] found that the bio-oil yield decreased by 10% when the pressure increased from 0.007 to 0.4 bar. Increasing from vacuum to atmospheric pressure results in desorption of primary volatiles and diffusion slowing down in the biomass porous structure. Then, the liquid yield decreases as more intra-particle tar secondary reactions forming gases and char, which is due to the longer residence time inside the biomass particle [15, 18]. Amutio et al. [15] conducted flash pyrolysis of lignocellulosic biomass under vacuum pressure (0.25 bar) and atmospheric pressure in a bench-scale reactor at 500 ℃. They reported that the liquid yield decreased from 77% to 75% and that the char yield increased by 2% as pressure increased. Moreover, there was almost no variation in the gas yield and compositions. Increasing the pressure from atmospheric to medium pressure not only significantly increases the tar

intra-particle holdup time, but it also enhances extra-particle free convection [16]. However, there is no consensus on pyrolysis product distribution with respect to pressure variation in this range. The liquid yield decreases with pressure, while the gas and char yields increase [19, 20]. Ateş et al. [19] conducted slow pyrolysis experiments at 1, 5 and 10 bar and 600 ℃ in a fixed-bed reactor. They found that the char yield increased by 11 and 10.4% at 5 and 10 bar, respectively, compared to 1 bar. The gas yield increased by 20.7% when the pressure increased from 1 to 10 bar. H_2, CO, and CH_4 increased by 70%, 21.7% and 16.2%, respectively, whereas CO_2 decreased by 44%. However, Newalkar et al. [20] performed flash pyrolysis (estimated heating rates of 1 000-10 000 ℃/s) of pine at high temperatures (600-1000 ℃) and high pressures (5-20 bar) in an entrained flow reactor. No obvious trends for the major gases (H_2, CO, CH_4 and CO_2) were observed except for C_2H_6, which decreased with pressure. Melligan et al. [21] found no pressure influence in the range 1 to 26 bar when they performed slow pyrolysis (heating rate 13 ℃/min) of Miscanthus at 550 ℃. A study on the pressurized pyrolysis of wheat straw in a tubular reactor at 500 ℃ revealed that the liquid and gas yields increased and decreased, respectively, with increasing pressure (from 0.689 to 2.758 bar), whereas the char yield remained constant [22].

Sweep gas purges the hot pyrolysis volatiles from the char matrix and surrounding hot region, which reduces the residence time for tar secondary reactions [23]. Theoretically, the sweep gas maximizes the liquid yield by inhibiting tar thermal cracking, reforming and repolymerization. Sweep gas also causes volatiles' dilution, which reduces extra-particle homogeneous reactions. A reduced concentration of volatiles limits permanent gases and water vapor transformation, which has little effect on the primary tar cracking reaction into gases and secondary tar [6]. However, the tertiary tar formation through the gas-phase nucleation mechanism [11] decreases due to the permanent gases and secondary tar dilution. Consequently, the liquid yield decreases with the sweep gas flow rate, whereas the gas yield increases. There are two different trends for the distribution of pyrolysis products with respect to the sweep gas

flow rate. The first trend is that the liquid yield increases at the expense of the gas yield within the lower sweep gas flow rate range, but it remains almost constant in the higher range [24-26]. However, there are still no standard divisions of sweep gas flow rate intervals. For example, Onay et al. [25] reported that the liquid and gas yields changed with the sweep gas flow rate from 50 to 100 ml/min. Muradov et al. [26] observed an increase in the liquid yield and a decrease in the gas yield at the lower range of argon flow rates (36-60 ml/min). The second trend is that a maximum liquid yield and a minimum gas yield can be observed with increasing sweep gas flow rates [27-29]. For example, Raja et al. [27] performed flash pyrolysis of oil cake in a fluidized bed reactor at 500 ℃ with different sweep gas flow rates. A maximum liquid yield of 64.25% and a minimum gas yield of 31.86% were obtained using a nitrogen flow rate of 1.75 m^3/h.

4.2 Experimental procedure

Four series of experiments were performed, as listed in Table 4-1. Run 1 to Run 9 were dedicated to investigating the final temperature effect, which ranged from 600 to 2000 ℃. The heating rate (50 ℃/s), pressure (0.44 bar), and argon flow rate (6 NL/min) were fixed during the tests. Then, Run 10 to Run 14 were conducted to determine the heating rate effect (ranging from 5 to 450 ℃/s) under constant argon flow rate 6 NL/min, pressure 0.44 bar and final temperature 1200 ℃. The pressure effect was investigated in two series of experiments: (1) Run 15 to Run 17 were conducted at three different pressures (0.44, 0.53 and 0.69 bar) while the temperature, heating rate and argon flow rate were fixed at 1200 ℃, 50 ℃ /s and 6 NL/min, respectively; (2) Run 18 to Run 21 were conducted using four different pressures (0.72, 0.85, 0.99 and 1.14 bar) at fixed values of temperature (1200 ℃), heating rate (50 ℃/s) and argon flow rate (12 NL/min). Finally, Run 22 to Run 24 were performed at 1200 ℃ and 50 ℃/s under 0.72 bar for 6, 9 and 12 NL/min to investigate the argon flow rate effect.

Each run was repeated at least 3 times to check the repeatability. The RSD for the experiment was less than 5%. The error bars indicate 95% confidence intervals.

Table 4-1: Pyrolysis conditions

	Temperature effect (Run 1-9)	Heating rate effect (Run 10-14)	Pressure effect (Run 15-21)	Argon flow rate effect (Run22-24)
Final temperature (℃)	600, 800, 900, 1000, 1200, 1400, 1600, 1800 and 2000	1200	1200	1200
Heating rate (℃/s)	50	5, 50, 150 and 450	50	50
Pressure (bar)	0.44	0.44	0.44[a], 0.53[a], 0.69[a], 0.72[b], 0.85[b], 0.99[b] and 1.14[b]	0.72
Argon flow rate (NL/min)	6	6	6 and 12	6, 9 and 12

[a] Under 6NL/min

[b] Under 12NL/min

4.3 Experimental Results

4.3.1 Effect of temperature on the product yields and gas composition

4.3.1.1 Effect of temperature on product yields

Figure 4-1 shows the product distributions versus the pyrolysis temperature. It is observed that temperature has a drastic influence on the product yields. As the pyrolysis temperature increases from 600 to 800 ℃, the char yield decreases from 16.8% to 9.4% and the gas yield increases from 20.9% to 27.8%. There is a slight increase in the liquid yield from 62.4 to 62.8%, which is similar to that reported by Lédé et al. operating with an image furnace [30]. This result suggests that the gas yield increase as temperature increases from 600 to 800 ℃ is due to char decomposition [1, 31]. As the temperature is increased to 900 ℃, the char and gas yields increase to 13.3% and 29%, respectively. The char and gas yields' increase is primarily attributed to the secondary tar reactions [7, 32], which can be confirmed by the liquid yield decrease to 57.7%. A maximum gas yield of 63.1% was obtained at a pyrolysis temperature of 1600 ℃. The gas yield increase in this temperature interval is primarily due to the secondary tar cracking and partly to the secondary char decomposition because the liquid and char yields decrease to 28.8% and 8.4%,

respectively [33]. However, a further increase in temperature causes a slight gas yield decrease (60.2% at 2000 ℃). The liquid yield increases to 32.3%, while the char yield decreases to 7.7% at the same temperature. The gas yield decrease at high temperature may be due to two reasons: (1) hydrocarbon polymerization, as reported by Septien et al. [9], and (2) decrease in tar secondary reactions due to the decrease of tar residence time in the high-temperature zone [34]. The most obvious gas yield increase (29% to 41.5%) and liquid yield decrease (57.7% to 46.8%) were observed between 900 and 1000 ℃, which indicates that most of the tar decomposition occurs in this temperature range. Taking the error bars into account, the char yield remained quite constant as approximately 8% when the temperature was greater than 1200 ℃, which is consistent with Neves et al.'s observation [6].

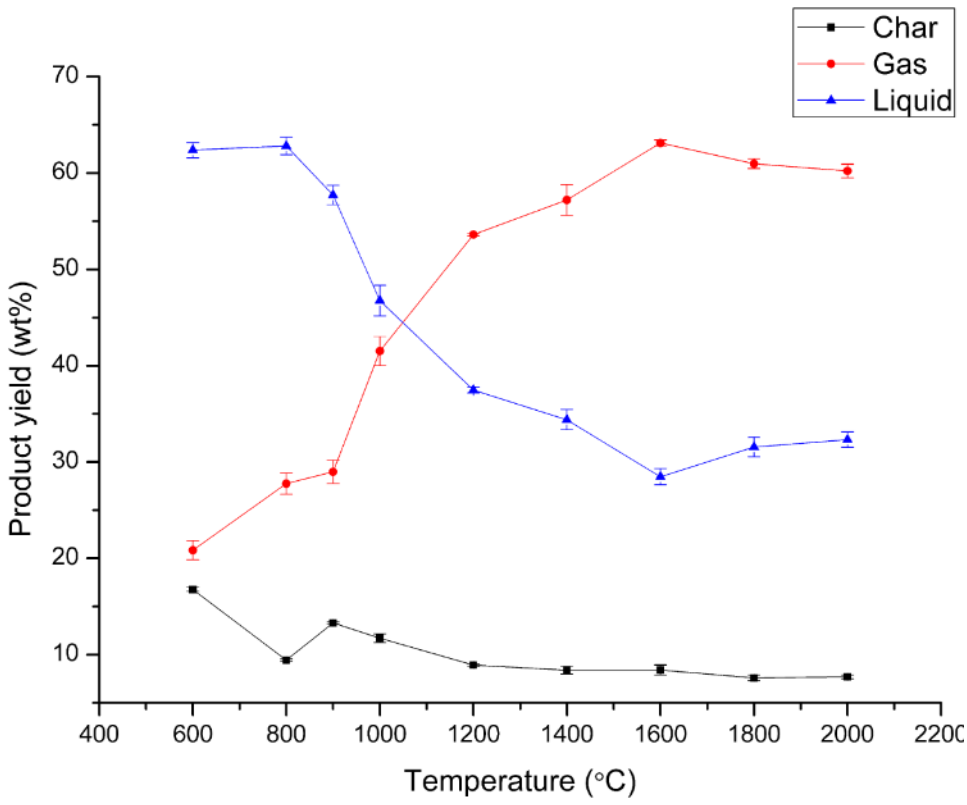

Figure 4-1: Product yields as a function of temperature (pyrolysis conditions: heating rate 50^{o}C/s, pressure 0.44bar, and argon flow rate 6NL/min).

4.3.1.2 Effect of temperature on gas composition

Figure 4-2 shows the temperature influence on the gas composition (a) and LHV (b). The temperature has a considerable effect on them. Figure 4-2a shows that the

main gas products are CO, CO_2, CH_4, H_2 and some C_2H_6. The secondary tar reactions prevail at temperatures greater than 600 ℃ [6]. H_2 and C_2H_6 primarily come from the secondary tar cracking reactions [35], which were not detected at 600 ℃, similar to the results obtained by Commandré et al. [8]. The molar yields of H_2 and CO significantly increase from 0 to 15 mol/kg of wood and from 4.08 to 17.55 mol/kg of wood, respectively, as the temperature increases from 600 to 1600 ℃. This result is similar to the increased syngas yield obtained during mangrove pyrolysis as the temperature increased from 600 to 900 ℃, observed by Ahmed et al. [36]. The rapid increase in H_2 and CO yields can be associated with tar secondary reactions [11]. However, a further increase in temperature to 2000 ℃ caused a small CO molar yield, decreasing to 17.33 molar/kg of wood, due to the reduced tar secondary reactions with the shorter residence time in the high-temperature zone [34]. The CH_4 yield first increased from 0.91 to 2.45 molar/kg of wood due to increased tar cracking when the temperature increased from 600 to 1200 ℃ [35]. Then, it decreased to 0.87 molar/kg of wood at 2000 ℃ due to its own cracking [37] or polymerization reaction [9]. From 600 to 800 ℃, the CO_2 yield decreased from 1.81 to 1.37 molar/kg of wood, which may be due to the reverse Boudouard reaction [26]. There was no appreciable change in the CO_2 and C_2H_6 yields (approximately 0.46 molar/kg of wood) when the temperature was higher than 800 ℃.

The LHVs (lower heating values) of the gas products significantly varied with temperature as a result of the gas composition change (Fig. 4-2b). The total gas product lower heating value increased 5-fold, from 1878±75 to 9621±305 kJ/kg of wood, as temperature increased from 600 to 1200 ℃. This result is somewhat similar to the total HHV of Botryococcus braunii pyrolysis gas product enhancement with temperature [38]. This variation trend mainly results from the variation in the LHVs of CO and H_2. Indeed, the LHVs of CO and H_2 significantly increased from 1153±50 to 4037±28 kJ/kg of wood and from 0 to 2953±180 kJ/kg of wood, respectively, as the temperature increased from 600 to 1200 ℃. Then, there was no statistically significant change in the total LHV at higher temperatures. This result indicates that

1200 ℃ is the optimum temperature for obtaining valuable combustible gas products.

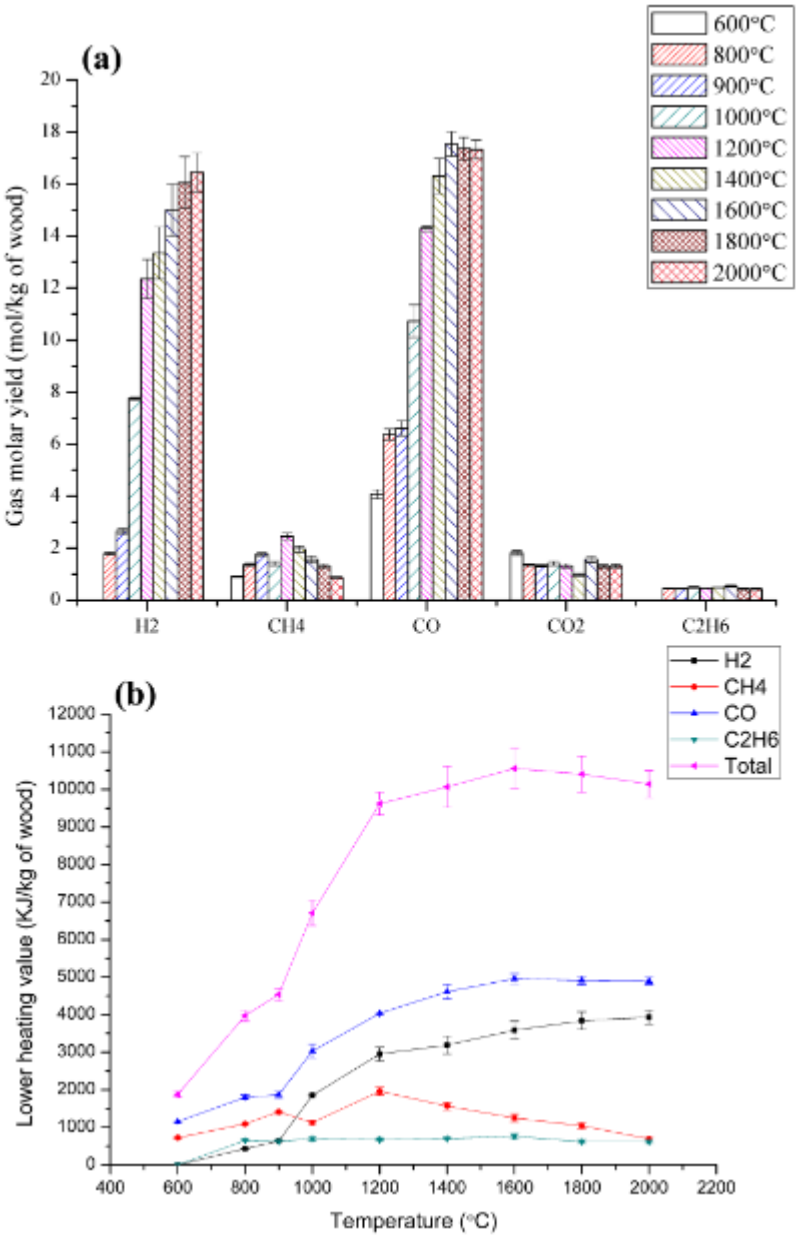

Figure 4-2: Gas characterization at different temperatures (pyrolysis conditions: heating rate 50^{o}C/s, pressure 0.44bar, and argon flow rate 6NL/min): (a) gas composition and (b) LHV.

4.3.2 Effect of heating rate on product yields and gas composition

4.3.2.1 Effect of heating rate on product yields

The product distribution is plotted as a function of heating rate in Figure 4-3 at the plateau temperature of 1200 ℃. As the heating rate increases from 5 to 50 ℃/s, the liquid and char yields substantially decrease from 60.6% to 37.5% and from 13.2% to

8.9%, respectively, whereas the gas yields sharply increases from 26.2% to 53.6%. This is due to the enhanced tar and char cracking reactions caused by the reduction of the heat and mass transfer limitations [39]. When the heating rate increases to 150 ℃/s, the liquid yield slightly increases to 41.5% and the gas yield decreases to 48.1%. The shorter tar residence time inside the sample with high heating rates [7] may explain this observation. Although the tar intra-particle residence time decreases, its temperature increases faster at a heating rate of 450 ℃/s. So, more tar can reach temperatures higher than 500 ℃ before leaving the high-temperature zone. Thus, there is more tar extra-particle cracking or reforming into gases [6]. Then, the liquid yield slowly decreases to 36.5% and the gas yield slightly increases to 54.5% as the heating rate increases to 450 ℃/s. On the other hand, it can be observed that the heating rate effect decreases when it is higher than 50 ℃/s. This result is probably due to heat and mass transfer limitations that are already overcome, which reduces their respective effects [5].

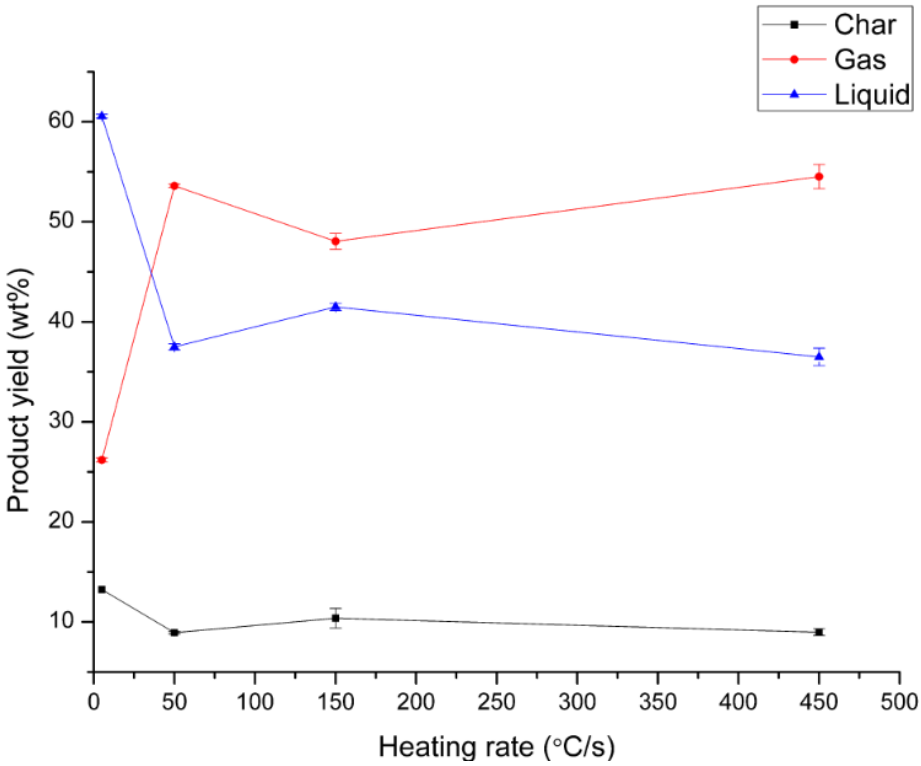

Figure 4-3: Product yields as a function of heating rate (pyrolysis conditions: temperature 1200°C, pressure 0.44bar, and argon flow rate 6NL/min.

4.3.2.2 Effect of heating rate on gas composition

The gas composition (a) and LHV (b) variations with heating rate are illustrated in Figure 4-4. The CO, H_2, CH_4, and C_2H_6 yields remarkably increase from 5.78 to 14.29 mol/kg of wood, from 2.75 to 12.35 mol/kg of wood, from 1.37 to 2.45 mol/kg of wood, and from 0 to 0.47 mol/kg of wood, respectively, as the heating rate increases from 5 to 50 ℃/s (Fig. 4-4a). Simultaneously, the CO_2 yield slightly decreases from 1.65 to 1.41 mol/kg of wood. As the heating rate increases to 150 ℃/s, the CO and H_2 yields slightly decrease to 12.71 and 9.40 mol/kg of wood, respectively, due to the reduced tar secondary reactions with shorter residence time [7, 34]. However, the CO and H_2 yields increase again to 14.75 and 11.45 mol/kg of wood when the heating rate increases to 450 ℃/s. There is almost no distinct influence of heating rate on the CO_2, CH_4, and C_2H_6 yields when it is greater than 50 ℃/s.

The total lower heating value of the gases remarkably increases from 3386 to 9621 kJ/kg of wood as the heating rate increases from 5 to 50 ℃/s (Fig. 4-4b). This increase is primarily due to CO, H_2, and CH_4 LHV variations. Among them, the CO, H_2, and CH_4 LHVs significantly increase from 1633 to 4038 kJ/kg of wood, from 658 to 2953 kJ/kg of wood, and from 1095 to 1961 kJ/kg of wood, respectively. Subsequently, the CO and H_2 LHVs decrease to 3594 and 2248 kJ/kg of wood with a heating rate of 150 ℃/s, and the total lower heating value decreases to 8487 kJ/kg of wood. However, the total lower heating value variation due to a heating rate greater than 50 ℃/s was not statistically significant. Therefore, a 50 ℃/s heating rate should be the optimum heating rate for obtaining valuable combustible gas products in a solar reactor.

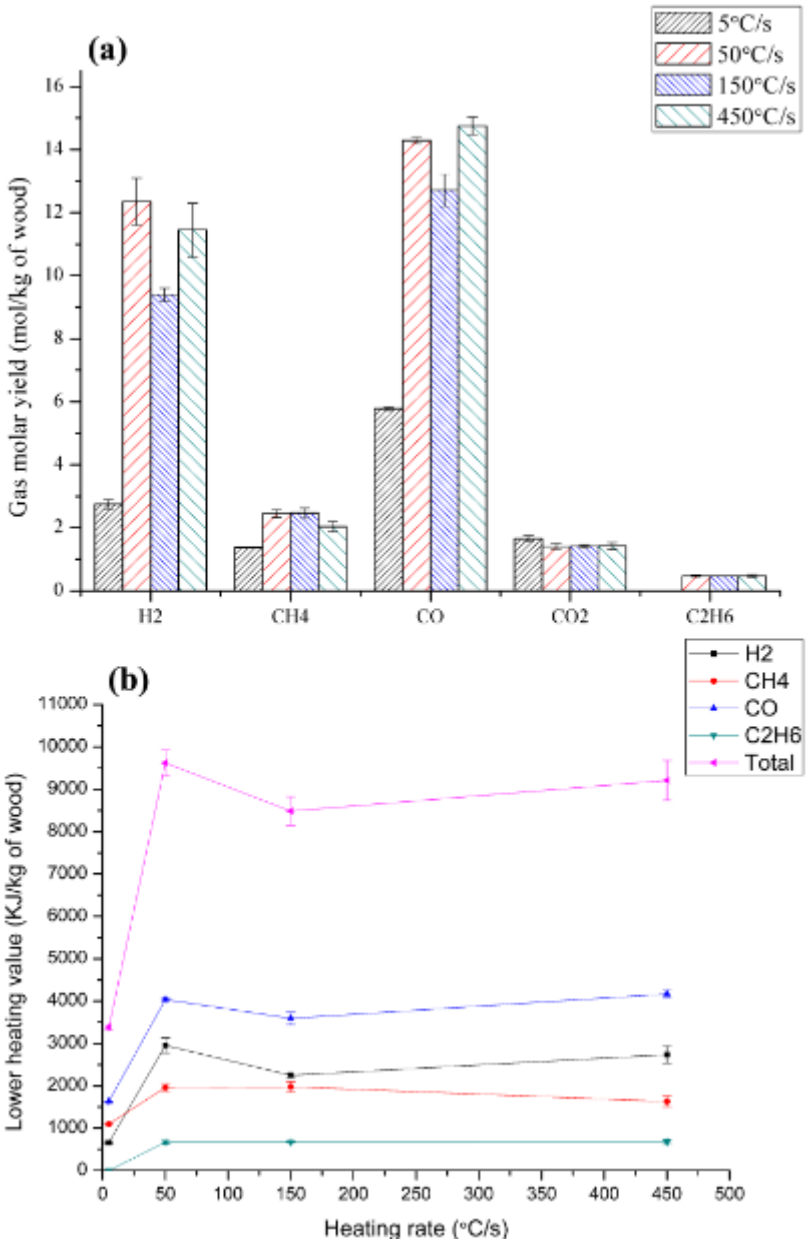

Figure 4-4: Gas characterization at different heating rates (pyrolysis conditions: temperature 1200°C, pressure 0.44bar, and argon flow rate 6NL/min): (a) gas composition and (b) LHV.

4.3.3 Effect of pressure on product yields and gas composition

4.3.3.1 Effect of pressure on product yields

The product distributions as a function of pressure are depicted in Figure 4-5a (lower than atmospheric pressure under an argon flow rate of 6 NL/min) and Figure 4-5b (higher than atmospheric pressure under an argon flow rate of 12 NL/min). There was no change in the pyrolysis products' distribution as the pressure varied

from 0.44 to 0.69 bar (Fig. 4-5a). This result is due to the invariable extra-particle tar secondary reactions, even with the pressure increase [16]. However, the gas yield increased from 60.5% to 62%, partly from the liquid yield decrease from 29.2% to 28.1%, even with a small pressure increase from 0.72 to 0.85 bar (near atmospheric pressure), as shown in Fig. 4-5b. As the pressure increased to atmospheric pressure, the tar intra-particle residence time significantly increased due to primary volatiles slowing in the char matrix. Then, the gas yield increased due to the greater intra-particle tar secondary reactions [15, 18]. Further pressure increase to 0.99 bar enhanced the free convection surrounding the sample [16], and thus, the gas yield clearly decreased to 56%, while the liquid yield increased to 33.6%. The improvement of tar blown out of the high-temperature zone with enhanced free convection may explain this observation. No obvious trend for the product distribution with respect to pressure from 0.99 to 1.14 bar was observed. This result is similar to that reported by Newalkar et al. [20] for pine flash pyrolysis at higher pressures (5-20 bar) in an entrained flow reactor. As shown in Fig. 4-5b, the char yield was approximately 10%, and this value was not sensitive to pressure changes. The small pressure variation range examined might be another reason for the absence of a product distribution with pressure in our case. In conclusion, the atmospheric pressure is a critical point determining the domains of intra-particle and extra-particle tar reactions.

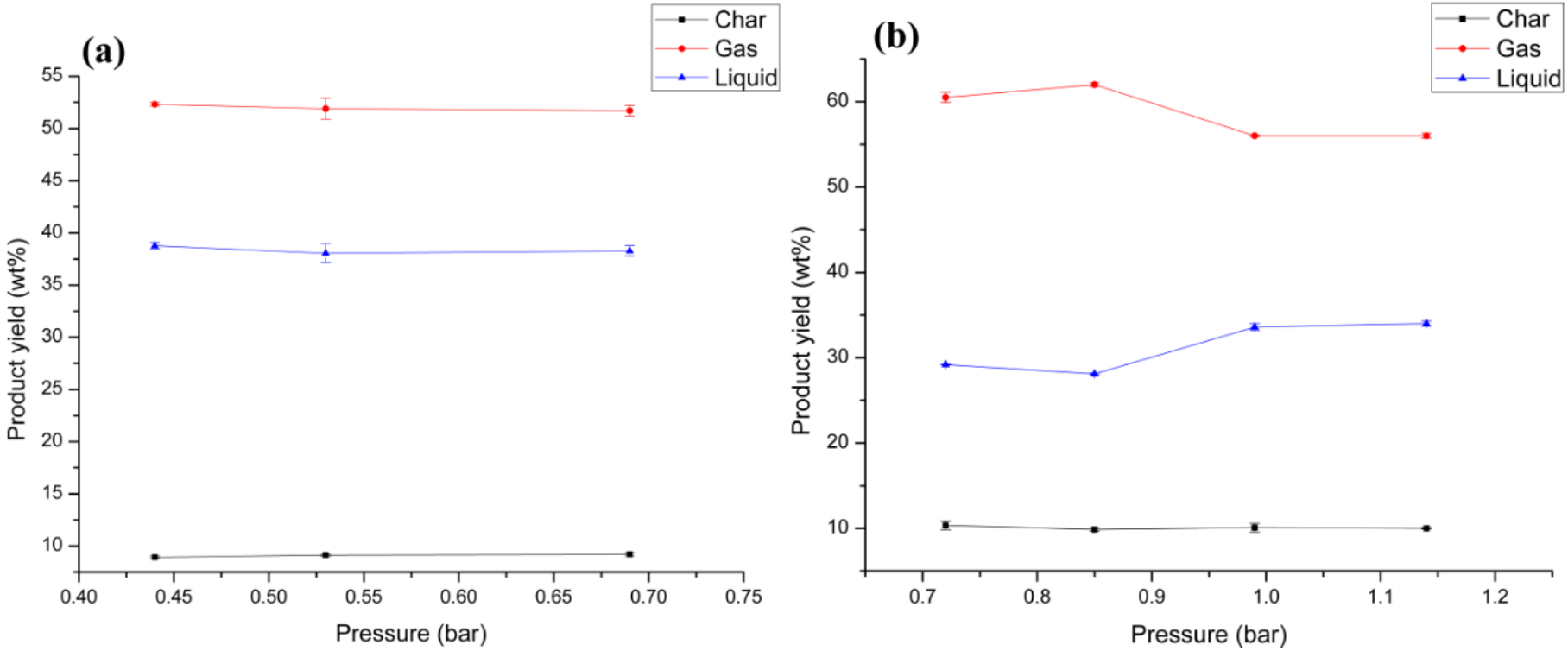

Figure 4-5: Product yields as a function of pressure (pyrolysis conditions: temperature 1200^{o}C and heating rate 50^{o}C/s): (a) under argon flow rate 6NL/min and (b) under argon flow rate 12NL/min.

4.3.3.2 Effect of pressure on gas composition

The gas compositions at different pressures are shown in Figure 4-6a (pressure lower than atmospheric pressure under an argon flow rate of 6 NL/min) and Figure 4-6b (higher than atmospheric pressure under an argon flow rate of 12 NL/min). Approximately 14.15 mols of CO, 11.25 mols of H_2, 2.26 mols of CH_4, 0.47 mols of C_2H_6, and 1.37 mols of CO_2 were produced from 1 kg of beech wood under pressures of 0.44, 0.53, and 0.69 bar (Fig. 4-6a). However, a part of the CO yield increase from 14.36 to 15.14 mol/kg of wood occurred at the expense of the CO_2 yield that decreased from 2.61 to 2.27 mor/kg of wood as the pressure increased from 0.72 to 0.85 bar (Fig. 4-6b). This result confirms that the reverse Boudouard reaction between CO_2 and the carbon in char is favored by a pressure increase because of the longer intra-particle residence time of gas [26]. Another part of the CO yield increase results from tar secondary reactions, which is confirmed by the liquid yield decrease from 29.2% to 28.1%. This may be due to more efficient intra-particle tar secondary reactions when increasing the pressure [15, 18]. At a higher pressure of 0.99 bar, 12.96 mols of CO and 2.52 moles of CO_2 were obtained from 1 kg of beech wood (Fig. 4-6b). Reduced tar extra-particle reactions and the reverse Boudouard reaction explain this observation. No appreciable gas composition change was observed when pressure increased from 0.99 to 1.14 bar.

Fig. 4-7a shows that there is no appreciable pressure influence on the total gas lower heating value: it was almost constant at 9200 kJ/kg of wood. Among them, the LHVs of CO, H_2, CH_4, and C_2H_6 contribute to 4000, 2700, 1800, and 700 kJ/kg of wood of the total gas heating value, respectively. There was a very small increase in the total lower heating value from 9775±250 to 10376±218 kJ/kg of wood as the pressure increased from 0.72 to 0.85 bar (Fig. 4-7b). Then, it decreased to 9000±427 kJ/kg of wood under a pressure of 0.99 bar and remained constant with a higher pressure of 1.14 bar.

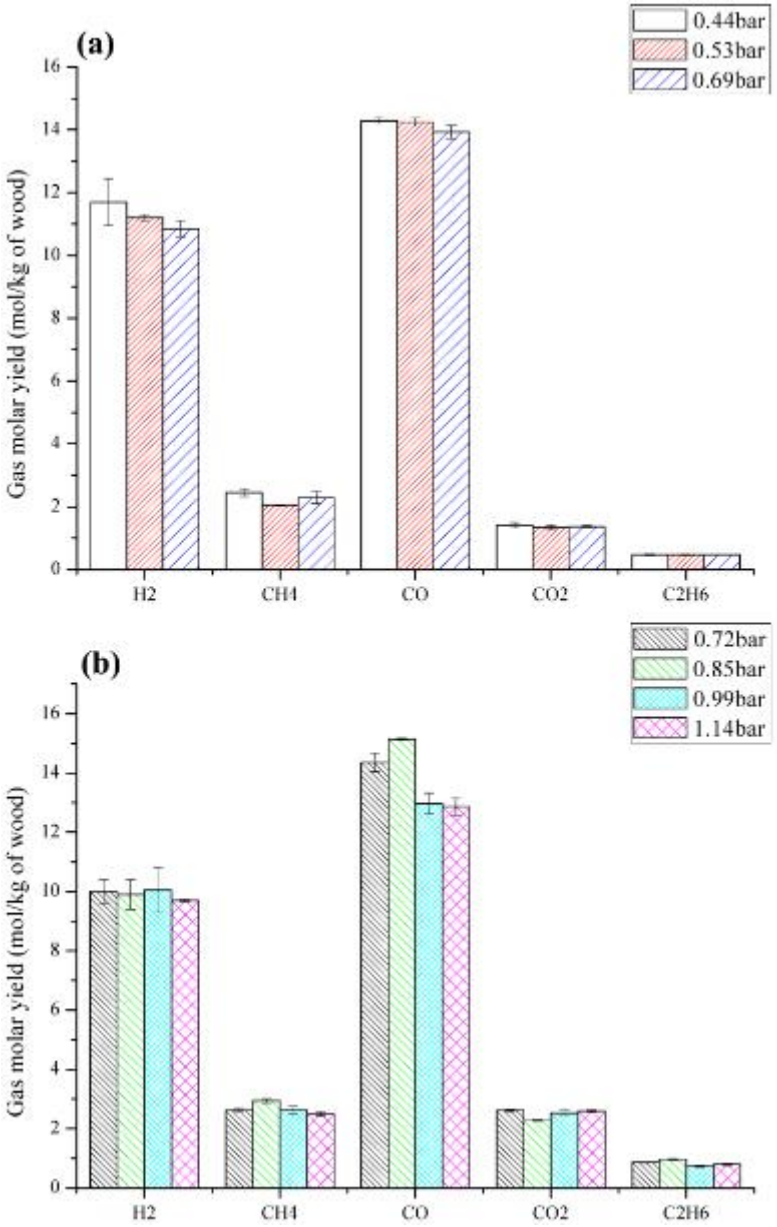

Figure 4-6: Gas composition at different pressures (pyrolysis conditions: temperature 1200°C and heating rate 50°C/s): (a) under argon flow rate 6NL/min and (b) under 12NL/min.

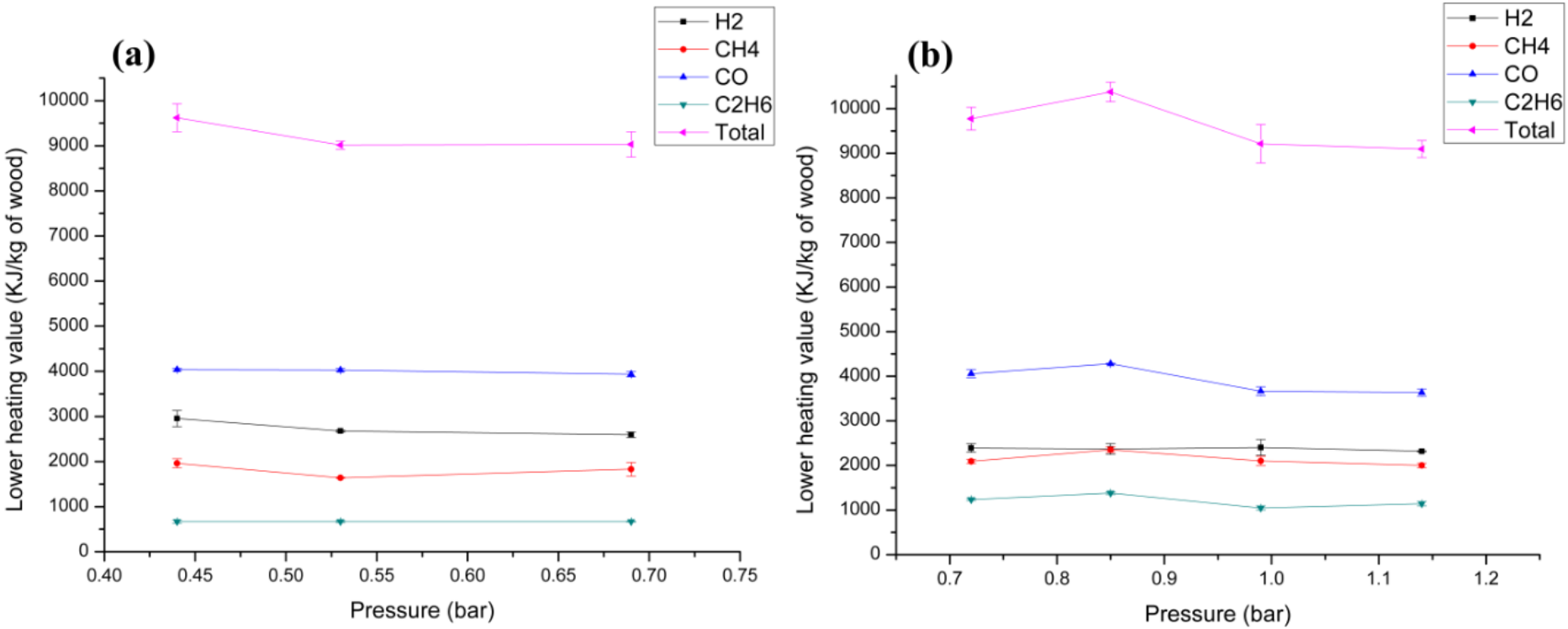

Figure 4-7: Gas LHV at different pressures (pyrolysis conditions: temperature 1200^{o}C and heating rate 50^{o}C/s): (a) under argon flow rate 6NL/min and (b) under argon flow rate 12NL/min.

4.3.4 Effect of argon flow rate on product yields and gas composition

4.3.4.1 Effect of argon flow rate on product yields

Figure 4-8 shows the product yields' variations with the argon flow rate. The gas yield slowly increases from 51.7% to 60.5% as the argon flow rate increases from 6 to 12 NL/min, whereas the liquid yield decreases from 37.5% to 27.2%. The char yield remains constant at 10% over the entire range of argon flow rate. From a general perspective, the intra-particle tar reactions include decomposition to form gases, and polymerization to form char [32]. Because the char yield is constant, the increase in gas yield from intra-particle tar reactions can be eliminated. In conventional reactors, an increase in the sweep gas flow rate generally results in a decrease in the tar residence time in the reactor [40], which inhibits tar secondary reactions [1, 23, 41]. In our case, the special design of the counter-current argon injector system causes a rotational flow field in the solar reactor. Consequently, there is almost no influence of the argon flow rate on the tar residence time. Moreover, the primary volatiles are more diluted at higher argon flow rates, which reduce gas extra-particle homogeneous reactions [6]. Finally, more gas and less liquid products are obtained when increasing the argon flow rate due to less gas-phase reactions producing tertiary tar [11]. There may be another reason to explain the lower liquid yield with higher argon flow rate. The argon gas volume increases with the argon flow rate at this high temperature, and therefore some vapors' partial pressures may not be able to increase to their vapor pressures [42]. Consequently, they cannot condense, and there are more possibilities for their secondary reactions into gas products.

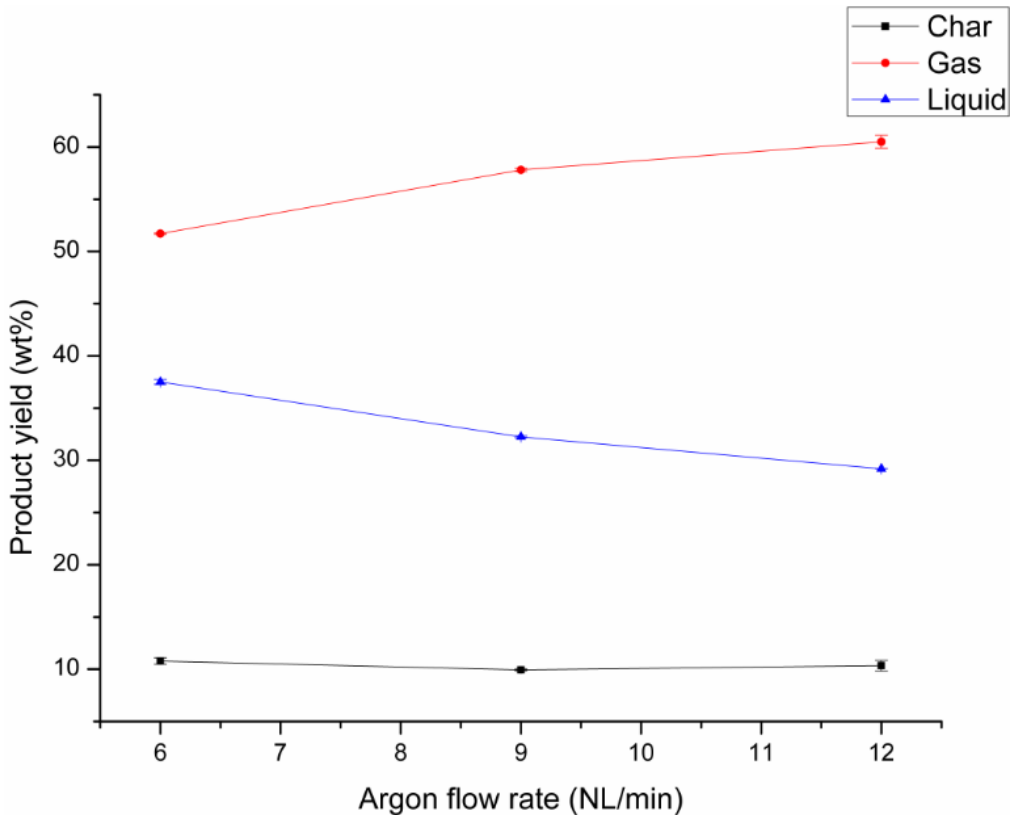

Figure 4-8: Product yields as a function of argon flow rate (pyrolysis conditions: temperature 1200^{o}C, heating rate 50^{o}C/s, pressure 0.72bar).

4.3.4.2 Effect of argon flow rate on gas composition

The gas composition (a) and LHV (b) are plotted in Figure 4-9 as a function of the argon flow rate. The CO, CO_2, and C_2H_6 yields remarkably increase from 13.52 to 14.36 mol/kg of wood, from 1.50 to 2.61 molar/kg of wood, and from 0.50 to 0.87 mol/kg of wood, respectively, when the argon flow rate increases from 6 to 12 NL/min (Fig. 4-9a). Moreover, no appreciable change in the H_2 and CH_4 contents was observed. CO_2 is produced in the primary pyrolysis stage, which can be converted into CO through a gasification reaction with char [43]. In fact, the CO_2 was quickly removed from the char matrix by the high argon flow rate, which inhibited the gasification reaction. Moreover, CO_2 extra-particle homogeneous reactions with light hydrocarbons or tar are inhibited due to the dilution [6]. Consequently, the CO_2 yield increased as the argon flow rate increased.

There was a general growth trend in the LHVs of the gas products, which mainly resulted from the increase in the CO yield as the argon flow rate increased from 6 to

12 NL/min (Fig. 4-9b). However, the 9% increase from 9000 ±484 to 9800 ±250 kJ/ kg of wood for the total LHV is not statistically significant. This result indicates that increasing the argon flow rate is not sufficient to increase the gas product LHV.

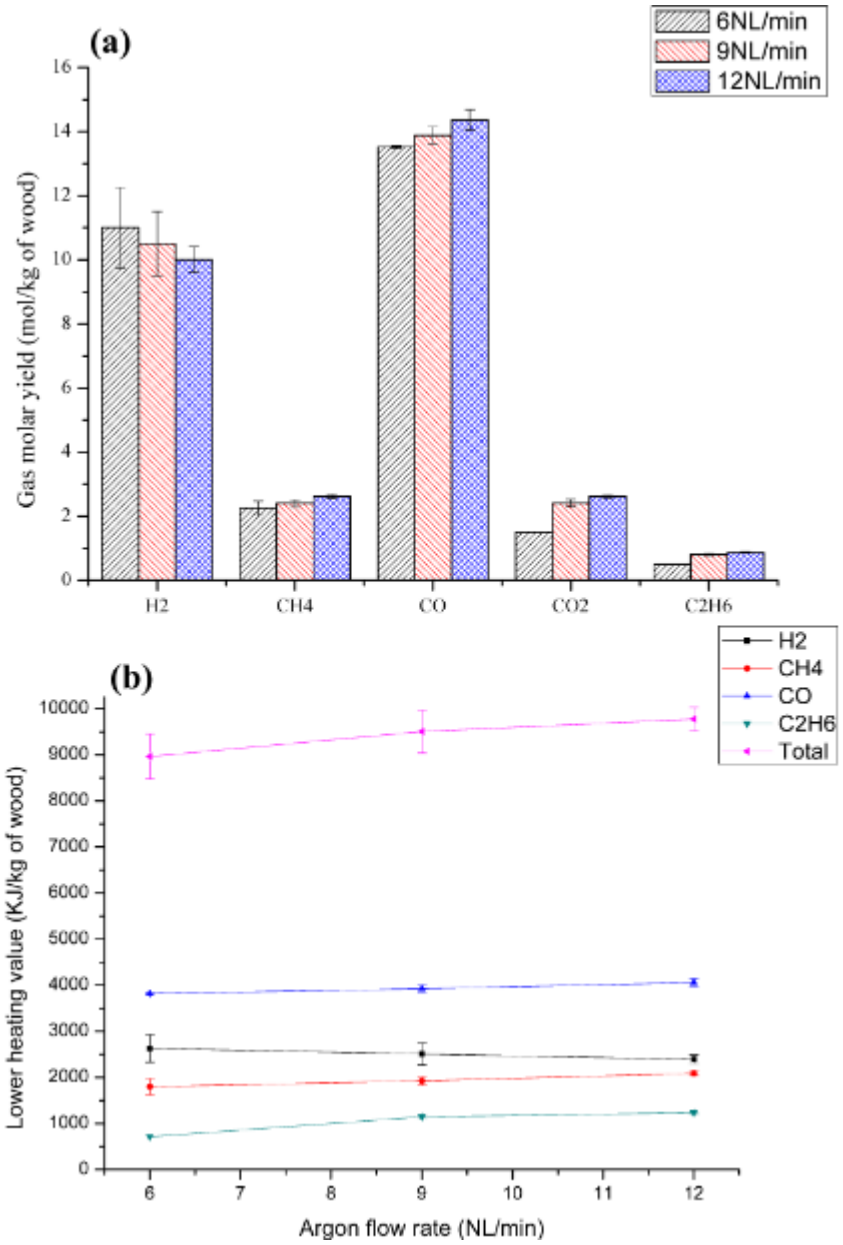

Figure 4-9: Gas characterization at argon flow rates (pyrolysis conditions: temperature 1200°C, heating rate 50°C/s, pressure 0.72bar): (a) gas composition and (b) LHV.

4.4 Conclusion

A solar reactor coupled with a 1.5 kW vertical-axis solar furnace was used for producing bio-fuels from biomass pyrolysis. The effects of temperature, heating rate,

pressure, and argon flow rate on the product distribution and gaseous products' composition were investigated to determine the optimal parameters for obtaining the maximum gas LHV (lower heating value). The key conclusions from this study are as follows:

(1) The temperature drastically affects the final product distribution and gas composition in solar pyrolysis. It is the key parameter governing solar pyrolysis reactions under such experimental conditions. The heating rate and argon flow rate also have a significant influence. These three parameters affect intra-particle and extra-particle tar reactions, which determine the final product distribution. By contrast, the pressure has minimal influence on the product distribution.

(2) Higher CO and H_2 yields are obtained at the plateau temperature of 1200 ℃, heating rate of 50 ℃/s and at atmospheric pressure, indicating that these parameters have an important effect on tar secondary reactions.

(3) The total gas LHV dramatically increases (5-fold) with increasing temperature (from 600 ℃ to 1200 ℃) and sample heating rate (from 5 ℃/s to 50 ℃/s), which is mainly due to variations in the CO and H_2 yields.

(4) A maximum gas LHV of 10376±218 kJ/kg of wood was obtained at 1200 ℃, 50 ℃/s, 0.85 bar and 12 NL/min under solar pyrolysis conditions.

References

[1] Uzun BB, Pütün AE, Pütün E. Fast pyrolysis of soybean cake: product yields and compositions. Bioresour Technol 2006;97:569-576.

[2] Pütün E. Catalytic pyrolysis of biomass: Effects of pyrolysis temperature, sweeping gas flow rate and MgO catalyst. Energy 2010;35:2761-2766.

[3] Şensöz S, Angın D. Pyrolysis of safflower (Charthamus tinctorius L.) seed press cake in a fixed-bed reactor: Part 2. Structural characterization of pyrolysis of bio-oils. Bioresour Technol 2008;99:5498-5504.

[4] Aysu T, Küçük M.M. Biomass pyrolysis in a fixed-bed reactor: Effects of pyrolysisparameters on product yields and characterization of products. Energy 2014;64:1002-1025.

[5] Akhtar J, Amin NS. A review on operating parameters for optimum liquid. Renew Sust Energ Rev 2012;16:5101-5109.

[6] Neves D, Thunman H, Matos A, Tarelho L, Gómez-Barea A. Characterization and prediction of biomass pyrolysis products. Prog Energy Combust Sci 2011;37:611-630.

[7] Chhiti Y, Salvador S, Commandré J-M, Broust F. Thermal decomposition of bio-oil: Focus on the products yields under different pyrolysis conditions. Fuel 2012; 102:274-281.

[8] Commandré J-M, Lahmidi H, Salvador S, Dupassieux N. Pyrolysis of wood at high temperature: The influence of experimental parameters on gaseous products. Fuel Process Technol 2011;92:837-844.

[9] Septien S, Valin S, Dupont C, Peyrot M, Salvador S. Effect of particle size and temperature on woody biomass fast pyrolysis at high temperature (1000-1400^{o}C). Fuel 2012;97:202-210.

[10] Funazukuri T, Hudgins RR, Silveston PL. Correlation of volatile products from fast cellulose pyrolysis. Ind Eng Chem Process Des Dev 1986;25:172-181.

[11] Morf P, Hasler P, Nussbaumer T. Mechanism and kinetics of homogeneous secondary reactions of tar from continuous pyrolysis of wood chips. Fuel 2002; 81:843-853.

[12] Seebauer V, Petek J, Staudinger G. Effects of particle size, heating rate and pressure on measurement of pyrolysis kinetics by thermogravimetric analysis. Fuel 1997;76:1277-1282.

[13] Demiral İ, Eryazıcı A, Şensöz S. Bio-oil production from pyrolysis of corncob (Zea mays L.). Biomass Bioenerg 2012;36:43-49.

[14] Williams PT, Besler S. The influence of temperature and heating rate on the slow pyrolysis of biomass. Renew Energ 1996;7:233-50.

[15] Amutio M, Lopez G, Agudo R, Artetxe M, Bilbao J, Olazar M. Effect of vacuum on lignocellulosic biomass flash pyrolysis in a conical spouted bed reactor. Energ Fuel 2011;25:3950-3960.

[16] Hajaligol MR, Howard JB, Peters WA. An experimental and modeling study of pressure effects on tar release by rapid pyrolysis of cellulose sheets in a screen heater. Combust & Flame 1993;95:47-60.

[17] Murwanashyakaa JN, Pakdela H, Roy C. Step-wise and one-step vacuum pyrolysis of birch-derived biomass to monitor the evolution of phenols. J Anal Appl Pyrol 2001;60:219-231.

[18] Garcìa-Pèrez M, Chaalab A, Roy C. Vacuum pyrolysis of sugarcane bagasse. J. Anal. Appl. Pyrol 2002;65:111-136.

[19] Ateş F, Miskolczi N, Saricaoğlu B. Pressurized pyrolysis of dried distillers grains with soluble and canola seed press cake in a fixed-bed reactor. Bioresour Technol 2015;177:149-158.

[20] Newalkar G, Iisa K, D'Amico AD, Sievers C, Agrawal P. Effect of temperature, pressure, and residence time on pyrolysis of pine in an entrained flow reactor. Energ Fuel 2014;28:5144-5157.

[21] Melligan F, Auccaise R, Novotny EH, Leahy JJ, Hayes MHB, Kwapinski W. Pressurised pyrolysis of Miscanthus using a fixed bed reactor. Bioresour Technol 2011;102:3466-3470.

[22] Mahinpey N, Murugan P, Mani T, Raina R. Analysis of bio-oil, biogas, and biochar from pressurized pyrolysis of wheat straw using a tubular reactor. Energ Fuel

2009;23:2736-2742.

[23] Pattiya A, Sukkasi S, Goodwin V. Fast pyrolysis of sugarcane and cassava residues in a free-fall reactor. Energy 2012;44:1067-1077.

[24] Onay O, Koçkar OM. Pyrolysis of rapeseed in a free fall reactor for production of bio-oil. Fuel 2006;85:1921–1928.

[25] Onay O. Fast and catalytic pyrolysis of pistacia khinjuk seed in a well-swept fixed bed reactor. Fuel 2007;86:1452–1460.

[26] Muradov N, Fidalgo B, Gujar AC, T-Raissi A. Pyrolysis of fast growing aquatic biomass- Leman minor (duckweed): Characterization of pyrolysis of products. Bioresour Technol 2010;101:8424-8428.

[27] Raja SA, Kennedy ZR, Pillai BC, Lee CLR. Flash pyrolysis of jatropha oil cake in electrically heated fluidized bed reactor. Energy 2010;35:2819-2823.

[28] Abnisa F, Daud WMAW, Husin WNW, Sahu JN. Utilization possibilities of palm shell as a source of biomass energy in Malaysia by producing bio-oil in pyrolysis process. Biomass Bioenerg 2011;35:1863-1872.

[29] Açıkalın K, Karaca F, Bolat E. Pyrolysis of pistachio: Effects of pyrolysis conditions and analysis of products. Fuel 2012;95:169-177.

[30] Authier O, Ferrer M, Mauviel G, Khalfi A-E, Lédé J. Wood Fast pyrolysis: Comparison of Lagrangian and Eulerian modeling approaches with experimental measurements. Ind Eng Chem Research 2009;48:4796-4809.

[31] Yang S.I, Wu M.S, Wu C.Y. Application of biomass fast pyrolysis part I: Pyrolysis characteristics and products. Energy 2014;66:162-171.

[32] Pattanotai T, Watanabe H, Okazaki K. Experimental investigation of intraparticle secondary reactions of tar during wood pyrolysis. Fuel 2013;104:468-475.

[33] Onay O. Influence of pyrolysis temperature and heating rate on the production of bio-oil and char from safflower seed by pyrolysis, using a well-swept fixed-bed reactor. Fuel Process Technol 2007;88:523-531.

[34] Beattie WH, Berjoan R, Coutures J-P. High-temperature solar pyrolysis of coal. Sol Energy 1983;31:137-143.

[35] Becidan M, Skreiberg Ø, Hustad JE. Products distribution and gas release in pyrolysis of thermally thick biomass residues samples. J Anal Appl Pyrol 2007;78:207-213.

[36] Ahmed I, Jangsawang W, Gupta AK. Energy recovery from pyrolysis and gasification of mangrove. Appl Energy 2012;91:173–179.

[37] López-González, Fernandez-Lopez M, Valverde J.L, Sanchez-Silva L. Pyrolysis of three different types of microalgae: Kinetic and evolved gas analysis. Energy 2014;73:33-43.

[38] Watanabe H, Li DL, Nakagawa O, Tomishige K, Kaya K, Watanabe MM. Characterization of oil-extracted residue biomass of Botryococcus braunii as a biofuel feedstock and its pyrolytic behavior. Appl Energy 2014;132:475–484.

[39] Salehi E, Abedi J, Harding T. Bio-oil from Sawdust: Pyrolysis of Sawdust in a Fixed-Bed System. Energ Fuel 2009;23:3767-3772.

[40] Sulaiman F, Abdullah N. Optimum conditions for maximising pyrolysis liquids of oil palm empty fruit bunches. Energy 2011;36:2352-2359.

[41] Şen N, Kar Y. Pyrolysis of black cumin seed cake in a fixed-bed reactor. Biomass Bioenerg 2011;35:4297-4304.

[42] Mante OD, Agblevor FA. Parametric study on the pyrolysis of manure and wood shavings. Biomass Bioenerg 2011;35:4417-4425.

[43] Menéndez JA , Domínguez A, Fernández Y, Pis JJ. Evidence of self-gasification during the microwave-induced pyrolysis of coffee hulls. Energ Fuel 2007;21:373–378.

Chapter 5: Box-Behnken experimental results on gas characterization

This chapter presents the results of the Box-Behnken design experimental study that aimed at optimizing a solar pyrolysis process for the production of combustible gases from beech wood. Response surface methodology (RSM) was used to study the interaction effects of temperature, heating rate and argon flow rate on the products distribution, gas LHV (lower heating value) and gas composition. The operating variables were: temperature (800-2000 ℃), heating rate (50-450 ℃/s) and argon flow rate (4-8NL/min). A second-order regression model was used to predict the responses. The proposed model describes well the experimental values. The analysis of variance (ANOVA) was performed with Minitab 17 software and the significant factor effects and their interaction effects were tested at 95% confidence interval. Material of this chapter has been published in Energy Conversion and Management[3].

5.1 State-of-the-art

Previous studies in conventional pyrolysis have shown that pyrolysis parameters such as temperature, heating rate and argon flow rate determine the products distribution and properties [1-3]. Although a lot of research has been carried out on operating parameters effect on conventional biomass pyrolysis, almost all the works only use the one-factor-at-a-time (OFAT) approach. This approach does not depict the combined effects of these operating parameters, although it is necessary to investigate their possible interactions for industrialized application. The parameters' influence rule (single factor effect and interaction effect) in conventional reactors can be treated as the reference when studying real solar reactor. A few researchers tried to use design of experiments (DOE) and response surface methodology (RSM) for

[3] Zeng K, Gauthier D, Lu JD, Flamant G. Parametric study and process optimization for solar pyrolysis of beech wood. Energy Conversion and Management 2015;106:987-998.

studying and optimizing multivariable system. Box-Behnken design [4, 5] and Central composite design (CCD) [6-10] were applied for maximizing bio-oil yields. As far as we know, the optimization of the gas products LHV (lower heating value) using the response surface methodology was never studied.

5.2 Response surface methodology (RSM)

The one-factor-at-a-time approach was used to select the influencing factors and their condition ranges for MINITAB experimental design. Finally, the temperature range (from 800 to 2000^{o}C), heating rate range (from 50 to 450^{o}C/s) and argon flow rate range (from 4 to 8NL/min) were determined as the influencing factor ranges for getting maximum gas products LHV. Then Box-Behnken design was chosen since it is best for three factors. A total number of 15 experimental runs including 3 central runs was generated. The natural unit factor levels and the measured response are shown in Table 5-1. A second-order regression model was used to approximate the response based on the general second-order Taylor series approximation of the form:

$$Y_i = \beta_0 + \sum_{j=1}^{k} \beta_j x_{ij} + \sum_{j=1}^{k} \beta_{jj} x_{ij}^{2} + \sum_{j=1}^{k-1} \sum_{j'>j}^{k} \beta_{jj'} x_{ij} x_{ij'} + \varepsilon_i \qquad (1)$$

A response surface methodology was used to study the temperature (T), heating rate (H) and argon flow rate (A) on the gas yield, char yield, liquid yield, gas LHV, CO molar yield and H_2 molar yield. The experiment results for each factor (T, H and A) were analyzed by analysis of variance (ANOVA) at an alpha level of 0.05 using Minitab 17 software. The statistical models were checked by lack-of-fit test and F-test to examine whether they were adequate to describe the observed data. Terms with p-value less than 0.05 were taken as significant terms with 95% confidence. The lack-of-fit p-value was required to be more than 0.05 for all fitted models. F-value stands for dividing explained variance by unexplained variance. High R-sq value and adjusted R-sq value implied that the model fitting effect was good. The high predicated R-sq indicated that the model was reliable for future forecast. Finally, the normal probability plots of the residuals were checked for the model adequacy.

Table 5-1: Box-Behnken experimental design and results (High heating rate range)

Run Order	Design pattern			Temperature	Heating rate	Argon flow rate	Gas yield	Char yield	Liquid yield	Gas LHV	CO molar yield	H_2 molar yield
	T	H	A	(^oC)	($^oC/s$)	(NL/min)	(wt.%)	(wt.%)	(wt.%)	(kJ/kg of wood)	(mol/kg of wood)	(mol/kg of wood)
1	0	0	0	1400	250	6	59.8	8.6	31.6	11210.8	16.9	19.5
2	-1	0	1	800	250	8	28	16.7	55.3	4064.7	5.3	2.8
3	0	0	0	1400	250	6	58.8	9.6	31.6	10961.7	16.2	17.9
4	0	-1	1	1400	50	8	60.2	8.8	31	10066.0	16.3	13.4
5	1	-1	0	2000	50	6	61.9	8.4	29.7	10248.0	17.7	16.5
6	1	0	-1	2000	250	4	66	10.2	23.8	13080.5	20.2	26.5
7	1	0	1	2000	250	8	71.5	8.2	20.3	13558.2	20.4	24.5
8	1	1	0	2000	450	6	74.6	6.7	18.7	14085.5	21.2	28.9
9	-1	1	0	800	450	6	27.5	14.9	57.6	4402.7	5.9	5.6
10	0	1	1	1400	450	8	67.6	9.7	22.7	11299.9	18.3	16.5
11	0	1	-1	1400	450	4	62.5	9.3	28.2	11713.6	17.7	19.9
12	0	-1	-1	1400	50	4	51	9.2	39.8	9260.4	15.4	14
13	-1	0	-1	800	250	4	23.8	15.6	60.6	4037.2	5.2	3.7
14	0	0	0	1400	250	6	57.9	8.7	33.4	10449.8	16.1	17.2
15	-1	-1	0	800	50	6	27.8	13.05	59.15	3971.5	6.4	1.8

5.3 Experimental Results

5.3.1 Gas yield model

Table 5-2 shows the analysis of variance (ANOVA) on the gas yield. The regression model F-test was significant (p-value < 0.05) with insignificant lack-of-fit (p-value > 0.05). This suggests that the gas yield depends on at least one of the factors. The high R-sq value of 99.71% indicates a good fit of the model accounting for more than 99% of the observed variability. The highly adjusted R-sq of 99.20% close to 99.71% implies that the model fitting is good. The high predicated R-sq of 96.00% means that the model is reliable for future forecast. The individual t-tests indicated that the main effect [temperature (T), heating rate (H) and argon flow rate (A)] coefficients, the second-order (T^2) and interaction term (TH) were significant (p-value less than $\alpha = 0.05$). Due to its highest F value of 1419.56, temperature (T) is selected as the most significant parameter to affect gas yield. The reduced gas yield model consisting of only statistically significant terms is provided in Eq. (2). The positive coefficients of T, A and TH mean that the gas yield increases with these parameters, and the negative coefficients of H and T^2 that it decreases with these parameters.

$$Gas\ yield = -59.0 + 0.12171T - 0.01835H + 1.5A - 0.000033T^2 + 0.000027T * H \quad (2)$$

Table 5-2: Analysis of variance table for gas yield with 95% confidence level

Source	DF	Adj SS	Adj MS	F-Value	P-Value
Model	9	4269.81	474.42	193.42	0.000[a]
Linear	3	3676.41	1225.47	499.61	0.000[a]
T	1	3481.95	3481.95	1419.56	0.000[a]
H	1	122.46	122.46	49.93	0.001[a]
A	1	72.00	72.00	29.35	0.003[a]
Square	3	546.52	182.17	74.27	0.000[a]
T*T	1	526.54	526.54	214.66	0.000[a]
H*H	1	4.14	4.14	1.69	0.251
A*A	1	0.69	0.69	0.28	0.618
2-Way Interaction	3	46.87	15.62	6.37	0.037[a]
T*H	1	42.25	42.25	17.22	0.009[a]
T*A	1	0.42	0.42	0.17	0.695
H*A	1	4.20	4.20	1.71	0.247
Error	5	12.26	2.4		
Lack-of-Fit	3	10.46	3.49	3.86	0.213
Pure Error	2	1.81	0.90		
Total	14	4282.08			

Model Summary: R-sq = 99.71% R-sq(adj) = 99.20% R-sq(pred) = 96.00%

[a] Significant term

The model was confirmed by analyzing the residual plots. The distributional assumption is valid, as indicated by most residuals falling on the straight line in normal probability plot or close to it (Figure 5-1a). No biase is suggested in the lack of apparent pattern of the residuals against fitted values (Figure 5-1b). The residual is in accordance with normal distribution shown in Figure 5-1c. The residual scatter plot shows no abnormality, which suggests that the model is normal (Figure 5-1d). The experimental and predicted values for gas yield are shown in Figure 5-2. It can be seen that predicted values agree well with experimental ones. In 95% confidence interval, 99% of variability in experimental data is accounted to the model described in Eq. (2).

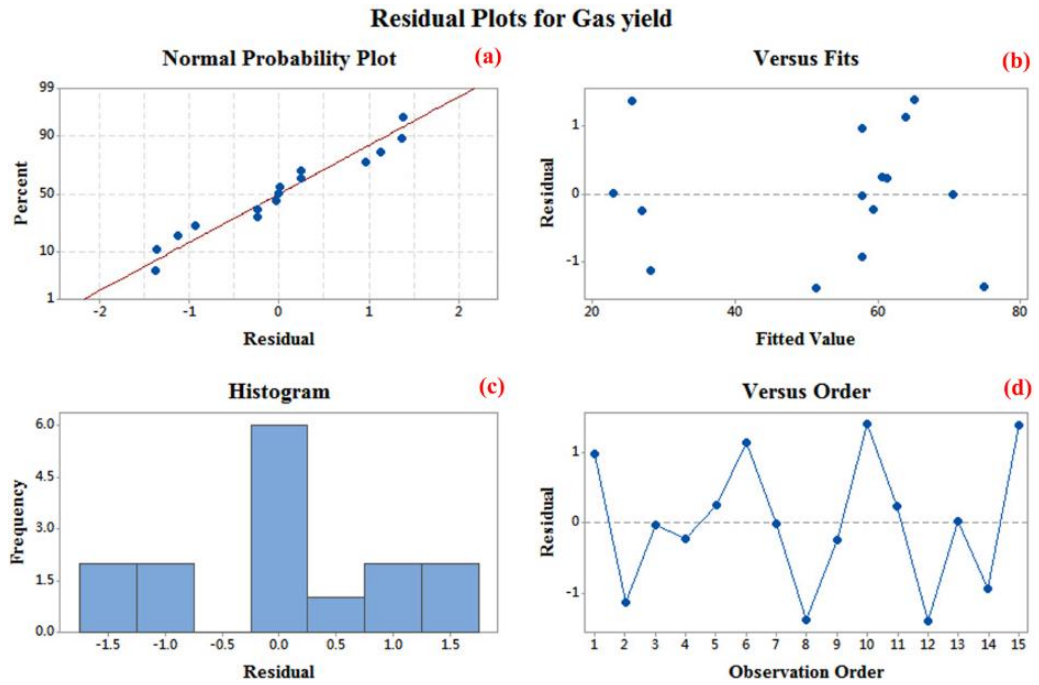

Figure 5-1: Residual plots for gas yield.

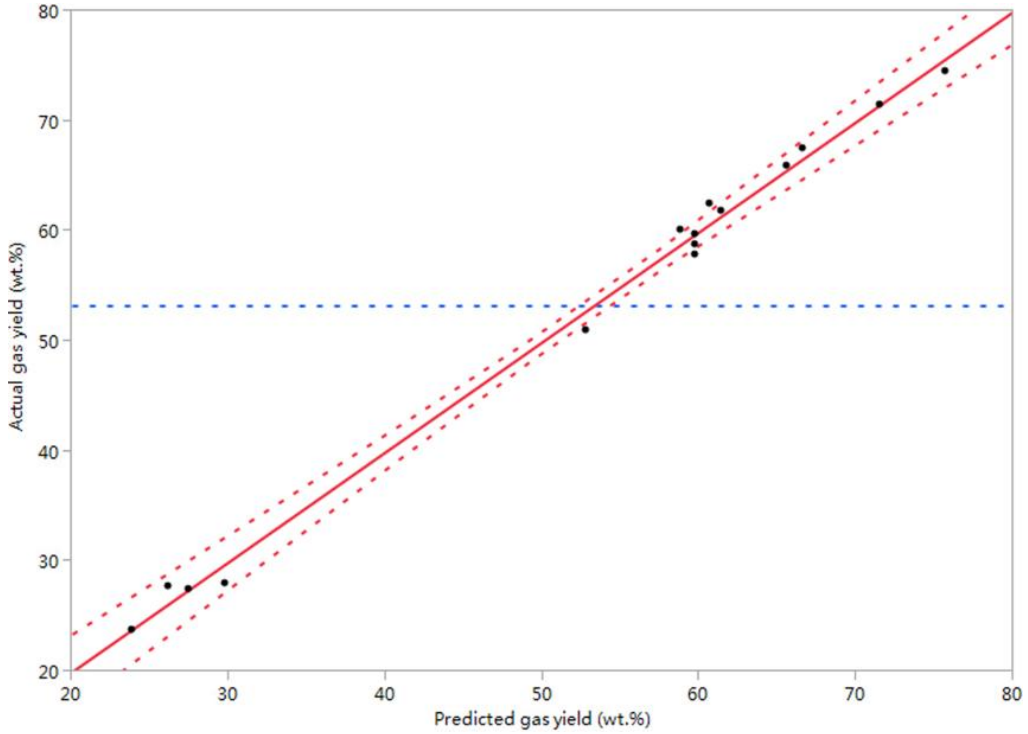

Figure 5-2: Comparison plot between actual (black symbols) and predicted (solid lines) yields of gas by using Eq. (2). Dotted lines represent 95% confidence interval.

5.3.1.1 Effects of temperature and heating rate

As can be seen from the surface plot with contour lines (Figure 5-3A), the gas yield generally increases with temperature. It is well understood that higher

temperatures cause secondary pyrolysis reactions into more gas products [11-13]. Besides, the temperature effect is stronger with higher heating rate. This observation is attributed to the fact that primary pyrolysis products reach high temperature (>500 ℃) faster with higher heating rates, and consequently there is more time for secondary reactions into gases. This previously unreported interaction effect between temperature and heating rate is also predicted by the positive coefficients of TH. Fast heating rate reduces the heat and mass transfer limitations, which favor bond-scission reactions and enhance the primary volatiles (tar and gases) yield [14]. The surface plot with contour lines (Figure 5-3A) suggest that heating rate increase barely affects the gas yield at temperatures lower than 1000 ℃, but it increases gas yield at higher temperatures. The reason may be that an increase in heating rate favors vapors production [14-16], thus more vapors possibly suffering thermal cracking reactions at sufficiently high temperature. Indeed the vapors' cracking is favored at higher temperatures [17]. Overall, it can be noticed that the gas yield variation corresponding to heating rate change is very small. It is probably due to heat and mass transfer limitations already overcome at fast heating rates, which reduce heating rate effect [1].

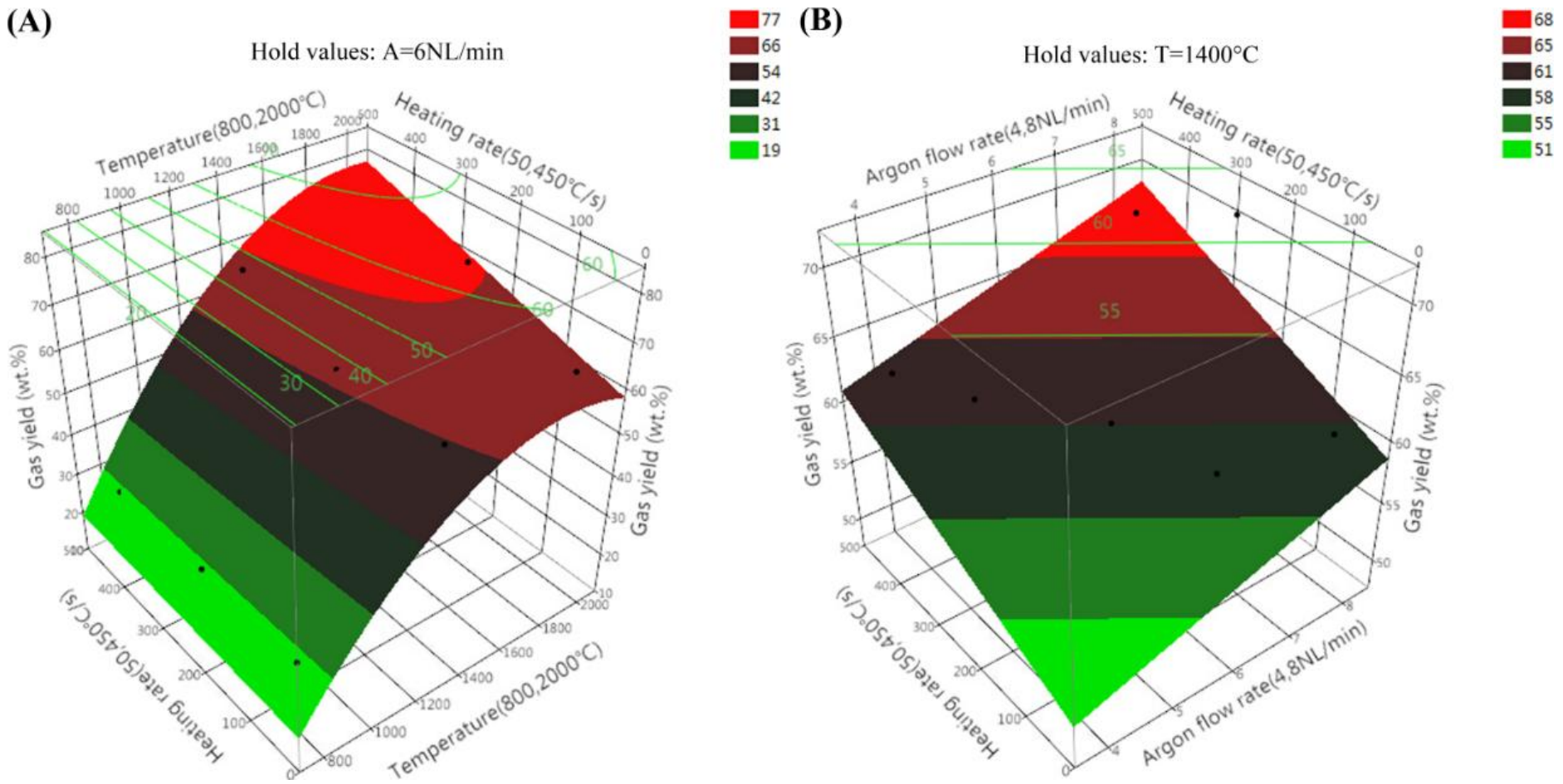

Figure 5-3: Gas yield response surface plot with actual experimental results (black symbols): (A) effect of temperature and heating rate with argon flow rate 6 NL/min, (B) effect of heating rate and argon flow rate at temperature 1400^{o}C.

5.3.1.2 Effects of heating rate and argon flow rate

The gas yield increases with argon flow rate from 4 to 8NL/min as indicated in surface plot Figure 5-3B. Most researchers have found that gas yield decreases with sweep gas increase, which was attributed to vapor shorter residence time in hot temperature zone that would minimize secondary reactions such as thermal cracking into gas products [18-20]. However, the argon flow rate has almost no influence on the tar residence time in solar reactor, owing to counter-current argon injector system. Our contrary argon flow rate effect could be that argon gas volume increases at high temperature and therefore some vapors' partial pressures decrease to a value lower than their equilibrium vapor pressures [4]. As a result, they may not condense thus leading to higher possibility for their secondary reactions into gas. By the way, the primary volatiles are more diluted at higher argon flow rate, which reduces gas extra-particle homogeneous reactions [21]. Finally, more gas products were obtained with argon flow rate increase due to less gas-phase reactions producing tertiary tar [22]. Figure 5-3B shows almost no interaction between the heating rate and argon flow rate, which is evident by the insignificant coefficient of HA (p-value = 0.247) in Table 5-2. No obvious interaction between argon flow rate and temperature is proved by the coefficient of TA (p-value = 0.695) in Table 5-2. Higher temperature combined with higher heating rate, and under higher argon flow rate, should induce higher gas yield.

5.3.2 Char yield model

The analysis of variance on the char yield is shown in Table 5-3. The overall F-test for the model was significant (p-value < 0.05) and the p-value for the lack-of-fit was insignificant (p-value > 0.05). The R-sq value accounted for more than 99.00% of the observed variability and the adjusted R-sq was 97.97%. The high predicated R-sq of 94.85% indicates that the model is reliable for future forecast. The model was confirmed by residual plot examination. Temperature was the only significant factor on the char yield. However, the second-order and a few interaction terms were also significant. T-tests indicated that [temperature (T)] coefficient, the second-order (T^2,

H^2, A^2) and interaction terms (TH and TA) were significant. Due to the highest F value of 477.78, the temperature (T) is selected as the most influential parameter to affect char yield. The char yield in solar pyrolysis of beech wood can be predicted as a function of statistically significant terms with Eq. (3). Figure 5-4 shows the predicted char yield using Eq. (3) with experimental values. The char yield model describes well the data as the experimental and predicted values are close to each other.

$$Char\ yield = 8.967 - 3.344T + 2.61T^2 - 0.815H^2 + 1.098A^2 - 0.888T*H - 0.775T*A \quad (3)$$

Table 5-3: Analysis of variance table for char yield with 95% confidence level

Source	DF	Adj SS	Adj MS	F-Value	P-Value
Model	9	127.925	14.2139	75.93	0.000[a]
Linear	3	89.712	29.9040	159.74	0.000[a]
T	1	89.445	89.4453	477.78	0.000[a]
H	1	0.165	0.1653	0.88	0.391
A	1	0.101	0.1012	0.54	0.495
Square	3	32.500	10.8333	57.87	0.000[a]
T*T	1	25.160	25.1604	134.40	0.000[a]
H*H	1	2.450	2.4500	13.09	0.015[a]
A*A	1	4.451	4.4508	23.77	0.005[a]
2-Way Interaction	3	5.713	1.9044		0.014[a]
T*H	1	3.151	3.1506	16.83	0.009[a]
T*A	1	2.402	2.4025	12.83	0.016[a]
H*A	1	0.160	0.1600	0.85	0.398
Error	5	0.936	0.1872		
Lack-of-Fit	3	0.329	0.1098	0.36	0.791
Pure Error	2	0.607	0.3033		
Total	14	128.861			
Model Summary: R-sq = 99.27% R-sq(adj) = 97.97% R-sq(pred) = 94.85%					
[a] Significant term					

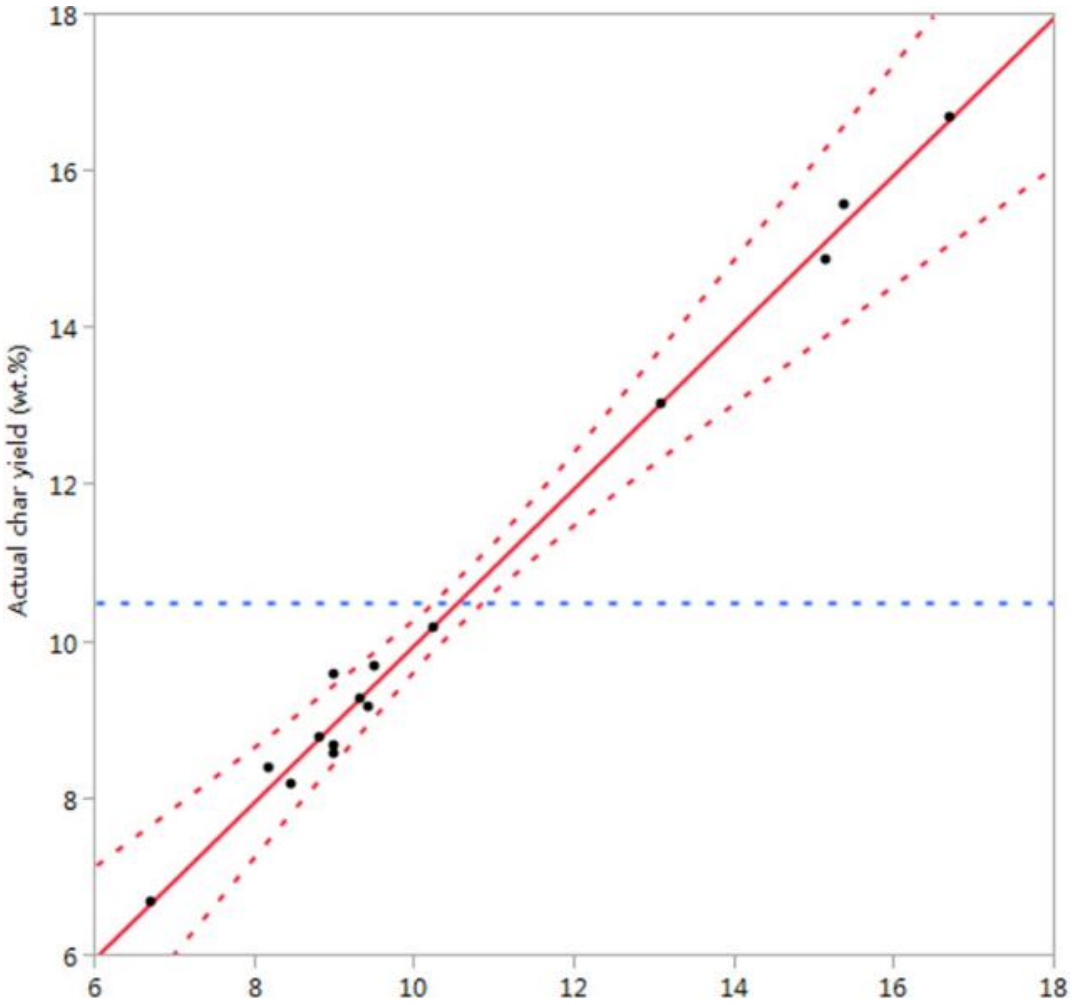

Figure 5-4: Comparison plot between actual (black symbols) and predicted (solid lines) yields of char by using Eq. (3). Dotted lines represent 95% confidence interval.

5.3.2.1 Effects of temperature and heating rate

The surface plot (Figure 5-5A) shows that char formation was enhanced at relatively lower temperatures. The low yield of char at high temperature may be attributed to the enhancement in biomass devolatilization or decomposition through secondary reactions [5]. Another reason may be the lower concentration of potential coke precursors (i.e. heavy molecular weight oxygenated compounds and phenolic compounds) due to their increased decomposition with temperature, which prevents extensive char formation [8]. A third explanation may be the reverse Boudouard reaction favored by temperature rise [18]. The effect of temperature on char yield in this study is in agreement with previous studies [17, 23]. It is also important to mention that the decrease in char yield with temperature is stronger when the heating

rate is relatively high. Research has shown that fast heating rate favors bond-scission reactions and reduces char yield, due to the reducing heat and mass transfer limitations [14]. Heating rate effect on the char yield in solar pyrolysis is a little complicated, as indicated in Figure 5-5A. Increase in heating rate from 50 ℃/s to higher heating rates at temperature lower than 1500 ℃ induces the char yield increase. The opposite observation of heating rate effect is speculated to be due to primary pyrolysis products reaching temperature higher than 500 ℃ faster, before leaving char matrix and then cracking into char. Decrease in heating rate from 450 ℃/s to lower heating rates at temperature higher than 1500 ℃ increases char yield. At high heating rate and relatively high temperatures, the biomass sample and primary pyrolysis products reach high temperature faster, and as a result they are exposed to more thermal cracking, thus leading to lower char yield [17]. Also, the promotion of char formation reactions seems to be inhibited at shorter tar residence time [5] inside the sample, caused by high heating rates [12].

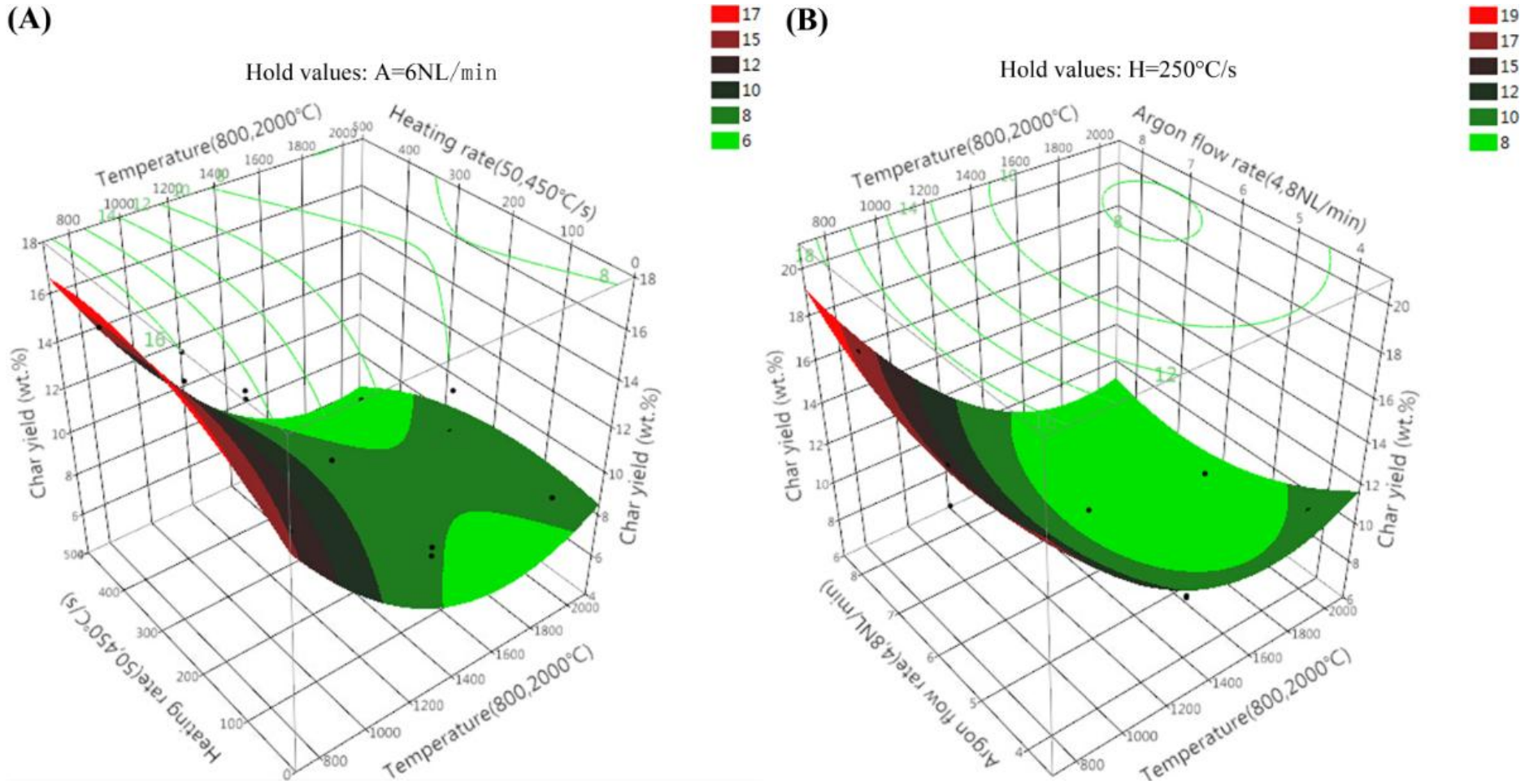

Figure 5-5: Char yield response surface plot with actual experimental results (black symbols): (A) effect of temperature and heating rate with argon flow rate 6 NL/min, (B) effect of temperature and argon flow rate at heating rate 250^{o}C/s.

5.3.2.2 Effects of temperature and argon flow rate

Figure 5-5B shows the interaction effect between argon flow rate and temperature. For temperature lower than around 1400 ℃, there is a small decrease of char yield with argon flow rate up to 6NL/min, then a relatively greater increase under higher argon flow rate. The char yield decrease is due to the reduction of tar thermal cracking into char as the primary pyrolysis products are swept away from char matrix quicker with higher argon flow rate. Tar secondary reactions into char and gas have more chances to occur because of the reduced vapor partial pressures with argon flow rate of 8NL/min [4]. At higher temperature, increasing argon flow rate to 6NL/min results in obvious decrease of char yield, then a relatively smaller increase under higher argon flow rate. The obvious char yield decrease may be explained by the fact that higher temperature provokes more char cracking [5], combined to less char formation under higher argon flow rate (less than 6NL/min).

5.3.3 Liquid yield model

The variance analysis shown in Table 5-4 indicates that the observed model for liquid yield is statistically significant at 95% confidence level. The R-sq value accounted for more than 99.00% of the observed variability and the adjusted R-sq was 98.69%. The high predicated R-sq of 93.50% indicates that the model is reliable for future forecast. The model was confirmed by residual plot examination. The individual t-tests indicate that the coefficients of temperature (T), heating rate (H) and argon flow rate (A), and the quadratic term of temperature (T^2) and interaction term (TH) were the only significant. Due to the highest F value of 865.63, temperature (T) was selected as the most influential parameter affecting the liquid yield. The liquid yield model after removing insignificant terms is provided in Eq. (4). The observed and predicted values for liquid yield are displayed in Figure 5-6. 98% of variability in observed data is accounted to the model described in Eq. (4). The negative coefficients of T, A and TH imply that the liquid yield decreases when these parameters increase.

$$Liquid\ yield = 130.4 - 0.09784T + 0.0073H - 1.444A + 0.000026T^2 - 0.00002T*H \quad (4)$$

Table 5-4: Analysis of variance table for liquid yield with 95% confidence level

Source	DF	Adj SS	Adj MS	F-Value	P-Value
Model	9	3022.12	335.79	118.39	0.000[a]
Linear	3	2653.58	884.53	311.85	0.000[a]
T	1	2455.25	2455.25	865.63	0.000[a]
H	1	131.63	131.63	46.41	0.001[a]
A	1	66.70	66.70	23.52	0.005[a]
Square	3	342.68	114.23	40.27	0.001[a]
T*T	1	321.50	321.50	113.35	0.000[a]
H*H	1	0.22	0.22	0.08	0.792
A*A	1	8.66	8.66	3.05	0.141
2-Way Interaction	3	25.86	8.62	3.04	0.131
T*H	1	22.33	22.33	7.87	0.038[a]
T*A	1	0.81	0.81	0.29	0.616
H*A	1	2.72	2.72	0.96	0.372
Error	5	14.18	2.84		
Lack-of-Fit	3	12.02	4.01	3.71	0.220
Pure Error	2	2.16	1.08		
Total	14	3036.30			
Model Summary: R-sq = 99.53% R-sq(adj) = 98.69% R-sq(pred) = 93.50%					
[a] Significant term					

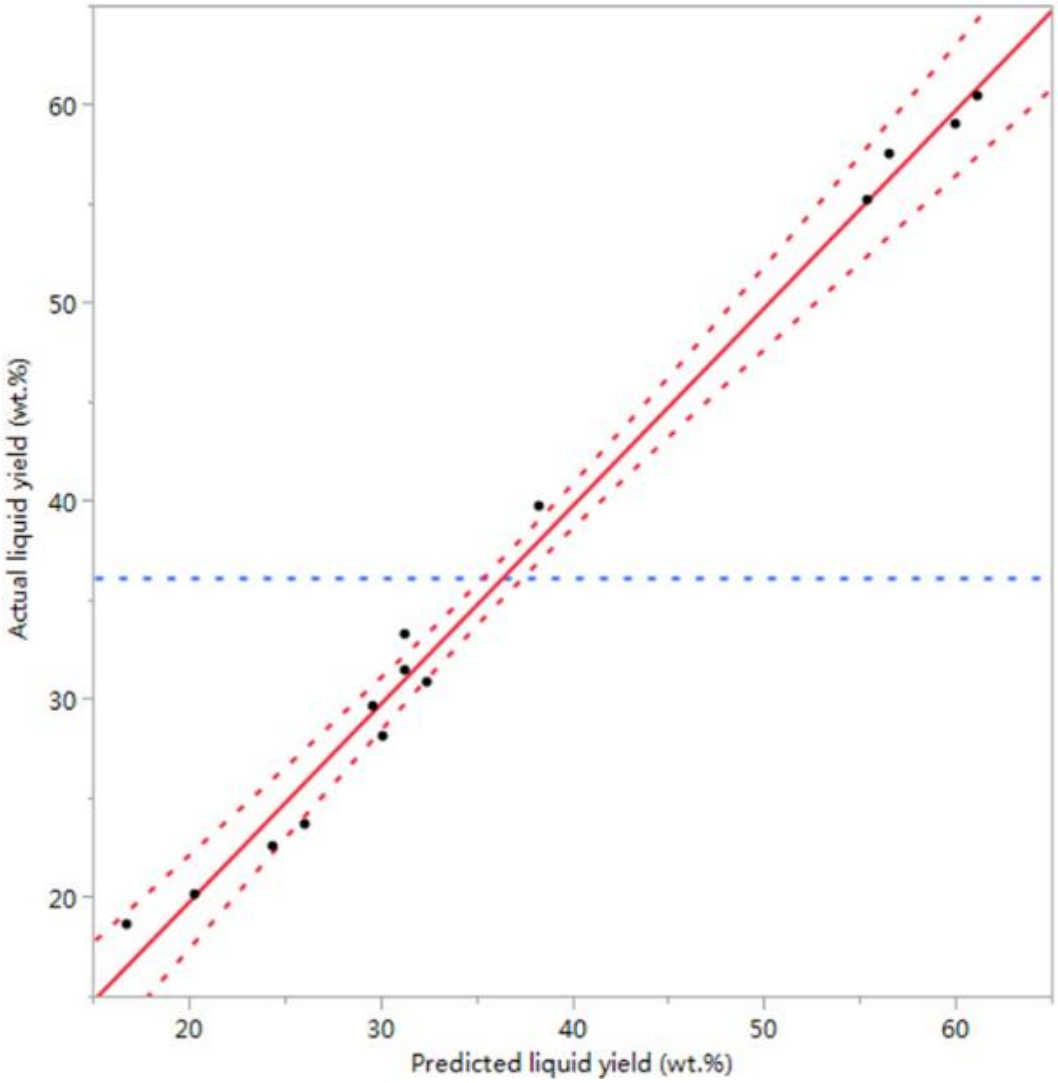

Figure 5-6: Comparison plot between actual (black symbols) and predicted (solid lines) yields of liquid by using Eq. (4). Dotted lines represent 95% confidence interval.

The surface plot (Figure 5-7A) suggests that the liquid yield decreases with temperature, at both low and high heating rates, although with a stronger effect at high heating rate. This result is in agreement with this interaction effect on the gas yield response (Figure 5-3A): higher temperatures and heating rates cause tar secondary pyrolysis reactions into gas products [12, 13, 22]. As shown in Figure 5-7B about the argon flow rate and temperature effects on the liquid yield, the liquid yield decreases when argon flow rate increases from 4 to 8NL/min, which is consistent with Jourabchi et al.'s results [24]. The liquid yield decrease with argon flow rate increase can be explained as follows: the argon gas volume increases with flow rate at high

temperature, causing lower partial pressures. Then, some vapors do not condense because of their reduced partial pressures, thus leading to lower liquid yield [4]. By the way, higher argon flow rate resulting in less liquid yield is probably due to less gas-phase reactions producing tertiary tar [22]. In addition, some of the vapors may have escaped condensation as the vapors' total residence time in the entire pyrolysis unit is reduced with rising argon flow rate [25]. Figure 5-7B shows almost no obvious interaction effect between argon flow rate and temperature, which is evidenced by the insignificant coefficient of TA (p-value = 0.616) in Table 5-4. In addition, the insignificant coefficient of HA (p-value = 0.372) proves there exists no interaction between heating rate and argon flow rate.

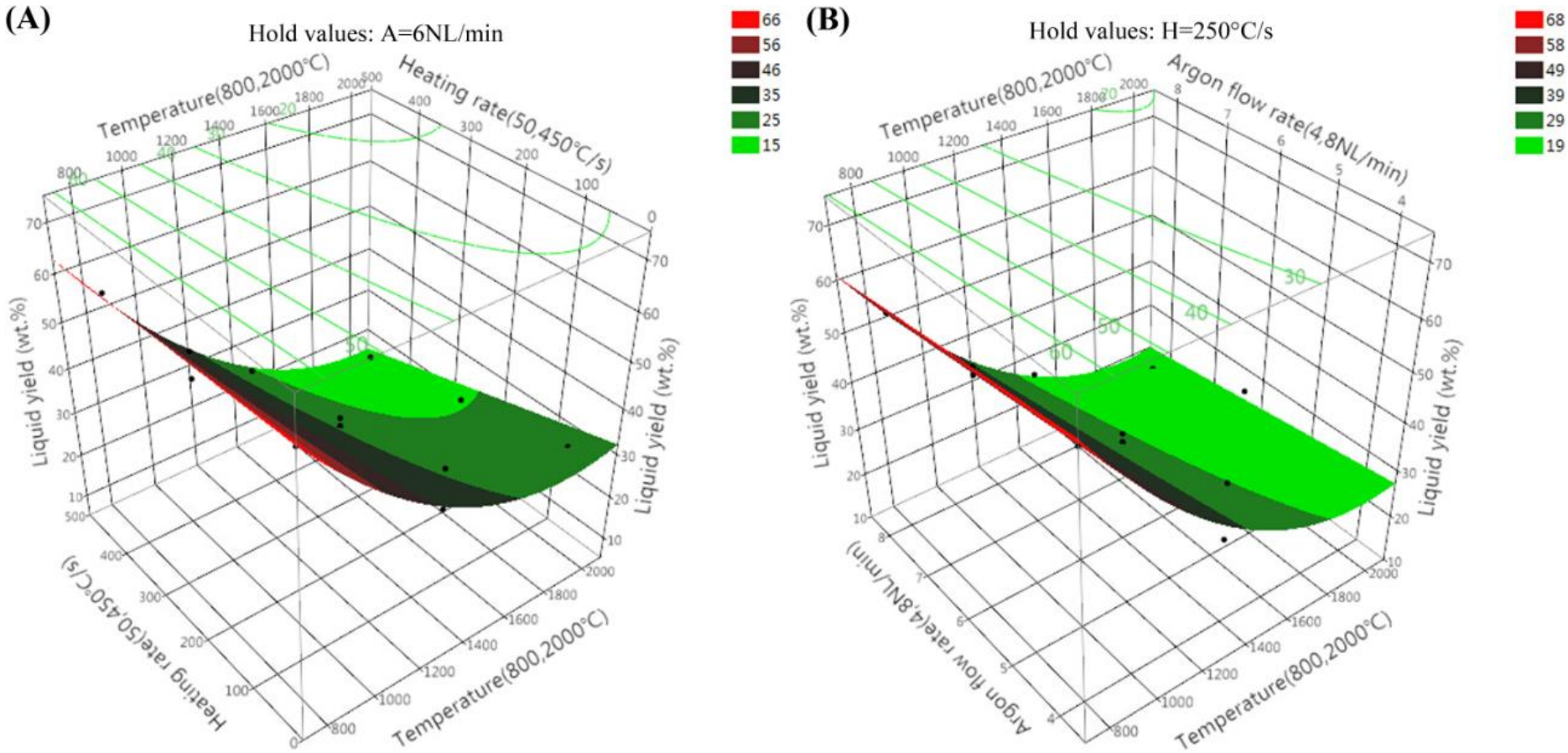

Figure 5-7: Liquid yield response surface plot with actual experimental results (black symbols): (A) effect of temperature and heating rate with argon flow rate 6 NL/min, (B) effect of temperature and argon flow rate at heating rate 250^{o}C/s.

5.3.4 Gas LHV and composition models

Temperature, heating rate and argon flow rate were shown to influence the solar pyrolysis product yield of beech wood. Furthermore, since the gas products (CO, H_2, CH_4, C_2H_6 and CO_2) are generated by complicated pathways (cracking, polymerization, reforming and water gas shift reactions), one may expect that these parameters also influence the gas product properties, in addition to their yields. This is why the LHV (lower heating value) and gas compositions (dominant species are CO and H_2) were analyzed for examining the temperature and heating rate effects on gas products properties.

5.3.4.1 Gas LHV model

The ANOVA analysis in Table 5-5 shows that the gas LHV model had significant F-test and insignificant lack-of-fit test. The R-sq and adjusted R-sq values were 99.35% and 98.18%, respectively. The high predicated R-sq of 91.91% indicates that the model is reliable for future forecast. Further adequacy of the model was confirmed by residual plot examination. The individual t-tests indicate that only the coefficients of temperature (T), heating rate (H), the quadratic term of temperature (T^2) and interaction term (TH) are significant. Due to the highest F value of 632.72, temperature (T) was selected as the most effecting parameter to affect gas products LHV. The gas products LHV in solar pyrolysis of beech wood can be predicted as a function of significant temperature (^oC), heating rate ($^oC/s$) and argon flow rate (NL/min) terms with Eq. (5). The predicted values using Eq. (5) validate the model when in front of experimental gas products LHV (Figure 5-8B). From the model, the positive coefficients of T and TH imply that the gas products LHV increase when these parameters increase.

$$Gas\ LHV = -10513 + 23.13T - 4.96H - 0.006327T^2 + 0.0071T * H \qquad (5)$$

Table 5-5: Analysis of variance table for gas LHV with 95% confidence level

Source	DF	Adj SS	Adj MS	F-Value	P-Value
Model	9	180114933	20012770	85.13	0.000[a]
Linear	3	156761150	52253717	222.27	0.000[a]
T	1	148748847	148748847	632.72	0.000[a]
H	1	7911705	7911705	33.65	0.002[a]
A	1	100599	100599	0.43	0.542
Square	3	20030653	6676884	28.40	0.001[a]
T*T	1	19506854	19506854	82.97	0.000[a]
H*H	1	586863	586863	2.50	0.175
A*A	1	44314	44314	0.19	0.682
2-Way Interaction	3	3323130	1107710	4.71	0.064
T*H	1	2900743	2900743	12.34	0.017[a]
T*A	1	50667	50667	0.22	0.662
H*A	1	371720	371720	1.58	0.264
Error	5	1175474	235095		
Lack-of-Fit	3	874385	291462	1.94	0.358
Pure Error	2	301088	150544		
Total	14	181290407			

Model Summary: R-sq = 99.35% R-sq(adj) = 98.18% R-sq(pred) = 91.91%

[a] Significant term

Heating rate is a significant factor, but Figure 5-8A shows that temperature is more influential. The temperature effect is obvious: the gas products LHV increases with temperature. C. Maguyon et al. [26] reported a similar result in their study on pyrolysis of Nannochloropsis oculata. This is actually an expected result since higher temperature causes more tar secondary reactions into more combustible gases (CO, H_2 and C_2H_6) [27]. Steam reforming reactions and water-gas shift reactions, which convert hydrocarbons into CO and H_2, are prone to occur at higher temperature [28]. By the way, with the same heating rate, the temperature effect on gas products LHV is more obvious when temperature is lower than 1400 ℃, probably because of the small variation of combustible gases over 1400 ℃. The temperature effect on gas products LHV is stronger and stronger when heating rate increases, owing to shorter heating up time to overpass 500 ℃. However, the heating rate influence is not readily apparent. For temperature above around 1000 ℃, the gas products LHV increases with heating rate. This is in accordance with Chihiro et al. [29] who found that cellulose pyrolysis yields of CO, H_2, and CH_4 increased drastically with an increased heating rate, above

570-610 ℃. For temperature below about 1000 ℃, there is no obvious effect of heating rate on the gas products LHV, because of a relatively lower possibility of thermal cracking at lower temperature [4].

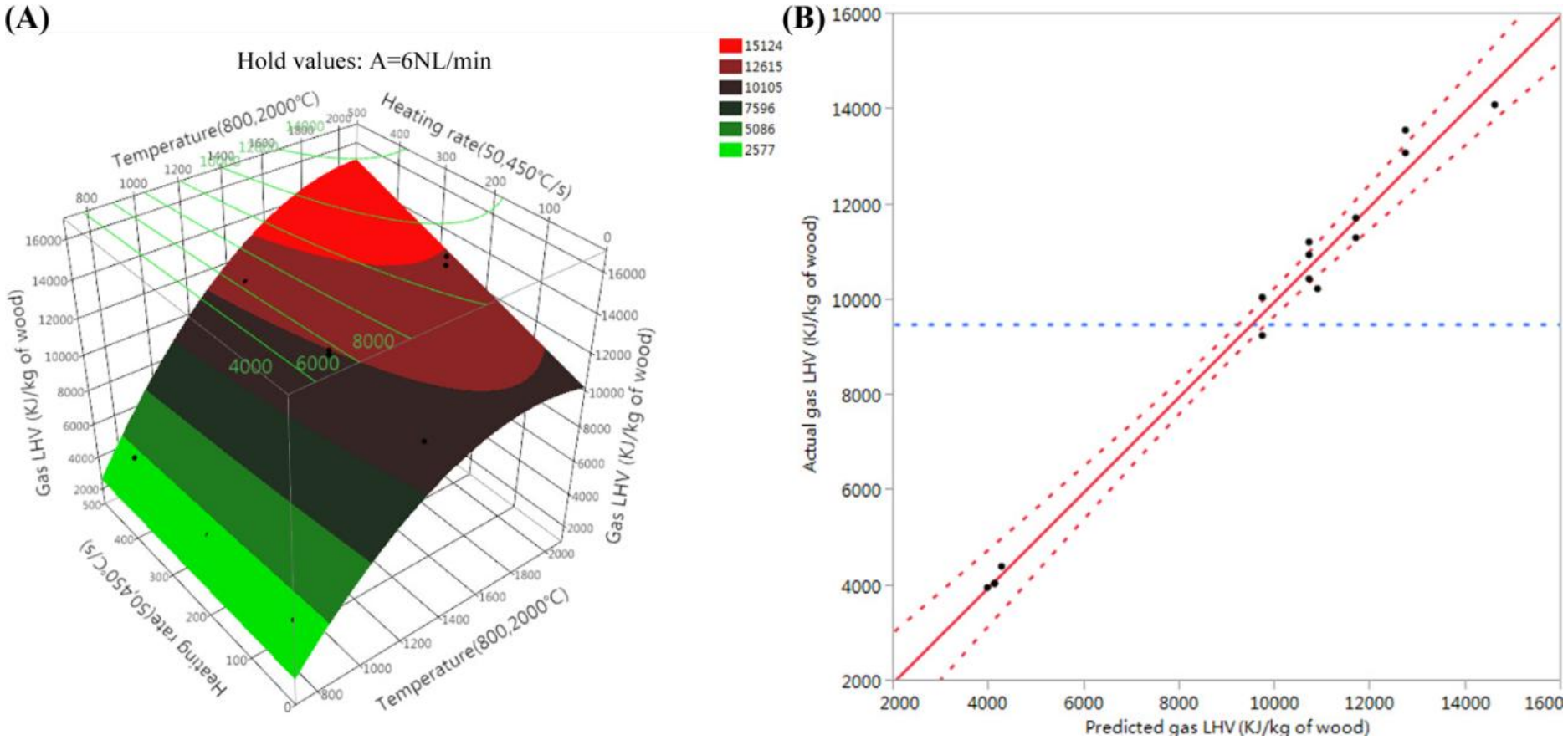

Figure 5-8: Gas LHV response surface plot (A) and model validation plot (B) showing temperature and heating rate effect with argon flow rate 6 NL/min.

5.3.4.2 Gas composition model

The reduced models for the mole yields of CO (Eq. 6) and H_2 (Eq. 7) are both statistically significant at 95% confidence level. The CO and H_2 models' residual plots show the adequacy for predicting the response. The ANOVA analysis in Table 5-6 and Table 5-7 indicate that the CO and H_2 model have significant F-test and insignificant lack-of-fit test. Both R-sq are high and account for more than 98.00% of the observed variability. The high predicated R-sq of 93.43% for CO model indicate that it is more reliable than that of H_2 model (90.42% for reduced model) for future forecast. P-value less than 0.05 indicate that the terms in the model are significant. In this case, temperature (T), heating rate (H), the quadratic term of temperature (T^2) and interaction term (TH) are significant to both responses. Figure 5-9B and Figure 5-10B demonstrate that the predicted values using Eq. (6) and Eq. (7) agree well with actual experimental results of CO and H_2 molar yields.

$$CO(molar\ yield) = -19.36 + 0.04016T - 0.0071H - 0.000011T^2 + 0.000008T * H \quad (6)$$

$$H_2(molar\ yield) = -21.84 + 0.03703T - 0.0093H - 0.000009T^2 + 0.000018T * H \quad (7)$$

Table 5-6: Analysis of variance table for CO molar yield with 95% confidence level

Source	DF	Adj SS	Adj MS	F-Value	P-Value
Model	9	471.511	52.390	113.59	0.000[a]
Linear	3	409.791	136.597	296.16	0.000[a]
T	1	402.570	402.570	872.82	0.000[a]
H	1	6.766	6.766	14.67	0.012[a]
A	1	0.455	0.455	0.99	0.366
Square	3	57.631	19.210	41.65	0.001[a]
T*T	1	55.519	55.519	120.37	0.000[a]
H*H	1	0.242	0.242	0.53	0.501
A*A	1	0.232	0.232	0.50	0.510
2-Way Interaction	3	4.090	1.363	2.96	0.137
T*H	1	4.057	4.057	8.80	0.031[a]
T*A	1	0.008	0.008	0.02	0.901
H*A	1	0.025	0.025	0.05	0.826
Error	5	2.306	0.461		
Lack-of-Fit	3	1.887	0.629	3.00	0.260
Pure Error	2	0.420	0.210		
Total	14	473.818			
Model Summary: R-sq = 99.51% R-sq(adj) = 98.64% R-sq(pred) = 93.43%					
[a] Significant term					

Table 5-7: Analysis of variance table for H2 molar yield with 95% confidence level

Source	DF	Adj SS	Adj MS	F-Value	P-Value
Model	9	1004.30	111.589	37.40	0.000[a]
Linear	3	935.80	311.933	104.54	0.000[a]
T	1	849.75	849.750	284.77	0.000[a]
H	1	80.01	80.011	26.81	0.004[a]
A	1	6.04	6.038	2.02	0.214
Square	3	47.66	15.886	5.32	0.051
T*T	1	39.80	39.804	13.34	0.015[a]
H*H	1	10.62	10.619	3.56	0.118
A*A	1	1.05	1.050	0.35	0.579
2-Way Interaction	3	20.85	6.949	2.33	0.191
T*H	1	18.71	18.706	6.27	0.054[b]
T*A	1	0.25	0.250	0.08	0.784
H*A	1	1.89	1.891	0.63	0.462
Error	5	14.92	2.984		
Lack-of-Fit	3	12.01	4.003	2.75	0.278
Pure Error	2	2.91	1.456		
Total	14	1019.22			

Model Summary: R-sq = 98.54% R-sq(adj) = 95.90% R-sq(pred) = 80.51%

[a] Significant term

[b] Taken as significant term

In the surface plot for CO molar yield (Figure 5-9A), it can be seen that the CO molar yield increases with temperature, and it increases faster at relatively higher heating rates. Some studies have reported that CO formation is highly influenced by secondary reactions of tar at temperature higher than 500 ℃ [30]. This suggests that primary tar cracking into CO is predominant at higher temperature [31], which is more obvious at higher heating rates owing to shorter heating up time to reach secondary temperature. Also, possible char decomposition or reversed Boudouard reaction (char with CO_2) at higher temperature and heating rate may induce the CO molar yield increase [18]. At lower temperature (1400 ℃), there is no obvious effect of heating rate on the CO molar yield. For relatively low heating rate of 50 ℃/s, there are more possibilities for tar secondary reactions into CO with longer residence time in the pellet [1]. This undermines lower heating rate effect on inhibition of primary volatiles production due to heat and mass transfer limitations [29]. However, at relatively higher temperatures, the CO molar yield increases with the heating rate.

This may come from the fact that high heating rates comparatively generate more volatiles [27], and they continue extra-particle secondary reactions at this temperature level, in spite of the reducing intra-particle residence time.

The interaction between temperature and heating rate shown in the surface plot (Figure 5-10A) generally indicates that H_2 molar yield is higher at higher temperature with higher heating rate. The combined effect of temperature and heating rate on H_2 molar yield is almost the same as that on CO molar yield, as shown by the similar display of surface plots (Figure 5-9A and Figure 5-10A). In addition, the molar yield ratio between CO and H_2 is nearly 1:1 under most experimental conditions, and therefore this gas mixture can be used as syngas [32]. The gas products LHV generally increases with temperature and heating rate mainly from CO and H_2 variations, which is indicated by their surface plot (Figure 5-8A) similar to those of CO and H_2.

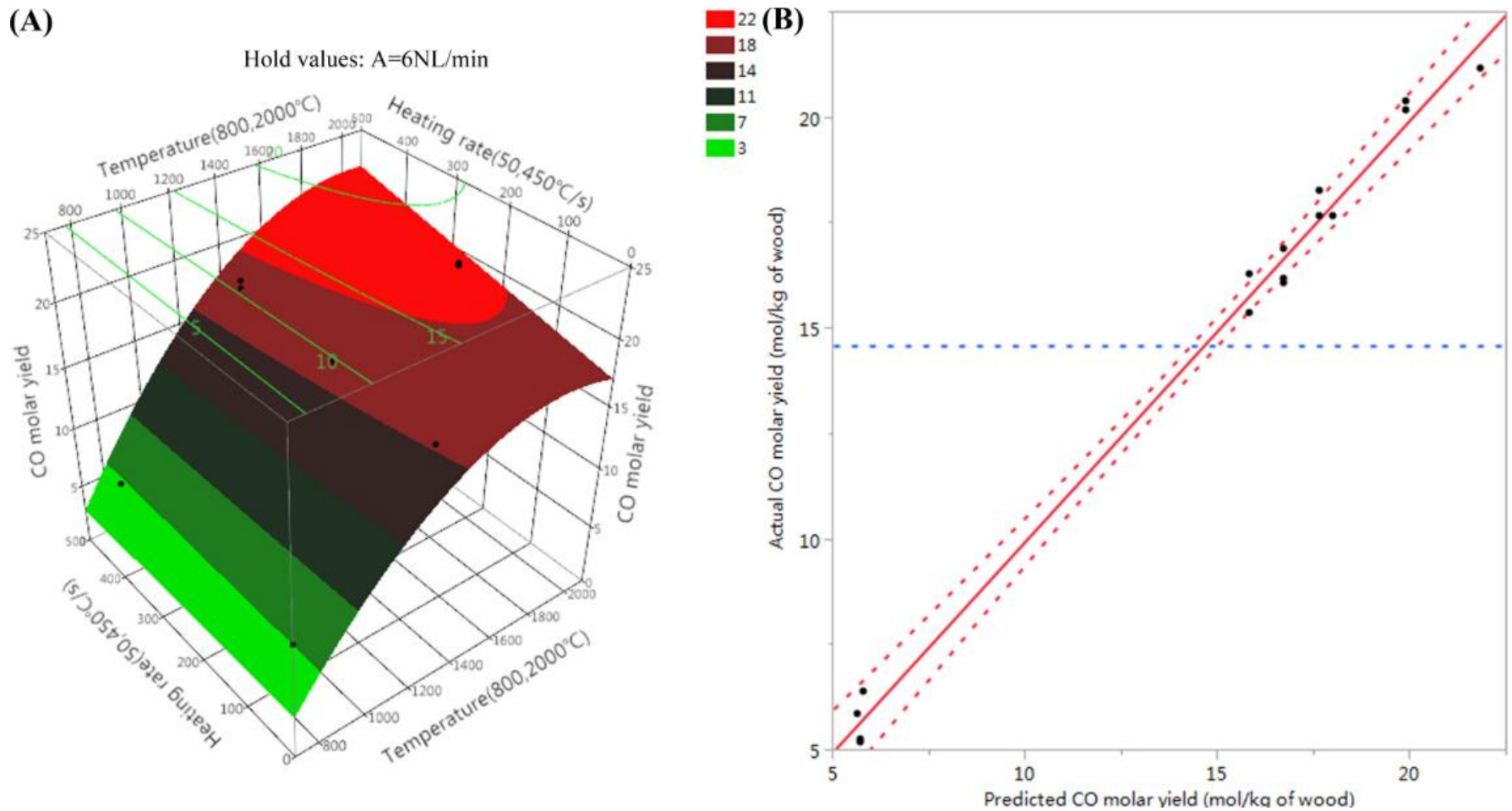

Figure 5-9: CO molar yield response surface plot (A) and model validation plot (B) showing temperature and heating rate effect with argon flow rate 6 NL/min.

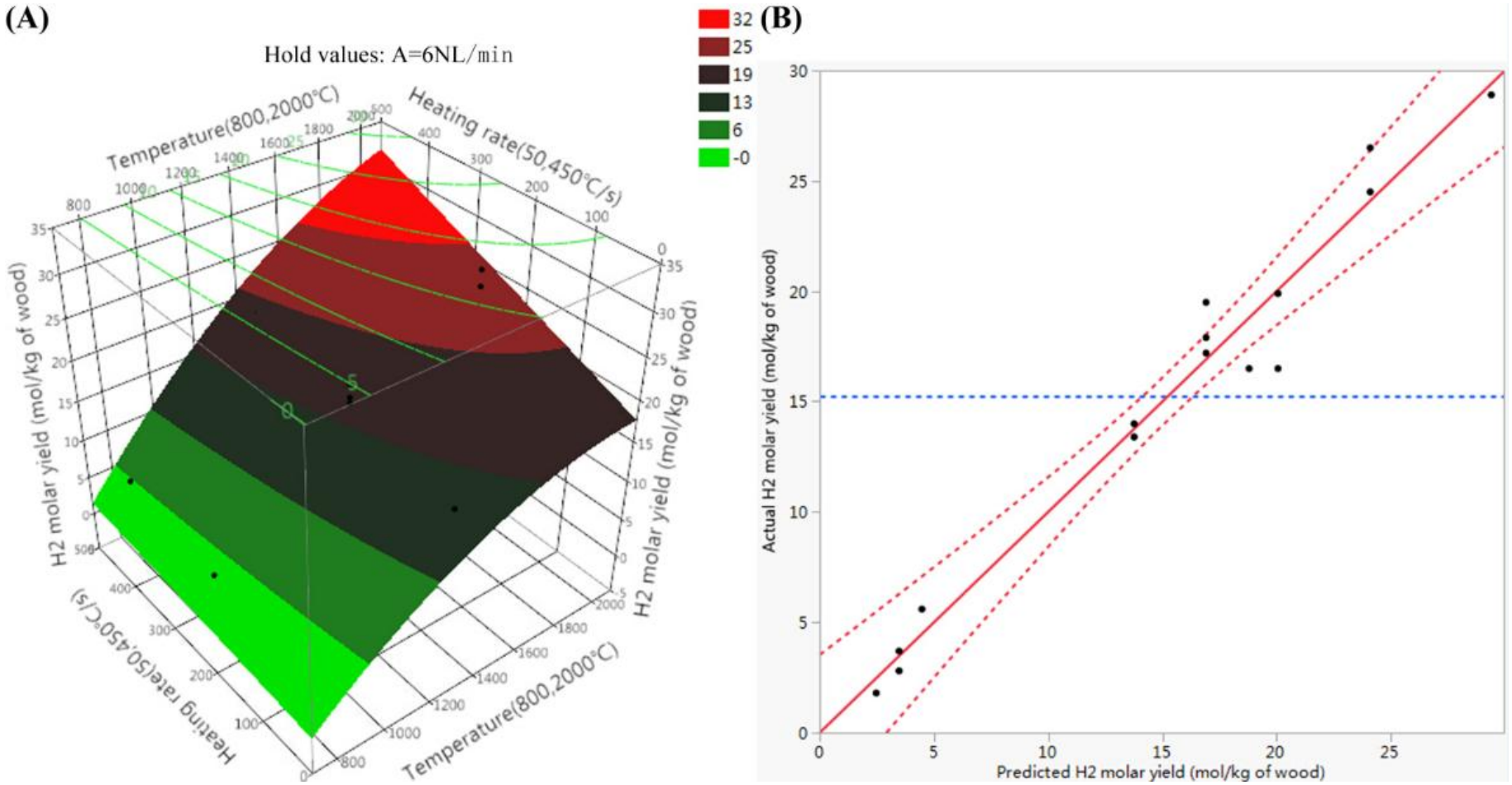

Figure 5-10: H_2 molar yield response surface plot (A) and model validation plot (B) showing temperature and heating rate effect with argon flow rate 6 NL/min.

5.4 Model validation and Process optimization

The products distribution, gas LHV and gas composition were studied under new experimental conditions (temperature: 1800 and 2000 ℃, heating rate: 50 and 450 ℃/s and argon flow rate: 4 and 6NL/min) given in Table 5-8, which displays also the predicted and experimental values. Obviously, these values are not included in the Box-Behnken design experimental study presented previously. The experimental values were in good agreement with the model predicted values. The relative errors are less than 5% for most values. So, it can be concluded that the models can be used for process optimization. The primary objective of our process of beech wood solar pyrolysis is to produce maximum gas LHV, and it is necessary to determine the optimum process parameters for it. The response function optimizer was applied using Minitab 17 software, selecting gas LHV maximization as the goal. The maximum gas LHV of 14 589 kJ/kg of beech wood (predicted value) was obtained under the following process conditions: 2000 ℃ temperature and 450 ℃/s heating rate. It agrees well (2% error) with the experimental result of 14 285.5 kJ/kg of beech wood. On the other hand, the response function prediction was used to examine the temperature effect. The gas LHV of 9833 kJ/kg of beech wood was obtained at temperature 1200 ℃. It increased by 47.7% when temperature increased to 2000 ℃. It is clearly worth to work under high temperature and high heating rate for solar pyrolysis process.

Table 5-8: Model validation

Experimental conditions			Gas yield (wt.%)			Char yield (wt.%)			Liquid yield (wt.%)			Gas LHV (kJ/kg of wood)			CO molar yield (mol/kg of wood)			H2 molar yield (mol/kg of wood)		
T (℃)	H (℃/s)	A (NL/min)	P	E	RE (%)	P	E	RE (%)	P	E	RE (%)	P	E	RE (%)	P	E	RE (%)	P	E	RE (%)
1800	50	6	62.2	61.6	1.0	7.8	7.4	5.4	29.3	31.0	5.5	11009.0	10405.9	5.8	18.1	17.4	4.0	17.1	16.1	6.2
2000	450	4	72.7	73.9	1.6	8.4	8.2	2.4	19.0	17.9	6.1	14589.1	14285.5	2.1	21.8	21.5	1.4	29.4	29.1	1.0

Note: T – temperature; H – heating rate; A – argon flow rate.

P – predicted value; E – experimental value; RE – relative error.

5.5 Conclusion

A Box-Behnken design of experiments was performed to identify the effects of process parameters on beech wood solar pyrolysis. Temperature and heating rate were the first and second influential factors, respectively. They drastically affect the final product distribution, gas composition and LHV in solar pyrolysis. On the contrary, the argon flow rate has little influence on solar pyrolysis process. Gas products LHV generally increase with temperature and heating rate, mainly due to CO and H_2 yield increase. The interaction between them enhances at both high ranges. The gas LHV can be increased four times by solar processing, from 3527 to 14 589 kJ/kg of beech wood. The maximum gas products LHV of solar pyrolyzed beech wood was obtained at 2000 ℃ and 450 ℃/s heating rate. Wood energy content is clearly upgraded by solar pyrolysis.

References

[1] Akhtar J, Amin NS. A review on operating parameters for optimum liquid. Renew Sust Energ Rev 2012;16:5101-5109.

[2] Neves D, Thunman H, Matos A, Tarelho L, Gómez-Barea A. Characterization and prediction of biomass pyrolysis products. Prog Energy Combust Sci 2011;37:611-630.

[3] Yaman S. Pyrolysis of biomass to produce fuels and chemical feedstocks. Energy Convers Manage 2004;45:651-671.

[4] Mante OD, Agblevor FA. Parametric study on the pyrolysis of manure and wood shavings. Biomass Bioenergy 2011;35:4417-4425.

[5] Mante OD, Agblevor F.A, McClung R. A study on catalyst paralysis of biomass with Y-zeolite based FCC catalyst using response surface methodology. Fuel 2013;108:451-464.

[6] Kansedo J, Lee KT. Process optimization and kinetic study for biodiesel production from non-edible sea mango (Cerbera odollam) oil using response surface methodology. Chem Eng J 2013;214:157-164.

[7] Raj RE, Kennedy ZR, Pillai B.C. Optimization of process parameters in flash pyrolysis of waste tyres to liquid and gaseous fuel in a fluidized bed reactor. Energy Convers Manage 2013;67:145-151.

[8] Brown J.N, Brown R.C. Process optimization of an auger pyrolyzer with heat carrier using response surface methodology. Bioresour. Technol. 2012;103:405-414.

[9] Ellens C.J, Brown R.C. Optimization of a free-fall reactor for the production of fast paralysis bio-oil. Bioresour. Technol. 2012:103:374-380.

[10] Abnisa F, Wan Daud W.M.A, Sahu J.N. Optimization and characterization studies on bio-oil production from palm shell by paralysis using response surface methodology. Biomass Bioenergy 2011;35:3604-3616.

[11] Mazlan MAF, Uemura Y, Osman NB, Yusup S. Fast pyrolysis of hardwood residues using a fixed bed drop-type pyrolyzer. Energy Convers Manage 2015;98:208-214.

[12] Chhiti Y, Salvador S, Commandré J-M, Broust F. Thermal decomposition of

bio-oil: Focus on the products yields under different pyrolysis conditions. Fuel 2012;102 :274-281.

[13] Commandré J-M, Lahmidi H, Salvador S, Dupassieux N. Pyrolysis of wood at high temperature: The influence of experimental parameters on gaseous products. Fuel Process Technol 2011;92:837-844.

[14] Salehi E, Abedi J, Harding T. Bio-oil from sawdust: pyrolysis of sawdust in a fixed-bed system. Energy & Fuel 2009;23:3767-3772.

[15] Şensöz S, Angın D. Pyrolysis of safflower (Charthamus tinctorius L.) seed press cake: Part 1. The effects of pyrolysis parameters on the product yields. Bioresour. Technol. 2008;99:5492-5497.

[16] Onay O. Influence of pyrolysis temperature and heating rate on the production of bio-oil and char from safflower seed by pyrolysis, using a well-swept fixed-bed reactor. Fuel Process Technol 2007;88:523-531.

[17] Mante OD, Agblevor FA. Parametric study on the pyrolysis of manure and wood shavings. Biomass Bioenergy 2011;35:4417-4425.

[18] Muradov N, Fidalgo B, Gujar AC, T-Raissi A. Pyrolysis of fast growing aquatic biomass- Leman minor (duckweed): Characterization of pyrolysis of products. Bioresour. Technol. 2010;101:8424-8428.

[19] Onay O. Fast and catalytic pyrolysis of pistacia khinjuk seed in a well-swept fixed bed reactor. Fuel 2007;86:1452–1460.

[20] Şensöz S, Angın D. Pyrolysis of safflower (Charthamus tinctorius L.) seed press cake: Part 1. The effects of pyrolysis parameters on the product yields. Bioresour. Technol. 2008;99:5492-5497.

[21] Neves D, Thunman H, Matos A, Tarelho L, Gómez-Barea A. Characterization and prediction of biomass pyrolysis products. Prog Energy Combust Sci 2011;37:611-630.

[22] Sharma RK, Bakhshi NN. Conversion of non-phenolic fraction of biomass derived pyrolysis oil to hydrocarbon fuels over HZSM-5 using a dual reactor system. Bioresour. Technol. 1993;45:195-203.

[23] Jourabchi SA, Gan SY, Ng HK. Pyrolysis of Jatropha curcas pressed cake for bio-oil production in a fixed-bed system. Energy Convers Manage 2014;78:518-526.

[24] Açıkalın K, Karaca F, Bolat E. Pyrolysis of pistachio: Effects of pyrolysis conditions and analysis of products. Fuel 2012;95:169-177.

[25] Jourabchi SA, Gan SY, Ng HK. Pyrolysis of Jatropha curcas pressed cake for bio-oil production in a fixed-bed system. Energy Convers Manage 2014;78:518-526.

[26] C. Maguyon MC, Capareda SC. Evaluating the effects of temperature on pressurized pyrolysis of Nannochloropsis oculata based on products yields and characteristics. Energy Convers Manage 2013;76:764-773.

[27] Becidan M, Skreiberg Ø, Hustad JE. Products distribution and gas release in pyrolysis of thermally thick biomass residues samples. J Anal Appl Pyrol 2007;78:207-213.

[28] Zhang LH, Xu CB, Champagne P. Overview of recent advances in thermo-chemical conversion of biomass. Energy Convers Manage 2010;51:969-982.

[29] Chihiro Fushimi, Kenichi Araki, Yohsuke Yamaguchi, Atsushi Tsutsumi. Effect of Heating Rate on Steam Gasification of Biomass. 2.Thermogravimetric-Mass Spectrometric (TG-MS) Analysis of Gas Evolution. Ind. Eng. Chem. Res 2003;42:3929-3936.

[30] Li S, Lyons-Hart J, Banyasz J, Shafer K. Real-time evolved gas analysis by FTIR method: an experiment study of cellulose pyrolysis. Fuel 2001;80:1809-1817.

[31] Shen DK, Gu S. The mechanism for thermal decomposition of cellulose and its main products. Bioresour. Technol. 2009;100:6496–6504.

[32] Nzihou A, Flamant G, Stanmore B. Synthetic fuels from biomass using concentrated solar energy - A review. Energy 2012;42:121-131.

Chapter 6: Char and bio-oil characterization

In the previous two chapters, the effects of solar pyrolysis operating parameters on products distribution, gas products composition and LHV have been presented. The optimum parameters were determined for the production of combustible gases. Pyrolysis co-products, bio-char and bio-oil, have many potential uses that improve the economic viability of bio-gas production as a fuel. However, the characterization of bio-char and bio-oil is the prerequisite to any further utilization.

In this chapter, the bio-char composition (CHNS), morphology (SEM and XRD), structure (BET) and reactivity (TGA) are investigated first at temperatures ranging from 600 to 2000^{o}C with heating rates 5 and 450^{o}C/s. Then bio-oil composition (CHNS), function groups (FTIR), chemical compounds (GC-MS), water content (Karl-Fisher) are determined at four different temperatures (600, 900, 1200 and 2000^{o}C) with heating rate 50^{o}C/s. Finally, the energetic upgrade factor for solar pyrolysis process is obtained. Char characterization has been published in Bioresource Technology[4].

6.1 State-of-the-art

Char is carbon-rich and it can be further used as a fuel (gasification and combustion) or as a decontamination adsorbent. Firstly, it is necessary to understand the char reactivity for designing a high efficiency gasification or combustion reactor [1]. Secondly, the appropriate pore structure and surface area are important for preparing decontamination adsorbent [2]. For the best possible use of char obtained from solar pyrolysis, its composition, surface area, pore structure and reactivity should be investigated. Char reactivity and morphological structure are especially affected by the pyrolysis conditions [3,4] The effects of pyrolysis conditions on the

[4] Zeng K, Minh DP, Gauthier D, Weiss-Hortala E, Nzihou A, Flamant G. The effect of temperature and heating rate on char properties obtained from solar pyrolysis of beech wood. Bioresource Technology 2015;182:114-119.

structure and reactivity of biomass chars have been investigated in several studies in relation to the following parameters: temperature [5-9], heating rate [10-12], residence time and pressure [1,13].

The char carbon content increases with temperature, which is the indication of increased structure ordering that lowers the reaction site concentration [14]. The char surface area increases with temperature up to 1173K and then slightly decreases [6]. There is a significant diminution in char reactivity when temperature increases above 1073K [11, 15]. At lower temperature (below 1073K), the volatile release intensifies, owing to the temperature increase that enlarges the char surface area. However, there are more and more structural ordering and micropore coalescence for char when temperature keeps on increasing even higher than 1073K.

The heating rate increase causes a weak decrease in the char carbon content and an increase in its hydrogen and oxygen contents. Moreover, the heating rate effect tends to disappear at high temperatures [16]. The presence of higher hydrogen and oxygen contents is related to the availability of active sites and thus to enhanced reactivity [17]. For slow heating rates (lower than $1^{o}C/s$), no major change takes place in the particle morphology as volatile is released through the natural porosity [18]. For fast heating rates (higher than $10^{o}C/s$), the original cellular structure is lost as a consequence of melting [19]. When the heating rate increases, the volatile release speeds up. Then large internal cavities and a more open structure of char is produced [11] owing to the fast volatile release that produces internal overpressure and coalescence of the smaller pores, which leads to the increase of surface area and pore volume. So the char reactivity increase with heating rate can be explained by the higher surface area and pore volume [1,13]. Besides, heating rate rising shortens tar vapor residence time in pores and reduces the condensation reaction leading to char reactivity increase [19]. However, char obtained at high heating rate has lower surface area compared to that at low heating rate at temperature $900^{o}C$ [6]. It is attributed to too high heating rate causing char interior higher temperature, then partial graphitization with formation of grapheme structure, which does not contribute to the

development of large surface area.

Bio-oil is dark brown and its elemental composition approximates that of biomass feedstock [20]. The bio-oil mainly consists in aromatic, aliphatic and naphthenic hydrocarbons and oxygenated compounds [21]. The maximum bio-oil yield up to 80 wt.% dry feed basis (64 wt.% organics and 16 wt.% water) can be obtained for fast pyrolysis of most woods at 500-520^{o}C with vapor residence time less than 1 s [22]. Bio-oil derived from wood fast pyrolysis typically has a heating value in the range 16-19 MJ/kg with moisture content of about 15-30 wt.% [23]. It can substitute fuel oil or diesel in boilers, furnaces, engines and turbines [24]. On the other hand, it can also be upgraded to high value products and special chemicals [25]. Many particular characteristics of bio-oil, such as elemental composition, HHV, moisture content and LHV, require consideration for possible applications..

6.2 Char characterization

6.2.1 Char composition

Table 6-1 gives the composition of char generated at different temperatures and heating rates. The carbon, hydrogen, nitrogen and sulfur were directly determined while oxygen was calculated by difference. Char is mainly composed of carbon with mass content higher than 75%. When the temperature increases to 1600^{o}C, the carbon content grows rapidly whereas the hydrogen and oxygen contents decline sharply. The char is completely carbonized with almost 100% carbon content at temperature 2000^{o}C. The carbon content increase with temperature is assumed to come from the carbonaceous structure graphitization at high temperature [26]. Between 600 and 800^{o}C, the hydrogen and oxygen contents' decrease is most obvious, owing to the char weak bonds' cracking and cleavage [27]. There is no obvious effect of heating rate on char composition when temperature is higher than 800^{o}C, in accordance with what was mentioned before [16].

Table 6-1: Effect of pyrolysis temperature and heating rate on char composition.

	Pyrolysis temperature (°C)				
	600	800	1200	1600	2000
Heating rate 5°C/s					
C (wt.%)	-	82.7±0.7	82.4±3.9	-	99.8±0.3
H (wt.%)	-	2.0±0.2	1.4±0.6	-	0
N (wt.%)	-	0.4±0.4	0.2±0.3	-	0
O (wt.%)	-	14.9±0.5	16±3.1	-	0.2±0.3
Heating rate 50°C/s					
C (wt.%)	76.4±3.3	80.9±0.4	82.3±0.5	94.4±1.7	99.8±0.7
H (wt.%)	2.6±0.2	1.4±0.2	1.0±0.2	0	0
N (wt.%)	0.3±0.3	0.5±0.1	0.6±0.1	0	0
O (wt.%)	20.7±1.2	17.2±0.3	16.1±0.3	5.6±1.7	0.2±0.7
Heating rate 150°C/s					
C (wt.%)	-	82.4±0.4	79.2±1.3	-	99.7±0.4
H (wt.%)	-	2.1±0.2	0.8±0.7	-	0
N (wt.%)	-	1.0±0.6	0.8±0.1	-	0
O (wt.%)	-	14.5±0.5	19.2±1.2	-	0.3±0.4
Heating rate 450°C/s					
C (wt.%)	-	82.5±0.1	80.3±0.9	-	99.8±0.8
H (wt.%)	-	1.8±0.2	1.1±0.1	-	0
N (wt.%)	-	0.4±0.4	0.7±0.1	-	0
O (wt.%)	-	15.3±0.3	17.9±0.7	-	0.2±0.8

6.2.2 Char morphology and structure

6.2.2.1 SEM analysis

Figure 6-1 shows a comparison of SEM images of raw beech sawdust and its chars produced at different temperatures, with the same heating rate 50°C/s. As can be seen from Fig. 6-1a, the raw wood is made of solid cells that are bounded together and there is almost no cavity. There are many small pores appearing in the char caused by devolatilization when pyrolyzing at 800°C (Fig. 6-1b). However, the char is more and more twisted and rough when temperature rises owing to the intensive volatile release, which means that the char deformation intensifies with temperature increase up to 1200°C (Fig. 6-1c). This trend can be explained by the release of volatiles and intermediate size organics increasing with temperature. The cracks and pores in the chars increase with temperature increase, as observed previously [6]. When the

temperature increases to 2000°C, the macropores disappear because of melting as illustrated in Fig. 6-1d. Small grains appear as spherules' agglomeration on the char surface (Fig. 6-1c). Moreover, char particles present more and more growth filament crystals (Fig. 6-1d). The grains and crystals observed on the char surface may be inorganic compounds that have migrated to the surface.

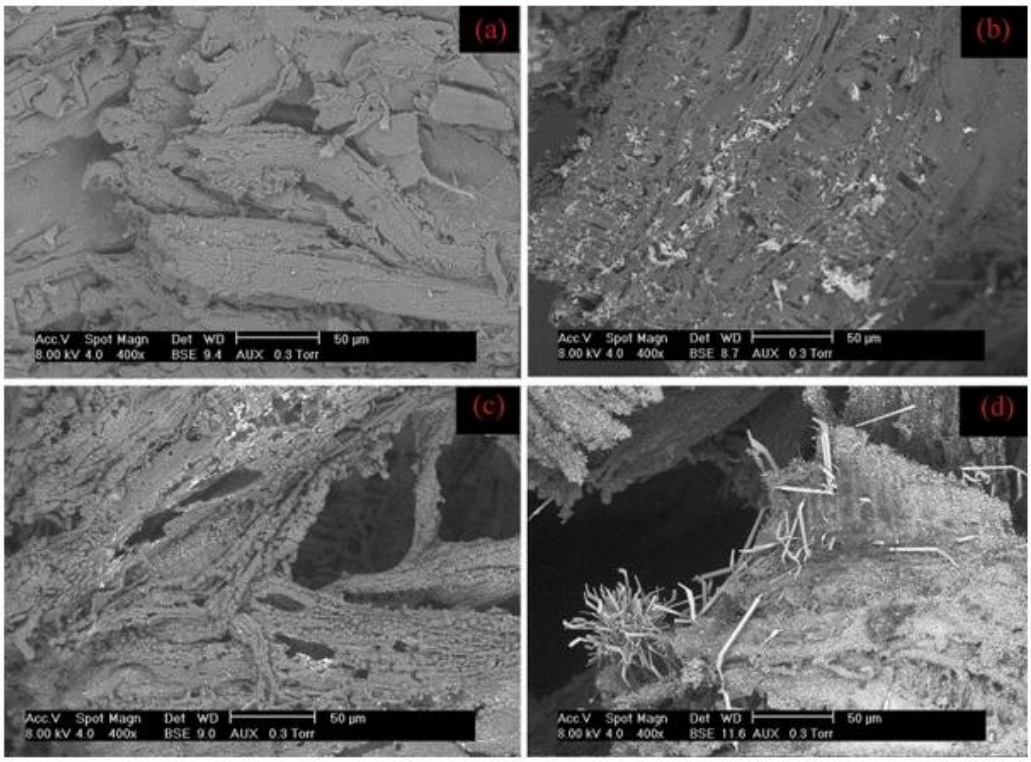

Figure 6-1: SEM pictures of parent material (raw beech sawdust) and chars obtained at different temperatures: (a) parent material, (b) 800°C, (c) 1200°C, (d) 2000°C, for 50 ℃/s heating rate.

The SEM images of chars produced at different heating rates and same temperature 1200°C are shown in Figure 6-2. There is no major morphological change from raw wood, except the rough surface observed for the char obtained at heating rate 5°C/s (Fig. 6-2a). The char produced with heating rate 150°C/s is a lot deformed, with many open pores (Fig. 6-2c). However, few pores are observed on the char when the heating rate is increased to 450°C/s (Fig. 6-2b). This may be due to high heating rate that results in plastic transformations and creates smoother surfaces with spherical cavities [13].

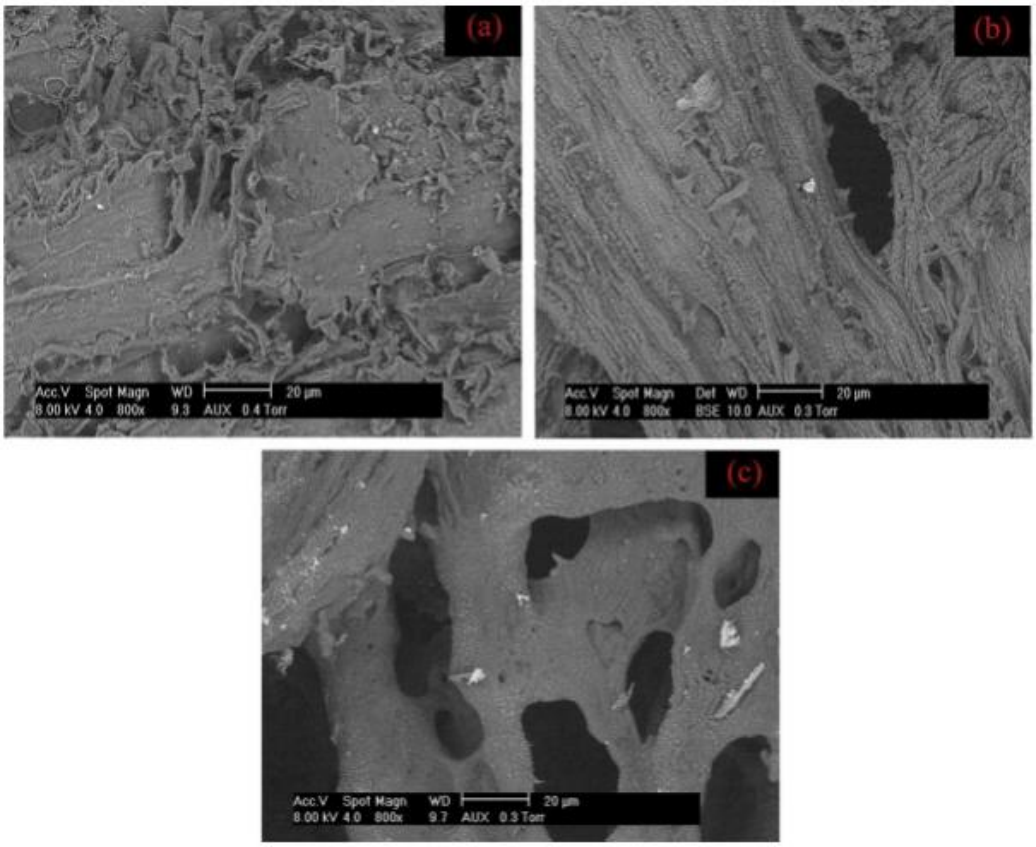

Figure 6-2: SEM pictures of chars obtained at different heating rates: (a) 5^{o}C/s, (b) 450^{o}C/s, (c) 150^{o}C/s for 1200 ℃ plateau temperature

6.2.2.2 XRD analysis

The comparison of X-ray diffraction spectra of chars prepared at different heating rates and temperatures are shown in Figure 6-3. The crystal plane indices C(002) and C(100) peak were present in the spectra, which correspond to 2 θ values around 25^{o}and 45^{o}. The degree of azimuthal orientation and parallel of the aromatic lamellae is represented by C(002), and C(100) reflects the aromatic lamina size. To investigate the temperature influence on char crystallinity, the heating rate was constant as 50^{o}C/s. As the temperature increases from 800 to 1600^{o}C, the C(002) peak slightly sharpens. However, the C(002) peak greatly sharpens at temperature 2000^{o}C. Then the degree of orientation of aromatic lamellae increases with temperature, especially at 2000^{o}C owing to the sharper C(002) peak [28]. The C(100) peak is sharper and sharper when the temperature rises from 800 to 1600^{o}C. The sharp trend is very clear at 2000^{o}C, and the higher the temperature, the higher the degree of

condensation of the aromatic ring, as proved by the sharper C(100) peak [28]. Two kinds of char obtained at heating rates 50 and 450°C/s were compared to study the heating rate effect on crystallinity. It was found that the C(002) and C(100) peaks are sharper for char at 50°C/s than for char at 450°C/s. This proves that the char prepared at high heating rate has low crystallinity because of melting (Cetin et al., 2004). With temperature increase and heating rate decrease (higher than 50°C/s), the crystallinity increases, which indicates that the char structure is more and more ordered and aromatic.

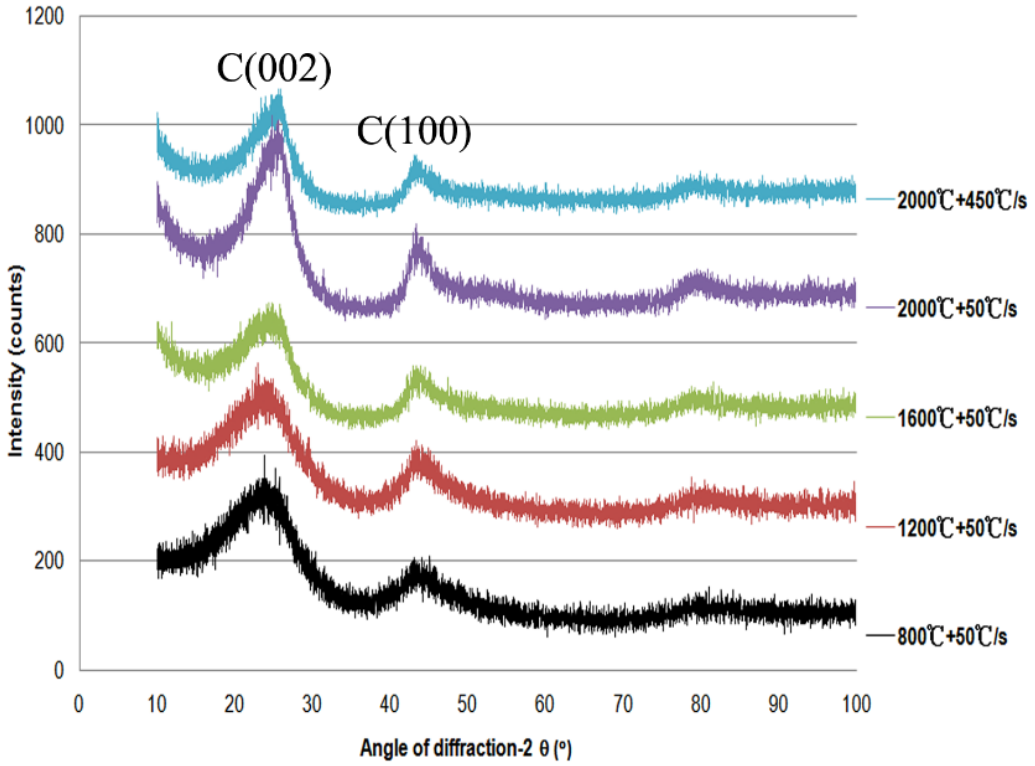

Figure 6-3: XRD spectra of chars prepared at different temperatures and heating rates.

6.2.2.3 BET analysis

The char surface area and pore volume were measured by means of N_2 adsorption at -196°C on the TriStar II 3020. Table 6-2 and Figure 6-4 show the effect of temperature on char textural properties. When the heating rate is 50°C/s, the BET surface area increases from 70.2m²/g to 110.2m²/g with temperature increase from 800℃ to 1200°C, then it decreases dramatically to 22.2m²/g at 2000°C. The pore volume increases about 17 times with increasing temperature from 800 to 1600°C,

then it slightly decreases at 2000°C. The result is similar to that reported in literature, which showed that the total surface area firstly increases with rising temperature lower than 900°C and then decreases when temperature keeps increasing [6]. When the temperature increases from 800 to 2000°C, there are two competing processes affecting the surface area: (1) intensifying volatile release [7]; (2) thermal deactivation over 900°C [29]. The first process causes the increase of surface area and pore volume. The second process induces char melting, pore fuse and structure ordering leading to the decrease of surface area and pore volume. Based on these results, it was easily found that the first process defeats the second process and dominates when temperature increases from 800 to 1200°C. Then, when temperature reaches 2000°C, the second process seems to become predominant causing the decrease of surface area and pore volume.

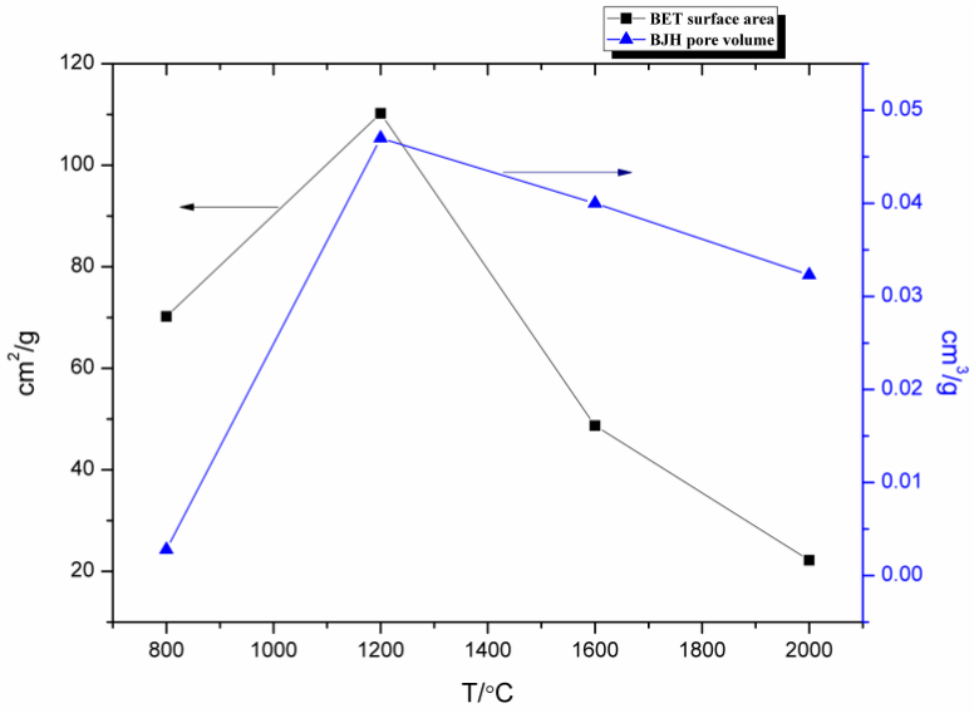

Figure 6-4: BET surface area and pore volume of chars prepared at different temperatures for heating rate 50°C/s

As depicted in Table 6-2 and Figure 6-5, a gradual increase of the BET surface area and pore volume can be observed with heating rate peaking around 150°C/s. This may be due to the higher heating rates resulting in char particles melting and creation

of smoother surfaces and spherical cavities [1,13,30]. Then there is a slight decrease when the heating rate increases to 450°C/s. It may be explained by char interior partial graphitization caused by inner high temperature at too high heating rates [6]. Between 5°C/s and 50°C/s, the BET surface area increases 14-fold while the pore volume increases about 6 times. After that, the change is not so obvious, showing the significant effect of fast heating rate on surface area and pore volume. Once the heating rate is equal to the flash heating rate, the influence is not so obvious. In addition, the surface area and pore volume increases 1.27 and 1.15 times when the heating rate increases from 50°C/s to 150°C/s, at temperature 1200°C. However, they increase about 3 and 2.5 times at 2000°C. As the heating rate keeps increasing to 450°C/s, they decrease about 1.1 and 1.2 times at 1200°C. Then, they decrease about 2 and 1.6 times when the temperature reaches 2000°C. By comparing the heating rate effects at 1200°C and 2000°C, it is easily found that the heating rate has more effect on the char surface area and pore volume at higher temperatures.

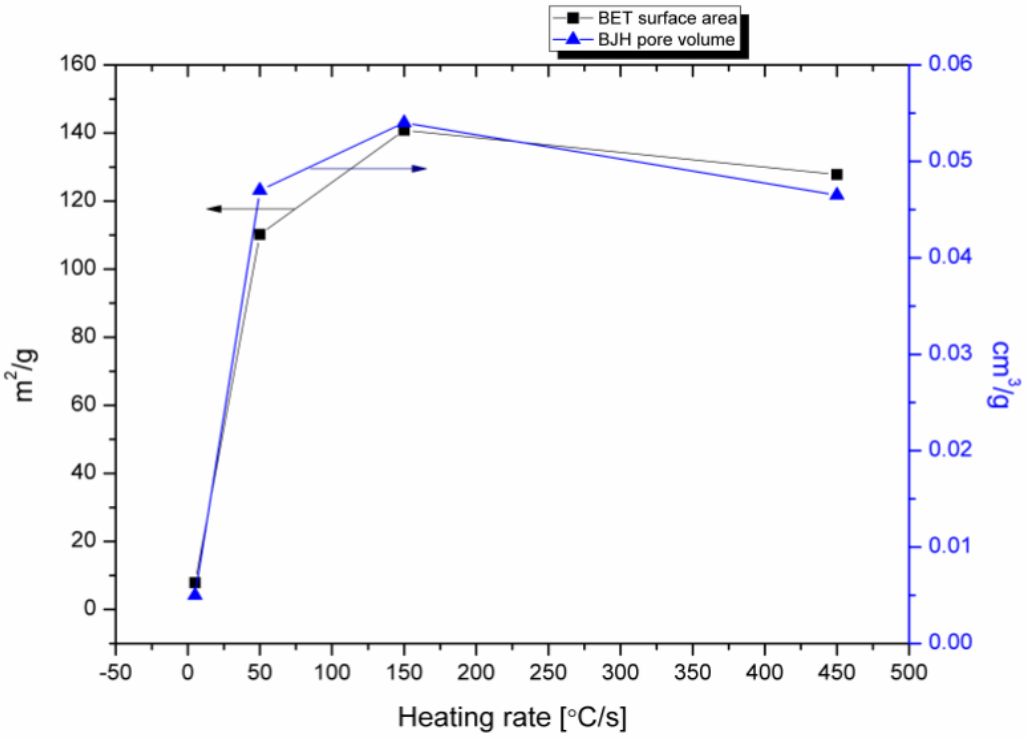

Figure 6-5: BET surface area and pore volume of chars prepared at different heating rates for temperature 1200°C

Table 6-2: Effect of pyrolysis temperature and heating rate on char surface area and pore volume.

	Pyrolysis temperature (^{o}C)			
	800	1200	1600	2000
Heating rate 5^{o}C/s				
BET Surface Area (m²/g)	-	7.9	-	-
`BJH Adsorption pore volume (cm³/g)	-	0.0050	-	-
Heating rate 50^{o}C/s				
BET Surface Area (m²/g)	70.2	110.2	48.7	22.2
`BJH Adsorption pore volume (cm³/g)	0.0028	0.0470	0.0400	0.0323
Heating rate 150^{o}C/s				
BET Surface Area (m²/g)	-	140.8	-	60.3
`BJH Adsorption pore volume (cm³/g)	-	0.0540	-	0.0790
Heating rate 450^{o}C/s				
BET Surface Area (m²/g)	-	127.8	-	31.5
`BJH Adsorption pore volume (cm³/g)	-	0.0465	-	0.0524

6.2.3 Char reactivity

The reactivity often characterizes the oxidation or gasification rate, which refers to the evolution of carbonaceous solid mass loss at an instant with respect to its mass at this time, which can be calculated by using Equation 1. The conversion expresses the degree of reaction completion which can be written as Equation 2.

$$R(t) = -\frac{1}{m(t)}\frac{dm(t)}{dt} = -\frac{m_2 - m_1}{(t_2 - t_1)m_1} \quad (1)$$

$$X = \frac{m_0 - m}{m_0} \quad (2)$$

Where m is the instantaneous sample mass, m_0 the initial sample mass, $R(t)$ the reactivity at time t, m_1 the sample mass at t_1 time when weight measurement starts, m_2 the sample mass at t_2 time when the weight measurement ends. The conversion degree (X=20%~80%) was selected as a representative reactivity value for each experiment.

The apparent reactivity values, at heating rate of 50^{o}C/s, corresponding to air oxidation of chars generated at 800, 1200, 1600 and 2000^{o}C have been plotted in

Figure 6-6. As shown in Figure 6-6, the reactivity of char generated at 1200°C is the highest, whereas it is the lowest at 2000°C. And the reactivity of char produced at 800°C is higher than toat of char obtained at 1600°C. This may be due to the highest surface area and pore volume produced at 1200°C. According to the CHNS results, the carbon and hydrogen contents increase and decrease respectively with temperature, which indicates increased structure ordering. The increased structure ordering is the indication for lowering the reaction site concentration [29]. It seems that the char reactivity reduces with temperature, if carbon and hydrogen concentrations are used as reactivity indicator. Indeed, the surface area and pore volume are more appropriate and accurate for reactivity evaluation. Besides, there is no big difference of reactivity for the chars obtained at various high temperatures. For example, the reactivity of char obtained at 1200°C is about 21% higher than that at 2000°C. It is probably due to char structure ordering that occurs at high temperature.

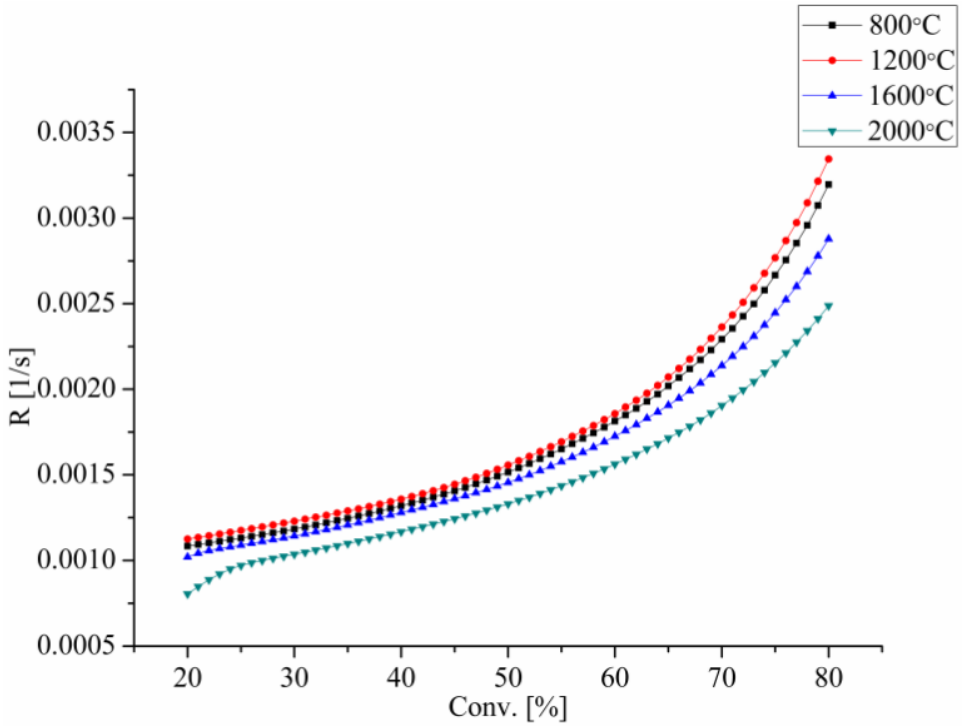

Figure 6-6: Temperature effect on char reactivity, chars prepared at same heating rate (50°C/s).

The apparent reactivity for chars prepared at temperatures 1200 and 800°C corresponding to different heating rates (5, 50, 150 and 450°C/s) have been illustrated,

respectively in Figure 6-7 and Figure 6-8. As can be seen from Figure 6-7, the reactivity increases when heating rate increases from 5 to 150°C/s. This may be due to the higher surface area of char generated at higher heating rate [1]. And then it slightly decreases at heating rate 450°C/s when temperature is 1200°C. This may be due to the interior partial graphitization occurring with too high heating rate [6]. Figure 6-7 shows that the reactivity of char obtained at heating rate 5°C/s is much lower than those at higher heating rates. For example, chars generated at 150°C/s have much higher reactivity (approx. 2.3 times) than those generated at 5°C/s. However, the char reactivity keeps on increasing with heating rate increasing from 5 to 450°C/s at temperature 800°C (Figure 6-8). This is because the fast volatile release produces internal overpressure and coalescence of the smaller pores, leading to surface area and pore volume increase with heating rate [11]. Another reason is that the temperature is too low (lower than 1200°C) for char interior partial graphitization, even with high heating rate 450°C/s. At first glance, the char obtained at 5°C/s has a pellet shape, which has more compact structure with smaller surface area. Chars produced at higher heating rates (50, 150 and 450°C/s) were non-compact powders, with bigger surface area and pore volume. Then the lower reactivity at lower heating rate can be attributed to the smaller surface area and pore volume with respect to the high heating rate [1,13,30].

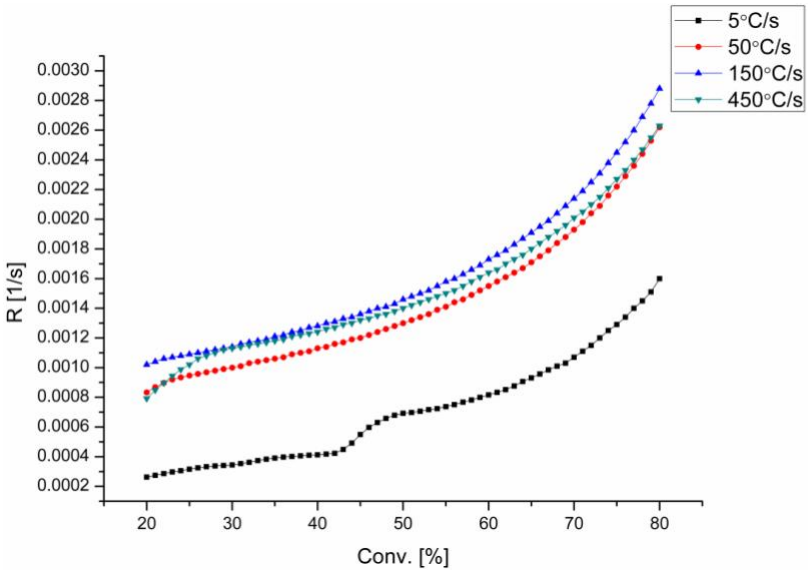

Figure 6-7: Heating rate effect on char reactivity, prepared at 1200°C.

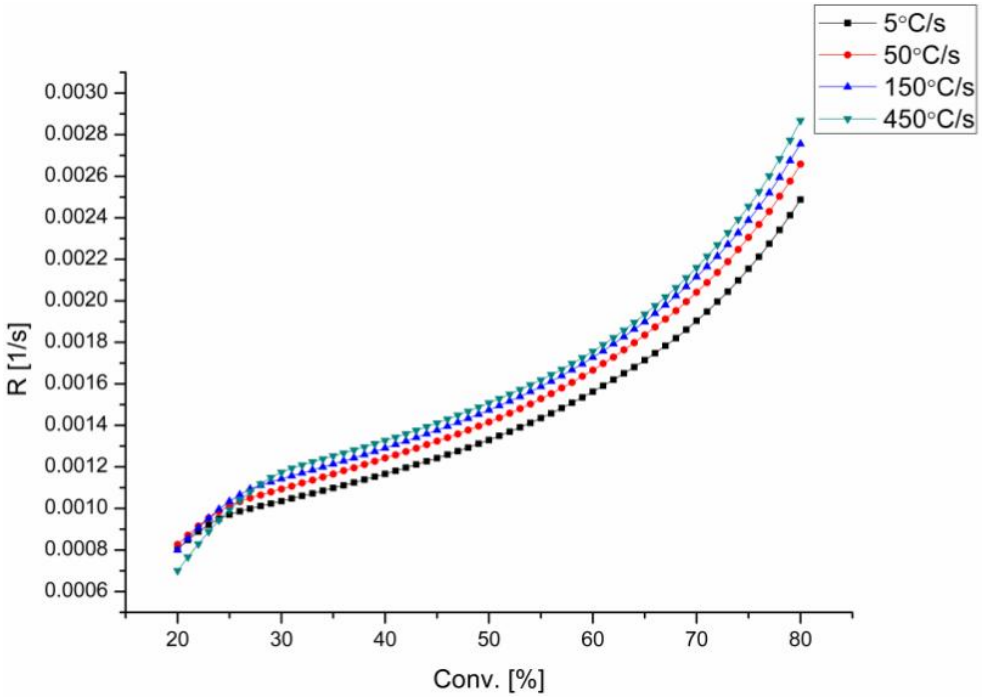

Figure 6-8: Heating rate effect on char reactivity, prepared at 800°C.

6.3 Bio-oil characterization

6.3.1 Bio-oil properties

Table 6-3 gives the properties of solar pyrolysis bio-oils generated at different temperatures. The carbon, hydrogen, nitrogen and sulfur were directly determined with CHNS, while oxygen was calculated by difference. The higher heating value (HHV) for bio-oil was calculated according to Eq. (3) in Ref. [31]. The lower heating value (LHV) was calculated from the HHV and moisture content by Eq. (4) [32].

$$HHV = 0.35Z_C + 1.18Z_H - 0.10Z_O - 0.02Z_N + 0.10Z_S - 0.02Z_A \quad (3)$$

$$LHV = HHV(1 - M) - 2.447M \quad (4)$$

Table 6-3: Properties of the solar pyrolysis bio-oils.

Composition	600 ℃ Bio-oil	900 ℃ Bio-oil	1200 ℃ Bio-oil	2000 ℃ Bio-oil	Typical Bio-oil [33]	Crude oil [33]
Water (wt%)	1.43	1.67	1.51	1.15	15–30	0.1
Density (kg/L)	-	-	-	-	1.05-1.25	0.86-0.94
Viscosity 50 ℃ (cP)	-	-	-	-	40-100	180
HHV (MJ/kg of tar)	30.74	30.73	33.24	33.11	16-19	44
LHV (MJ/kg of tar)	30.26	30.18	32.70	32.70	-	44
C (wt%)	58.1	57.4	58.8	58.6	55–65	83.86
O (wt%)	30.16	30.61	27.7	27.88	28–40	<1
H (wt%)	11.37	11.61	13.08	13.04	5–7	11-14
S (wt%)	0.0826	0.0835	0.0357	0.0658	<0.05	<4
N (wt%)	0.37	0.38	0.42	0.48	<0.4	<1
Ash (wt%)	-	-	-	-	<0.2	0.1
H/C	2.35	2.43	2.67	2.67	0.9–1.5	1.5–2.0
O/C	0.39	0.4	0.35	0.36	0.3–0.5	~0

The water content is 1.67% for bio-oil obtained at 900^{o}C and 1.15% for that obtained at 2000^{o}C. There is no obvious effect of temperature on the bio-oil water content. The small reduction of bio-oil moisture content at 2000^{o}C may be explained by the water consumption due to more gasification reaction at higher temperature [34]. In comparison with conventional pyrolysis bio-oil, the solar pyrolysis bio-oil has lower water content, which is suitable for a fuel to be combusted in boiler, furnace and engine. As shown in Table 6-3, temperature has no big influence of the element concentration of solar pyrolysis bio-oil. The carbon content is around 58%, and the oxygen is lower in the bio-oil than in the feedstock as pyrolysis partitions O into NCG gases (CO_2 and CO) [35]. The hydrogen in solar pyrolysis bio-oil is about twice that of conventional pyrolysis bio-oil, thus doubling the HHV in comparison to conventional pyrolysis bio-oil. The low oxygen and high hydrogen contents of the solar pyrolysis bio-oil is attractive for its utilization as fuel [36]. Calculated HHV and LHV for solar pyrolysis bio-oils obtained at temperatures 600 and 900^{o}C are around 31 and 30MJ/g, respectively. They increase to 33 and 32MJ/kg for temperatures 1200 and 2000^{o}C due to the hydrogen content increase with temperature. The solar

pyrolysis bio-oil LHV is only about 68% of crude oil LHV, owing to its lower carbon content and higher oxygen content [37].

6.3.2 Bio-oil compounds

Solar pyrolysis bio-oils collected at 600, 900, 1200 and 2000°C were analyzed by gas chromatography-mass spectrometry (GC/MS). Bio-oils obtained from 600 to 1200°C are very complex mixtures of C4-C26 organic compounds. It changes into mainly C6-C16 compound mixture at 2000°C, because of the thermal cracking of long-chain tars at high temperature [38]. Compounds with peak areas around or greater than 2% are considered to be most abundant products [39]. The major tar compounds resulting from solar pyrolysis are shown in Table 6-4. It can be seen that the bio-oil formed at 600°C contains high concentration of compounds such as Phthalic acid, 3-Furaldehyde, Azulene, Phenol, 2,6-dimethoxy- and 1,3,5,7-Cyclooctatetraene. Mourant et al. [40] have reported similar high acid concentration from fast pyrolysis of wood at 500°C. The cellulose and hemi-cellulose, which have high oxygen content, mainly form oxygen-rich primary tars like acids at low temperature [41]. When temperature increases from 600 to 800°C, more and more secondary tars like phenols are produced by breakage, decarboxylation (CO_2 formation), decarbonylation (CO formation) of primary tar [42] and Diels-Alder reactions followed by dehydrogenation [43]. Over 800°C, dealkylation and dehydroxylation reactions [44] generate lower aromatic molecules such as benzene. Light tars like Phenol and benzene are precursors of heavy tars (tertiary tar). At 900°C, Benzene, 1-ethenyl-4-methyl-, Benzene, 1-propynyl-, Phenol, 2-methyl- and Phenol, 3-methyl-, Naphthalene and Acenaphthylene appear as main compounds in solar pyrolysis bio-oil. It is explained by: (1) direct combination of two aromatic species producing a dimer [45] and (2) addition of light unsaturated hydrocarbons to aromatic rings leading to PAH formation and growth [46]. These two processes are enhanced with temperature. Then azulene, Benzene, 1-propynyl- and acenaphthylene increase a lot when temperature reaches 1200°C. At very high temperature (2000°C), heavy tars like acenaphthylene increase a lot due to the PAH growth with temperature [47].

There is no oxygen-containing compound detected at 2000°C as they are destructed at high temperatures [48]. And a lot of primary, secondary and tertiary tars are most probably at values lower than the GC/MS detection limit.

The number of compound species detected by GC/MS is plotted versus temperature in Figure 6-9. From 600 to 900°C, the number of identified tar species increases from about 52 to 71. This can be explained by more kinds of secondary and tertiary species formed by breakage, decarboxylation (CO_2 formation), decarbonylation (CO formation) of primary tar and heavy tars' formation. From 900 to 1200°C, it decreases slightly to 69 due to the tar (both light and heavy) destruction at high temperature. The destruction effect sharply enhances at 2000°C, since the number of identified tar species decreases to 28.

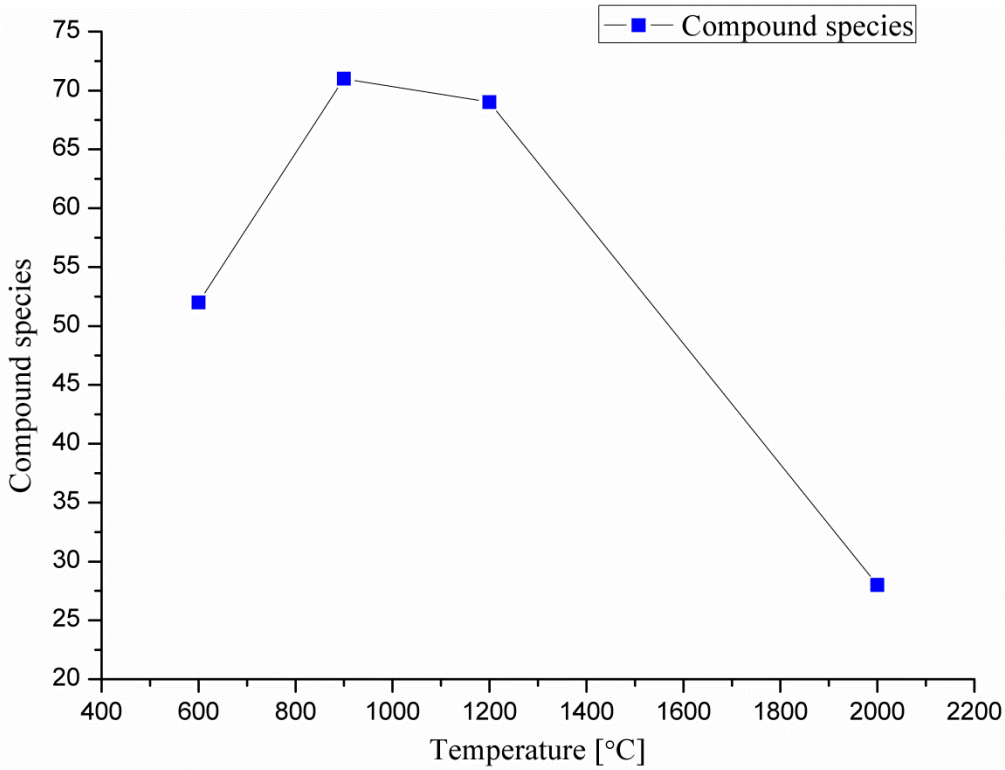

Figure 6-9: Bio-oil compound species number detected by GC/MS as a function of temperature (pyrolysis conditions: heating rate 50°C/s, pressure 0.44bar, and argon flow rate 6NL/min).

Table 6-4: Major tar compounds resulting from solar pyrolysis.

600°C			900°C			1200°C			2000°C		
Area %	Name	Formula	Area%	Name	Formula	Area %	Name	Formula	Area %	Name	Formula
5.35	3-Furaldehyde	$C_5H_4O_2$	4.09	3-Furaldehyde	$C_5H_4O_2$	4.87	Phenylethyne	C_8H_6	8.05	Phenylethyne	C_8H_6
2.25	1,3,5,7-Cyclooctatetraene	C_8H_8	7.55	1,3,5,7-Cyclooctatetraene	C_8H_8	10.56	1,3,5,7-Cyclooctatetraene	C_8H_8	6.22	1,3,5,7-Cyclooctatetraene	C_8H_8
3.20	Azulene	$C_{10}H_8$	13.8	Azulene	$C_{10}H_8$	21.25	Azulene	$C_{10}H_8$	28.13	Azulene	$C_{10}H_8$
2.26	Phenol, 2,6-dimethoxy-	$C_8H_{10}O_3$	2.49	Ethylbenzene	C_8H_{10}	2.39	Ethylbenzene	C_8H_{10}	2.54	Fluorene	$C_{13}H_{10}$
2.34	Phenanthrene	$C_{14}H_{10}$	2.36	1,2-Cyclopentanedione	$C_5H_6O_2$				3.02	Phenanthrene	$C_{14}H_{10}$
45.65	Phthalic acid, di(2-propylpentyl) ester	$C_{24}H_{38}O_4$	5.23	Phosphonic acid, (p-hydroxyphenyl)-	$C_6H_7O_4P$	3.48	Phosphonic acid, (p-hydroxyphenyl)-	$C_6H_7O_4P$			
			3.81	Benzene, 1-ethenyl-4-methyl-	C_9H_{10}	3.70	Benzene, 1-ethenyl-3-methyl-	C_9H_{10}			
			8.69	Benzene, 1-propynyl-	C_9H_8	14.25	Benzene, 1-propynyl-	C_9H_8	14.33	Benzene, 1-propynyl-	C_9H_8
			2.04	Phenol, 2-methyl-	C_7H_8O						

			3.32	Phenol, 3-methyl-	C_7H_8O						
			2.45	Naphthalene, 1-methyl-	$C_{11}H_{10}$	2.47	Naphthalene, 1-methyl-	$C_{11}H_{10}$			
			2.00	Naphthalene, 2-methyl-	$C_{11}H_{10}$				2.20	Naphthalene, 2-methyl-	$C_{11}H_{10}$
			2.76	Acenaphthylene	$C_{12}H_8$	6.34	Acenaphthylene	$C_{12}H_8$	17.34	Acenaphthylene	$C_{12}H_8$

6.4 Solar pyrolysis energy balance

This paragraph aims at determining the energy content (HHV and LHV) of the solar pyrolysis products with respect to the energy content of the initial biomass and, thus, to deduce the energy gain due to the solar process.

6.4.1 Elemental balance

The bio-oil mass is calculated from mass balance. Then the elemental balance is checked to determine the analysis accuracy of bio-oil, bio-char and bio-gas. As far as elements C, H, O are concerned, about 1% of the initial carbon and 0.17% of hydrogen are missing. The formula of the missing mass is therefore C_nH_{2n}, which is quite similar to C_2H_4 and C_2H_2 formulas. Consequently, it may be assumed that this missing part can be partly attributed to light hydrocarbon (C_nH_m) gases that are not measured by the Micro GC.

6.4.2 Energy distribution

The Solar pyrolysis product yields and heating values are listed in Table 6-5. The beech wood heating value was determined by GALLENKAMP Auto Adiabatic Bomb Calorimeter according to ASTM D 240. The char heating values were determined from Eqs. (3) and (5) [49].

$$LHV = HHV - 2.442 \times 8.936 (H/100) \quad (5)$$

Table 6-5: Solar pyrolysis product yields and energy distributions

Beech wood								
C	H	O*	N	S	Ash	Moisture	HHV (MJ/kg)	LHV (MJ/kg)
50.8	5.9	42.9	0.3	0.02	0.4	6	18.5	17

Solar pyrolysis process				
Temperature (°C)	600	900	1200	2000
Gas yield (wt.%)	20.85	28.98	53.6	60.21
Char yield (wt.%)	16.77	13.3	9.92	7.7
Tar yield (wt.%)	62.38	57.72	37.48	32.32
Gas LHV (MJ/kg of wood)	1.88	4.54	9.62	10.14
Char product LHV (MJ/kg of wood)	4.61	4.06	2.81	2.67
Tar product LHV (MJ/kg of wood)	18.88	17.41	12.26	10.57
Total product LHV (MJ/kg of wood)	25.37	26.01	24.69	23.38

Figure 6-10 plots the energy distribution of the solar pyrolysis products at different temperatures. The total product energy was slightly higher at 600 and 900°C, which may be due to the higher energy value of the greater amount of bio-oil in comparison to the pyrolysis at higher temperatures (1200 and 2000°C). Whatever the temperature, the bio-oil energy

contributes to more than 50% of the total product energy content. Since the bio-oil production significantly decreases with temperature, the bio-oil energy content at 600 and 900^{o}C is significantly higher (18.88 and 17.41MJ/kg of wood, respectively) than those at 1200 and 2000^{o}C (12.26 and 10.57 MJ/kg of wood, respectively). Besides, the bio-gas production significantly increases with temperature, and the bio-gas energy content at 600 and 900^{o}C is significantly lower (1.88 and 4.54MJ/kg of wood, respectively) than those at 1200 and 2000^{o}C (9.62 and 10.14 MJ/kg of wood, respectively).

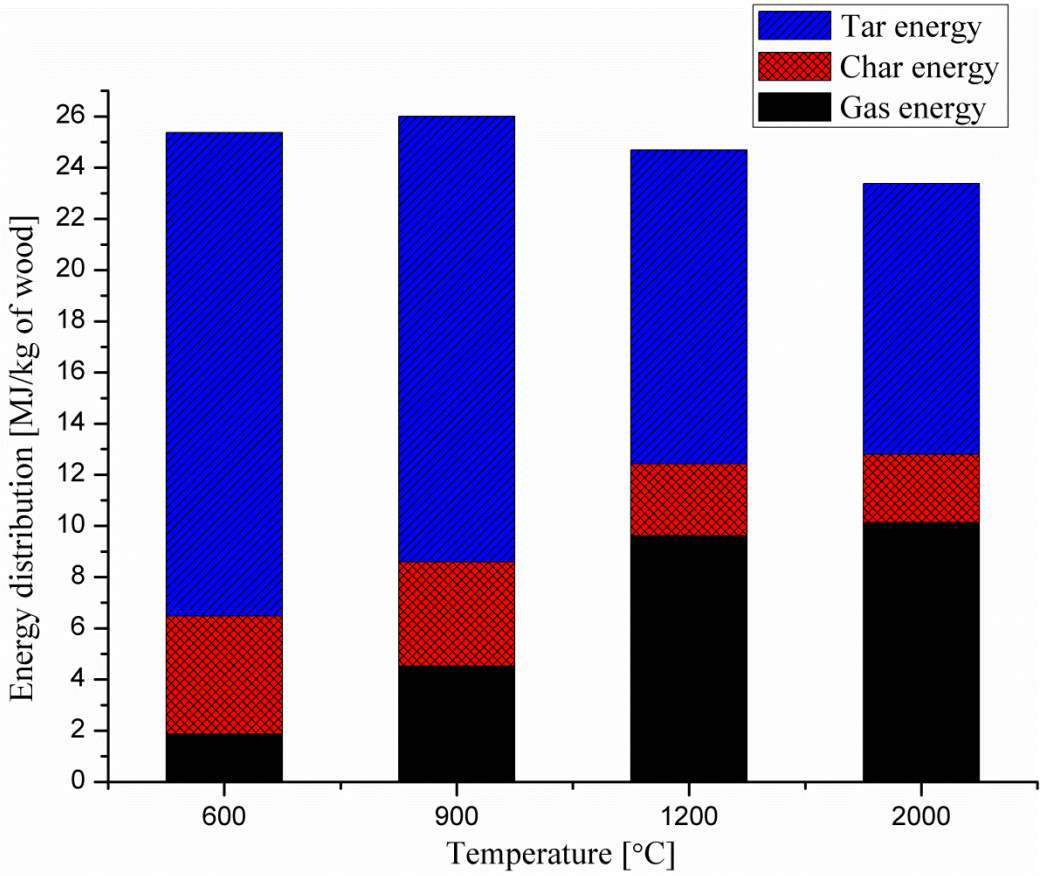

Figure 6-10: Solar pyrolysis product energy distribution as a function of temperature (pyrolysis conditions: heating rate 50^{o}C/s, pressure 0.44bar, and argon flow rate 6NL/min).

6.4.3 Energy upgrade factor

The energy upgrade factor is defined as the ratio of the sum of heating values of produced bio-oil, bio-gas and bio-char to the heating value of the processed biomass feedstock. The upgrade factor can be written as follows:

$$U = \frac{m_{oil} LHV_{oil} + m_{gas} LHV_{gas} + m_{char} LHV_{char}}{m_{biomass} LHV_{biomass}} \quad (6)$$

Where m and LHV indicate mass and lower heating values, respectively.

The solar pyrolysis energy upgrade factor is plotted versus temperature in Figure 6-11.

As shown in Figure 6-11, the energy upgrade factor increases from 1.49 to 1.53 when temperature increases from 600 to 900 ℃. Then it decreases slightly to 1.45 at 1200 ℃ and more significantly to 1.38 at 2000 ℃. The energy upgrade factor variation is due to the bio-oil yield decrease with temperature.

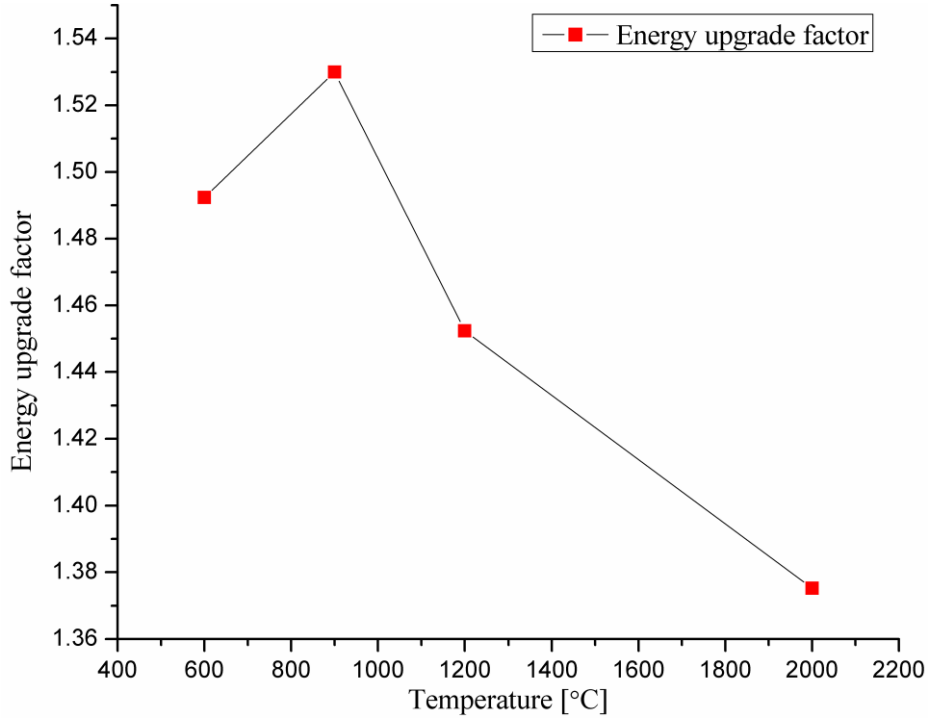

Figure 6-11: Energy upgrade factor as a function of temperature (pyrolysis conditions: heating rate 50°C/s, pressure 0.44bar, and argon flow rate 6NL/min).

The energy upgrade factors *U* for conventional pyrolysis, solar gasification and solar pyrolysis processes are compared in Table 6-6. For solar gasification/pyrolysis processes, *U* values greater than 1 indicate the successful solar energy storage in chemical form, and fuel calorific value upgrading achievement. Besides, the solar pyrolysis upgrade factor is 1.5 higher than that of solar gasification (1.3), meaning that more solar energy is stored by solar pyrolysis than by solar gasification. It is probably due to the 100% mass balance assumption of solar pyrolysis process. Conventional pyrolysis upgrade factor less than 1 is presumably due to liquid tars and carbonaceous solids deposits within the pyrolysis installation, which were not taken into account when calculating the product calorific value.

Table 6-6: Energy upgrade factor comparison

Process	Feedstock	Upgrade factor	Reference
Conventional pyrolysis	Forest waste	0.92	[50]
Solar gasification	Beech Charcoal	1.3	[51]
Solar pyrolysis	Beech wood	1.5	-

6.5 Conclusion

Char properties are influenced by the solar pyrolysis temperature and heating rate. The char yield decreases with temperature and heating rate. Char carbonized degree increases with temperature increase and heating rate decrease (when higher than 50^{o}C/s). The BET surface area and pore volume firstly increase when temperature rises from 800 to 1200^{o}C, then decrease at higher temperatures. They first increase with heating rate peak around 150^{o}C/s, and then decrease at 450^{o}C/s when temperature is higher than 1200^{o}C. The bigger the BET surface area and pore volume of the char, the higher the char reactivity, which means that they are good indicators of the char reactivity.

There is no obvious effect of temperature on the water content and element concentration of bio-oil. The number of identified tar species increased from about 52 to 71, and the energy upgrade factor increased from 1.49 to 1.53, when the operating temperature increased from 600 to 900 ℃. It indicates the successful solar energy storage in chemical form, and about 50% fuel calorific value upgrading achievement. The energy upgrade factor variation depends on the bio-oil yield as it contributes to about 50% of the total product energy content.

References

[1] Cetin E, Gupta R, Moghtaderi B. Effect of pyrolysis pressure and heating rate on radiata pine char structure and apparent gasification reactivity. Fuel 2005;84:1328-1334.

[2] Demirbas A, Pehlivan E, Altun T. Potential evolution of Turkish agricultural residues as bio-gas, bio-char and bio-oil sources. Int. J. Hydrogen Energy 2006;31:613-620.

[3] Blasi CD. Combustion and gasification rates of lignocellulosic chars. Prog. Energy Combust. Sci 2009;35:121-140.

[4] Raveendran K, Ganesh A. Adsorption characteristics and pore-development of biomass-pyrolysis char. Fuel 1998;77:769-781.

[5] Fu P, Hu S, Xiang J, Sun L.S, Su S, An S.M. Study on the gas evolution and char structural change during pyrolysis of cotton stalk. J. Anal. Appl. Pyrolysis 2012a;97:130-136.

[6] Fu P, Hu S, Xiang J, Sun L.S, Su S, Wang J. Evaluation of the porous structure development of chars from pyrolysis of rice straw: Effects of pyrolysis temperature and heating rate. J. Anal. Appl. Pyrolysis 2012b;98:177-183.

[7] Kim K.H, Kim JY, Cho TS, Choi JW. Influence of pyrolysis temperature on physicochemical properties of biochar obtained from the fast pyrolysis of pitch pine (Pinus rigida). Bioresour. Technol 2012;118:158-162.

[8] Min F.F, Zhang M.X, Zhang Y, Cao Y, Pan WP. An experimental investigation into the gasification reactivity and structure of agricultural waste chars. J. Anal. Appl. Pyrolysis 2011;92:250-257.

[9] Bonelli PR, Della Rocca P.A, Cerrella EG, Cukierman AL. Effect of pyrolysis temperature on composition, surface properties and thermal degradation rates of Brazil nut shells. Bioresour. Technol 2001;76:15-22.

[10] Mermoud F, Salvador S, Van de Steene L, Golfier F. Influence of the pyrolysis heating rate on the steam gasification of large wood char particle. Fuel 2006;85:1473-1482.

[11] Guerrero M, Ruiz MP, Alzueta MU, Bilbao R, Millera A. Pyrolysis of eucalyptus at different heating rates: studies of char characterization on oxidation reactivity. J. Anal. Appl. Pyrolysis 2005:74:307-314.

[12] Fushimi C, Araki K, Yamaguchi Y, Tsutsumi A. Effect of Heating Rate on Steam Gasification of Biomass. 1. Reactivity of Char. Ind. Eng. Chem. Res 2003;42:3922-3928.

[13] Cetin E, Moghtaderi B, Gupta R, Wall T.F. Influence of pyrolysis conditions on the structure and gasification reactivity of biomass chars. Fuel 2004:83:2139-2150.

[14] Kumar M, Gupta R.C. Influence of carbonization conditions on the gasification acacia

and eucalyptus wood chars by carbon dioxide. Fuel 1994;73:1922-1925.

[15] Chen G, Yu Q, Sjostrom K. Reactivity of char from pyrolysis of birch wood. J. Anal. Appl. Pyrolysis 1997;40:491-499.

[16] Antal M.J, Grønli M. The art, science and technology of charcoal production. Ind. Eng. Chem. Res 2003;42:1619-1640.

[17] Laurendeau N.M. Heterogeneous kinetics of coal char gasification and combustion. Prog. Energy Combust. Sci 2009;35:121-140.

[18] Della Rocca P.A, Cerrella EG, Bonelli PR, Cuckierman AL. Pyrolysis of hard-woods residues: on kinetics and char characterization. Biomass and Bioenergy 1999;16:79-88.

[19] Kurosaki F, Ishimaru K, Hata T, Bronsveld P, Kobayashi E, Imamura Y. Microstructure of wood charcoal prepared by flash heating. Carbon 2003;41:3057-3062.

[20] Bridgwater A V. Review of fast pyrolysis of biomass and product upgrading. Biomass and Bioenergy 2012;38:68-94.

[21] Moral U, Şensöz S. Pyrolysis of hornbeam shell (Carpinus betulus L.) in a fixed bed reactor: Characterization of bio-oil and bio-char. Fuel 2015;150:672-678.

[22] Bridgwater AV. Principles and practice of biomass fast pyrolysis processes for liquids. Journal of Analytical and Applied Pyrolysis 1999;51:3-22.

[23] Bridgwater AV. Renewable fuels and chemicals by thermal processing of biomass. Chemical Engineering Journal 2003;91:87-102.

[24] Capareda S, Imam T. Characterization of bio-oil, syngas and bio-char from switchgrass pyrolysis at various temperatures. Journal of Analytical and Applied Pyrolysis 2012;93:170-177.

[25] Özbay N, Apaydın-Varol E, Uzun BB, Pütün AE. Characterization of bio-oil obtained from fruit pulp pyrolysis. Energy 2008;33:1233-1240.

[26] Chen Y, Yang H, Wang X, Zhang S, Chen H. Biomass-based pyrolytic polygeneration system on cotton stalk pyrolysis: influence of temperature. Bioresour. Technol 2012;107:411-418.

[27] Demirbas A. Effects of temperature and particle size on bio-char yield from pyrolysis of agricultural residues. J. Anal. Appl. Pyrolysis 2004;72:243-248.

[28] Cui Z.Z, Li D.C, Qiao G.J, Li J.S. Preparation of porous carbon template with controllable channels by phenolic resin pyrolyzing. J. Inorg. Mater 2006;21:848-854.

[29] Lu L.M, Kong C.H, Sahajwallab V, Harris D. Char structure ordering during pyrolysis and combustion and its influence of char reactivity. Fuel 2002;81:1215-1225.

[30] Mohanty P, Nanda S, Pant K.K, Naik S, Kozinski J.A, Dalai A.K. Evaluation of the

physiochemical development of biochars obtained from pyrolysis of wheat straw, timothy grass and pinewood. J. Anal. Appl. Pyrolysis 2013;104:485-493.

[31] Channiwala S.A, Parikh P.P. A unified correlation for estimating HHV of solid, liquid and gaseous fuels. Fuel 2002;81:1051-1063.

[32] Gaur S, Reed TB. An atlas of thermal data for biomass and other fuels (No. NREL/TP--433-7965). National Renewable Energy Lab, Golden, CO (United States). 1995.

[33] Dickerson T, Soria J. Catalytic fast pyrolysis: a review. Energies 2013;6:514-538.

[34] Yang HP, Yan R, Chen HP, Lee DH, Zheng CG. Characteristics of hemicellulose, cellulose and lignin pyrolysis. Fuel 2007;86:1781-1788.

[35] Mullen C A, Boateng A A, Goldberg N M, et al. Bio-oil and bio-char production from corn cobs and stover by fast pyrolysis. Biomass and Bioenergy 2010;34:67-74.

[36] Huber GW, Iborra S, Corma A. Synthesis of transportation fuels from biomass: chemistry, catalysts, and engineering. Chemical reviews 2006;106:4044-4098.

[37] Yang Y, Brammer JG, Ouadi M, Samanya J, Hornung A, Xu HM. Characterisation of waste derived intermediate pyrolysis oils for use as diesel engine fuels. Fuel 2013;103:247-257.

[38] Demirbas A. The influence of temperature on the yields of compounds existing in bio-oils obtained from biomass samples via pyrolysis. Fuel Processing Technology 2007;88:591-597.

[39] Ozbay N et al. Characterization of bio-oil obtained from fruit pulp pyrolysis. Energy 2008;32:1233-1240

[40] Mourant et al. Effects of temperature on the yields and properties of bio-oil from the fast pyrolysis of mallee bark. Fuel 2013;108:400-408.

[41] Wolfesberger U, Aigner I, Hofbauer H. Tar content and composition in producer gas of fluidized bed gasification of wood – influence of temperature and pressure. Environ Prog Sustainable Energy 2009;28:372–379.

[42] Cypres R. Aromatic hydrocarbons formation during coal pyrolysis. Fuel Processing Technology 1987;15:1-15.

[43] Morf P, Hasler P, Nussbaumer T. Mechanisms and kinetics of homogeneous secondary reactions of tar from continuous pyrolysis of wood chips. Fuel 2002;81:843-853.

[44] Taralas G, Kontominas M.G, Kakatsios X. Modeling the thermal destruction of toluene (C7H8) as tar-related species for fuel gas cleanup. Energy & Fuels 2003;17:329-337.

[45] Ledesma E.B, Kalish M.A, Nelson P.F, Wornat M.J, Mackie J.C. Formation and fate of PAH during the pyrolysis and fuel-rich combustion of coal primary tar. Fuel

2000;79:1801-1814.
[46] Ledesma E.B, Marsh N.D, Sandrowitz A.K, Wornat M.J. An experimental study on the thermal decomposition of catechol. Proceedings of the Combustion Institute 2002; 29:2299-2306.
[47] Fuentes-Cano D, Gómez-Barea A, Nilsson S, Ollero P. The influence of temperature and steam on the yields of tar and light hydrocarbon compounds during devolatilization of dried sewage sludge in fluidized bed. Fuel 2013;108:341-350.
[48] Zhang Y, Kajitani S, Ashizawa M, Oki Y. Tar destruction and coke formation during rapid pyrolysis and gasification of biomass in a drop-tube furnace. Fuel 2010; 89:302-309.
[49] Pattiya A, Suttibak S. Production of bio-oil via fast pyrolysis of agricultural residues from cassava plantations in a fluidised-bed reactor with a hot vapour filtration unit. Journal of Analytical and Applied Pyrolysis 2012;95:227–235.
[50] Mohan D, Pittman Jr CU, Steele PH. Pyrolysis of wood/biomass for bio-oil.
Energ Fuel 2006;20:848-889.
[51] Piatkowski N, Wieckert C, Steinfeld A. Experimental investigation of a packed-bed solar reactor for the steam gasification of carbonaceous feedstocks. Fuel Processing Technology 2009;90:360-366.

Chapter 7: Modeling

This section describes the modeling associated to the experimental results obtained in solar pyrolysis, which were presented in the previous chapter. A two-dimensional, unsteady single particle model was developed and used to simulate the solar pyrolysis process. The main interest of this part is to get more information about the intra-particle heat/mass transfer and tar secondary reactions. FLUENT 12.1.4 was used as the modeling framework implemented with a complete set of user-defined functions (UDFs).

7.1 Numerical Model

7.1.1 Proposed kinetic scheme

The modified wood pyrolysis kinetic scheme (Figure 7-1) employed in this study is based on the models proposed by Park et al. [1] and Suuberg et al. [2]. The kinetic parameters and heats of pyrolysis reactions for the modified model were obtained from literature; they are listed in Table 7-1. Reaction rates were assumed to follow Arrhenius law shown in Eq. (1). Arrhenius' equation gives the dependence of the rate constant k_i of a chemical reaction on the absolute temperature T (in kelvins), where A_i is the pre-exponential factor (or simply the pre-factor), E_i is the activation energy, and R is the universal gas constant . Wood is assumed to first break into three primary products (gas, primary tar and intermediate solid) by three competing endothermic reactions [1]. Then, primary tar decomposes into gas, char and secondary tar by successive intra-particle secondary reactions due to the high residence time inside the pellet with high temperature. Intermediate solid is converted only to char with an exothermic reaction [2]. According to the adopted mechanism, the final yield of tar and gas by solar pyrolysis results from primary pyrolysis and secondary pyrolysis within the pellet [3].

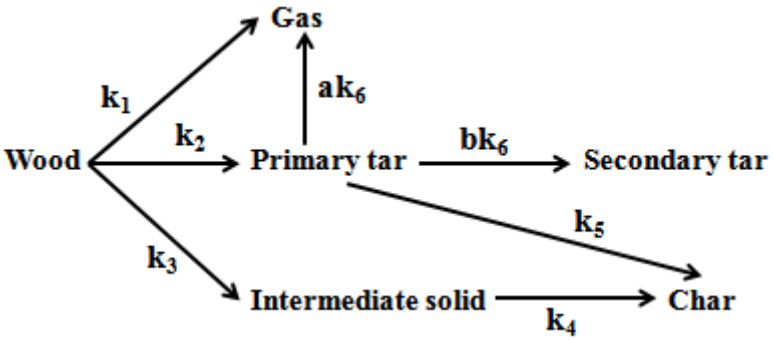

Figure 7-1: Modified wood pyrolysis model

$$k_i = A_i \exp\left(-E_i / RT\right) \quad (1)$$

Table 7-1: Kinetic parameters and reaction heat

Reaction i	A_i (1/s)	E_i (J/kmol)	Δh_i (kJ/kg)	Reference
1	4.38×10^{9}	152700	80	[1]
2	1.08×10^{10}	148000	80	[1]
3	3.27×10^{6}	111700	80	[4]
4	1.38×10^{10}	161000	-300	[1]
5	1.0×10^{5}	108000	-42	[1]
6	3.30×10^{11}	141000	-42	[2]

Stoichiometric coefficients a and b (Fig. 7.1) are the mass fraction of primary tar converted by the reaction to gas and secondary tar, respectively [3]. Chan et al. have assumed that the coefficients a and b are adjustable, however, the detailed values are not presented [5]. The coefficients a and b are considered as 0.5 and 0.5, and supposed to be constant with temperature in [3]. a and b were determined experimentally as 0.65 and 0.35 for wood slow pyrolysis [6]. It was reported that increasing the temperature and heating rate led to lower tar yield and higher gas yield resulting from tar secondary reactions [7, 8]. This implies that stoichiometric coefficient a (the mass fraction of primary tar converted by the reaction to gas) is generally higher at higher temperature and heating rate. For this reason, stoichiometric coefficients a and b are adjusted with temperature and heating rate in this model to fit the experimental results, as shown in Table 7-2.

Table 7-2: Stoichiometric coefficients a and b used in the model

			Heating rate intervals (^{o}C/s)	
			Slow	Fast
			≤10	≥50
Temperature Intervals (^{o}C)	Low	≤600	a=0.18; b=0.82	a=0.18; b=0.82
	High	900~1200	a=0.43; b=0.57	a=0.5; b=0.5
	Very high	1600~2000	a=0.5; b=0.5	a=0.7; b=0.3

The woody biomass typically contains about 40-47 wt% cellulose, 25-35 wt% hemicellulose, and about 16-31 wt% lignin [9]. These components degrade differently through various reactions depending on the temperature to yield different product spectra [10]. Then the use of first-order Arrhenius type reactions is a simplified assumption that does not take into account all complex pyrolysis reactions. Tar is a complex mixture of condensable hydrocarbons, which includes single to 5-ring, other oxygen-containing and complex polycyclic aromatic hydrocarbons [11]. Levoglucosan and phenol are known as the major

compounds of primary and secondary tars, respectively [12]. Therefore, primary and secondary tars are assumed to be levoglucosan and phenol for model simplification. Besides, several reactions with different intermediate products are lumped into limited reactions and products for simplification. With this simplified model, the evolution of pyrolysis lump products together with heat and mass transfer can be interpreted.

7.1.2 Main assumptions

A few assumptions of this mathematic model are made for simplifying and solving the problem:

(1) The beech wood pellet is described by a 2D axi-symmetrical mesh.

(2) The beech wood pellet is homogeneous with isotropic particle structure.

(3) All phases are at the same temperature and pressure (Local thermodynamic equilibrium in the particle).

(4) Gas, primary and secondary tars are in gaseous phase, where they obey ideal gas law.

(5) Dry beech wood pellet is considered.

(6) Wood shrinkage is not considered.

(7) There is no extra-particle tar secondary reaction.

7.1.3 Governing Equations

7.1.3.1 Mass and Momentum balances

The wood instantaneous mass balance is given in Eq. (2).

$$\frac{\partial \rho_w}{\partial t} = -\left(k_1 + k_2 + k_3\right)\rho_w \quad (2)$$

The intermediate solid instantaneous mass balance contains two terms, one from biomass conversion to itself and the other for its conversion to char as given in Eq. (3).

$$\frac{\partial \rho_{is}}{\partial t} = k_3\rho_w - k_4\rho_{is} \quad (3)$$

In a similar way, the char instantaneous mass balance is calculated by Eq. (4)

$$\frac{\partial \rho_c}{\partial t} = k_4\rho_{is} + \varepsilon k_5\rho_{t1} \quad (4)$$

The Argon, gas, primary tar and secondary tar are expressed by two-dimensional cylindrical coordinate system shown in Eq. (5), to Eq. (8).

$$\frac{\partial\left(\varepsilon\rho_{Ar}\right)}{\partial t} + \frac{\partial}{\partial x}\left(\rho_{Ar}v_x - \frac{\partial\left(D\rho_{Ar}\right)}{\partial x}\right) + \frac{1}{r}\frac{\partial}{\partial r}\left(r\rho_{Ar}v_r - r\frac{\partial\left(D\rho_{Ar}\right)}{\partial r}\right) = 0 \quad (5)$$

$$\frac{\partial\left(\varepsilon\rho_g\right)}{\partial t} + \frac{\partial}{\partial x}\left(\rho_g v_x - \frac{\partial\left(D\rho_g\right)}{\partial x}\right) + \frac{1}{r}\frac{\partial}{\partial r}\left(r\rho_g v_r - r\frac{\partial\left(D\rho_g\right)}{\partial r}\right) = S_g \quad (6)$$

$$\frac{\partial(\varepsilon\rho_{t1})}{\partial t}+\frac{\partial}{\partial x}\left(\rho_{t1}v_x-\frac{\partial(D\rho_{t1})}{\partial x}\right)+\frac{1}{r}\frac{\partial}{\partial r}\left(r\rho_{t1}v_r-r\frac{\partial(D\rho_{t1})}{\partial r}\right)=S_{t1} \quad (7)$$

$$\frac{\partial(\varepsilon\rho_{t2})}{\partial t}+\frac{\partial}{\partial x}\left(\rho_{t2}v_x-\frac{\partial(D\rho_{t2})}{\partial x}\right)+\frac{1}{r}\frac{\partial}{\partial r}\left(r\rho_{t2}v_r-r\frac{\partial(D\rho_{t2}t)}{\partial r}\right)=S_{t2} \quad (8)$$

The source terms for gas, primary tar and secondary tar are given in Eq. (9), Eq. (10) and Eq. (11).

$$S_g=k_1\rho_w+\varepsilon ak_6\rho_{t1} \quad (9)$$

$$S_{t1}=k_2\rho_w-\varepsilon(k_5+k_6)\rho_{t1} \quad (10)$$

$$S_{t2}=\varepsilon bk_6\rho_{t1} \quad (11)$$

For 2D axi-symmetric geometries, the axial and radial momentum conservation equations can be written as Eq. (12), Eq. (13) and Eq. (14).

$$\frac{\partial}{\partial t}(\varepsilon\rho v_x)+\frac{1}{r}\frac{\partial}{\partial x}(r\rho v_xv_x)+\frac{1}{r}\frac{\partial}{\partial r}(r\rho v_rv_x)=-\frac{\partial p}{\partial x}+\frac{1}{r}\frac{\partial}{\partial x}\left[r\mu\left(2\frac{\partial v_x}{\partial x}-\frac{2}{3}\left(\nabla\times\vec{v}\right)\right)\right]+\frac{1}{r}\frac{\partial}{\partial r}\left[r\mu\left(\frac{\partial v_x}{\partial r}+\frac{\partial v_r}{\partial x}\right)\right]+F_x \quad (12)$$

$$\frac{\partial}{\partial t}(\varepsilon\rho v_r)+\frac{1}{r}\frac{\partial}{\partial x}(r\rho v_xv_r)+\frac{1}{r}\frac{\partial}{\partial r}(r\rho v_rv_r)=-\frac{\partial p}{\partial r}++\frac{1}{r}\frac{\partial}{\partial x}\left[r\mu\left(\frac{\partial v_r}{\partial x}+\frac{\partial v_x}{\partial r}\right)\right]+\frac{1}{r}\frac{\partial}{\partial r}\left[r\mu\left(2\frac{\partial v_r}{\partial r}-\frac{2}{3}\left(\nabla\times\vec{v}\right)\right)\right]-2\mu\frac{v_r}{r^2}+\frac{2}{3}\frac{\mu}{r}\left(\nabla\times\vec{v}\right)+F_r \quad (13)$$

$$\nabla\times\vec{v}=\frac{\partial v_x}{\partial x}+\frac{\partial v_r}{\partial r}+\frac{v_r}{r} \quad (14)$$

The real-time porosity ε_t can be expressed as Eq. (15).

$$\frac{1-\varepsilon}{1-\varepsilon_0}=\frac{\rho_w+\rho_{is}+\rho_c}{\rho_0} \quad (15)$$

Where μ is the viscosity, ε_0, ρ_0 and ρ_t are the wood initial porosity, density and the real-time sum of the solid density.

The real-time permeability B of pyrolysis wood is interpolated from the value of pure wood and char as in Eq. (16).

$$B=\eta B_c+(1-\eta)B_w \quad (16)$$

Where η is the conversion factor defined as Eq. (17).

$$\eta = 1 - \frac{\rho_w + \rho_{is}}{\rho_0} \quad (17)$$

7.1.3.2 Energy balance

The dynamic energy conservation is written in Eq. (18)

$$\left(C_{p,w}\rho_w + C_{p,is}\rho_{is} + C_{p,c}\rho_c + \varepsilon C_{p,t1}\rho_{t1} + \varepsilon C_{p,t2}\rho_{t2} + \varepsilon C_{p,g}\rho_g\right)\frac{\partial T}{\partial t} = \frac{\partial}{\partial x}\left(\lambda_{eff(x)}\frac{\partial T}{\partial x}\right) + \frac{1}{r}\frac{\partial}{\partial r}\left(r\lambda_{eff(r)}\frac{\partial T}{\partial r}\right) + Q \quad (18)$$

Where Q is the heat generation, given in Eq. (19):

$$Q = -\left(k_1\Delta h_1 + k_2\Delta h_2 + k_3\Delta h_3\right)\rho_w - k_4\Delta h_4\rho_{is} - \varepsilon\left(k_5\Delta h_5 + k_6\Delta h_6\right)\rho_{t1} \quad (19)$$

The thermal conductivity of pellet is calculated as linear functions of the wood and char [13] shown in Eq. (20). And the pellet radiativity is calculated based on Eq. (21) [14]. The properties of beech wood and char used for the modeling are given in Table 3.

$$\lambda_{cond} = (1-\eta)\lambda_w + \eta\lambda_c \quad (20)$$

$$\lambda_{rad} = 16\sigma T^3 e d_{pore}/3 \quad (21)$$

Then the pellet effective thermal conductivity can be expressed by the function of phonon conductivity and radiative contribution given in Eq. (22). Table 7-3 shows the thermo-physical data used in the model.

$$\lambda_{eff} = (1-\varepsilon)\lambda_{cond} + \varepsilon\left(\lambda_{rad} + \lambda_v\right) \quad (22)$$

Table 7-3: Thermo-physical data used in the model

Property	Value	Ref.
Radius	R=5×10^{-3}, m	Measured
Length	L=5×10^{-3}, m	Measured
Initial pellet density	$\rho_{w,0} = 764$, kg/m^3	Measured
Initial pellet porosity	$\varepsilon_{w,0} = 0.365$	Measured
Wood permeability	$B_w = 7.25\times10^{-13}$, m^2	[15]
Pore diameter	$d_{pore} = 0.00005$, m	[16]
Initial char density	$\rho_{c,0} = 2000$, kg/m^3	[15]
Char permeability	$B_c = 10^{-11}$, m^2	[15]
Intrinsic wood thermal conductivity	$\lambda_w = 0.291 + 0.000836\times0.33T$, W/mK	[17]

Intrinsic char thermal conductivity	$\lambda_c = 1.47 + 0.0011T$, W/mK	[14]
Intrinsic volatile thermal conductivity	$\lambda_v = 0.0258$, W/mK	[16]
Wood specific heat capacity	$C_{p,w} = 2300 - 1500\exp(-0.0055T)$,	[15]
Intermediate solid specific heat capacity	$C_{p,is} = 2300 - 1500\exp(-0.0055T)$	[15]
Char specific heat capacity	$C_{p,c} = 1430 + 0.355T - 7.3210T^{-2}$	[15]
Primary tar specific heat capacity	$C_{p,t1} = -100 + 4.4T - 1.57\times10^{-3}T^2$	[16]
Secondary tar specific heat capacity	$C_{p,t2} = -100 + 4.4T - 1.57\times10^{-3}T^2$	[16]
Secondary gas specific heat capacity	$C_{p,g} = 770 + 0.629T - 1.91\times10^{-4}T^2$	[16]
Viscosity	$\mu = 3.0\times10^{-5}$, Pa.s	[6]
Atmosphere pressure	$P_0 = 0.083$ Mpa	Measured
Stefan Boltzmann constant	$\sigma = 5.67\times10^{-8}$, W/m^{2}K^4	-
Universal gas constant	$R = 8.314$, J/molK	-
Emissivity	$e = 0.95$	[18]

7.2 Boundary and initial conditions

Figure 7-2a schemes the beech wood pellet top being irradiated in a transparent Pyrex reactor. The sidewall and bottom are insulated by the crucible and foam. Due to symmetry, only half of the pellet is shown in Fig. 7-2b.

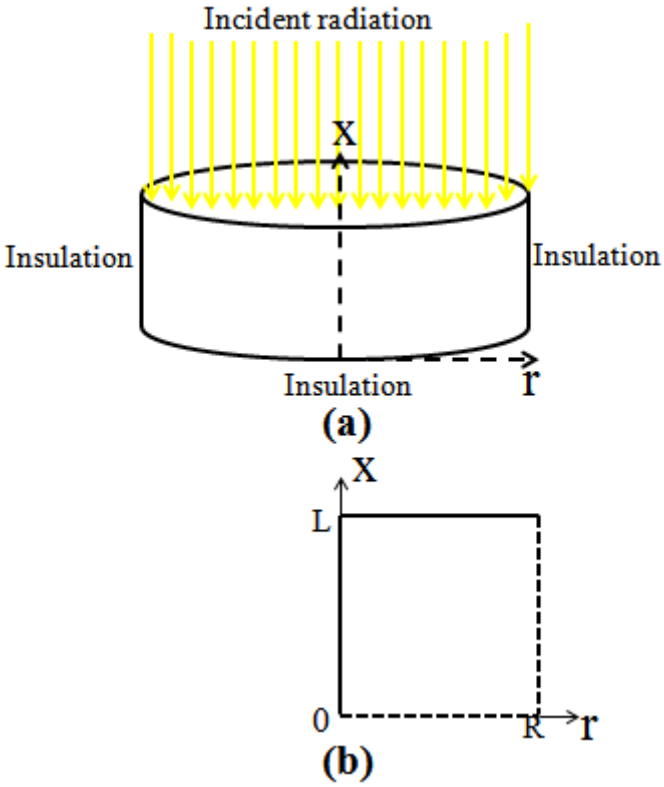

Figure 7-2: (a) Pellet boundary conditions; (b) Axi-symmetric coordinate

(1) For the irradiated top surface (x = L), the thermal boundary condition is established as the temperature measured during the experiments as shown in Eq. (23).

$$T(L,r,t) = T_{\exp}(t) \quad (23)$$

$$\rho_{Ar}(L,r,t) = \rho_{Ar,bulk} \quad (24)$$

$$\rho_i(L,r,t) = \rho_{i,bulk} \; (i = g, t1, t2) \quad (25)$$

$$P = P_0 \quad (26)$$

(2) For the adiabatic sidewalls (r = R) and bottom surface (x = 0)

$$\left.\frac{\partial T}{\partial r}\right|_{r=R} = 0 \quad (27)$$

$$\left.\frac{\partial \rho_i}{\partial r}\right|_{r=R} = 0 \quad (28)$$

$$v = 0 \quad \text{(no slip condition)} \quad (29)$$

$$\left.\frac{\partial T}{\partial x}\right|_{x=0} = 0 \quad (30)$$

$$\left.\frac{\partial \rho_i}{\partial x}\right|_{x=L} = 0 \quad (31)$$

$$v = 0 \quad \text{(no slip condition)} \quad (32)$$

(3) For the cylindrical pellet center (r = 0)

$$\left.\frac{\partial T}{\partial r}\right|_{r=0} = 0 \quad (33)$$

$$\left.\frac{\partial \rho_i}{\partial r}\right|_{r=0} = 0 \quad (34)$$

$$\left.\frac{\partial v}{\partial r}\right|_{r=0} = 0 \quad \text{(symmetry)} \quad (35)$$

A uniform temperature is assigned to the irradiated top surface as initial condition. The initial state of an experiment run is assumed to be at 473K.

7.3 Numerical solution

The presented governing equations are solved in 2-D with the CFD software FLUENT 12.1.4 using the finite volume discretization method. The momentum equation, the species mass transport equation, the energy equation and the conductive heat transfer equation in the porous particle are solved by FLUENT software. User-defined functions (UDFs) are programmed in C++ language and complemented to the FLUENT code. UDFs mass sources for gas phases (gas, primary tar and secondary tar) and energy sources for pyrolysis reactions are programmed. And the reaction rates, porosity, effective conductivity and permeability of pellet are also programmed.

The "pressure-based method" was used to solve the momentum equation. All scalars are discretized by secondary discretization scheme for obtaining more accurate results. Finally the unsteady simulation was carried out with a step size of 0.005 s and 100 iterations per time step.

7.4 Results and discussion

7.4.1 Influence of temperature and heating rate on the product distribution

The model was validated in front of data from solar pyrolysis experiments ran under heating rates 10 (slow) and 50^{o}C/s (fast) to the final temperatures 600, 900, 1200, 1600 and 2000^{o}C. Figures 7-3, 7-4 and 7-5 show the total yield of product species at different temperatures and heating rates. As shown in Figure 7-3, the gas product yield generally increases with temperature and heating rate. The gas yield increase is probably due the enhanced tar intra-particle secondary reactions at higher temperatures and heating rates [8]. The model predicts well the experimental gas yields at slow and fast heating rates. The predicted trends of char yield evolution with temperature and heating rate are the same as the experimental trends (Figure 7-4). Higher temperature and higher heating rate lead to lower

char yield [19]. However, simulation overestimates experimental results for char yield. This is due to the ignored heterogeneous reactions between char and tar because of lack of kinetic data for such reactions. Calculated data of liquid yields fit excellently experimental data at both heating rates presented in Figure 7-5, which shows that the liquid yield decreases with the heating rate. The heating rate increase has two effects: (1) The tar intra-particle residence time decreases; (2) the tar temperature increases faster. Obviously, the secondary effect is predominant for pellet sample used. Then, tar decomposition reactions are enhanced within the pellet before the tar is possibly released.

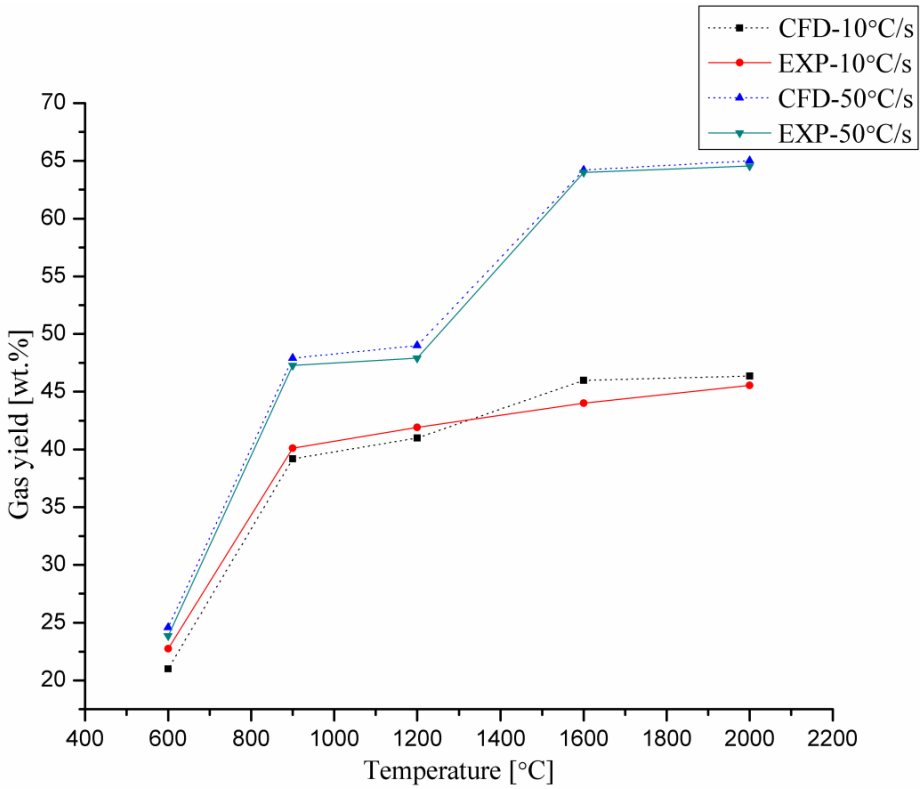

Figure 7-3: Gas yield comparison between the CFD model prediction values and experimental results

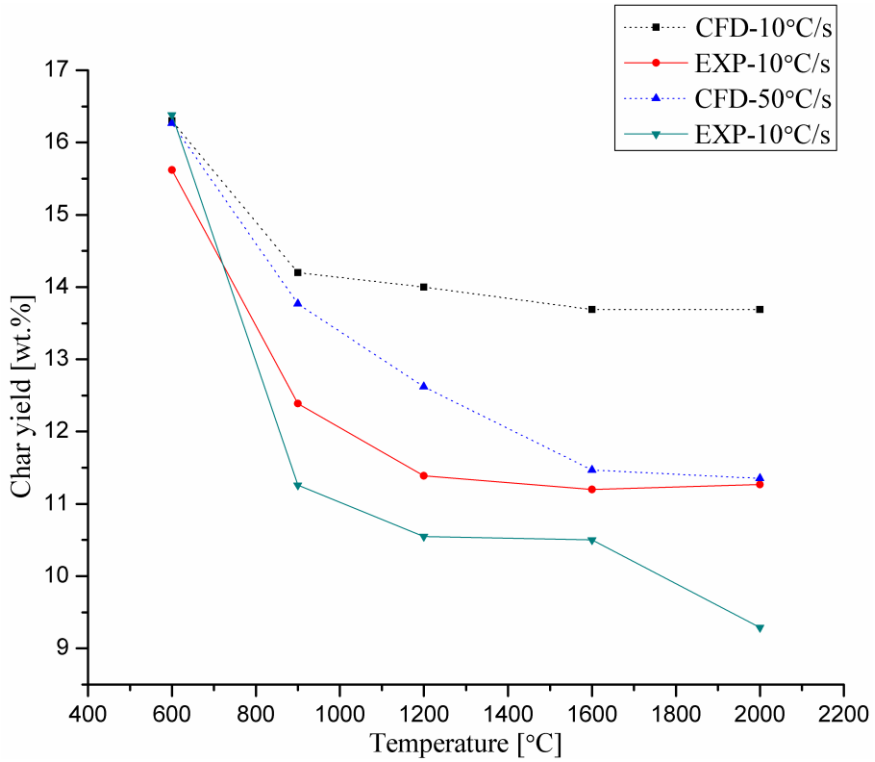

Figure 7-4: Char yield comparison between the CFD model prediction values and experimental results

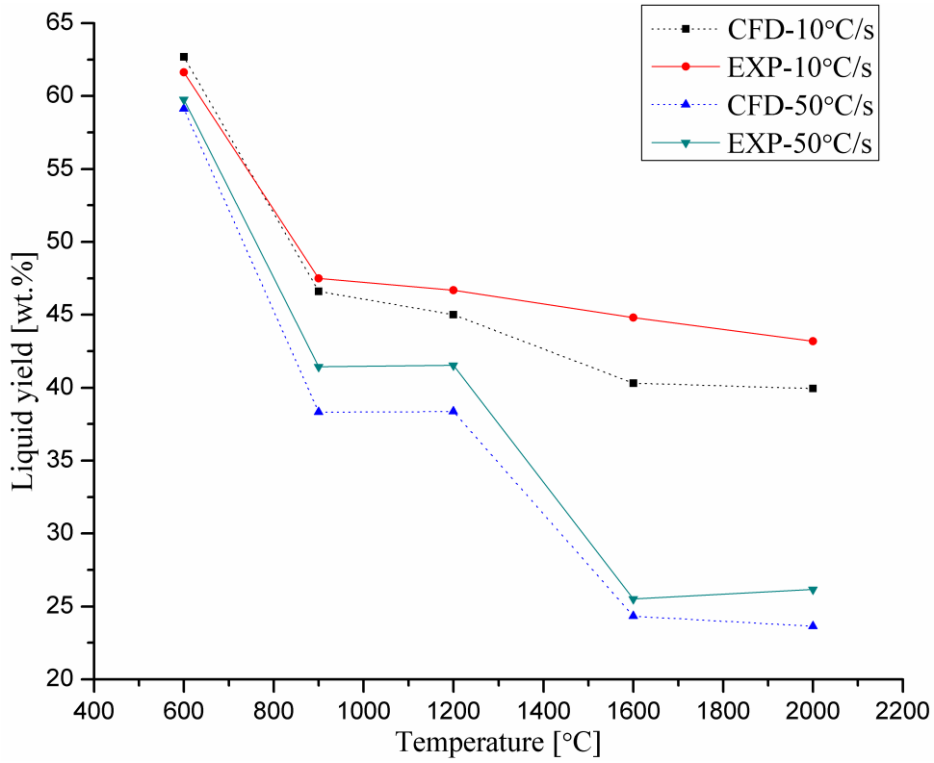

Figure 7-5: Liquid (tar) yield comparison between the CFD model prediction values and experimental results

7.4.2 Influence of temperature and heating rate on weight loss history

Figure 7-6 shows the weight loss history of the pyrolyzed wood under different final

temperatures (900 to 2000°C) with different heating rates (10 and 50°C/s). It is clearly seen that sample heating continues until about 10 s when active decomposition of the sample starts, whatever the final temperature with fast heating rate 50°C/s. However the sample decomposition begins only at about 30s with slow heating rate (10°C/s). This implies that the biomass conversion rate at the process onset does not significantly depend on the final temperature, which was also observed by Okekunle et al. [20]. Fast heating rate reduces the time required for the sample to overpass 250 ℃ where primary pyrolysis occurs [21]. With heating rate 50°C/s, the weight loss profile begins to be steeper and steeper when the final temperature increases from 900 to 2000°C. This may be due to the fact that the heat transfer rate in the pellet increases with the final temperature, thereby accelerating the pyrolysis reaction. The longest reaction time is about 150s when the final temperature is 900°C with heating rate 10°C/s, and it decreases to about 80s at the highest temperature and heating rate.

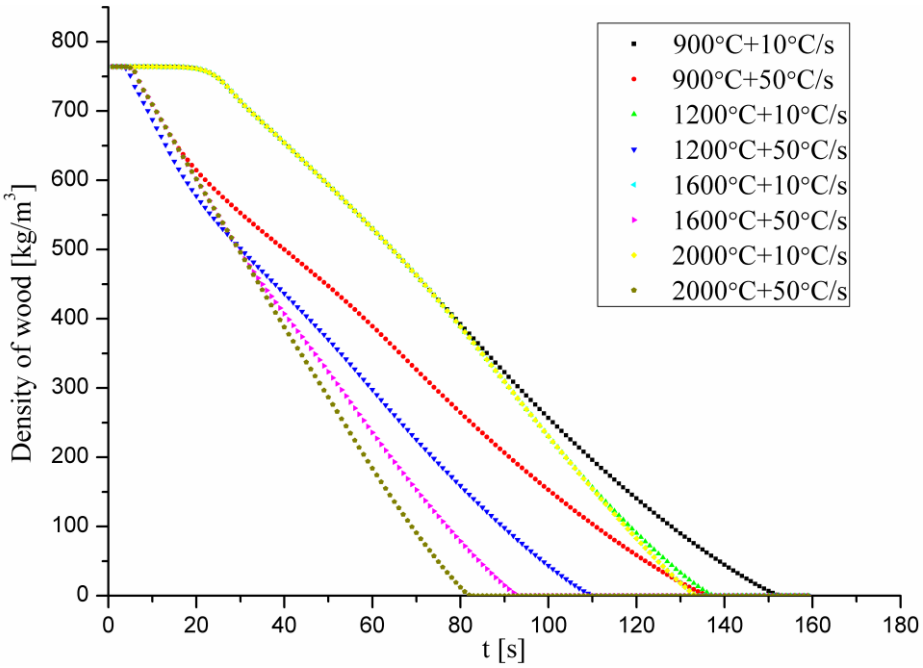

Figure 7-6: Weight loss history of the pyrolyzed wood under different temperatures and heating rates

7.4.3 Influence of temperature and heating rate on gases evolution

Figure 7-7 plots the gas release flow rate at different reactor temperatures and heating rates. The figure shows the peaks of gas release rate profiles increase with temperature. This comes from the intra-particle tar secondary reactions that are enhanced at higher temperatures, thereby resulting in drastic increase in the rate of gas release with time. Besides, the gas release rate peaks appear earlier at fast heating rate (50°C/s) than at slow heating rate (10°C/s). The gas release rate profiles at fast heating rate 50°C/s display two peaks. At low temperature,

CO and CO_2 (and water vapor) evolution is mainly due to extractives and hemicellulose degradation and cellulose degradation leading to gas and char formation [22]. As temperature increases, the secondary reaction of tar (mainly from high temperature cellulose degradation) mainly produces CO and H_2 [23]. Then the first peak can be considered to originate from the primary pyrolysis reaction, and the second peak may be explained by the tar intra-particle reactions. However, there is only one peak for the gas release rate profiles at slow heating rate ($10^oC/s$). A possible explanation is that longer time is required for the sample to overpass 500^oC, which is the critical temperature for tar secondary reaction. So the primary reaction will last longer time at slow heating rate, and therefore the secondary and primary reactions may occur together. And finally the gas release peaks from primary and secondary reactions are mingled into one peak, as shown in Figure 7-7.

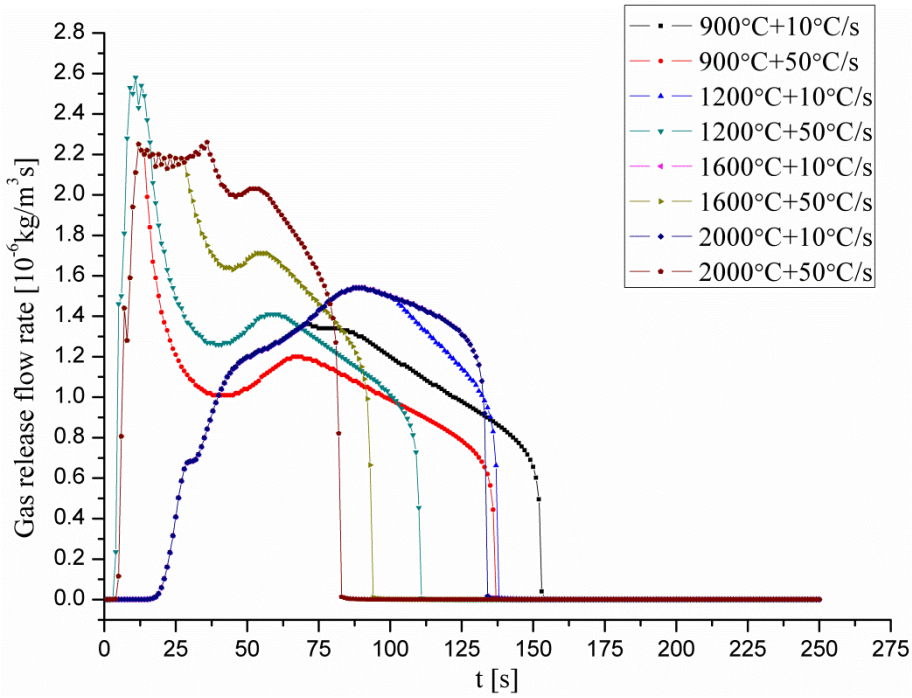

Figure 7-7: Gas release flow rate of the pyrolyzed wood under different temperatures and heating rates

7.5 Conclusions

Solar pyrolysis characteristics of beech wood under different temperatures and heating rates were investigated theoretically by CFD modeling and simulation results compared with experimental data. The 2D unsteady numerical model predictions are in good agreement with the experimental results. The evolution of the final products and mass losses of biomass are enhanced with temperature and heating rate. Moreover, the higher the temperature and heating rate, the higher the gas yield. This emphasises the intra-particle tar secondary reaction into gas for pyrolysis of big size sample under high temperature and heating rate.

Stoichiometric coefficients about the mass fraction of primary tar converted by the reaction to gas and secondary tar were determined at different temperatures and heating rates for the first time.

References

[1] Park WC, Atreya A, R. Baum H. Experimental and theoretical investigation of heat and mass transfer processes during wood pyrolysis. Combustion & Flame 2010;157:481-494.

[2] Suuberg M.E, Milosavljevic I, Oja V. Two-regime global kinetics of cellulose pyrolysis: the role of tar evaporation. In Symposium (International) on Combustion 1996;26:1515-1521.

[3] Grieco E, Baldi G. Analysis and modeling of wood pyrolysis. Chemical Engineering Science 2011;66:650-660.

[4] Blasi CD, Branca C. Kinetics of primary product formation from wood pyrolysis. Industrial & Engineering Chemistry Research 2001;40:5547-5556.

[5] Chan WC, Kelbon M, Krieger BB. Modelling and experimental verification of physical and chemical processes during pyrolysis of a large biomass particle. Fuel 1985;64:1505-1513.

[6] Ratte J, Marias F, Vaxelaire J, Bernada P. Mathematical modelling of slow pyrolysis of a particle of treated wood waste. Journal of Hazardous Materials 2009;170:1023-1040.

[7] Zanzi R, Sjostrom K, Bjornbom E. Rapid pyrolysis of agricultural residues at high temperature. Biomass Bioenergy 2002;23:357-366.

[8] Zeng K, Gauthier D, Li R, Flamant G. Solar pyrolysis of beech wood: Effects of pyrolysis parameters on the product distribution and gas product composition. Energy 2015;93:1648-1657.

[9] Mohan D, Pittman Jr CU, Steele PH. Pyrolysis of wood/biomass for bio-oil. Energy & Fuels 2006;20:848-889.

[10] Yang H, Yan R, Chen H, Zheng C, Lee DH, Liang DT. In-depth investigation of biomass pyrolysis based on three major components: hemicellulose, cellulose and lignin. Energy & Fuels 2006;20:383-393.

[11] Devi L, Ptasinski K.J, Janssen F.J. A review of the primary measures for tar elimination in biomass gasification processes. Biomass and Bioenergy 2003;24:125-140.

[12] Morf P, Hasler P, Nussbaumer T. Mechanisms and kinetics of homogeneous secondary reactions from continuous pyrolysis of wood chips. Fuel 2002;81:843-53.

[13] Al-Haddad M, Rendek E, Corriou JP, Mauviel G. Biomass fast pyrolysis: experimental analysis and modeling approach. Energy & Fuels 2010;24:4689-4692.

[14] Thunman H, Leckner B. Thermal conductivity of wood—models for different stages of combustion. Biomass & Bioenergy 2002;23:47-54.

[15] Blondeau J, Jeanmart H. Biomass pyrolysis at high temperatures: Prediction of gaseous species yields from an anisotropic particle. Biomass & Bioenergy 2012;41:107-121.

[16] Grønli MG, Melaaen MC. Mathematical model for wood pyrolysis comparison of experimental measurements with model predictions. Energy & Fuels 2000;14:791-800.
[17] Harada T, Hata T, Ishihara S. Thermal constants of wood during the heating process measured with the laser flash method. Journal of Wood Science 1998;44:425-431.
[18] Babu BV, Chaurasia AS. Modeling for pyrolysis of solid particle: kinetics and heat transfer effects. Energy Conversion and Management 2003;44:2251-2275.
[19] Zeng K, Gauthier D, Lu J, Flamant G. Parametric study and process optimization for solar pyrolysis of beech wood. Energy Conversion and Management 2015;106:987-998.
[20] Okekunle PO. Effect of peak temperature on biomass pyrolysis characteristics in thermally thin regime in a fixed-bed reactor. Mathematical Theory & Modeling 2015;5:136-146.
[21] Neves D, Thunman H, Matos A, Tarelho L, Gómez-Barea A. Characterization and prediction of biomass pyrolysis products. Progress in Energy & Combustion Science 2011;37:611-630.
[22] Blasi CD. Modeling and simulation of combustion processes of charring and non-charring solid fuels. Progress in Energy & Combust Science 1993;19:71-104.
[23] Rath J, Staudinger G. Cracking reactions of tar from pyrolysis of spruce wood. Fuel 2001;80:1379-1389.

Chapter 8: Conclusion and outlook

The three year PhD study was conducted to get a better understanding of biomass pyrolysis under direct concentrated solar radiation. In order to achieve this goal, the influence of several parameters, final temperature, heating rate, pressure and argon flow rate were carefully studied by the means of experiments and simulation. This work was organized in four steps.

First of all, the influences of single-factor: temperature (600-2000 ℃), heating rate (5-450 ℃/s), pressure (0.48-1.18bar) and argon flow rate (6-12NL/min) on solar pyrolysis product distribution and gas composition were determined by one-factor-at-a-time (OFAT) approach.

Secondly, the combined effects of temperature (800-2000 ℃), heating rate (50-450 ℃/s) and argon flow rate (4-8NL/min) on solar pyrolysis gas product composition were investigated through response surface methodology (RSM).

Thirdly, the bio-char and bio-oil collected during the solar pyrolysis experiments were characterized and the energetic upgrade factor was determined.

Finally, the experimental observations were integrated into a two-dimensional unsteady single particle model. The model accurately predicts the solar pyrolysis product yields under different temperatures and heating rates

The most important conclusion obtained with the analysis of experimental and modeling results are:

(1) The temperature drastically affects the final product distribution and gas composition in solar pyrolysis. It is the key parameter governing solar pyrolysis reactions under such experimental conditions. The heating rate and argon flow rate also have a significant influence. These three parameters affect intra-particle and extra-particle tar reactions, which determine the final product distribution. By contrast, the pressure has minimal influence on the product distribution.

(2) Higher CO and H_2 yields are obtained at the plateau temperature of 1200 ℃, heating rate of 50 ℃/s and at atmospheric pressure, indicating that these parameters have an important effect on tar secondary reactions.

(3) The total gas LHV dramatically increases (5-fold) with increasing temperature (from 600 ℃ to 1200 ℃) and sample heating rate (from 5 ℃/s to 50 ℃/s), which is mainly due to variations in the CO and H_2 yields.

(4) The interaction between temperature and heating rate enhances at both high ranges.

The gas LHV can be increased four times by solar processing, from 3527 to 14 589 kJ/kg of beech wood. The maximum gas products LHV of solar pyrolyzed beech wood was obtained at 2000 ℃ and 450 ℃/s heating rate.

(5) Char properties are influenced by the solar pyrolysis temperature and heating rate. The char yield decreases with temperature and heating rate. Char carbonized degree increases with temperature increase and heating rate decrease (when higher than 50^{o}C/s). The BET surface area and pore volume firstly increase when temperature rises from 800 to 1200^{o}C, then decrease at higher temperatures. They first increase with heating rate peak around 150^{o}C/s, and then decrease at 450^{o}C/s when temperature is higher than 1200^{o}C. The bigger the BET surface area and pore volume of the char, the higher the char reactivity, which means that they are good indicators of the char reactivity.

(6) There is no obvious effect of temperature on the water content and element concentration of bio-oil. The number of identified tar species increased from about 52 to 71, and the energy upgrade factor increased from 1.49 to 1.53, when the operating temperature increased from 600 to 900 ℃.

(7) For the first time we measured the solar energy storage in solar pyrolysis products as chemical form. The energy upgrade factor is about 1.5. This means that the products contain 50% more energy than the initial biomass does. Its variation depends on the bio-oil yield as it contributes to about 50% of the total product energy content.

(8) The 2D unsteady CFD particle model predictions are in good agreement with the experimental results. The evolution of the final products and mass losses of biomass are enhanced with temperature and heating rate. This emphasises the intra-particle tar secondary reaction into gas for pyrolysis of big size sample under high temperature and heating rate. Stoichiometric coefficients about the mass fraction of primary tar converted by the reaction to gas and secondary tar were determined at different temperatures and heating rates for the first time.

As a general conclusion, it can be stated that solar pyrolysis of biomass is a good way to store solar energy in chemical form, about 50% fuel calorific value upgrading achievement can be obtained by solar pyrolysis. The higher temperature and heating rate is interesting for enhanced solar pyrolysis gas (mainly CO and H_2) production from tar secondary reaction.

Future research should focus on the following main experimental and numerical topics:

(1). Investigate the influence of biomass characteristics on the solar pyrolysis with existing setup. Such as, moisture content, particle size, metal content.

(2) Develop a reactor (such as bubbling fluidized bed) with a continuity feeder for solar

pyrolysis. Try to link the already determined optimal conditions to the larger scale continuous process.

(3). Test other kinds of carbonaceous feedstocks (such as, MSW and sludge).

(4).Test other kinds of processes (such as, gasification and desiccation) with concentrated solar energy.

(5). Examine the role of metals on pyro-gasifiaction reactions. Laser-Induced Breakdown Spectroscopy (LIBS) can be applied for metal (Such as, Na, K and Ca) evolution study for solar pyrolysis or gasification of biomass.

(6). Modify the particle model applying competitive, multi-component comprehensive kinetic mechanisms (such as Ranzi's mechanism). Then the gas composition can be predicted for solar pyrolysis.

(7) Develop a more accurate global model emphasizing tar extra-particle reaction in the solar reactor, thus the temperature and flow field in the solar reactor will be determined.

List of Tables

List of Figures

French Summary

Introduction

Historiquement, tout développement économique a toujours été fortement corrélé à une utilisation accrue de l'énergie. De nos jours, les énergies fossiles fournissent 82 % des besoins énergétiques mondiaux [1]. La demande énergétique mondiale est prévue pour augmenter de 37 % d'ici 2040, en raison de l'augmentation de la population mondiale et en raison de la croissance économique. Or, la vitesse de consommation des énergies fossiles est beaucoup plus importante que leur vitesse de formation. Cela va inévitablement entraîner des crises de l'énergie dans le futur. De plus, la combustion des énergies fossiles est la source majeure d'émissions de gaz à effet de serre, ce qui contribue fortement au réchauffement climatique.

Dans le but de satisfaire la demande en énergie dans le long terme tout en réduisant les émissions de CO_2, un maximum d'énergies renouvelables devrait être utilisé. Les énergies renouvelables ne contribuent qu'à 19% de notre consommation globale d'énergie, d'après le rapport REN21 de 2014 [2]. L'énergie solaire et la biomasse sont des énergies renouvelables ayant un potentiel très important. Cependant, elles ne constituent qu'une très faible part dans la production d'énergie renouvelable mondiale [3]. Comme le montre la Figure 1, l'énergie solaire a une très faible contribution dans la production d'énergie primaire mondiale : moins de 1.0% [4]. La biomasse représente quant à elle 9% des besoins énergétiques mondiaux. Le Tableau 1 montre le scénario mondial prévu pour les énergies renouvelables d'ici à 2040. D'après le Conseil Européen sur les énergies renouvelables (European Renewable Energy Council, EREC 2006), les énergies renouvelables satisferont à environ 50% des besoins énergétiques mondiaux en 2040. Entre 2010 et 2040, un développement important de la production d'énergie va être observé pour le solaire (de 4.4 à 1332 Mtep) et pour la biomasse (de 1080 à 3271 Mtep)[1].

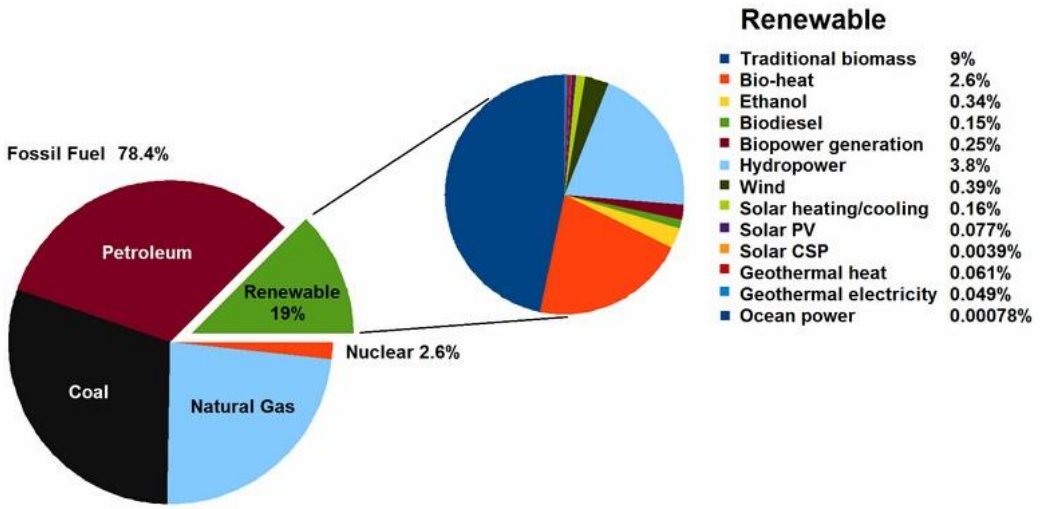

Figure 1: Consommation mondiale d'énergie primaire par sources (2013) [2]

Tableau 1: Scénario de développement des énergies renouvelables jusqu'en 2040 [2]

	2001	2010	2020	2030	2040
Total consumption (Million ton oil equivalent)	10038	10549	11425	12352	13310
Biomass	1080	1313	1791	2483	3271
Large hydro	22.7	266	309	341	358
Geothermal	43.2	86	186	333	493
Small hydro	9.5	19	49	106	189
Wind	4.7	44	266	542	688
Solar thermal	4.1	15	66	244	480
Photovoltaic	0.2	2	24	221	784
Solar thermal electricity	0.1	0.4	3	16	68
Marine (tidal/wave/ocean)	0.05	0.1	0.4	3	20
Total renewable energy source	1365.5	1745.5	2694.4	4289	6351
Contribution of renewable energy source (%)	13.6	16.6	23.6	34.7	47.7

D'une part le rayonnement solaire est dilué, intermittent, et inéquitablement réparti sur la surface de la Terre. D'autre part, la pyrolyse conventionnelle nécessite un apport énergétique extérieur qui provient généralement d'une source non renouvelable, ce qui diminue l'efficacité de conversion énergétique et cause des problèmes environnementaux. Ces défauts ont donc restreint jusqu'à présent l'utilisation de l'énergie solaire et de la biomasse à de

faibles proportions du mix énergétique mondial. Une stratégie pour pallier ces défauts est de combiner ces deux énergies. En effet, l'énergie solaire concentrée peut fournir la chaleur nécessaire au processus de pyrolyse de la biomasse. On transforme ainsi la biomasse en un carburant solaire, comme le montre la Figure 2. Trois avantages principaux peuvent être avancés pour cette combinaison [8] : (1) Le rejet de gaz polluant est évité ; (2) La valeur calorifique de la matière première du carburant est augmentée ; (3) L'énergie solaire intermittente est stockée chimiquement sous la forme d'un carburant. Ces avantages font des « carburants solaires » (issus de la pyrolyse solaire) une solution attractive dans la quête de carburants propres et renouvelables.

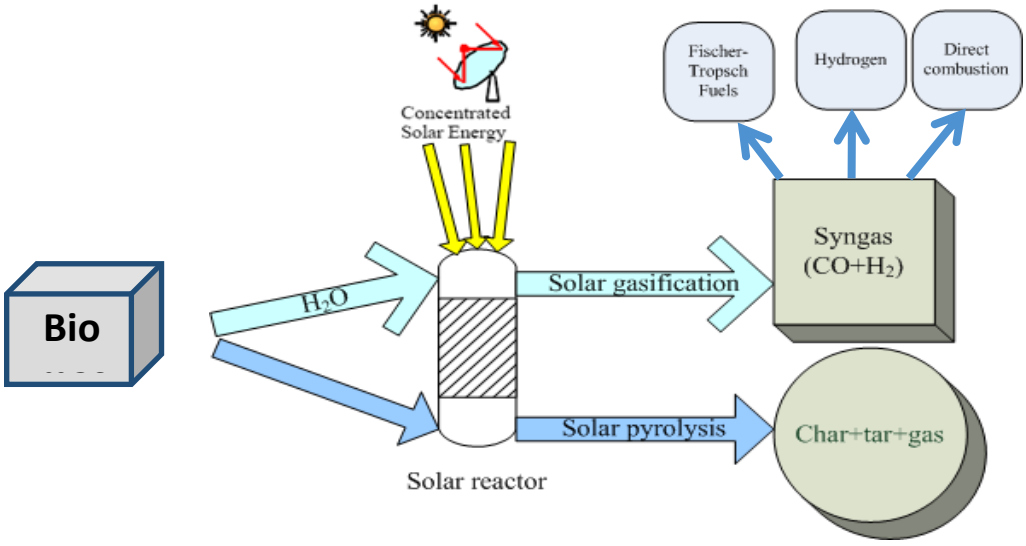

Figure 2: Etapes de la pyrolyse et de la gazéification solaire.

La pyrolyse solaire de la biomasse utilise un rayonnement solaire hautement concentré comme source de chaleur à haute température pour entraîner des réactions de pyrolyse de la biomasse dans une atmosphère neutre. L'énergie solaire, en apportant l'énergie nécessaire au changement d'enthalpie induit par les réactions pyrolytiques, est stockée chimiquement, et cela augmente la capacité énergétique de la matière première. Les systèmes de concentration de l'énergie solaire génèrent des densités de flux très importantes grâce à des miroirs ou à des lentilles qui concentrent les rayons du soleil sur une petite surface (le réacteur solaire). En appliquant une irradiation directe par le soleil, la biomasse peut atteindre les températures nécessaires à sa pyrolyse plus rapidement et avec une meilleure efficacité que par un processus de chauffe indirect. D'avantage de gaz de pyrolyse peut donc être produit en effectuant une pyrolyse solaire flash directe (grâce à une montée à haute température très rapide). En conséquence, les produits gazeux de la pyrolyse ont une valeur calorifique plus

importante que ceux produits par gazéification conventionnelle [13,14]. Ils peuvent donc être utilisés comme carburant pour de la production d'électricité ou de chaleur, et peuvent être transportés. Cependant, il n'existe que très peu d'études concernant la production par pyrolyse de ces gaz à haute valeur énergétique [15].

Cette thèse a pour but de mieux comprendre la pyrolyse de la biomasse dans un réacteur solaire. L'objectif premier est de quantifier la distribution des produits de la réaction pyrolytique, et d'en déterminer la composition, en fonction des paramètres du procédé. Le second objectif est de déterminer les conditions optimales pour obtenir un pouvoir calorifique inférieur des gaz (PCI) maximal. Dans le même temps, le bio-charbon et la bio-huile obtenus pendant les expériences de pyrolyse ont été caractérisées, et l'augmentation de la valeur énergétique du produit a été quantifiée. A notre connaissance c'est la première fois que cette mesure a été réalisée.

Etat de l'art

Très peu de recherches ont porté sur la pyrolyse de matériaux carbonés par pyrolyse solaire. Dans les années 1980, Beatie et al. [4] ont obtenu un maximum de production de gaz de 31 mmol/g de charbon à partir de pyrolyse solaire directe avec un flux de 1 MW/m². Antal et al. [5] ont utilisé un simulateur solaire (simulant un four solaire avec une densité de flux allant jusqu'à 2 MW/m²) avec un lit fluidisé pour effectuer une pyrolyse flash et ont obtenu 63% de liquide, 11% de charbon et 26% de gaz. Tabatabaie-Raissi et al. [6] ont mesuré par analyse thermogravimétrique une production de charbon allant de 6.6 à 8.4% à partir d'une pyrolyse de cellulose sous un rayonnement allant jusqu'à 10 MW/m². Chan et al. [7, 8] ont étudié la pyrolyse de bois de pin avec un simulateur solaire et ont trouvé que la production de charbon, de goudron et de gaz étaient respectivement de 20-26%, 33-52% et de 11-27%, les valeurs trouvées dépendant de la densité de flux appliquée. Plus tard, 21-29% de charbon, 25-40% de goudron et 30-50% de gaz ont été obtenus à partir de pyrolyse de différents types de bois (avec des densités de flux de 0.08 et 0.13 MW/m²) [9]. Lédé et al [10-12] ont montré que la production de liquide (environ 62%) ne dépend pas de la densité du flux de chaleur (de 0.3 à 0.8 MW/m²), contrairement à la production de gaz qui augmente au dépend de la production de charbon. Récemment, quelques études ont porté sur l'utilisation d'un four à image pour la pyrolyse [13, 14]. Cependant, les travaux portant sur la pyrolyse utilisant un vrai four solaire pour produire du bio-charbon [15] et de la bio-huile [16, 17] sont rares, en particulier dans des conditions bien contrôlées. Des analyses

plus approfondies de l'influence des paramètres de la pyrolyse sur la distribution des produits dans un véritable réacteur solaire sont nécessaires. Les résultats devraient être différents de ceux obtenus avec un réacteur conventionnel car deux zones de température coexistent dans un réacteur solaire (l'environnement autour de l'échantillon est « froid »), comme décrit dans [5] et modélisé dans [18].

Il est communément admis que l'énergie solaire intermittente peut être stockée chimiquement sous la forme de carburants solaires (bio-huile et bio-charbon). Presque toutes les recherches sur le sujet ont uniquement caractérisé l'huile produite, ne montrant alors qu'une partie des gains obtenus par pyrolyse solaire. La totalité des gains, et tout particulièrement l'augmentation de la valeur énergétique des produits de la pyrolyse, n'a pas encore été déterminée, alors qu'elle est un critère d'évaluation très important de la conversion solaire de la biomasse. Il est donc nécessaire de caractériser tous les produits de la pyrolyse.

Matériels et méthodes

La Figure 3 montre un schéma du montage expérimental de pyrolyse solaire à l'échelle laboratoirequi a été utilisé dans cette étude. Un système de pyrolyse solaire a été conçu et fabriqué en plaçant un réacteur de pyrolyse de biomasse au point focal d'un four solaire à axe vertical. Dans un tel four solaire un héliostat est asservi pour suivre la course du soleil et ainsi renvoyer les rayons parfaitement à la verticale afin d'illuminer un miroir parabolique fixe faisant face au sol (2 m de diamètre et 0.85 m de distance focale). La puissance et la densité de flux maximales de ce système sont respectivement d'environ 1.5 kW et 12 000 kW/m². Un obturateur composé de lames mobiles de composite de carbone permet de réguler le rayonnement incident, et donc le flux solaire concentré impactant l'échantillon et, en conséquence, sa température. Le réacteur est composé d'un ballon en Pyrex possédant un diamètre de 185 mm (volume de 6 L) entourant l'échantillon, placé dans un creuset posé sur une platine réfrigérée. Le creuset est positionné au point focal Le volume interne est balayé d'un flux d'argon contrôlé par un débitmètre massique (Bronkhorst, EL-FLOW®). Un analyseur infrarouge de gaz (3100-SYNGAS), portable, est utilisé pour contrôler la concentration d'oxygène durant le processus de balayage. Le balayage de gaz est utilisé pour continuellement garder propres les parois du réacteur, ainsi que le hublot en fluorine servant à la visée pyrométrique. Une vannepointeau contrôle le flux de gaz sortant du réacteur et la pression. La température de surface de l'échantillon est mesurée grâce à un pyromètre optique «solar blind » (KLEIBER, monochromatique et opérant à 5.2 µm dans une bande

d'absorption de l'H_2O) visant l'échantillon à travers un hublot en fluorine (transparente à cette longueur d'onde). La vitesse de chauffe et la température finale souhaitées sont rentrées dans un contrôleur PID qui contrôle l'ouverture de l'obturateur en comparant la température mesurée de l'échantillon et la consigne.

Après la pyrolyse, les produits (la vapeur condensée et les gaz incondensables) passent d'abord à travers un système de récupération des liquides qui est constitué d'un tube de cuivre chauffé et d'un train de condensation à glace sèche (neige carbonique). Le train de condensation à glace sèche est formé de trois ballons contenant chacune approximativement 100 mL du solvant isopropanol (2-propanol). Le tube de cuivre est maintenu à environ 250 °C. Tous les ballons sont immergées dans de la glace sèche (température entre environ -25 °C et -15 °C). Une vanne pointeau et une pompe à vide sont placés en aval du train de condensation. Les gaz incondensables sont ensuite aspirés par la pompe à vide et collectés dans un sac à échantillons. Enfin, la composition des produits gazeux est analysée par chromatographie en phase gazeuse (SRA Instruments MicroGC 3000).

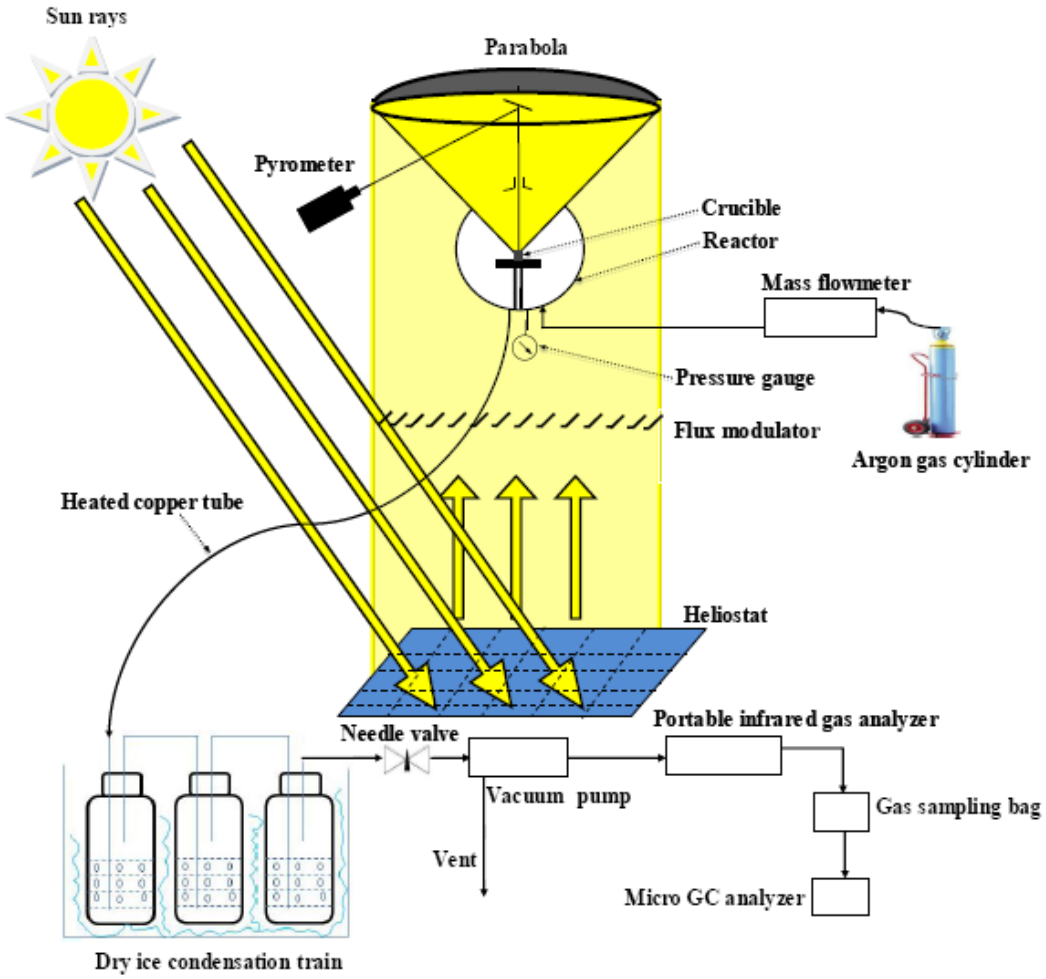

Figure 3: Schéma du réacteur solaire de pyrolyse

Des granulés de bois de hêtre composés de sciure compressée ont été utilisés comme matière première pour les expérimentations (Figure 4). Ces granulés sont de forme cylindrique, avec un diamètre de 10 mm et une hauteur de 5 mm, ce qui correspond environ à 0.3 g. La sciure, d'une taille d'environ 0.35-0.80 mm, a été fournie par l'entreprise française SPPS (www.sppsfrance.com).

Figure 4: sciure de bois de hêtre et

La matière première a été caractérisée par analyse globale (cendre, humidité, matière volatile et carbone fixé), par analyse élémentaire (C, H, O, N, S) et par constituants chimiques. Les valeurs obtenues sont reportées dans le Tableau 2.

Tableau 2: Les principales propriétés du bois de hêtre

Ultimate analysis	C	wt.%	50.8
	H	wt.%	5.9
	O*	wt.%	42.9
	N	wt.%	0.3
	S	wt.%	0.02
Proximate analysis	Volatile matter	wt.%, dry	85.3
	Fixed Carbon*	wt.%, dry	14.3
	Ash	wt.%, dry	0.4
	Moisture	wt.%	6
Chemical components	Hemicellulose*	wt.%	20.5
	Cellulose	wt.%	64.0
	Lignin	wt.%	15.5

* by difference

Quatre séries d'expérimentations (un facteur à la fois) ont été conduites et sont listées dans le Tableau 3. Les séries 1 à 9 ont été conduites dans le but de déterminer l'effet de la température finale, variant 600 à 2000 °C. La vitesse de chauffe (50 °C/s), la pression (0.44 bar), et le débit d'argon (6 NL/min) ont été fixés durant ces tests. Les séries 10 à 14 concernent l'étude de l'effet de la vitesse de chauffe (allant de 5 à 450°C/s) sous un débit d'argon constant de 6 NL/min, une pression de 0.44 bar et une température finale de 1200 °C. L'effet de la pression a été étudié dans deux séries d'expérimentations : (1) Les séries 15 à 17 ont été conduites à trois pressions différentes (0.44, 0.53 et 0.69 bar) tandis que la température, la vitesse de chauffe et le débit d'argon ont été fixés à respectivement 1200°C, 50°C/s et

6 NL/min ; (2) Les séries 18 à 21 ont été conduites en utilisant quatre pressions différentes (0.72, 0.85, 0.99 et 1.14 bar), à des valeurs fixées de température de plateau (1200 °C), de vitesse de chauffe (50°C/s) et de débit d'argon (12 NL/min). Enfin, les séries 22 à 24 ont été effectuées à 1200 °C et 50 °C/s sous 0.72 bar et 12 NL/min pour étudier l'effet du débit d'argon.

Tableau 3: Les différentes conditions de pyrolyse

	Temperature effect (Run 1-9)	Heating rate effect (Run 10-14)	Pressure effect (Run 15-21)	Argon flow rate effect (Run22-24)
Final temperature (°C)	600, 800, 900, 1000, 1200, 1400, 1600, 1800 and 2000	1200	1200	1200
Heating rate (°C/s)	50	5, 50, 150 and 450	50	50
Pressure (bar)	0.44	0.44	0.44[a], 0.53[a], 0.69[a], 0.72[b], 0.85[b], 0.99[b] and 1.14[b]	0.72
Argon flow rate (NL/min)	6	6	6 and 12	6, 9 and 12

[a] Under 6NL/min

[b] Under 12NL/min

L'approche par modification d'un seul paramètre à la fois a été utilisée pour sélectionner les facteurs prépondérants et les gammes de conditions expérimentales souhaitées pour la l'étude expérimentale avec la méthode MINITAB. Finalement, la gamme de température (de 800 à 2000 °C), la gamme de vitesse de chauffe (de 50 à 450 °C/s) et la gamme de débit d'argon (de 4 à 8 NL/min) ont été choisis comme gammes de facteurs d'influences pour obtenir un PCI des produits maximal. Un protocole de type Box-Behnken a été ensuite choisi car il est le meilleur pour trois des facteurs. Un nombre total de 15 séries d'expérimentations, incluant trois séries centrales, a été généré. Les éléments de ce protocole et les résultats sont présentés dans le Tableau 4. Un modèle de régression du second ordre a été utilisé pour corréler les réponses. On obtient alors un modèle basé sur les approximations générales en

séries de Taylor du second degré, de la forme (1):

$$Y_i = \beta_0 + \sum_{j=1}^{k} \beta_j x_{ij} + \sum_{j=1}^{k} \beta_{jj} x_{ij}^2 + \sum_{j=1}^{k-1} \sum_{j>j}^{k} \beta_{jj'} x_{ij} x_{ij'} + \varepsilon_i \qquad (1)$$

Tableau 4: Plan d'expérience de Box-Behnken et résultats

RunOrder	Design pattern			Temperature	Heating rate	Argon flow rate	Gas yield	Char yield	Liquid yield	Gas LHV	CO molar yield	H_2 molar yield
	T	H	A	(^{o}C)	(^{o}C/s)	(NL/min)	(wt.%)	(wt.%)	(wt.%)	(kJ/kg of wood)	(mol/kg of wood)	(mol/kg of wood)
1	0	0	0	1400	250	6	59.8	8.6	31.6	11210.8	16.9	19.5
2	-1	0	1	800	250	8	28	16.7	55.3	4064.7	5.3	2.8
3	0	0	0	1400	250	6	58.8	9.6	31.6	10961.7	16.2	17.9
4	0	-1	1	1400	50	8	60.2	8.8	31	10066.0	16.3	13.4
5	1	-1	0	2000	50	6	61.9	8.4	29.7	10248.0	17.7	16.5
6	1	0	-1	2000	250	4	66	10.2	23.8	13080.5	20.2	26.5
7	1	0	1	2000	250	8	71.5	8.2	20.3	13558.2	20.4	24.5
8	1	1	0	2000	450	6	74.6	6.7	18.7	14085.5	21.2	28.9
9	-1	1	0	800	450	6	27.5	14.9	57.6	4402.7	5.9	5.6
10	0	1	1	1400	450	8	67.6	9.7	22.7	11299.9	18.3	16.5
11	0	1	-1	1400	450	4	62.5	9.3	28.2	11713.6	17.7	19.9
12	0	-1	-1	1400	50	4	51	9.2	39.8	9260.4	15.4	14
13	-1	0	-1	800	250	4	23.8	15.6	60.6	4037.2	5.2	3.7
14	0	0	0	1400	250	6	57.9	8.7	33.4	10449.8	16.1	17.2
15	-1	-1	0	800	50	6	27.8	13.05	59.15	3971.5	6.4	1.8

Résultats expérimentaux

La Figure 5 montre la distribution des produits en fonction de la température de pyrolyse. On peut observer que la température a une influence drastique sur la formation des produits. Lorsque la température de pyrolyse augmente de 600 à 800 °C, la production de charbon diminue de 16.8% à 9.4% et la production de gaz augmente de 20.9% à 27.8%. Lorsque la température augmente jusqu'à 900°C, les productions de charbon et de gaz augmentent respectivement jusqu'à 13.3% et 29%. Une production maximale de gaz de 63.1% a été obtenue pour une température de pyrolyse de 1600 °C. Cependant, une augmentation supplémentaire de la température cause une légère diminution de la production de gaz (60.2% à 2000 °C). La production de liquide augmente jusqu'à 32.3%, tandis que la production de charbon diminue jusqu'à 7.7% à la même température.

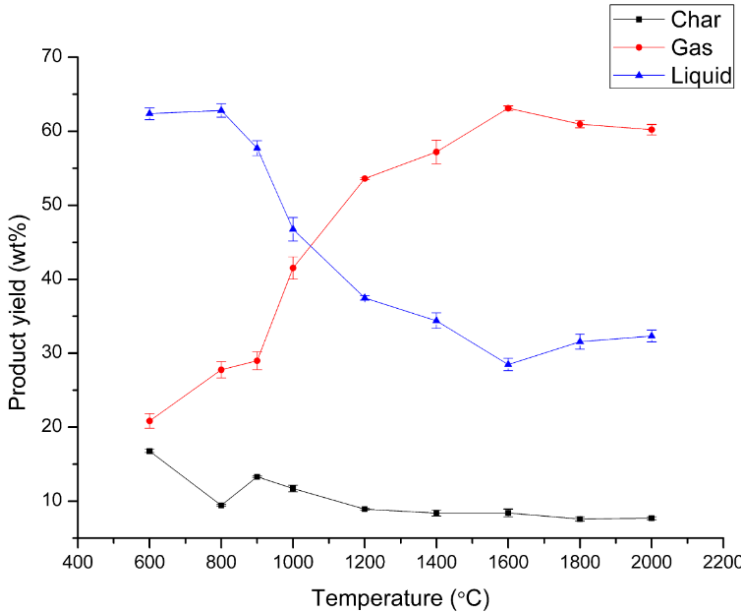

Figure 5: Rendement en produits de pyrolyse (50°C/s, 0.44bar, argon : 6NL/min).

La Figure 6 représente l'influence de la température sur la composition des gaz (a) et sur le PCI (b). Lorsque la température croit de 600 à 1600 °C, la production molaire de H_2 et de CO augmente significativement : de 0 à 15 mol/kg de bois pour l'H_2 et de 4.08 à 17.55 mol/kg de bois pour le CO. Cependant, une augmentation

supplémentaire de la température jusqu'à 2000°C entraîne une légère diminution de la producttion de CO, passant alors à 17.33 mol/kg de bois. La production de CH_4 augmente d'abord, de 0.91 à 2.45 mol/kg de bois, en raison d'une augmentation du craquage des goudrons quand la température croit de 600 à 1200 °C. Ensuite, elle diminue jusqu'à 0.87 mol/kg de bois à 2000 °C.. De 600 à 800 °C, la production de CO_2 diminue de 1.81 à 1.37 mol/kg de bois, ce qui peut être dû à la réaction inverse de Boudouard. Il n'y a eu aucun changement significatif dans la production de CO_2 et de C_2H_6 (environ 0.46 mol/kg de bois) quand la température était supérieure à 800 °C.

Les PCI des produits gazeux varient fortement avec la température, en raison de la modification de la composition des gaz (Fig. 6). Le PCI total des gaz a été multiplié par 5, passant de 1878 ±75 à 9621 ±305 kJ/kg de bois, lorsque la température est passée de 600 à 1200 °C. Cette tendance résulte principalement de la variation des PCI du CO et de l'H_2. En effet, les PCI du CO et de l'H_2 ont significativement augmenté, passant respectivement de 1153 ±50 à 4037 ±28 kJ/kg de bois et de 0 à 2953 ±180 kJ/kg de bois (toujours lorsque la température a été augmentée de 600 à 1200 °C). Au-delà, il n'y a eu aucun changement statistique significatif dans le PCI total à plus haute température.

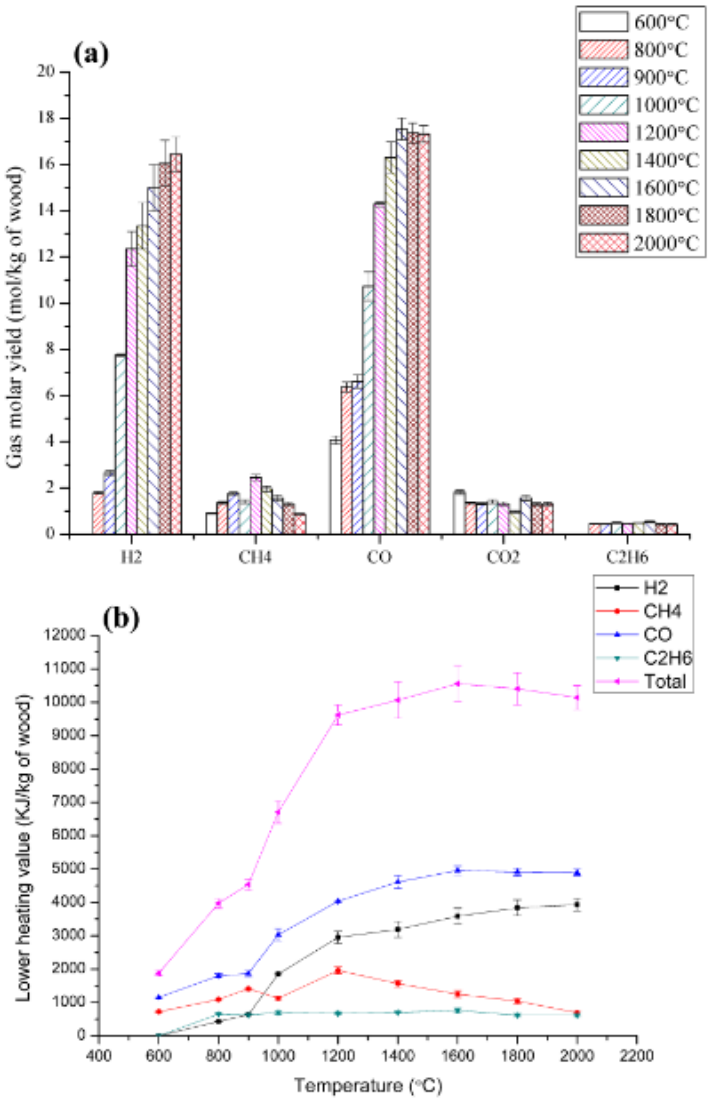

Figure 6: Composition et PCI des gaz en fonction de la température (50°C/s, 0.44bar, argon : 6NL/min): (a) composition et (b) PCI.

La distribution des produits est tracée en fonction de la vitesse de chauffe sur la Figure 7, pour une température finale de 1200 ℃. Lorsque la vitesse de chauffe passe de 5 à 50 ℃/s, la production de liquide et de charbon diminuent fortement, passant respectivement de 60.6% à37.5% et de 13.2% à8.9%, tandis que la production de gaz augmente brusquement et croit de 26.2 à 53.6%. Lorsque la vitesse de chauffe augmente à 150°C/s, le rendement de liquide augmente légèrement jusqu'à 41.5% et la production de gaz diminue jusqu'à 48.1%. Puis la production de liquide diminue lentement jusqu'à 36.5% et celle de gaz augmente légèrement jusqu'à 54.5%, lorsque la vitesse de chauffe passe à450 ℃/s.

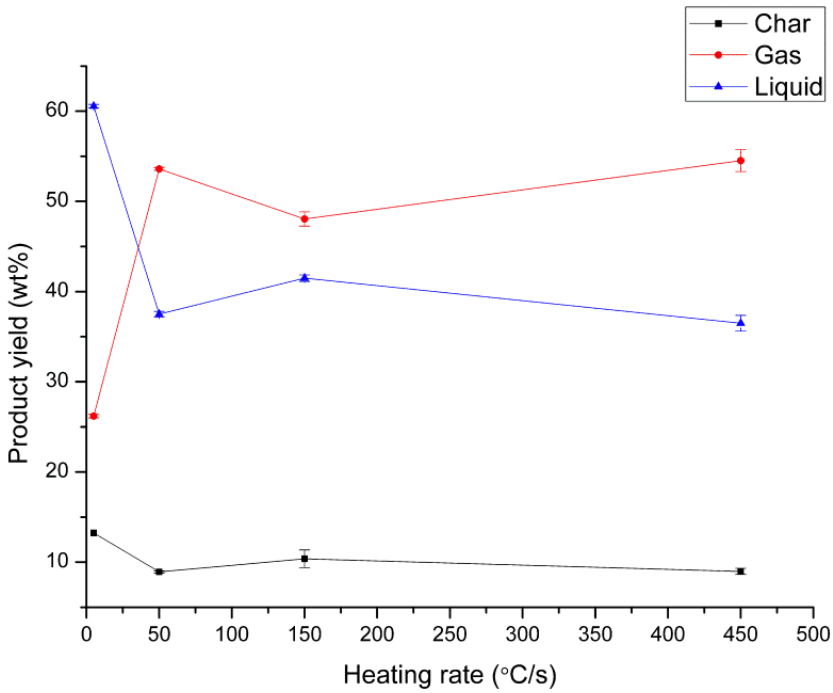

Figure 7: Les différentes productions en function de la vitesse de chauffe(conditions de pyrolyse: température de1200°C, pression de 0.44bar, et débit d'argon de 6NL/min.

La composition des gaz (a) et les variations de PCI (b) avec la vitesse de chauffe sont illustrées dans la Figure 8. La production de CO, d'H_2, de CH_4 et de C_2H_6 augmentent de façon très importante : elles passent respectivement de 5.78 à 14.29 mol/kg de bois, de 2.75 à 12.35 mol/kg de bois, et de 0 à 0.47 mol/kg de bois, lorsque la vitesse de chauffe augmente de 5 à 50 °C/s (Fig. 8a). Simultanément, la production de CO_2 diminue légèrement et varie de 1.65 à 1.41 mol/kg de bois. Lorsque la vitesse de chauffe croit à 150 °C/s, les rendements de CO et de H_2 diminuent légèrement et atteignent respectivement 12.71 et 9.40 mol/kg de bois. Toutefois, lorsque la vitesse de chauffe augmente jusqu'à 450°C/s, les productions de CO et de H_2 augmentent encore jusqu'à 14.75 et 11.45 mol/kg de bois. Il n'y a quasiment pas d'influence de la vitesse de chauffe sur les rendements en CO_2, de CH_4 et de C_2H_6 lorsque celle-ci est supérieure à50 °C/s.

Lorsque la vitesse de chauffe croit de 5 à 50 °C/s, le pouvoir calorifique inférieure total des gaz augmente de façon remarquable, passant de 3386 à

9621 kJ/kg de bois (Fig. 8b). Cette augmentation est principalement due aux variations des pouvoirs calorifiques du CO, d'H_2 et de CH_4. Cependant, les variations du pouvoir calorifique inférieur total avec la vitesse de chauffe ne sont pas très significatives lorsque cette dernière est supérieure à 50 °C/s.

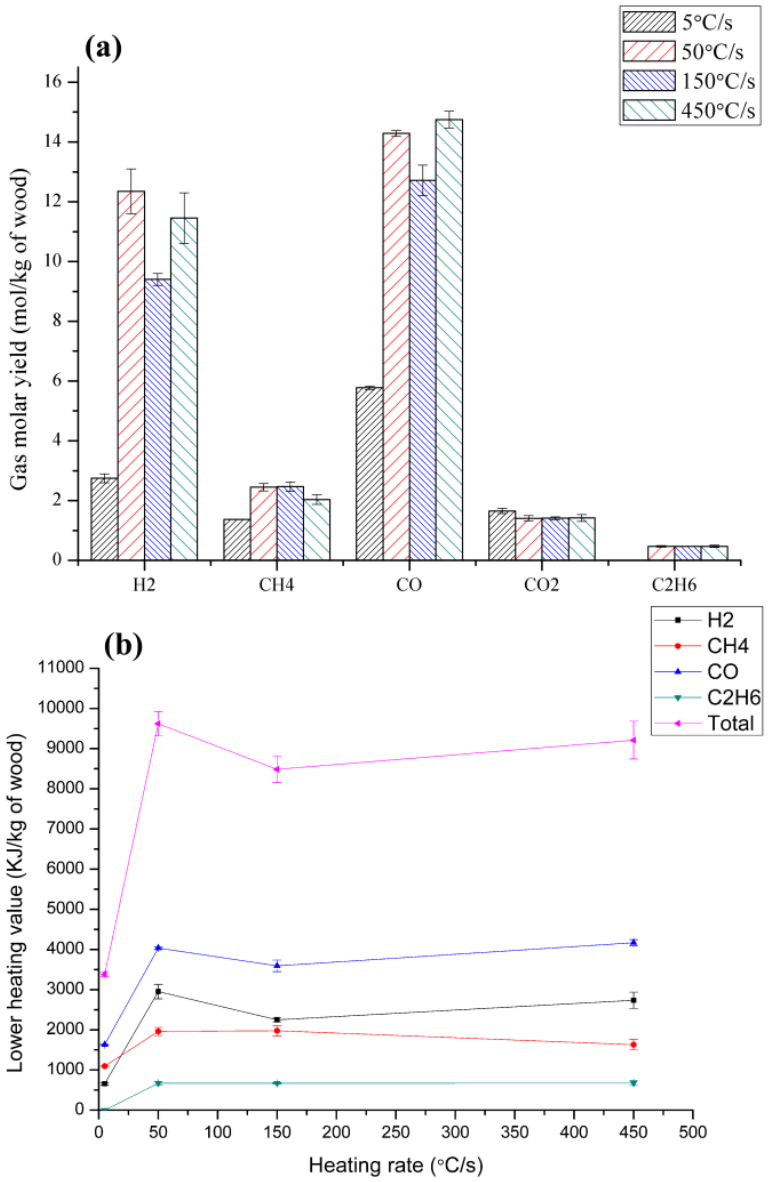

Figure 8: Caractérisation des gaz à différentes vitesses de chauffe (conditions de pyrolyse: température de 1200°C, pression de 0.44bar et débit d'argon de 6NL/min): (a) composition des gaz et (b) PCI.

Comme on peut le voir sur les surfaces de réponse (Figure 9A), l'effet de la température est plus important lorsque la vitesse de chauffe est grande. On pense que

cette effet est dû au fait que les produits de la pyrolyse primaire sont chauffés à hautes températures (>500 °C) plus rapidement lorsque la vitesse de chauffe est grande. Il y a donc plus de temps pour des réactions secondaires dans les gaz. Cette interaction entre les effets de la température et de la vitesse de chauffe n'avait pas encore été reportée dans la littérature scientifiqur et est également confirmé par le fait que le produit de la température finale et de la vitesse de chauffe (T*H) est positif. Les surfaces de réponse(Figure 9A) suggèrent également que l'augmentation de la vitesse de chauffe affecte très peu la production de gaz à des températures inférieures à 1000 °C, mais augmentent leur production à des températures supérieures. Le modèle réduit de production de gaz limité uniquement aux termes significatifs statistiquement est donné par l'Eq. (2).

$$Gas\ yield = -59.0 + 0.12171T - 0.01835H + 1.5A - 0.000033T^2 + 0.000027T*H \quad (2)$$

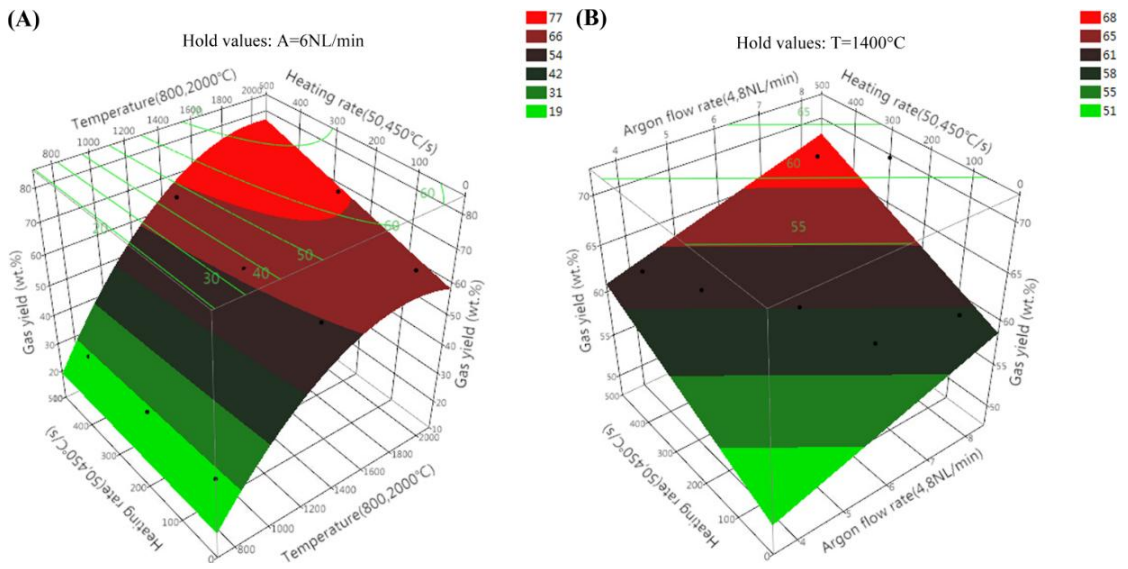

Figure 9: Surface de réponse pour le rendement en gaz (results expérimentaux: symboles noirs): (A) Influence de la temperature et de la vitesse de chauffe, Ar : 6 NL/min, (B) Influence de la vitesse de chauffe et du débit d'argon, 1400°C.

La Figure 10 représente la distribution énergétique des produits de la pyrolyse solaire à différentes températures. L'énergie totale produite est légèrement supérieure pour des températures de 600 et de 900 °C, ce qui pourrait être dû à la valeur énergétique plus importante de la bio-huile dont le rendement est supérieur à ces

températures. Quelle que soit la température, l'énergie de la bio-huile contribue à plus de 50% au contenu énergétique total des produits. Puisque la production de bio-huile diminue fortement avec la température, les contenus énergétiques de la bio-huile à 600 et à 900 °C sont significativement supérieurs (18.88 et 17.41 MJ/kg de bois, respectivement) que ceux à 1200 et à 2000 °C (12.26 et 10.57 MJ/kg de bois, respectivement). De plus, la production de biogaz augmente significativement avec la température, et les contenus énergétiques du biogaz à 600 et à 900 °C sont bien moins importants (1.88 et 4.54 MJ/kg de bois, respectivement) que ceux à 1200 et 2000 °C (9.62 et 10.14 MJ/kg de bois, respectivement).

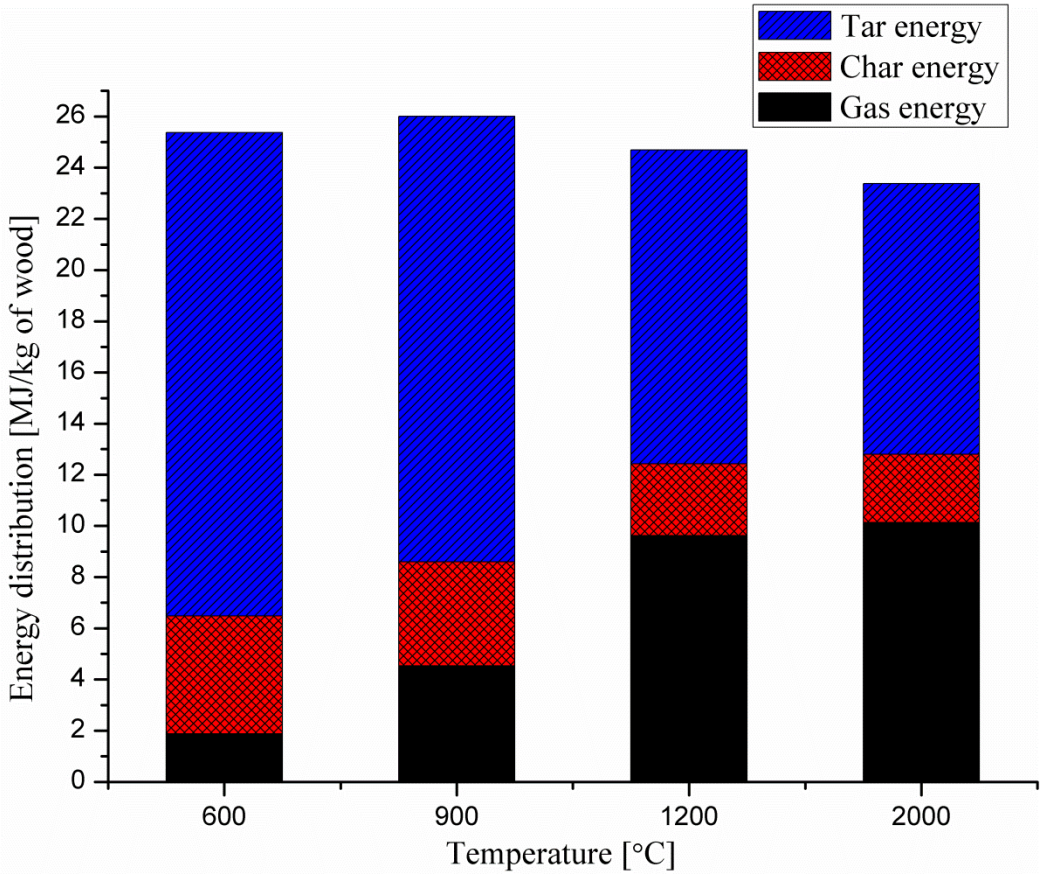

Figure 10: PCI des produits de pyrolyse en fonction de la température (50°C/s, 0.44bar, argon 6NL/min).

Le facteur d'accroissement énergétique de la pyrolyse solaire (rapport entre PCI des produits et le PCI du bois initial) est tracé en fonction de la température sur la Figure 11. Comme le montre cette figure, ce facteur augmente de 1.49 à 1.53 lorsque la température croit de 600 à 900°C. Puis il diminue légèrement jusqu'à 1.45

à 1200°C et de façon plus importante, jusqu'à 1.38, à 2000°C. Les variations de ce facteur sont dues à la diminution de la production de bio-huile avec la température.

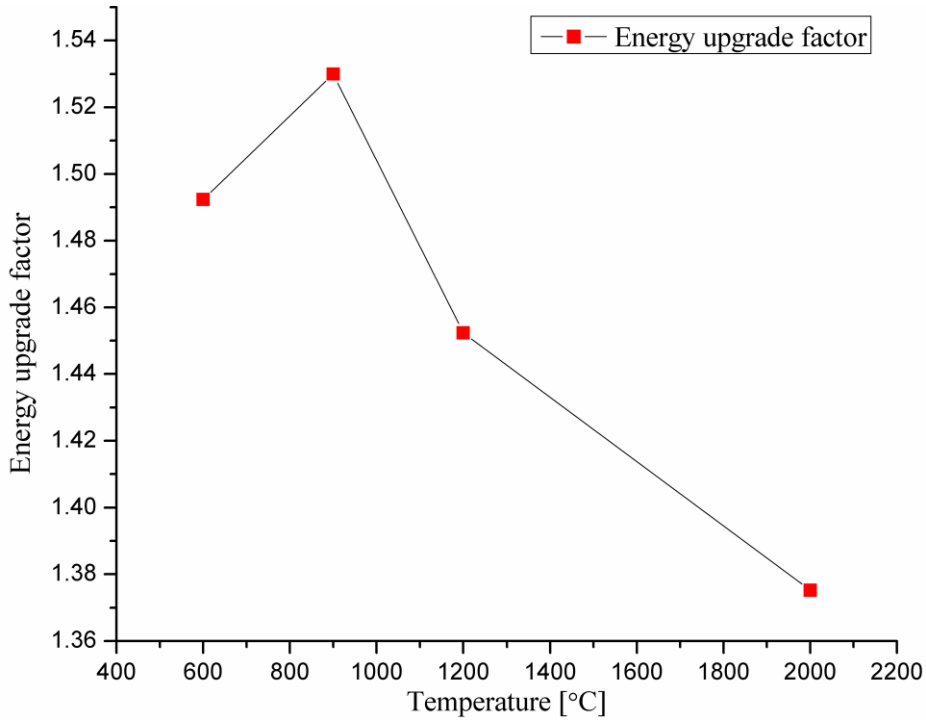

Figure 11: Facteur d'accroissement énergétique en fonction de la température(50°C/s, 0.44bar, et 6NL/min d'argon).

Les facteurs d'accroissement énergétique U pour les procédés de pyrolyse conventionnelle, de gazéification solaire et de pyrolyse solaire sont comparés dans le Tableau 5. Pour les procédés de gazéification et de pyrolyse des valeurs de U supérieures à 1 indiquent que le stockage solaire sous forme chimique est réussi, et que la valeur énergétique du carburant est augmentée. Le facteur d'accroissement énergétique de la pyrolyse solaire (1.5) est plus élevé que celui de la gazéification solaire (1.3), ce qui signifie que d'avantage d'énergie solaire peut-être stocké par pyrolyse solaire que par gazéification solaire. Cela est certainement dû à l'hypothèse de conservation de 100% de la masse pour le procédé de pyrolyse solaire. Le facteur U de la pyrolyse conventionnelle est inférieur à 1 car une partie de la charge est consommée pour fournir l'énergie nécessaire aux réactions.

Tableau 5: Comparaison des facteurs d'accroissement énergétique

Process	Feedstock	Upgrade factor
Conventional pyrolysis	Forest waste	0.92
Solar gasification	Beech Charcoal	1.3
Solar pyrolysis	Beech wood	1.5

Modèle numérique

Un schéma de la cinétique de pyrolyse du bois représenté sur la Figure 12 est utilisé dans cette étude. Les paramètres cinétiques et les enthalpies de réaction de pyrolyse ont été obtenus dans la littérature scientifique. Les coefficients stœchiométriques a et b sont ajustés avec la température et avec la vitesse de chauffe pour concorder avec les résultats expérimentaux, comme le montre le Tableau 6.

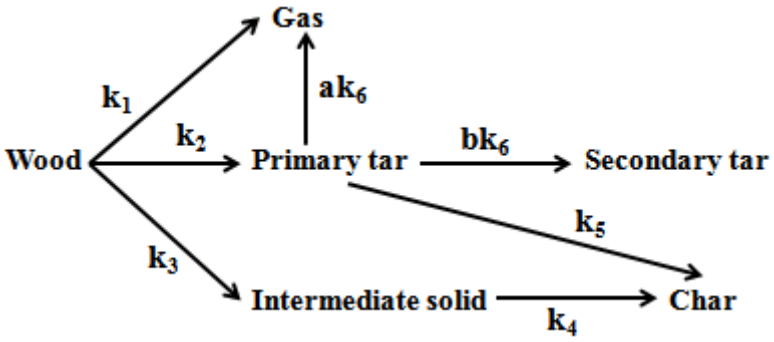

Figure 12: Modèle cinétique de pyrolyse

Tableau 6: Les coefficients stoechiométriques a et b utilizes dans le modèle

			Heating rate intervals (^{o}C/s)	
			Slow	Fast
			≤10	≥50
Temperature Intervals (^{o}C)	Low	≤600	a=0.18; b=0.82	a=0.18; b=0.82
	High	900~1200	a=0.43; b=0.57	a=0.5; b=0.5
	Very high	1600~2000	a=0.5; b=0.5	a=0.7; b=0.3

La Figure 13 schématise la zone supérieure des granulés de bois de hêtre, qui est irradiée dans le réacteur. Les côtés et le dessous du réacteur sont isolés par le creuset

et par de la mousse. En raison de la symétrie, uniquement la moitié des granulés est montrée sur la Fig. 13b.

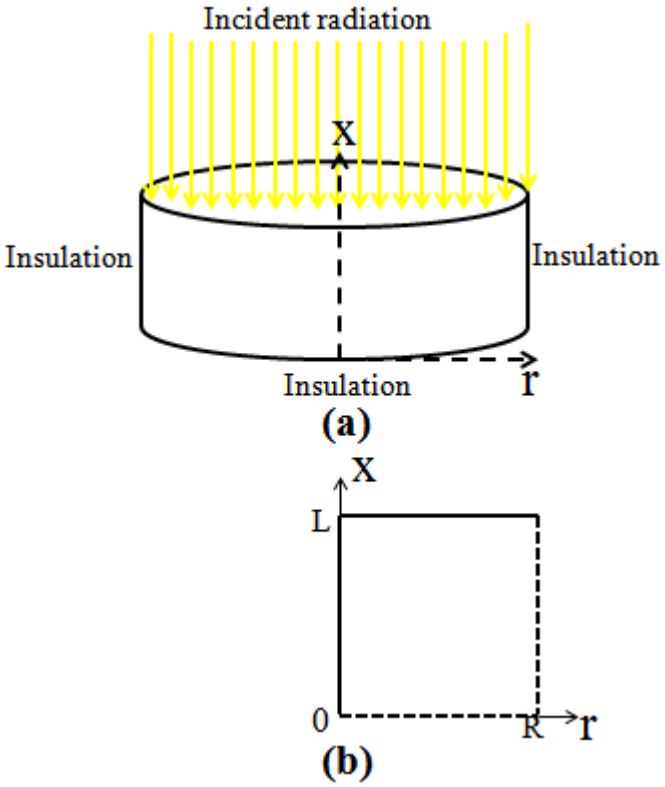

Figure 13: (a) Conditions aux limites; (b) Coordonnées axisymétriques

Résultats numériques

Le modèle a été validé par confrontation avec les données expérimentales de pyrolyse solaire effectuée à des vitesses de chauffe de 10 °C/s (lente) et 50 °C/s (rapide) et avec des températures finales de 600, 900, 1200, 1600 et 2000 °C. Les Figures 14 et 15 montrent la production totale de gaz et de liquide à différentes températures et à différentes vitesses de chauffe. Comme le montre la Figure 14, la production de gaz a tendance à augmenter avec la température et avec la vitesse de chauffe. L'augmentation de la production de gaz est probablement due à des réactions secondaires intra-particules du goudron qui sont intensifiées lorsque la température et la vitesse de chauffe augmentent. Les données calculées pour la production de liquide sont en excellente accordance avec les données expérimentales pour les deux vitesses de chauffe (Figure 15), et montrent que la production de liquide diminue avec celle-ci.

L'augmentation de la vitesse de chauffe a deux effets : (1) Le temps de séjour intra-particule pour le goudron diminue ; (2) la température du goudron augmente plus rapidement. Il est évident que le second effet est prédominant pour les échantillons de granulés utilisés. Ensuite, les réactions de décomposition du goudron sont intensifiées dans les granulés avant que le goudron puisse être libéré.

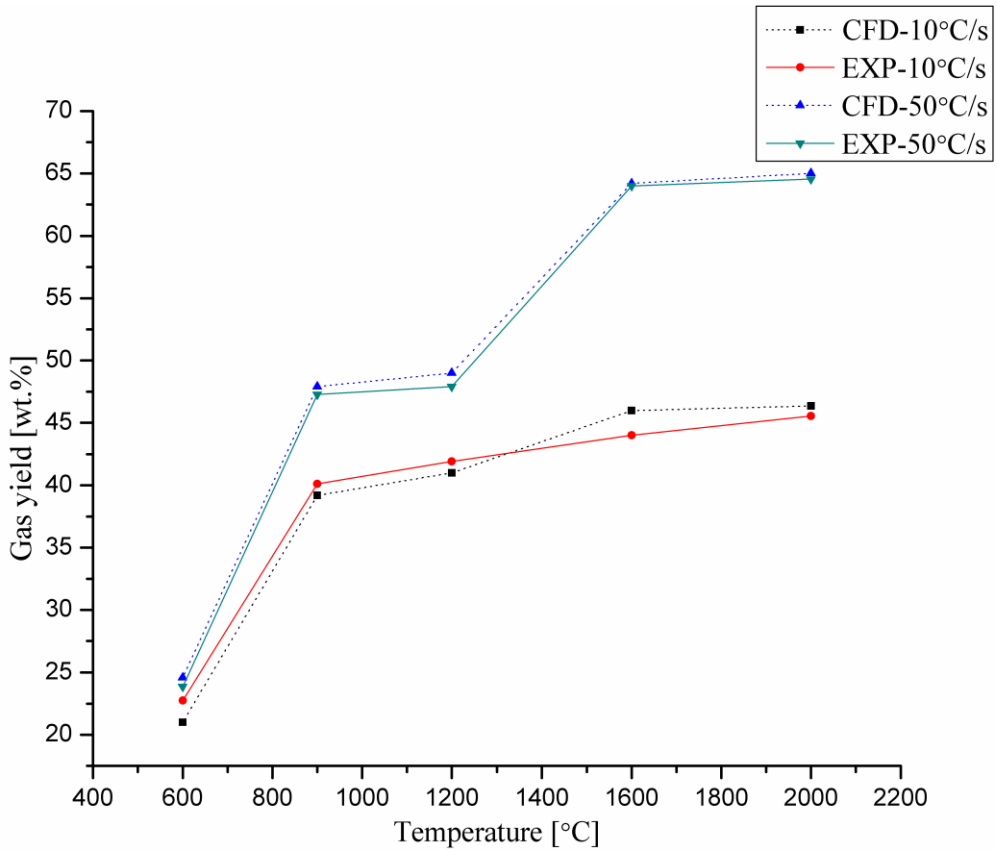

Figure 14: Comparaison entre les resultats simulés et les mesures pour le rendement en gaz.

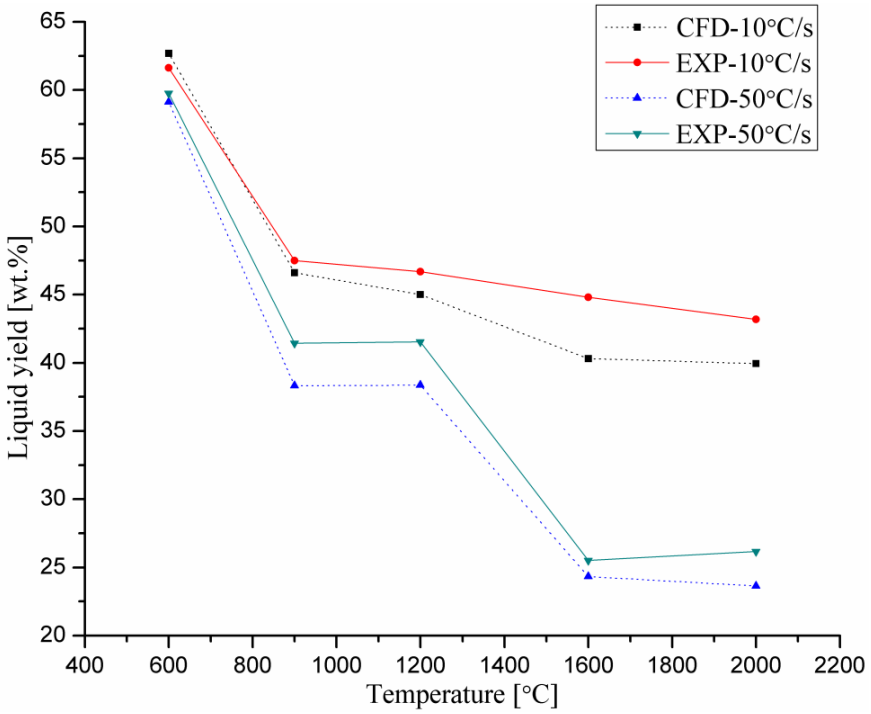

Figure 15: Comparaison entre le rendement simulé et mesuré pour le rendement en liquide.

Conclusion

(1) Pour la pyrolyse solaire, la température influence fortement la distribution finale des produits et la composition des gaz. C'est le paramètre clé, qui influence les réactions de pyrolyse solaire dans des conditions expérimentales mises en oeuvre.

(2) La production de CO et de H_2 la plus importante est obtenue pour la température finale de 1200 ℃, la vitesse de chauffe de 50 ℃/s et à pression atmosphérique, ce qui indique que ces paramètres ont un effet important sur les réactions secondaires du goudron.

(3) Le pouvoir calorifique inférieur total des gaz augmente très fortement (il est multiplié par 5) avec la température (de 600 à 1200 ℃) et avec la vitesse de chauffe des échantillons (de 5 à 50 ℃/s), résultat surtout dû aux variations de production de CO et de H_2.

(4) La conjugaison d'une température et d'une vitesse de chauffe élevées intensifie le processus. Le PCI du gaz peut être multiplié par 4 par voie solaire,

augmentant de 3257 à 14 589 kJ/kg de bois de hêtre. Le PCI maximum des gaz produits par pyrolyse solaire de bois de hêtre a été obtenu à 2000 °C et à une vitesse de chauffe de 450 °C/s

(5) Les propriétés du charbon sont influencées par la température de pyrolyse solaire et par la vitesse de chauffe. La production de charbon diminue avec la température et la vitesse de chauffe. Les propriétés du charbon de bois varie fortement avec les conditions de pyrolyse.. L'aire de Brunauer–Emmett–Teller (BET) et le volume des pores augmentent quand la température croit de 800 à 1200 °C puis diminue après. Plus l'aire de BET et plus les volumes des pores du charbon sont élevés, plus la réactivité du charbon est grande, ce qui signifie que ces deux paramètres sont de bons indicateurs de la réactivité du charbon.

(6) Il n'y a pas d'effet remarquable de la température sur la quantité d'eau et sur la concentration des éléments dans la bio-huile. Le nombre d'espèces identifiées composant le goudron augmente de 52 à 71, et le facteur d'accroissement énergétique augmente de 1.49 à 1.53, lorsque les températures de pyrolyse augmente de 600 à 900 °C.

(7) Pour la première fois, nous avons mesuré quantitativement l'effet de stockage chimique de l'énergie solaire dans des produits de pyrolyse solaire. Le facteur d'accroissement énergétique est d'environ 1.5. Cela signifie que les produits contiennent 50% plus d'énergie que la biomasse initiale. La variation de ce facteur dépend de la production de bio-huile, car elle contribue à environ 50% du contenu énergétique total des produits.

(8) Les prédictions du modèle particulaire 2D sont en bon accord avec les résultats expérimentaux. L'évolution des produits finaux et des pertes de masse de la biomasse avec la température et la vitesse de chauffe est bien représentée par le modèle. Les réactions secondaires intra-particules du goudron pour la pyrolyse de gros échantillons sont favorisées à hautes températures et à des vitesses de chauffe élevées. Grâce à cette comparaison, nous avons pu identifier les coefficients

stœchiométriques concernant la fraction massique des goudrons primaires et secondaires convertis en gaz à différentes températures et à différentes vitesses de chauffe.

Pour conclure, il peut être affirmé que la pyrolyse solaire de la biomasse est un bon moyen de stocker chimiquement l'énergie solaire. Environ 50% d'augmentation de la valeur énergétique du carburant peut être obtenue par pyrolyse solaire. De hautes températures associées à des vitesses de chauffe élevées intensifient la production de gaz pyrolytiques (principalement du CO et de l'H_2) par réactions secondaires du goudron.